First Principles Studies of Gas Adsorption

in Metal Organic Frameworks

by

Kuang Yu

A dissertation submitted in partial fulfillment of the requirements for the degree of

Doctor of Philosophy

(Chemistry)

at the

University of Wisconsin-Madison

2013

Date of final oral examination: 07/22/2013

This dissertation is approved by the following members of the Final Oral Committee:

> J.R. Schmidt, Assistant Professor, Chemistry
>
> Qiang Cui, Professor, Chemistry
>
> Gilbert Nathanson, Professor, Chemistry
>
> Daniel Fredrickson, Assistant Professor, Chemistry
>
> Dane Morgan, Associate Professor, Material Science and Engineering

Abstract

This thesis focuses on using theoretical and computational techniques to study gas absorption in metal organic frameworks (MOFs). Due to their relevance in carbon capture processes, we are mainly interested in predicting carbon dioxide (CO_2) absorption properties in MOFs. The ultimate goal of these studies is to establish a methodology capable of computing the gas loading behavior of MOFs with minimal empirical inputs, such that high throughput structure screening can be carried out via computer simulation. We are also dedicated to understanding the underlying physics of guest-framework interactions, as it will enable us to provide general guidelines to design MOFs with better gas adsorption performance.

In this thesis, we will investigate two classes of MOFs, namely those with and without open metal sites. MOFs with coordinatively saturated metal centers are dominated by weak nonbonding interactions between the guest molecules and the organic ligands. Therefore, a consistent set of force field parameters will be developed for both guest molecules and frameworks based on first principles calculations. Utilizing symmetry adapted perturbation theory (SAPT), we will decompose the interaction energies into distinct physical meaningful terms, which will then be fit with physically motivated functional forms. We will show that the resulting potential has minimum empirical parameters, is extraordinary accurate, and is transferrable across different chemical environments. In addition, we will develop a novel algorithm which will accelerate our simulations by several orders of magnitude, thus enabling us to conduct large-scale structure screening. The aforementioned techniques will be used to investigate several industrially-relevant problems, including the cooperative synergistic effects between different types of organic ligands.

In contrast to the first class of MOFs, the loading isotherms of systems with open metal centers are largely controlled by several strong binding sites, in which perturbation theory generally fails to converge. Consequently, the SAPT-based techniques used previously are no longer applicable; instead, we will study these systems using density functional theory (DFT) methods. We will illustrate the effect of flue gas contaminants on the metal centers, an important concern for this class of MOFs in industrial

application. Finally, we will explore the physical properties of the open-metal binding sites by studying the IR spectrum of the adsorbed molecules.

Though all these studies, we are able to establish a deep understanding to the MOF gas adsorption behavior, and we will illustrate the advantages of computer simulation techniques in this area.

Published Work and Work in Preparation

1.   Yu, K.; Schmidt, J. R., Elucidating the Crystal Face- and Hydration-Dependent Catalytic Activity of Hydrotalcites in Biodiesel Production. *J Phys Chem C* **2011,** 115, (5), 1887-1898.

2.   Yu, K.; McDaniel, J. G.; Schmidt, J. R., Physically Motivated, Robust, ab Initio Force Fields for CO_2 and N_2. *J Phys Chem B* **2011,** 115, (33), 10054-10063.

3.   Yu, K.; McDaniel, J. G.; Schmidt, J. R., Ab Initio, Physically Motivated Force Fields for CO_2 Adsorption in Zeolitic Imidazolate Frameworks. *J Phys Chem C* **2012,** 116, (2), 1892-1903.

4.   Yu, K.; Schmidt, J. R., Many-body effects are essential in a physically motivated CO_2 force field. *Journal of Chemical Physics* **2012,** 136, (3), 034503.

5.   Yu, K.; McDaniel, J. G.; Schmidt, J. R., An efficient multi-scale lattice model approach to screening nano-porous adsorbents. *Journal of Chemical Physics* **2012,** 137, (24), 244102.

6.   Yu, K.; Kiesling, K.; Schmidt, J. R., Trace Flue Gas Contaminants Poison Coordinatively Unsaturated Metal-Organic Frameworks: Implications for CO_2 Adsorption and Separation. *J Phys Chem C* **2012,** 116, (38), 20480-20488.

7.   Yu, K.; McDaniel, J. G.; Schmidt, J. R., Microscopic Origins of Enhanced Gas Adsorption and Selectivity in Mixed-Linker Metal-Organic Frameworks. *J Phys Chem C, submitted* **2013**.

8.   Yu, K.; Schmidt, J. R., Comment on "How Well Do Metal-Organic Frameworks Tolerate Flue Gas Impurities?". *J Phys Chem C* **2013,** 117, (6), 3192-3192.

Table of Contents

List of Figures

List of Tables

Acknowledgments

First of all, and most importantly, I would like to thank my parents for their understanding and their selfless support during my pursuit of a Ph. D. degree. They were the first people who helped me enjoy the beauty of the nature, the passion of exploration, and the happiness of revealing the mystery of the truth. As ordinary working people, like so many others in China, they inspired my interests in science and technology, and gave me the courage to select a career of scientific research. I would particularly thank their rigorous disciplinary training in my early childhood, which give me the capability of managing time and keeping a healthy lifestyle. Their instruction will be a precious treasure for my whole life.

I would also acknowledge all the theoretical chemistry professors in UW, Madison: Professor Jim Skinner, Professor Qiang Cui, Professor Arun Yethiraj and Professor Ned Sibert. They compose a group of top-level researchers, and it is a great honor for me to have the opportunity to work with them in Madison. Their advice is of paramount importance to me, and their rich knowledge and patience always make our discussions extraordinary fruitful and enjoyable.

It is also my great pleasure to have worked with my group colleagues for the past five years, as we shared lots of memorable time together. I would like to give special credit to Jesse McDaniel, as we collaborated on the same project for four years. He is the best editor for all my publications. I am extraordinarily thankful for the rodeo games, baseball games, paintball games, parties and running schedules he arranged for me, as he has put so many efforts to introduce the American culture to me.

Finally, I owe the utmost gratitude to my advisor, Professor JR Schmidt, who taught me the way of conducting scientific research. His enthusiasm and intelligence always set up a perfect example for me to follow, and he is always available to help when I am confused or frustrated. As JR's first student, it is truly amazing to witness him building up everything from scratch and gradually expanding his research territory. I am grateful to have such a genius and devoted advisor at the beginning of my research career. His five years of mentoring is certainly appreciated.

Chapter 1. General Introduction

Table of Contents

1.1 Introduction to Carbon Dioxide Sequestration Problem

The increasing atmospheric concentration of carbon dioxide (CO_2), the major component of greenhouse gas, has raised worldwide concerns. The climate changes associated with global warming create huge challenges to human society, on both a local and global scale. The CO_2 concentration in the atmosphere has increased by more than 30% in the past two and half centuries, largely due to human activities in the industrial era.[1] In order to restrict average global temperature increases to within 2-3°C, it is necessary to stabilize the atmospheric CO_2 levels to 550 ppm by 2100.[1] In order to accomplish this, CO_2 emissions must be reduced by 7-70% compared to the current level, a goal which can ultimately be achieved through replacing fossil fuels with other renewable energy sources (solar, wind, hydroelectric *etc.*). Because a significant amount of time and capital investment will be required to develop

technologies related to these renewable energy sources, it is also necessary to simultaneously develop more easily-implemented strategies for temporarily mitigating and reducing CO_2 emissions. Carbon capture and storage (CCS) is one such strategy, and is one of the more practical techniques currently available industrially.

Put simply, CCS processes use adsorbents to capture CO_2 from flue gas, storing the captured gas in multiple forms, such as underground injections, ocean storage, mineral carbonates, and woody biomass.[2, 3] As a temporary solution, CCS is mainly suitable for large fix point carbon sources (such as coal-fired power plants), which accounts for about 60% of global CO_2 emission.[4] For distributed carbon sources such as automobiles, CCS can also be utilized. Provided traditional automobile engines can be replaced with clean energy carriers such as H_2, the energy input required to produce the carrier can be obtained from stationary power plants, where CCS process can be implemented.[4] Consequently, there is a wide range of applications for CCS, making it of paramount importance to improve the energy and economic efficiency of this process.

There are three typical techniques utilized in the CCS process: post-combustion, pre-combustion, and oxy-fuel combustion. In the post-combustion process, CO_2 is selectively removed from the flue gas after the combustion of fossil fuels. Typically, post-combustion flue gas is at atmosphere pressure, and ranges in temperature from 60 to 400°C, depending on different combustion conditions. The flue gas is composed primarily of N_2 (~70% by volume), CO_2 (~15%), and H_2O (~10-20%). The remainder of the gas is made up of excess O_2 and trace amounts of other contaminants (SO_x, NO_x *etc.*).[5] The ideal adsorbent in this working condition should have a high selectivity for CO_2 over N_2 at low CO_2 partial pressures, and must be reasonable stable against high temperature, high humidity, and acid contamination.

In the pre-combustion process, fossil fuels are first converted to a mixture of CO_2 and H_2 via stream reforming/partial oxidation and water gas shift reactions; the CO_2 is then separated out, while the remaining H_2 can be used as a carbon free fuel. The CO_2/H_2 mixture produced in this process has much

higher pressure and higher CO_2 concentration (up to 60% by volume), and is consequently more amenable to the CCS process, although the initial fuel conversion steps are more elaborate and costly.[4]

The last technique, oxy-fuel combustion, utilizes high purity oxygen, instead of air, as an oxidizer, thus generating flue gases both free of N_2 and with high CO_2 concentrations. Despite its promise as a CCS technique, oxy-fuel combustion is currently still in demonstration phase, and is thus not currently used in large scale industrial applications.[4]

Among the three procedures, the post-combustion process is most amenable to retrofitting the existing coal-fired plants, since it does not require modifications to the current combustion process. Therefore, this thesis will focus primarily on the post-combustion process, as it is currently considered to be among the most viable alternatives.

A key step of the post-combustion gas separation is to extract pure CO_2 from the flue gas mixture using gas adsorption. Two viable procedures are available for this step: Pressure Swing Adsorption (PSA) and Temperature Swing Adsorption (TSA).[6] The flue gas is fed into the column filled with adsorbent at high pressure or low temperature, respectively, and after the column is saturated with CO_2, it is purged at low pressure or high temperature. The difference of the CO_2 loading capacities at adsorption and purging conditions represents the working capacity, which is the most important indicator for the adsorbent efficiency. In our simulations, this working capacity will be a major descriptor of the quality of a certain type of adsorbent.

A key improvement for the post-combustion process is the development of a better and more cost-effective adsorbent. Currently, the dominant post-combustion process technique utilizes an aqueous amine scrubber, for example, monoethanolamine (MEA). As a chemical adsorbent, MEA binds CO_2 molecule reversibly to form a carbamate-like compound with high adsorption energy and excellent selectivity. However, the MEA technique suffers from several severe problems that limits its further application. First of all, the O_2 present in the flue gas oxidizes the scrubber and cause degradations of the solvent and corrosions to the equipment, increasing operating costs. Furthermore, several contaminant

species such as SO_x and NO_x form stable, non-regeneratable salts with MEA and cause a steady loss of amine. To compensate for this effect, extra preprocesses are required to remove the sulfur and nitrogen from the flue gas before it is fed to the CCS system. Most importantly, the cost of running MEA scrubbing system is extremely high due to the tremendous energy cost to regenerate the MEA after the saturation.[7, 8]

To overcome the shortcomings of amine scrubbers, several types of alternative adsorbents are under development, including polymer membranes,[9] ionic liquids,[10] and porous solid materials[11] (zeolites, nano-tubes, metal organic frameworks *etc.*). Besides large working capacity, high selectivity, high diffusivity and reasonable stability are the basic requirements for any new practical adsorbents. Moreover, the new adsorbent should also have much lower heat capacities, thus the energy cost in the regeneration process can be reduced. This thesis will focus on metal organic frameworks (MOFs), a new class of absorbants that have shown excellent performance for all the properties mentioned above.

1.2 Metal Organic Frameworks (MOFs) — A Promising New Material for Gas Adsorption

Metal organic frameworks (MOFs) are a family of crystalline porous solid that are composed of two different secondary building units (SBUs): metal centers and organic linker groups. Metal centers are bridged by polydentate organic ligands to form three-dimensional networks and nanometer scale micro-pores. Small guest molecules, such as CO_2, N_2, CH_4 or H_2, can reside in and between the pores interact with the organic linkers and/or metal centers. MOFs have attracted an enormous amount of interest due to their potential applications in areas such as gas separation,[12] gas storage,[13] chemical sensing,[14] drug delivery,[15] and heterogeneous catalysis.[16] Due to the many different metal centers, organic ligands, functional groups, and connection topologies that are possible in MOFs, there exists a huge library of MOF-type structures (>100,000 possible structures).[17] Careful tuning of the chemical properties and

three-dimensional topologies of MOF leads to specifically tailored structures that are suitable for a wide range of applications. Here, we will focus on identifying optimal MOF structures for the selective adsorption of CO_2. Due to the tremendous number of possible MOF geometries and structures, experimentally identifying these MOF structures is nontrivial. Therefore, in the following chapters, we will use computer simulation techniques to facilitate the prediction of MOF properties. General guidelines will be provided to design MOFs with better performance.
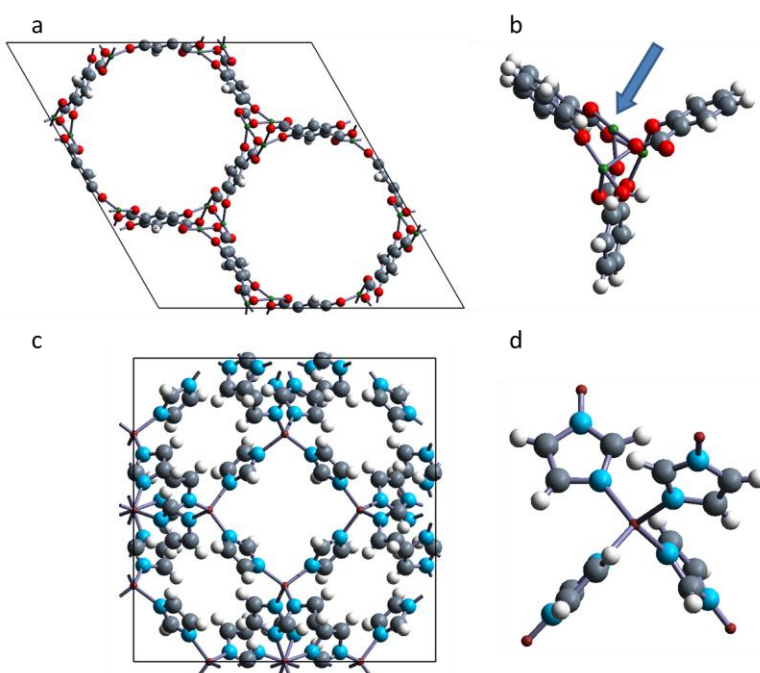
Figure 1.1: Structures of MOFs. a) Unit cell of Mg-MOF-74. b) Local structure model of Mg-MOF-74. The arrow points to the open Mg site, c) Unit cell of unfunctionalized ZIF-8. d) Local structure of unfunctionalized ZIF-8.

Most MOFs can be categorized into two classes: those with coordinatively unsaturated open metal sites (CUS) and those without (see Figure 1.1). The former class, which includes the M-MOF-74 series,[18-22] HKUST-1[23] and MIL-101,[24] have metal sites that bind guest molecules strongly. This class of MOFs is also more vulnerable to water vapor or contaminants. The latter class has metal centers fully coordinated and buried inside the organic linkers. MOF-5[25] and the zeolitic imidazolate frameworks (ZIFs) family[26-34]

are typical examples of this type of MOF. For coordinatively saturated MOFs, only the linker vicinities are accessible for the guest molecules; consequently, weak nonbonding interactions, such as dispersion or induction, dominate the adsorption process. This is in contrast to the strong binding observed in MOFs with CUS. Generally, coordinatively saturated MOFs are chemically more stable, but require more delicate designs to enhance the adsorption energy. In this thesis, both classes of MOFs will be studied, using both electronic structure calculations and classical dynamic simulations.

1.3 Existing Work and Challenges in Theoretical Simulation

The two different classes of MOFs (namely, coordinatively saturated and coordinatively unsaturated MOFs) present new challenges to the theoretical simulation community; each class requires a unique strategy to predict different MOF properties.[35] Many MOFs (typically MOFs with CUS) have strong binding sites that dominate the adsorption process. In these cases, simple adsorption models, such as the Langmuir model, can be utilized to describe the system. Input parameters of the Langmuir model, such as adsorption energies associated with different sites, are calculated using electronic structure methods. Due to the multi-reference characteristics of the transition metal ions, the fidelities of low-level methods like density functional theory (DFT) are not guaranteed, and careful benchmarks are necessary. While potentially more accurate, the applications of high-level post Hartree-Fock techniques (e.g. MP2, coupled cluster, CASSCF *etc.*) are limited to small cluster models due to their computational expense. Many studies have been performed using all of these types of calculations, ranging from normal DFT to CASPT, with either truncated cluster models or full periodical structures.[35] There are also some efforts dedicated to develop computationally inexpensive force field descriptions for the strong binding metal sites, with parameters fitted to MP2[36] or coupled cluster levels of theory.[37-39] However, these existing *ab initio* based force fields for open metal sites often fail to provide both accurate and robust predictions, and need to be further improved in order to achieve their full utility. In this thesis, both DFT and ab initio methods will

be utilized to study the open metal centers of a few particularly interesting systems. More accurate force field development for exposed metal ions is subject to future research.

Other MOF systems dominated by linker-guest interactions (typical of MOFs with coordinatively saturated metal centers) are also worth consideration, due to their extraordinary stabilities against high temperature, humidity and various solvents. The linker-guest interactions in these systems are much more versatile and tunable compared to the metal-guest interactions. These interactions are weak physical contacts, small in magnitude compared to chemical bond, and difficult to compute using low level DFT methods. Moreover, the loading capacity is related exponentially to the adsorption energy; hence high accuracy in energy calculation (about 2~3kJ/mol of error) is required to ensure the final error be controlled within 20%. Of the abovementioned *ab initio* calculations, only the (rather expensive) coupled cluster level of theory is expected to provide the necessary level of accuracy for these systems. Furthermore, these weak interacting systems do not have well defined adsorption sites, necessitating the use of finite temperature sampling, a technique that is not viable with pure electronic structure approaches. To date, most studies utilize classical simulation technique, typically grand canonical Monte Carlo (GCMC), in conjunction with generic force fields parameterized empirically.[35] While easy to implement and fast to compute, these empirical potentials (UFF,[40] DREIDING,[41] OPLS[42] *etc.*) are in general not transferable and accurate enough.

Part of the goal of this thesis is to develop a robust, physically-motivated force field for MOF systems based on highly accurate ab initio calculations. And the carefully benchmarked potentials are utilized in the classical simulations to help solving practical problems related to MOF applications. Moreover, we will attempt to develop a general methodology to build intermolecular force fields based on first principles calculations, for any generic system. This thesis will illustrate the advantage of fitting individual energy decomposition terms with clear physical meanings and using physically-motivated functional forms. Further details will be discussed in the next three chapters (Chapter 2-4).

1.4 Overview

Before starting the main body of the thesis, the contents are briefly summarized in this section. The structure of this thesis is as following.

In the Chapter 2 and 3, an innovative CO_2/N_2 force field (SYM model) is developed, on the basis of symmetry adapted perturbation theory (SAPT). The interactions energies are computed with a physically meaningful decomposition, and are fitted term by term using proper functionals forms. This model is extremely transferable and shows superior performance compared to all other existing models for both oligomer and bulk properties. This model is utilized to describe the guest-guest interactions in all later simulations and it also serves as a "proof of concept" example to illustrate the validity of our force field development methodology. In Chapter 3, we illustrate the importance of incorporating many body terms in designing ab initio based force fields. We elaborate several feasible ways to implement many body effects, which are readily generalized to any generic force field development.

In Chapter 4, the methodology established in the previous two chapters is utilized to design transferable potentials for zeolitic imidazolate frameworks (ZIFs), a particular class of MOFs. SAPT calculations are carried out between the guest molecules and carefully designed cluster models of ZIFs, and the resulting force field (ZIFFF) is tested with various ZIF structures. It is shown that the ZIFFF is transferable with all the test cases. Furthermore, its accuracy exceeds all existing generic force fields, even though no experimental data input is used.

In Chapter 5, a novel and fast simulation technique for studying nanoporous solid gas adsorption is developed on the basis of the lattice model. Using a rigid-framework assumption, the continuous adsorption space is discretized and a lattice model is constructed. Parameters are calculated using atomistic simulation. This method retains comparable accuracies to traditional atomistic GCMC simulations, but has the advantage of being two to three orders of magnitude faster than these methods.

This lattice model allows for large scale screening on a significantly reduced time scale, and enables the use of more accurate, expensive polarizable force fields.

In Chapter 6, the ZIFFF/SYM force field and the fast lattice model simulation technique are combined to solve a practical problem in the MOF community. Following work done by Yaghi and coworkers, we systematically study the synergistic effect exist in the mix ligand MOF systems. We demonstrate the microscopic mechanism underlying this phenomenon, and predict a few MOF systems that may experience significant synergistic effects.

For Chapter 7, we turn our focus to systems with coordinatively unsaturated open metal sites (CUS). In this chapter, the contaminant effect, a critical piece of information in industrial application, is studied for two particularly interesting MOF systems: Mg-MOF-74 and MIL-101. Using various electron structure techniques and Langmuir-type models, we successfully identify the most detrimental contaminant species for the target MOF systems.

In Chapter 8, we illustrate how computation technique can be utilized to facilitate understanding the interaction of the adsorbates with coordinatively unsaturated metal sites. Cooperating with experimentalists, we study the IR frequency shift for both H_2 and CO_2 molecules adsorbed in the MOF-74 series of MOFs. We are able to not only predict the experimental frequency shift in a reasonable accuracy, but also make direct connection between the experimental data and the underlying physics. Through the theoretical analysis, we successfully reproduce the observed IR spectrum. And more importantly, we achieved deeper insights to the physical properties of the guest-metal interactions.

Finally, in Chapter 9, we summarize the previous results and derive our final conclusion, that theoretical simulations are extremely useful in designing better gas adsorbents. In addition, several possible directions are proposed for future research.

Bibliography

1.   *Climate Change 2001: Synthesis Report*. Intergovernmental Panel on Climate Change: 2001.

2.   Lackner, K. S., A guide to CO_2 sequestration. *Science* **2003,** 300, (5626), 1677-1678.

3.   Oelkers, E. H.; Cole, D. R., Carbon Dioxide Sequestration: A Solution to a Global Problem. *Elements* **2008,** 4, (5), 305-310.

4.   *Carbon Dioxide Capture and Storage*. Intergovernmental Panel on Climate Change: 2005.

5.   *Carbon Capture 2020 Workshop summary*; NETL: University of Maryland Inn & Conference Center, College Park, MD 20742, 2009.

6.   Yang, R. T., *Gas separation by adsorption processes*. Butterworth Publishers,Stoneham, MA: 1986.

7.   Davison, J.; Freund, P.; Smith, A. *Putting Carbon Back into the Ground*; IEA Greenhouse Gas R&D Programme: 2001.

8.   Adams, D.; John, D. *Capturing CO_2*; IEA Greenhouse Gas R&D Programme: 2007.

9.   Merkel, T. C.; Lin, H. Q.; Wei, X. T.; Baker, R., Power plant post-combustion carbon dioxide capture: An opportunity for membranes. *J Membrane Sci* **2010,** 359, (1-2), 126-139.

10.   Karadas, F.; Atilhan, M.; Aparicio, S., Review on the Use of Ionic Liquids (ILs) as Alternative Fluids for CO_2 Capture and Natural Gas Sweetening. *Energ Fuel* **2010,** 24, 5817-5828.

11.   Samanta, A.; Zhao, A.; Shimizu, G. K. H.; Sarkar, P.; Gupta, R., Post-Combustion CO_2 Capture Using Solid Sorbents: A Review. *Ind Eng Chem Res* **2012,** 51, (4), 1438-1463.

12.   Li, J. R.; Kuppler, R. J.; Zhou, H. C., Selective gas adsorption and separation in metal-organic frameworks. *Chem Soc Rev* **2009,** 38, (5), 1477-1504.

13.   Ma, S. Q.; Zhou, H. C., Gas storage in porous metal-organic frameworks for clean energy applications. *Chem Commun* **2010,** 46, (1), 44-53.

14.   Allendorf, M. D.; Bauer, C. A.; Bhakta, R. K.; Houk, R. J. T., Luminescent metal-organic frameworks. *Chem Soc Rev* **2009,** 38, (5), 1330-1352.

15.   Liedana, N.; Galve, A.; Rubio, C.; Tellez, C.; Coronas, J., CAF@ZIF-8: One-Step Encapsulation of Caffeine in MOF. *Acs Appl Mater Inter* **2012,** 4, (9), 5016-5021.

16.   Lee, J.; Farha, O. K.; Roberts, J.; Scheidt, K. A.; Nguyen, S. T.; Hupp, J. T., Metal-organic framework materials as catalysts. *Chem Soc Rev* **2009,** 38, (5), 1450-1459.

17.   Wilmer, C. E.; Leaf, M.; Lee, C. Y.; Farha, O. K.; Hauser, B. G.; Hupp, J. T.; Snurr, R. Q., Large-scale screening of hypothetical metal-organic frameworks. *Nat Chem* **2012,** 4, (2), 83-89.

18.   Dietzel, P. D. C.; Blom, R.; Fjellvag, H., Base-induced formation of two magnesium metal-organic framework compounds with a bifunctional tetratopic ligand. *Eur J Inorg Chem* **2008**, (23), 3624-3632.

19.   Dietzel, P. D. C.; Johnsen, R. E.; Blom, R.; Fjellvag, H., Structural changes and coordinatively unsaturated metal atoms on dehydration of honeycomb analogous microporous metal-organic frameworks. *Chem-Eur J* **2008,** 14, (8), 2389-2397.

20.   Dietzel, P. D. C.; Morita, Y.; Blom, R.; Fjellvag, H., An in situ high-temperature single-crystal investigation of a dehydrated metal-organic framework compound and field-induced magnetization of one-dimensional metaloxygen chains. *Angew Chem Int Edit* **2005,** 44, (39), 6354-6358.

21.   Matzger, A. J.; Caskey, S. R.; Wong-Foy, A. G., Dramatic tuning of carbon dioxide uptake via metal substitution in a coordination polymer with cylindrical pores. *J Am Chem Soc* **2008,** 130, (33), 10870-10871.

22.   Rosi, N. L.; Kim, J.; Eddaoudi, M.; Chen, B. L.; O'Keeffe, M.; Yaghi, O. M., Rod packings and metal-organic frameworks constructed from rod-shaped secondary building units. *J Am Chem Soc* **2005,** 127, (5), 1504-1518.

23.   Chui, S. S. Y.; Lo, S. M. F.; Charmant, J. P. H.; Orpen, A. G.; Williams, I. D., A chemically functionalizable nanoporous material [Cu-3(TMA)(2)(H2O)(3)](n). *Science* **1999,** 283, (5405), 1148-1150.

24.   Ferey, G.; Mellot-Draznieks, C.; Serre, C.; Millange, F.; Dutour, J.; Surble, S.; Margiolaki, I., A chromium terephthalate-based solid with unusually large pore volumes and surface area. *Science* **2005,** 309, (5743), 2040-2042.

25.   Li, H.; Eddaoudi, M.; O'Keeffe, M.; Yaghi, O. M., Design and synthesis of an exceptionally stable and highly porous metal-organic framework. *Nature* **1999,** 402, (6759), 276-279.

26.   Banerjee, R.; Furukawa, H.; Britt, D.; Knobler, C.; O'Keeffe, M.; Yaghi, O. M., Control of Pore Size and Functionality in Isoreticular Zeolitic Imidazolate Frameworks and their Carbon Dioxide Selective Capture Properties. *J Am Chem Soc* **2009,** 131, (11), 3875-3877.

27.   Banerjee, R.; Phan, A.; Wang, B.; Knobler, C.; Furukawa, H.; O'Keeffe, M.; Yaghi, O. M., High-throughput synthesis of zeolitic imidazolate frameworks and application to CO_2 capture. *Science* **2008,** 319, (5865), 939-943.

28.   Hayashi, H.; Cote, A. P.; Furukawa, H.; O'Keeffe, M.; Yaghi, O. M., Zeolite a imidazolate frameworks. *Nat. Mater.* **2007,** 6, (7), 501-506.

29.   Morris, W.; Doonan, C. J.; Furukawa, H.; Banerjee, R.; Yaghi, O. M., Crystals as molecules: Postsynthesis covalent functionalization of zeolitic imidazolate frameworks. *J Am Chem Soc* **2008,** 130, (38), 12626-+.

30.   Morris, W.; He, N.; Ray, K. G.; Klonowski, P.; Furukawa, H.; Daniels, I. N.; Houndonougbo, Y. A.; Asta, M.; Yaghi, O. M.; Laird, B. B., A Combined Experimental-Computational Study on the Effect of Topology on Carbon Dioxide Adsorption in Zeolitic Imidazolate Frameworks. *The Journal of Physical Chemistry C* **2012,** 116, (45), 24084-24090.

31.   Morris, W.; Leung, B.; Furukawa, H.; Yaghi, O. K.; He, N.; Hayashi, H.; Houndonougbo, Y.; Asta, M.; Laird, B. B.; Yaghi, O. M., A Combined Experimental-Computational Investigation of Carbon Dioxide Capture in a Series of Isoreticular Zeolitic Imidazolate Frameworks. *J Am Chem Soc* **2010,** 132, (32), 11006-11008.

32.   Park, K. S.; Ni, Z.; Cote, A. P.; Choi, J. Y.; Huang, R. D.; Uribe-Romo, F. J.; Chae, H. K.; O'Keeffe, M.; Yaghi, O. M., Exceptional chemical and thermal stability of zeolitic imidazolate frameworks. *Proc. Natl. Acad. Sci. U. S. A.* **2006,** 103, (27), 10186-10191.

33.   Phan, A.; Doonan, C. J.; Uribe-Romo, F. J.; Knobler, C. B.; O'Keeffe, M.; Yaghi, O. M., Synthesis, Structure, and Carbon Dioxide Capture Properties of Zeolitic Imidazolate Frameworks. *Accounts Chem. Res.* **2010,** 43, (1), 58-67.

34.   Wang, B.; Cote, A. P.; Furukawa, H.; O'Keeffe, M.; Yaghi, O. M., Colossal cages in zeolitic imidazolate frameworks as selective carbon dioxide reservoirs. *Nature* **2008,** 453, (7192), 207-U6.

35.   Getman, R. B.; Bae, Y.-S.; Wilmer, C. E.; Snurr, R. Q., Review and Analysis of Molecular Simulations of Methane, Hydrogen, and Acetylene Storage in Metal–Organic Frameworks. *Chem Rev* **2011,** 112, (2), 703-723.

36.   Dzubak, A. L.; Lin, L. C.; Kim, J.; Swisher, J. A.; Poloni, R.; Maximoff, S. N.; Smit, B.; Gagliardi, L., Ab initio carbon capture in open-site metal-organic frameworks. *Nat Chem* **2012,** 4, (10), 810-816.

37.   Chen, L. J.; Grajciar, L.; Nachtigall, P.; Duren, T., Accurate Prediction of Methane Adsorption in a Metal-Organic Framework with Unsaturated Metal Sites by Direct Implementation of an ab Initio Derived Potential Energy Surface in GCMC Simulation. *J Phys Chem C* **2011,** 115, (46), 23074-23080.

38.   Grajciar, L.; Bludsky, O.; Nachtigall, P., Water Adsorption on Coordinatively Unsaturated Sites in CuBTC MOF. *J Phys Chem Lett* **2010,** 1, (23), 3354-3359.

39.   Grajciar, L.; Wiersum, A. D.; Llewellyn, P. L.; Chang, J. S.; Nachtigall, P., Understanding CO_2 Adsorption in CuBTC MOF: Comparing Combined DFT-ab Initio Calculations with Microcalorimetry Experiments. *J Phys Chem C* **2011,** 115, (36), 17925-17933.

40.   Rappe, A. K.; Casewit, C. J.; Colwell, K. S.; Goddard, W. A.; Skiff, W. M., Uff, a Full Periodic-Table Force-Field for Molecular Mechanics and Molecular-Dynamics Simulations. *J Am Chem Soc* **1992,** 114, (25), 10024-10035.

41.   Mayo, S. L.; Olafson, B. D.; Goddard, W. A., Dreiding - a Generic Force-Field for Molecular Simulations. *J Phys Chem-Us* **1990,** 94, (26), 8897-8909.

42.   Jorgensen, W. L.; Maxwell, D. S.; TiradoRives, J., Development and testing of the OPLS all-atom force field on conformational energetics and properties of organic liquids. *J Am Chem Soc* **1996,** 118, (45), 11225-11236.

Chapter 2. Physically-Motivated, Robust, *ab initio* Force Fields for CO₂ and N₂

Table of Contents

2.1 Introduction

Within the past decade, there has been significant interest in understanding the interactions of carbon dioxide (CO_2) due to its critical role in global warming. The growing importance of processes such as CO_2/CH_4 separation, synthesis gas (syngas) chemistry, and flue gas separation highlights the need to understand the physical interactions involving CO_2 under industrially relevant temperatures and pressures. In particular, the latter example has recently been the subject of much attention in order to design efficient post-combustion carbon capture and sequestration (CCS) systems for coal-fired power plants.[1] Here the primary challenge is the separation of the relatively dilute CO_2 from the more abundant nitrogen (N_2) gas, utilizing technologies such as chemical sorbants, porous materials,[2, 3] or ionic liquids.[4-6] Computer simulation techniques have been applied to these areas with the goal of providing physical insight into the gas sorption and separation process.[7, 8] The reliability of these techniques relies on the accuracy of the force field being used to describe both the interaction of the gas and gas/sorbent over a wide range of conditions.

In this chapter we present accurate, physically motivated, *ab initio* force fields for CO_2 and N_2. These force fields are novel in that they are essentially parameter-free and based on extremely accurate *ab initio* calculations. They contain *explicit* terms to account for all of the dominant fundamental interactions between molecules (Pauli repulsion, electrostatics, induction, dispersion…), each represented by a physically-appropriate functional form and fitted *individually* based on the results of an *ab initio* energy decomposition. As such, the resulting force fields are extremely robust and transferable, reproducing a vast array of structural, thermodynamic, and dynamic properties over large portions of the phase diagram

and for gas mixtures. We also anticipate that they will be well-suited for use in simulating CO_2 interactions in complex media such as porous solids (metal-organic frameworks, zeolites) and ionic liquids where traditional empirical force fields often struggle.

The earliest attempts to develop classical force fields for CO_2 date back to the early 1970's.[9, 10] Later, Murphy *et al.* developed an atom sites based model with three Lennard-Jones centers and a point quadrupole moment placed at the molecular center of mass (MSM model).[11, 12] After the work done by Galassi *et al.*[13] and Kushta *et al.*[14, 15], this model was followed by the two-center Lennard-Jones plus point quadrupole (2CLJQ) model of Moller *et al.*,[16] which was carefully benchmarked to vapor-liquid phase equilibria (VLE) properties. One year later, in 1995, Harris and Yung published their EPM2 model,[17] which is one of the most widely used classical models for CO_2 today. EPM2 model is a flexible model with three Lennard-Jones sites and three point charges each located on atom centers. EPM2 model yields very accurate liquid-vapor coexistence curve and critical point, although its bond length and charges are scaled by 0.97-0.98 with respect to its precursor, EPM, which is much less accurate in phase coexistence calculations. More recently Potoff and Siepmann developed their TraPPE model,[18] which contains a more reasonable bond length and yields comparable accuracy in VLE calculations to EPM2. The TraPPE model was also developed for various other species, such as N_2 and alkanes, making it a convenient choice when simulating mixtures.

Further work has since been done to improve the description of various model properties, including a modified 2CLJQ model by Vebrec *et al.*,[19] a rigid three Lennard-Jones plus three charges model proposed by Zhang and Duan,[20] and a full flexible version by Zhu *et al.*[21] The latest work along these lines is a three Lennard-Jones sites plus point quadrupole (3LJQ) model published by Merker *et al.* in 2010,[22] which yields excellent agreement with experiment in various types of properties, including densities, second virial coefficients, radial distribution function, diffusion coefficients and VLE data. However, as with EPM2, the authors were forced to scale the quadrupole moment and bond length by 8% to achieve high accuracy. Finally, of particular note is the GCPCDO model published in 2011 by Persson, which is

the first model to explicitly treat three body interactions.[23] This model has one anisotropic polarizable site and three body dispersion terms, yielding improved second and third virial coefficients; many macroscopic properties including VLE data were not benchmarked, likely due to the computational expense of the model.

It is important to note that all these models were directly fitted to experimental data. This may lead to the occurrence of unphysical parameters in these models, causing their accuracy to often rely on some implicit error cancellation. Not only is this theoretically unsatisfying, it also means that the model transferability is questionable. An alternative approach is to parameterize a force field using *ab initio* calculations. Along these lines, Tsuzuki *et al.* developed a CO_2 model fit directly to interaction energies computed with MP2 level of theory.[24, 25] Although they achieved a nice fit to the pairwise potential, a relatively large error in the density and diffusion coefficient was observed; other important macroscopic properties such as VLE data were not presented. Bukowski *et al.,* also developed an *ab initio* derived force field, fitting a potential based on symmetry-adapted perturbation theory (SAPT) calculations.[26] However, they mainly focused on geometries of dimers and trimers and did not attempt to simulate bulk systems. Furthermore, in contrast to the present models, they fit only the *total* interaction energy, rather the individual energy *components*. The latter approach not only provides access to explicit energy decomposition, but more importantly should increase the robustness of the potential in alternative environments other than the neat fluid. Other examples of *ab initio* based model can also be found, most of which are based on an MP2 level of theory[27-30].

Our present goal in this work is to design a physically motivated CO_2 model based on first-principle calculations, achieving at least comparable accuracy for bulk properties as the previously mentioned empirical models. Our approach, based on a physically-motivated functional form with explicit terms for each relevant fundamental interaction, and fitted individually to energy decomposed *ab initio* calculations, should yield more physical insight and better transferability and robustness than previous empirical models. Specifically, we use a combination of density fitting DFT-SAPT[31-36] and coupled cluster

calculations with extremely large basis sets to compute decomposed interaction energies, which are used to fit physically distinct terms of our force field. This combination of computational approaches yields extremely accurate interaction energies along with a well-defined and physically meaningful energy decomposition.

Finally, in conjunction with our CO_2 model, a new N_2 model was constructed using an identical methodology. Although N_2 is a common component in mixtures involving CO_2, much less work has been done in the construction of N_2 force fields. Still, some examples of these force fields do exist,[18, 19, 37-40] including a polarizable shell model[41] fit to experimental properties. In addition to empirical N_2 potentials, several *ab initio* potentials exist, including work done by Bern *et al.*[42] and Van de avoird *et al.*[43] in the 1980s. Following that line are several models based on CCSD(T),[44, 45] SAPT[46, 47], or MCSCF[48], but bulk property benchmarks for most of these models have not been carried out. We apply our own methodology to the construction of a robust, physically motivated, *ab initio* model for N_2. The resulting model should be useful in simulating not only neat N_2 but also common gas mixtures. Both the CO_2 and the N_2 models are named as the "Schmidt, Yu, McDaniel" (SYM) model.

2.2 Computational Details

2.2.1 *Ab initio* Calculations

All *ab initio* calculations were carried out using the MolPro 2009 package.[49] The density fitting DFT-SAPT[31-36] method was used to calculate all dimer interactions during parameter fitting in conjunction with the PBE exchange correlation functional.[50, 51] A long range asymptotic correction[52] was used in the DFT part of the calculation in order to guarantee a correct asymptotic behavior of the electron density, which is essential for accurate SAPT results. The asymptotic correction requires an ionization potential for each molecular species, and these were calculated at the PBE0/AVTZ level. A dimer-centered basis sets (DCBS) consisting of Dunning style aug-cc-pVQZ basis plus midbond functions were used in all SAPT

calculations. The basis was augmented with additional midbond basis functions, consisting of 5s5p3d2f even tempered basis functions (ratio of 2.5) centered at $\zeta = 0.5$, 0.5, 0.3, 0.3 au, respectively, and placed at the midpoint between the respective centers of mass of the two molecules of the dimer. The midbond functions are essential for accurate calculation of dispersion energies.[53]

For all CCSD(T) calculations, an aug-cc-pVQZ and additional 5s3p1d1f even tempered midbond basis was used. Counterpoise corrections are conducted to remove basis set superposition error (BSSE).

2.2.2 Molecular Dynamics (MD) Simulations in Homogeneous Region

All MD simulations were carried out using the Gromacs 4 simulation package.[54] All simulations in the homogeneous region of the phase diagram were done with 1000 gas molecules. Electrostatic interactions were described with the Particle-mesh Ewald (PME) method in conjunction with a 14Å real space cutoff. The Buckingham component of the potential was computed using a 15Å cutoff and long range energy/pressure corrections. The Nose-Hoover thermostat and Parrinello-Rahman barostat were utilized for temperature and pressure coupling, with coupling times of 0.2 and 1.0ps, respectively. A cubic box with isotropic coupling was used for NPT simulations, and a 1fs time step was used for all simulations.

2.2.3 Chemical Potential / VLE Calculations

Test particle insertion (TPI) calculations were utilized to evaluate the chemical potential of the vapor/liquid in order to determine phase coexistence conditions. All TPI calculations were conducted using a custom version of MCCCS Towhee simulation package which was modified to enable the use of polarizable models via a shell model.[55] A conjugate gradient algorithm[56] was used to optimize the shell positions. In a typical chemical potential calculation, a 1ns NPT trajectory was run using Gromacs, saving snapshots every 1ps. Then these 1000 snapshots were analyzed using Towhee with 1000 trial insertions were conducted for each snapshot. The insertions utilized a rotational biased method to enhance the sampling[57] in which ten test insertions were conducted for every trial insertion. The Buckingham potential

without electrostatics was used as the biasing potential. The chemical potential of the system in the NPT ensemble is then calculated as follows:

$$\mu_{tot} = \mu_{ex} + \mu_{id}$$

$$\mu_{ex} = -kT \ln \left(\frac{\langle w(n)V \exp(-\beta(\Delta U - \Delta U_{bias})) \rangle}{n \langle V \rangle} \right) \tag{2.1}$$

$$\mu_{id} = -kT \ln \left(\frac{1}{\Lambda^3} \left\langle \frac{V}{N} \right\rangle \right)$$

where $w(n)$ is the Rosenbluth weight, Λ is the thermal De Broglie wavelength, ΔU is the change in the potential energy upon trial particle insertion, and n is the number of test insertions for each trial insertion (set equal to 10).

2.3 Results and Discussion

2.3.1 CO$_2$ Model Fitting

An NVT MD simulation was first run at high (liquid-like) CO$_2$ density using the TraPPE parameters to generate representative dimer configurations for further analysis. High temperatures (3000K) were used to enhance the sampling in repulsive regions. 776 dimer configurations are randomly selected from the trajectory to be used in subsequent SAPT calculations.

SAPT naturally decomposes the interaction energy into different terms with distinct physical meaning:

$$E_{\text{int}} = E_{pol}^{(1)} + E_{exch}^{(1)} + E_{ind}^{(2)} + E_{ind-exch}^{(2)} + E_{disp}^{(2)} + E_{disp-exch}^{(2)} + E_{\delta hf} \tag{2.2}$$

Here $E_{pol}^{(1)}$ is the electrostatic interaction due to the zeroth order (unperturbed) electron density of isolated monomers. This electrostatic term is modeled by our force field using atom centered point charges fit to the experimental gas phase quadrupole moment. Additional terms are used to take account of charge penetration effects, yielding a final functional form,

$$E_{pol}^{(1)} \cong \sum_{i>j} f(r_{ij}) \frac{q_i q_j}{r_{ij}} + \sum_{i>j} A_{ij}^{elect} \exp(-B_{ij} r_{ij}) \qquad (2.3)$$

At least for the present cases we found that we were able to eliminate the screening function, setting $f(r_{ij}) = 1$, without any significant loss of accuracy. We thus used this approximation for the remainder of the present work.

The first order exchange repulsion term, $E_{exch}^{(1)}$, was described using pairwise additive exponential terms in the force field,

$$E_{exch}^{(1)} \cong \sum_{i>j} A_{ij}^{exch} \exp(-B_{ij} r_{ij}) \qquad (2.4)$$

This Buckingham functional form is more physical than the commonly used r^{-12} repulsive terms in the Lennard-Jones potential as it more accurately describes the overlap of monomer electron densities, which themselves asymmetrically decay exponentially.

The polarization / induction energy components, $E_{pol}^{(2)} = E_{ind}^{(2)} + E_{ind-exch}^{(2)}$, were reproduced using a shell model.[58] In the shell model, a positive core charge (q_{core}), located at the nucleus, and a negative shell charge (q_{shell}), are added to each polarizable atom site. The total apparent charge on a polarizable site is thus $q = q_{core} + q_{shell}$. The two charges are connected by a harmonic spring, and at the positions of the shells are optimized at each simulation time step to reflect the adiabatic relaxation of the electronic polarization. The difference between the energy of this optimized system and the energy of the corresponding non-polarizable system (the with shell charge localized at the nucleus) is defined as polarization energy of the shell model, U_{shell}.

While calculating the intramolecular shell-shell interaction a polarization catastrophe may arise due to the short distance between polarizable sites. A screening function was proposed by Thole,[59, 60] and is

applied to damp the intramolecular dipole-dipole interactions to avoid such a divergence. The Thole damping functions can be written as follows:

$$U_{ij} = T(r_{ij}) \frac{q_i q_j}{r_{ij}}$$

$$T(r_{ij}) = 1 - \left(1 + \frac{p r_{ij}}{2(\alpha_i \alpha_j)^{1/6}}\right) e^{-p r_{ij}/(\alpha_i \alpha_j)^{1/6}}$$

(2.5)

where, p is a dimensionless Thole parameter and α_i, α_j are the polarizabilities of the two interacting sites, which are calculated using equation q_{shell}^2 / k, where k is the spring constant. In this case, the spring constant k and the Thole parameter p were fixed to be 0.1 au and 2.0, respectively.

To fit the shell charges (equivalent to polarizabilities), we carried out SAPT calculations involving a single point charge (Li^+) and CO_2 molecule and used the resulting induction energies from these calculations for the fit. The two components of molecular polarizability derived from this fit ($\alpha_\| = 3.913$ Å^3, $\alpha_\perp = 2.137$ Å^3) are very close to experimental values[61] (4.034 Å^3 and 1.927 Å^3, respectively). In addition to the shell model, an extra exponential term was used to fit the CO_2-CO_2 induction components to take account of charge penetration effects. The total functional form used to model the CO_2-CO_2 induction energy is thus

$$E_{pol}^{(2)} \cong U_{shell} + \sum_{i>j} A_{ij}^{ind} \exp(-B_{ij} r_{ij})$$

(2.6)

Second order dispersion energy, $E_{VdW}^{(2)} = E_{disp}^{(2)} + E_{disp-exch}^{(2)}$, was fit using the standard r^{-6} functional form,

$$E_{VdW}^{(2)} \cong -\sum_{i>j} f(r_{ij}) \frac{C_{ij}}{r_{ij}^6}$$

(2.7)

where once again we approximated $f(r_{ij}) = 1$ without significant loss of accuracy.

Finally, the delta Hartree-Fock terms, $E_{\delta hf}$, which have been used and described previously,[31] represent primarily higher order contributions to polarization and/or exchange and are typically quite small at equilibrium intermolecular distances. These energies were computed by the difference of the Hartree-Fock dimer interaction energy and the HF-SAPT interaction energy components:

$$E_{\delta hf} = E_{int}^{HF} - E_{pol}^{(1)} - E_{exch}^{(1)} - E_{ind}^{(2)} - E_{ind-exch}^{(2)} \tag{2.8}$$

This energy was fit using simple exponential functions,

$$E_{\delta hf} \cong \sum_{i>j} A_{ij}^{\delta hf} \exp(-B_{ij} r_{ij}) \tag{2.9}$$

During the fitting procedure, CO_2 bond length and angles were constrained to be 1.164Å and 180°, near to the experimental values. Only the amplitudes of the exponential functions, $\{A_{ij}\}$, were fit to SAPT interaction energies as other parameters have been fixed based on physical considerations, *vide infra*. The same pairwise exponents were used for all types of energy terms, which were determined using the following procedure. First, the electron density overlap $S_{ij}(r)$ for any pair of atoms (C-C, C-O, O-O) was approximated by assuming a spherically symmetric density distribution and exponential density tail decay for each individual atom: $n(r) \rightarrow \exp(-2r\sqrt{2\mu})$,[62] where μ is the experimental atomic ionization potential. Then, all pairwise $S_{ij}(r)$ were fit with exponential functions to give initial guesses for all pairwise exponents B_{ij}^0 under the hypothesis that the asymptotic exponential decay of many of the energy terms should be proportional to the decay in the calculated density overlap. Finally, the first order exchange energies from CO_2-CO_2 calculations, $E_{exch}^{(1)}$, were fit using the functional form, $\sum_{i>j} A_{ij}^{exch} \exp(-\lambda B_{ij}^0 r_{ij})$, in which a common scaling factor was obtained; in the present cases we find $\lambda \approx 1.2$, reflecting the fact that initial exponents are only asymptotically correct. Subsequently, the exponents $B_{ij} = \lambda B_{ij}^0$ were used in all remaining energy terms.

The remaining exponential coefficients, $\{A_{ij}\}$, for the various energy terms are fit individually to the results of the corresponding terms in the SAPT calculation, with fixed B_{ij}, using least mean square error approach. In order to ensure the most physically meaningful parameters and further reduce their number, we fit only *atomic* exponential coefficients, $\{A_{ii}\}$, with the cross terms being calculated using standard combination rules, $A_{ij} = \sqrt{A_{ii}A_{jj}}$.

We can write the final total classical potential as:

$$U_{tot} = \sum_{i>j} \frac{q_i q_j}{r_{ij}} + \sum_{i>j} \left(A_{ij}^{tot} \exp(-B_{ij} r_{ij}) - \frac{C_{ij}}{r_{ij}^6} \right) + U_{shell} \tag{2.10}$$

where *i, j* run over all three atoms in the CO_2 molecule, and $A_{ij}^{tot} = A_{ij}^{elec} + A_{ij}^{exch} + A_{ij}^{ind} + A_{ij}^{\delta hf}$ is a summation of all terms' contribution. Note here no special damping function is needed in practice for point charge or dispersion interactions. The final fitting results for all terms and the total interaction energy are shown in the supporting information of reference 63, yielding an RMS error between the fitted and *ab initio* interactions energies of only 0.28 mH (0.74 kJ/mol). The final fitted parameters are given in Table 2.1.

k_{spring} (kJ/mol/Å^2)	937.72		
r_{co} (Å)	1.164		
	C	O	
q (e)	0.65738	-0.32869	
q_{shell} (e)	-0.89712	-0.77973	
	C-C	C-O	O-O
A^{tot} (kJ/mol)	56303.43	141828.66	327475.66
B (Å^{-1})	3.5105	3.6993	3.9288
C (kJ/mol·Å^6)	689.059	1124.173	1834.045
A^{elect} (kJ/mol)	-27846.98	-67560.09	-163908.84
A^{exch} (kJ/mol)	95510.43	223264.61	521902.07

A^{ind} (kJ/mol)	-13425.10	-7751.66	-4475.81
$A^{\delta hf}$ (kJ/mol)	2065.05	-6124.34	-26042.05

Table 2.1. Fitted parameters for CO2 molecules. C coefficient in the table is scaled by 0.935, as described in the text.

2.3.2 CO$_2$ Second Virial Coefficient

The second virial coefficients of our CO$_2$ model were calculated by integrating Mayer function,[64]

$$B_2(T) = -2\pi \int_0^\infty [\langle e^{-\beta u(r)} \rangle - 1] r^2 dr \qquad (2.11)$$

where the average was taken by random sampling two molecular orientations at a fixed intermolecular separation. The results are shown in Figure 2.1:
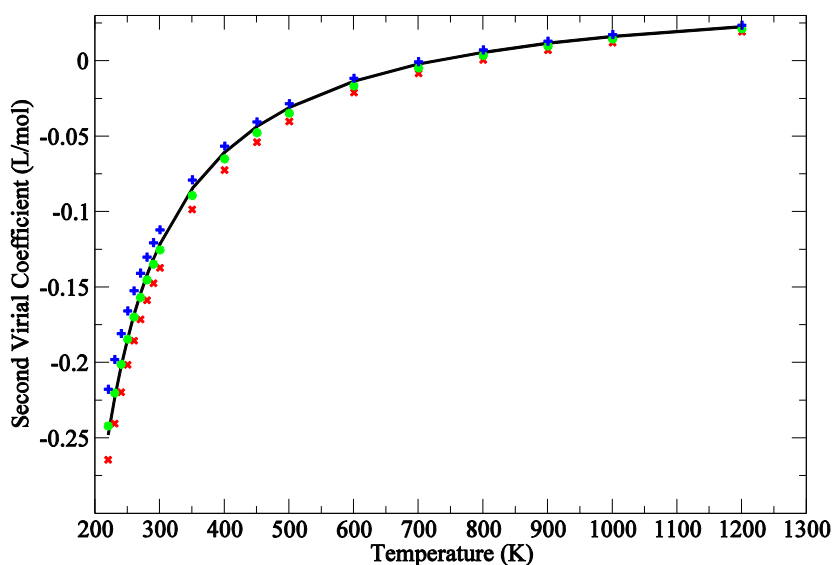
Figure 2.1. Second Virial coefficients for CO$_2$. Results from unscaled (red cross), scaled data with 0.935 scaling factor (blue plus) and scaled data with 0.97 sclaing factor (green star) are shown along with experimental data[65] (solid).

As shown, the unscaled model exhibits B$_2$ coefficients are close to experimental value in general, although slight underestimation can still be observed, illustrating some small systematical error during the fitting. A scaling factor of 0.97 corrects the error and achieves an excellent agreement with experimental results, representing a perfect description on the CO$_2$ dimer interaction. However, when applied, these

perfect parameters (scaled by 0.97) to the bulk lead to densities that are systematically too high. In fact, in order to obtain high quality bulk data, we have to scale the dispersion coefficient by 0.935, overcorrected by about 3.5%. This tradeoff in B_2 and bulk properties has also been observed by Persson *et al.* and was explained in terms of three body effects.[23] Although our model accounts for polarization, which is a major contribution to many body interactions, three-body dispersion and exchange interactions are missing from our model.

Using a combination of MP2 and HF calculations on CO_2 trimers, we attempt to estimate the magnitude of this correction. For both calculations, aug-cc-pVDZ basis was used to accelerate the speed, and BSSE was removed by counterpoise correction. Three-body interaction energies for both MP2 and HF were computed as:

$$\Delta E_{ABC} = E_{ABC} - E_{AB} - E_{BC} - E_{AC} + E_A + E_B + E_C \tag{2.12}$$

Attributing the difference in the MP2 and HF interaction energies primarily to dispersion, the three-body dispersion is estimated by $\Delta E_{ABC}^{MP2} - \Delta E_{ABC}^{HF}$. Our analysis showed that there is typically a positive energy contribution from three-body dispersion, opposing the negative two-body dispersion contributions. Using this methodology, we would estimate the magnitude of three-body dispersion at typically ~3% of the magnitude of two-body dispersion (thus weakening the dispersive interactions), which agrees with the discrepancy between the perfect (0.97) and effective (0.935) scale factors. Motivated by these results, we applied the scaling factor of 0.935 to the dispersion energy contribution, yielding the most accurate bulk densities. Consequently, the scaled potential exhibits somewhat worse agreement with B_2 coefficients in the low temperature region.

Note that this dispersion scale factor is the *only* empirical parameter in this model, and is motivated by our explicit trimer calculations. The dispersion scale factor is essentially accounting for three-body dispersion in an average manner. Our scaling factor of 0.935, corresponding to 3.5% correction from perfect dimer parameters, illustrates that three-body dispersion is an important component for a highly

accurate CO_2 force field. In order to arrive at a force field which is computationally efficient and amenable to popular simulation packages we employ a mean field treatment of many-body dispersion effects via simple scale factor and utilize this model for all subsequent calculations in this chapter. Many-body interactions are computed explicitly and discussed in more careful and detailed fashion in the following chapter (Chapter 3) of this thesis.

2.3.3 CO_2 Properties in Homogeneous Region

Densities of CO_2 at different points in the phase diagram were computed and compared to experiment, the results of which are shown in Figure 2.2.[65] The densities in a wide range of points are well reproduced by our model, with all relative errors all less than 4% and the vast majority of cases within 2%. The largest errors appear in the low temperature, very high density region, most likely because of the relatively poorer fitting in the highly repulsive potential region.
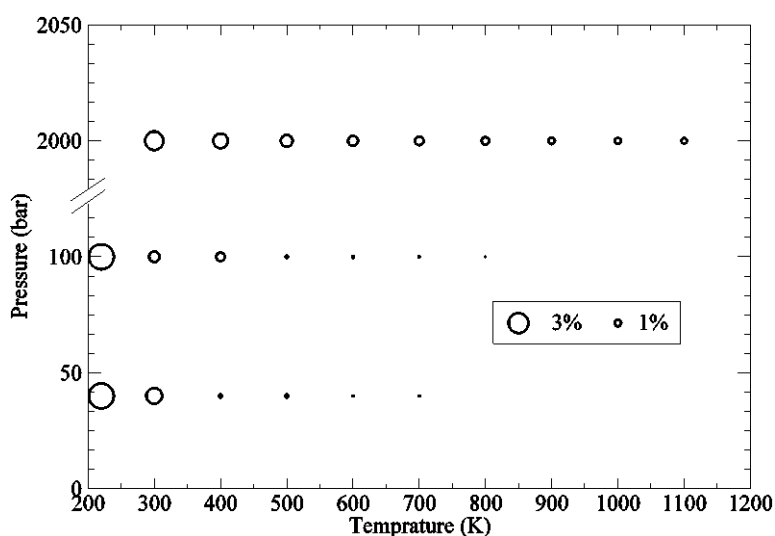
Figure 2.2. Observed deviation between experimental and model CO_2 densities under a wide variety of conditions.

The structure of liquid CO_2 is benchmarked by comparing the calculated intermolecular scattering function with experiments.[66] The simulation is done in the NPT ensemble at 239 K and 14.5 bar, mirroring the experimental conditions. The intermolecular scattering function is calculated by the Fourier

transform of the radial distribution function, and the results are shown in Figure 2.3.[66] A slight shift can

be observed in the first peak, while in general the shape of the whole curve is well reproduced.

$$i_m(K) = \frac{4\pi n}{K} \int_0^\infty r(g_m(r)-1)\sin(Kr)dr \qquad (2.13)$$

$$g_m(r) = 0.403 g_{OO}(r) + 0.464 g_{CO}(r) + 0.133 g_{CC}(r) \qquad (2.14)$$
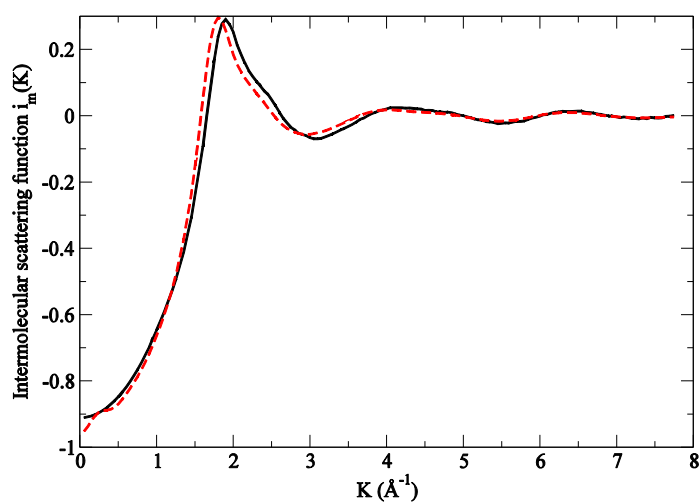
Figure 2.3. Intermolecular scattering function for liquid CO_2: simulation (red dashed) versus experimental data (black solid).

Self-diffusion coefficients are also predicted by MD simulations and compared to experiments,[67, 68] and

are shown in Figure 2.4. The agreement with experiment is nearly quantitative and as good as newly

published empirical models,[22] despite the fact that the present model is essentially parameter free.
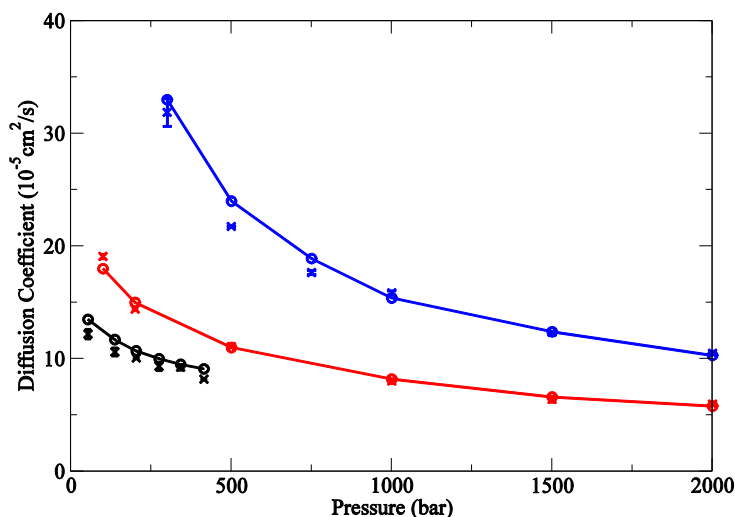
Figure 2.4. Diffusion coefficients, simulation results (cross) in 273K (black), 298K (red) and 373K (blue) with experimental data (circle)

The temperature dependence of the CO_2 heat capacity is also computed. A series of NPT simulations were conducted at 100 bar and various temperatures, followed by enthalpy calculations based on these simulations. The temperature dependence of the enthalpy is interpolated using cubic splines to generate a smooth curve. Then the numeric derivative was taken from the H-T curve, which is the intermolecular contribution to the isobaric heat capacity. The intramolecular contribution was computed via the harmonic oscillator approximation:

$$C_p^{intra} = \sum_i \frac{(h\nu_i / kT)^2 e^{-h\nu_i/kT}}{(1 - e^{-h\nu_i/kT})^2} \tag{2.15}$$

where i runs over all normal modes of CO_2, and vibration frequencies ν_i were taken from experiment;[69] the results are shown alongside the corresponding experimental values[65] in Figure 2.5. The peak around 320K is due to critical phenomenon, which provides a challenging test. Our model accurately predicts the position and the height of this peak and performs excellently in all the other regions, confirming this model's capability in predicting thermodynamic properties.
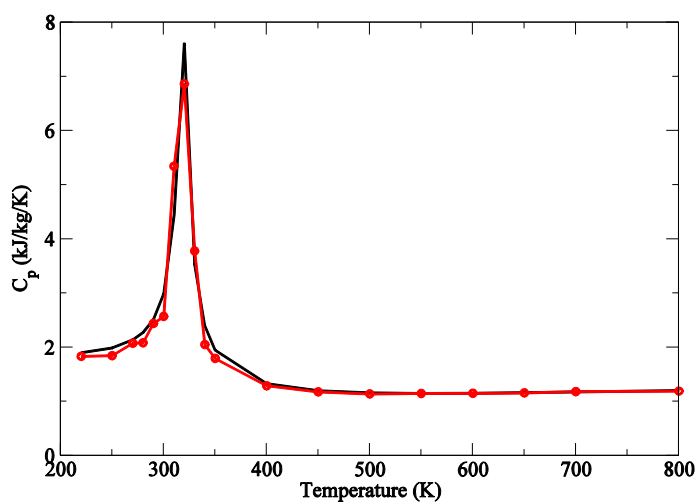
Figure 2.5. Heat capacity calculated by simulation (red circles) compared to experimental data (black solid)

One last interesting calculation we performed in the homogeneous region was an energy decomposition for the bulk CO_2 system at various densities and state points. This is the special advantage for our physically motivated force fields: since all the terms were fit individually, the resulting interaction energy is naturally decomposable under conditions of finite temperature and pressure in a standard simulation. One liquid state (300 K/100 bar), one supercritical state (350 K/100 bar) and two gas states (300 K/40 bar and 300 K/10 bar) were tested. Table 2.2 lists the contribution of the different physical types of interactions by percentage relative to the total interaction potential. Several interesting conclusions can be drawn from these data. First, for the neat CO_2 system, dispersion, exchange and electrostatic interactions account for approximately 90% of the interaction energy, with induction and the delta Hartree-Fock (higher order effects) contribution playing a less significant role in the total interaction. This likely explains the apparent success of the previous non-polarizable empirical models. Yet although the induction contribution is small, it is critical in determining accurate densities; neglecting this term in the total energy yields very significant errors in the observable properties. Previous empirical models must therefore implicitly include this contribution in their Lennard-Jones potential in a mean field fashion. Although this may reproduce neat CO_2 properties, it may not be robust enough in highly polar

environments. Second, it can be observed that with decreasing density, the magnitudes of exchange repulsion, dispersion attraction, and induction all decrease, which is consistent with the increasing molecular separations. Third, in the low density limit, with increasing average separation between molecules, the relative contribution from all terms seem to approach constant values. This is somewhat non-intuitive, as one might expect long range dispersion interactions to become disproportionately dominant in the low density limit. The fact that this is not the case is probably due to the pairwise position correlation between different molecules as the radial distribution function approaches its low-density limit.

(%)	liquid	supercritical	gas/40bar	gas/10bar
Density(mol/L)	17.916	5.073	1.832	0.422
exchange	-118.9	-110.1	-104.2	-102.2
electrostatic	55.7	50.9	50.7	51.5
dispersion	151.5	148.0	142.7	140.1
induction	7.1	6.8	6.6	6.6
δhf	4.7	4.4	4.1	4.1
total	100.0	100.0	100.0	100.0

Table 2.2. Energy decomposition for bulk CO_2 in different conditions.

2.3.4 CO_2 Vapor-liquid Equilibria

The VLE behavior is critical in predicting CO_2 absorption behavior in different types of systems. For various temperatures, vapor phase and liquid phase NPT simulations were run at three different pressures around the co-existence pressure. Test particle insertion was used to compute the chemical potentials in these simulations. The resulting $\mu - P$ curves were interpolated to determine the crossing point, P_0, which corresponds to the co-existence pressure for the model. Then NPT simulations were run for the two phases at P_0 to determine the respective equilibrium densities. Finally, the supercritical point was obtained by extrapolating the $\rho - T$ curves, utilizing the following equations[70]:

$$\frac{\rho_l + \rho_g}{2} = \rho_c + A(T - T_c) \tag{2.16}$$

$$\rho_l - \rho_g = B(T - T_c)^{0.32} \tag{2.17}$$

Figure 2.6 compares the simulation results to experimental data.[65] It can be seen that in general, our model predicts very accurate coexistence pressure. The typical error is between 1-2 bar, with all values slightly higher than experiment.
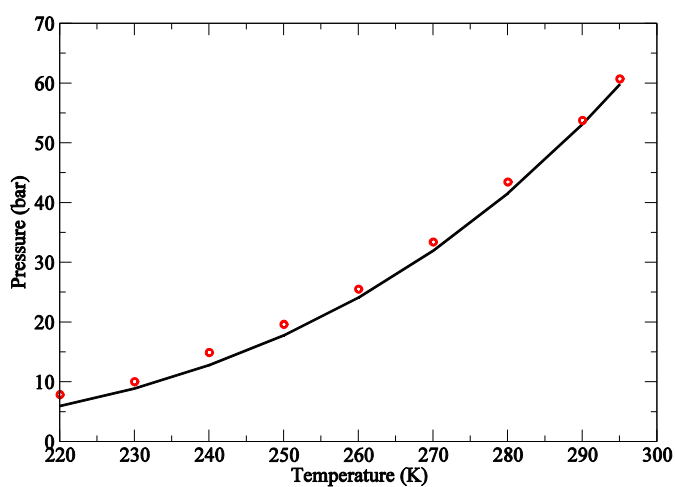
Figure 2.6. Temperature dependence of vapor-liquid coexistence pressure. Calculated data (circles) is compared with experimental data (solid).
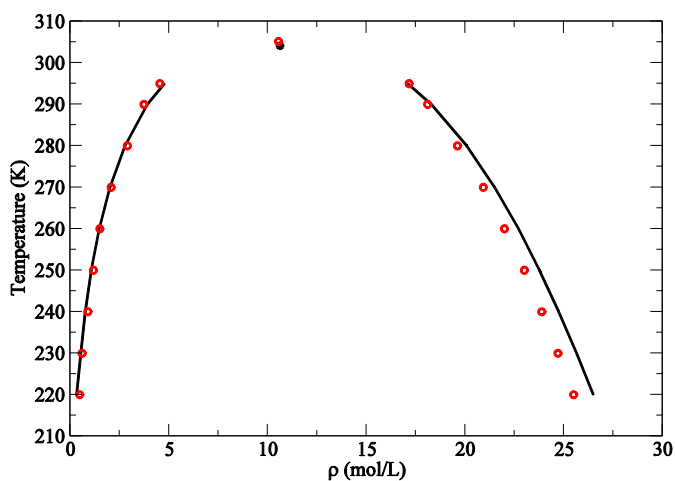
Figure 2.7. Coexistence density from simulation (circles) compared to experimental data. The two points on the top are the critical points, from our simulation (circle) and experiment (star).

Figure 2.7 shows the $\rho - T$ phase diagram. The phase behavior is in general well predicted. The critical point from the simulation is 305.17 K, 10.547 mol/L, which is almost identical to the experimental value of 304.13 K and 10.625 mol/L.[22] The major errors in our model occur in the low temperature liquid region, where around a 3% error in the density can be observed, consistent with the deviation that we found in the homogeneous low temperature liquid system.

The evaporation heat data, calculated in both simulated and experimental equilibrium densities are also available in the ESI of reference 63. The results in simulated densities show typically <5% of error, mainly due to the density error we observed in VLE calculations. This reason is confirmed by the nearly perfect performance of the evaporation heat calculated in experimental density.

2.3.5 N_2 Model Fitting

We also develop an N_2 model, proceeding analogously to the case of CO_2. The molecule is represented by three sites, including two nitrogen atoms and one dummy site (D) at the molecular center of mass. The dummy site interacts only via a partial charge to reproduce the gas phase quadrupole moment; no shell or Buckingham parameters are associated with this dummy site. Like CO_2, N_2 is also a rigid model with $r_{NN} = 1.10$Å, close to the experimental value.

It was found that second order truncated SAPT did not converge to high enough accuracy for the N_2 dimer system, despite its success for the CO_2 dimer. This is likely due to the extremely weak interactions of N_2 molecules, meaning that dispersion must be calculated to extraordinary accuracy. Therefore we include a CCSD(T) correction, which was calculated by the difference between the CCSD(T) interaction energy and the SAPT total energy, and was added to the dispersion term in the SAPT energy decomposition. The fitting scheme was analogous to that used for CO_2, and will not be repeated here. As explained below, it was found that a scaling factor for the dispersion term was also needed for the N_2 molecule. Fitting this scaling factor to B_2 coefficients led to a value of 0.94, which is coincidentally close to the scaling factor for the CO_2 model. However, as we will discuss below, the scaling factors have

different physical meanings. Final fittings can be found in the ESI of reference 63, and parameters are

listed in Table 2.3. The RMS value of this fitting is 0.094 mH (0.25kJ/mol).

	D	N
k_{spring} (kJ/mol/Å^2)	937.72	
r_{NN}	1.10	
q (e)	0.95904	-0.47952
q_{shell} (e)	-	-0.86920
A (kJ/mol)	-	305111.67
B (Å^{-1})	-	3.7842
C (kJ/mol·Å6)	-	1437.022
A^{elect} (kJ/mol)	-	-141553.93
A^{exch} (kJ/mol)	-	484166.43
A^{ind} (kJ/mol)	-	-7381.34
A$^{\delta hf}$ (kJ/mol)	-	-30119.49

Table 2.3. Fitted parameters for N2 molecules. The C coefficient in the table was scaled by 0.940, as explained in the text.

2.3.6 N$_2$ Second Virial Coefficients

The second virial coefficient for N$_2$ was calculated using the same procedure as stated above, and the

results are shown in Figure 2.8. Contrary to what we saw in the analogous CO$_2$ calculation, where the

initial 2-body potential was nearly perfect, the unscaled parameters for N$_2$ give B$_2$ values that are too

negative at low temperatures, meaning the fitted potential is slightly too attractive. This similar

phenomenon has also been observed in two previous works that used complicated angular-dependent

functional forms to derive an *ab initio* N$_2$ dimer potential.[46, 47] Thus we believe that this error originates

from the underlying *ab initio* calculations rather than our fitting procedure.
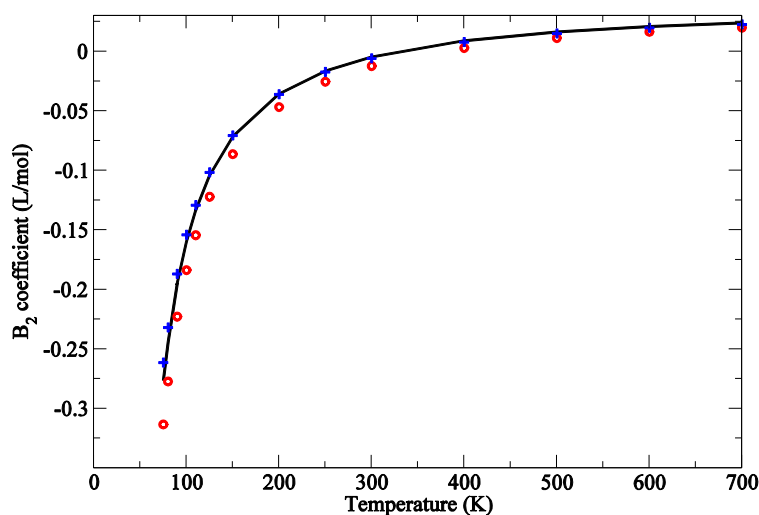
Figure 2.8. Second virial coefficient for N_2 molecules. Results from unscaled model (circles) and scaled model (plus) are plotted along with experimental data[71] (solid).

In order to verify this assumption, we computed the Mayer function $-2\pi r^2[\langle e^{-\beta u(r)}\rangle - 1]$ using CCSD(T) calculations at three different intermolecular distances. 800 dimer geometries were randomly sampled at each distance and CCSD(T) calculations were carried out to obtain interaction energies for these geometries, which were used to determine the value of Mayer function. The results are nearly identical to those we determine from our fitted potential, confirming that source of the discrepancy is not with the fitting, but rather due to insufficiencies in the underlying *ab initio* calculations. Even though these errors seem to be very small (we estimate around 0.1 mH at the dimer minimum), they are significant in that the N_2 interactions are very weak, making N_2 properties extraordinarily sensitive to these small errors. Since CCSD(T) is the upper limit of our computational capabilities, we decided to simply use the empirical scaling factor of 0.94 applied to the dispersion energies to correct this two body interaction error, and all subsequent simulations are done with this scaling factor. The scaled parameters also give improved densities compared to the unscaled parameters. Therefore, we do not see the same B_2 coefficient-density tradeoff that we saw in CO_2, confirming that the problem lies with the two-body

potential. Presumably higher-level coupled cluster calculations accounting for triple and/or quadruple excitations would make such scaling unnecessary.

2.3.7 N_2 Properties in Homogeneous Region

Densities for pure N_2 were tested over a wide range of the phase diagram. The deviations of the density compared to experiments[72] are presented in Figure 2.9. The deviations are even smaller than those of CO_2, with errors less than 1.5%, with the larger deviations occurring in the high density gas region.
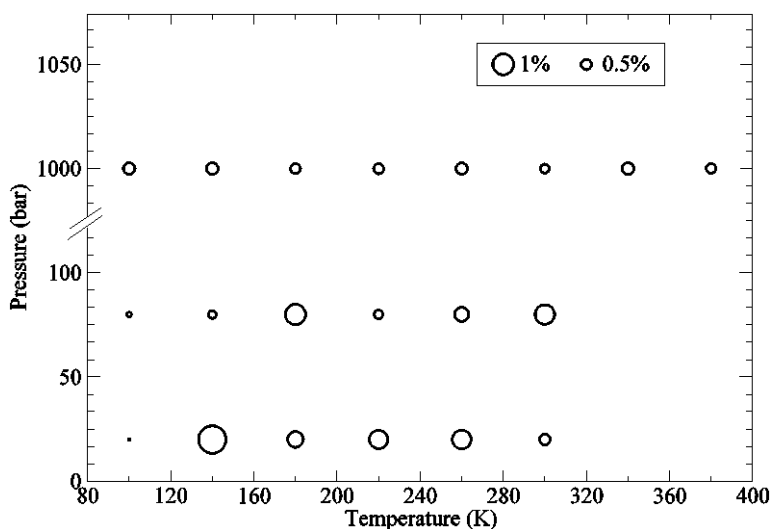
Figure 2.9. Observed deviation between experimental and model N_2 densities under a wide variety of conditions.

The liquid structure of N_2 was studied by comparing the scattering structure factor with neutron scattering experiments.[73] The NVT simulation was conducted at 77.4 K with a density of 28.7 mol/L, mimicking experimental conditions. The total structure factor has contributions from both inter- and intramolecular parts, and was calculated using,[74]

$$S(K) = 1 + \frac{\sin Kd}{Kd} + S_m(K) \tag{2.18}$$

Here d is the nitrogen-nitrogen bond length, fixed at 1.10Å, and $S_m(K)$ is the intermolecular contribution, which was calculated by the Fourier transform of the radial distribution function. Figure

2.10 plots the simulation and experimental results. Excellent agreement is obtained by our model, with essentially quantitative agreement.
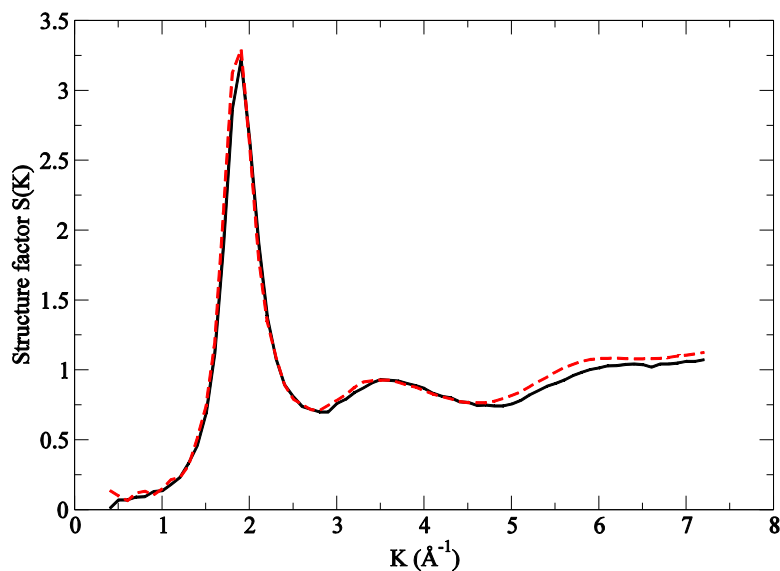
Figure 2.10. Structure factor for liquid nitrogen. Calculated curve (red dashed) is plotted with experimental curve (black solid)

Diffusion coefficients were also examined at various points along the vapor-liquid coexistence line. Results are compared with an empirical equation derived from experimental data[75] and are presented in Figure 2.11. Note that the experiment was done with N^{15} instead of N^{14}. However, the differences of diffusion coefficients between these two species are small relative to the uncertainties of experimental data and our simulation results. The agreement between our simulations and experiment is excellent considering the uncertainty of the experimental data.
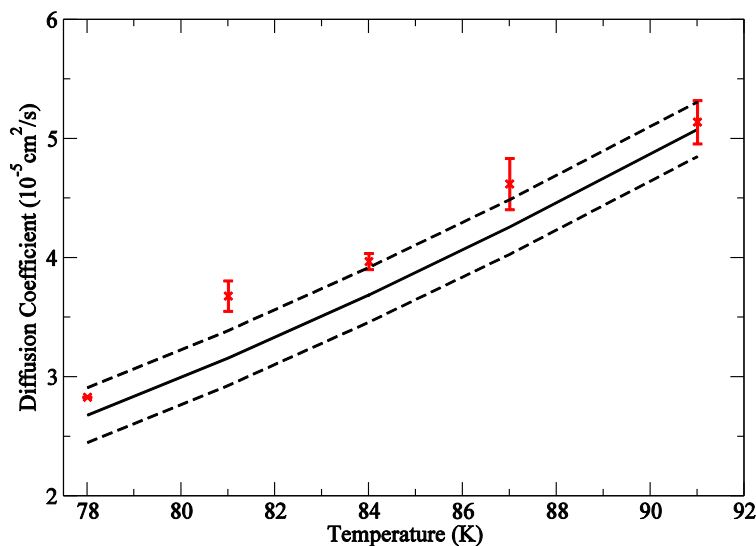
Figure 2.11. N_2 diffusion coefficients along vapor-liquid coexistence line. Simulation results (red cross) are plotted along with the empirical equation (black solid) fit to experimental values, and the corresponding estimated experimental uncertainty (black dashed).

We note that VLE data for N_2 was not calculated since it is somewhat computationally demanding and of significantly less interest as compared to CO_2.

2.3.8 Mixture Properties

In addition to the properties of neat CO_2 and N_2, we also benchmarked mixture properties due to their relevance in many technological and industrially applications. SAPT calculations were done between CO_2 and N_2 for comparison. Cross terms for CO_2 and N_2 interactions were not fit but rather determined by simple combination rule for a regular Buckingham potential.

$$A_{ij} = \sqrt{A_{ii} A_{jj}}$$
$$B_{ij} = 2 / (1 / B_{ii} + 1 / B_{jj}) \quad\quad (2.19)$$
$$C_{ij} = \sqrt{C_{ii} C_{jj}}$$

In the ESI of reference 63, the comparison between our classical model using the combination rule and SAPT interaction energies can be found. The comparison is quite good with an RMS error of only 0.3 mH (0.79 kJ/mol), essentially the same as for neat CO_2, confirming the robustness and physical nature of our

parameters. Although small, the error in the cross terms is systematically too repulsive, probably due to the scaling factor that we used for the CO_2 force field. Given these promising results, we directly utilize the combination rules to simulation properties of the bulk mixtures.

The densities of mixtures were calculated, and compared to the experimental data.[76] These mixtures were studied at variety of temperatures, pressures, and the molar ratios of CO_2. Results for various molar ratios are rather similar, and the deviations of densities in the molar ratio of 0.503 are illustrated in Figure 2.12. Excellent agreement is obtained, comparable with that of the pure CO_2 system, again confirming the robustness of this force field.
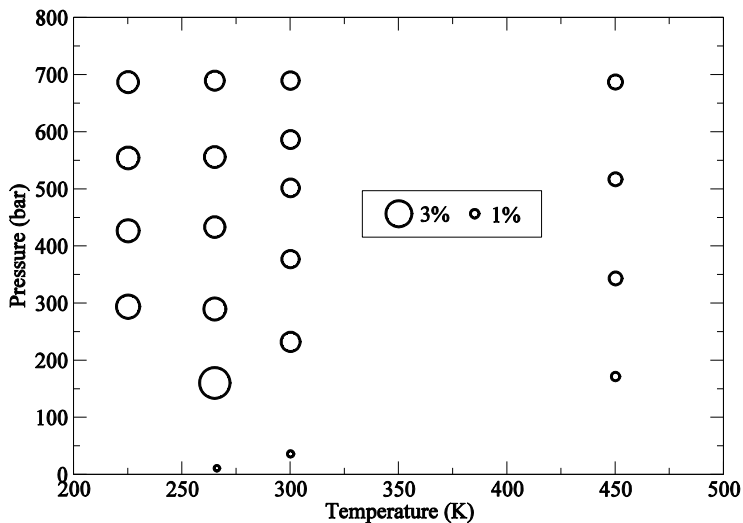
Figure 2.12. Deviations of the calculated CO_2/N_2 mixture for mixture densities compared to the corresponding experimental densities over a wide variety of conditions.

2.3.9 Model Performance

The polarizable shell model adopted in this work is more computationally intensive than traditional non-polarizable point charge models like EPM2 or TraPPE, primarily due to the self-consistent iterations required at each time step. Although this limitation can be mitigated via sophisticated techniques such as a predictor corrector method[77] or extended Lagrangian approaches,[78] we have not yet attempted to implement these methodologies. While these methods are inapplicable to Monte Carlo simulation

methods, they would be a promising alternative in MD simulations to accelerate significantly the speed. We have also parameterized our model for use with long cutoffs (14Å for real space electrostatics and 15Å for Buckingham potential were used in all simulations) to ensure that all structure in the radial distribution function has vanished prior to the application of long-range corrections. However, we note that with long range correction these cutoffs can be decreased to 10Å for real space electrostatics and 11Å for Buckingham potential without any significant change in the potential and density, and approximately doubling the simulation speed. Thus, even in a naïve implementation, our present model is only approximately one order of magnitude slower than the simplest empirical model. Furthermore, the standard form of the potential means that the model can be implemented in most standard molecular simulation packages that support shell polarization (such as Gromacs) without modification.

2.4 Conclusions

A physically motivated, first-principles based polarizable force field was developed for CO_2 and N_2. Exchange, electrostatic, induction and dispersion interaction parameters were fit to individual components of SAPT dimer energy calculations. The resulting CO_2 and N_2 force field was benchmarked against experimental data for various types of properties, including the second virial coefficient, density, scattering structure factor, heat capacity and vapor-liquid coexistence curves. In general, excellent agreement with experimental data was obtained with our model.

Our force field is novel in that it utilizes the natural energy decomposition of SAPT to explicitly partition the classical interaction energy into physically distinct terms. This allows for trivial energy decomposition in bulk simulations, enabling more physical insight than that provided with widely used empirical models. More importantly, the "physical" nature of the force field suggests that the results should be robust, yielding the right answer, for the right reason, without relying on a subtle cancellation of errors. We would expect that this robustness would manifest itself in many ways, including the

transferability of the model to novel environments for which it was not explicitly parameterized, particularly if the remainder of the system has been parameterized in a similar "physical" manner.

Here, we provide one explicit of this transferability, looking at the properties of CO_2 and N_2 mixtures. Using simple combination rules in the absence of additional parameterization, we find not only good agreement with SAPT mixed-dimer calculations, but also accurate description of bulk mixtures, evidencing the robustness of the methodology. As such, we anticipate that these models will be extremely useful particularly for examining interactions of CO_2 and N_2 with complex solid and liquid media, where traditional empirical, non-polarizable force fields are likely to fail.

Bibliography

1.   *Carbon Dioxide Capture and Storage*. Intergovernmental Panel on Climate Change: 2005.

2.   Phan, A.; Doonan, C. J.; Uribe-Romo, F. J.; Knobler, C. B.; O'Keeffe, M.; Yaghi, O. M., Synthesis, Structure, and Carbon Dioxide Capture Properties of Zeolitic Imidazolate Frameworks. *Accounts Chem. Res.* **2010,** 43, (1), 58-67.

3.   Demessence, A.; D'Alessandro, D. M.; Foo, M. L.; Long, J. R., Strong CO_2 Binding in a Water-Stable, Triazolate-Bridged Metal-Organic Framework Functionalized with Ethylenediamine. *J Am Chem Soc* **2009,** 131, (25), 8784-+.

4.   Wick, C. D.; Chang, T. M.; Dang, L. X., Molecular Mechanism of CO_2 and SO_2 Molecules Binding to the Air/Liquid Interface of 1-Butyl-3-methylimidazolium Tetrafluoroborate Ionic Liquid: A Molecular Dynamics Study with Polarizable Potential Models. *J Phys Chem B* **2010,** 114, (46), 14965-14971.

5.   Gurkan, B. E.; de la Fuente, J. C.; Mindrup, E. M.; Ficke, L. E.; Goodrich, B. F.; Price, E. A.; Schneider, W. F.; Brennecke, J. F., Equimolar CO_2 Absorption by Anion-Functionalized Ionic Liquids. *J Am Chem Soc* **2010,** 132, (7), 2116-+.

6.   Gurkan, B.; Goodrich, B. F.; Mindrup, E. M.; Ficke, L. E.; Massel, M.; Seo, S.; Senftle, T. P.; Wu, H.; Glaser, M. F.; Shah, J. K.; Maginn, E. J.; Brennecke, J. F.; Schneider, W. F., Molecular Design of High Capacity, Low Viscosity, Chemically Tunable Ionic Liquids for CO_2 Capture. *J Phys Chem Lett* **2010,** 1, (24), 3494-3499.

7.   Yazaydin, A. O.; Snurr, R. Q.; Park, T. H.; Koh, K.; Liu, J.; LeVan, M. D.; Benin, A. I.; Jakubczak, P.; Lanuza, M.; Galloway, D. B.; Low, J. J.; Willis, R. R., Screening of Metal-Organic Frameworks for Carbon Dioxide Capture from Flue Gas Using a Combined Experimental and Modeling Approach. *J Am Chem Soc* **2009,** 131, (51), 18198-+.

8.   Liu, B.; Smit, B., Molecular Simulation Studies of Separation of CO_2/N_2, CO_2/CH_4, and CH_4/N_2 by ZIFs. *J Phys Chem C* **2010,** 114, (18), 8515-8522.

9.   Gibbons, T. G.; Klein, M. L., Thermodynamic Properties for a Simple Model of Solid Carbon-Dioxide - Monte-Carlo, Cell Model, and Quasiharmonic Calculations. *J Chem Phys* **1974,** 60, (1), 112-126.

10.   Macrury, T. B.; Steele, W. A.; Berne, B. J., Intermolecular Potential Models for Anisotropic Molecules, with Applications to N_2, CO_2, and Benzene. *J Chem Phys* **1976,** 64, (4), 1288-1299.

11.   Murphy, W. F.; Montero, S., The Determination of the Harmonic Force-Field of Acetylene Using Raman Intensities. *Mol Phys* **1981,** 44, (1), 187-196.

12.   Murthy, C. S.; Oshea, S. F.; Mcdonald, I. R., Electrostatic Interactions in Molecular-Crystals - Lattice-Dynamics of Solid Nitrogen and Carbon-Dioxide. *Mol Phys* **1983,** 50, (3), 531-541.

13.   Galassi, G.; Tildesley, D. J., Phase-Diagrams of Diatomic-Molecules Using the Gibbs Ensemble Monte-Carlo Method. *Mol Simulat* **1994,** 13, (1), 11-24.

14.   Kuchta, B.; Etters, R. D., Prediction of a High-Pressure Phase-Transition and Other Properties of Solid CO_2 at Low-Temperatures. *Phys Rev B* **1988,** 38, (9), 6265-6269.

15.   Etters, R. D.; Kuchta, B., Static and Dynamic Properties of Solid CO_2 at Various Temperatures and Pressures. *J Chem Phys* **1989,** 90, (8), 4537-4541.

16.   Moller, D.; Fischer, J., Determination of an Effective Intermolecular Potential for Carbon-Dioxide Using Vapor Liquid-Phase Equilibria from Npt Plus Test Particle Simulations. *Fluid Phase Equilibr* **1994,** 100, 35-61.

17.   Harris, J. G.; Yung, K. H., Carbon Dioxides Liquid-Vapor Coexistence Curve and Critical Properties as Predicted by a Simple Molecular-Model. *J Phys Chem-Us* **1995,** 99, (31), 12021-12024.

18.   Potoff, J. J.; Siepmann, J. I., Vapor-liquid equilibria of mixtures containing alkanes, carbon dioxide, and nitrogen. *Aiche J* **2001,** 47, (7), 1676-1682.

19.   Vrabec, J.; Stoll, J.; Hasse, H., A set of molecular models for symmetric quadrupolar fluids. *J Phys Chem B* **2001,** 105, (48), 12126-12133.

20.   Zhang, Z. G.; Duan, Z. H., An optimized molecular potential for carbon dioxide. *J Chem Phys* **2005,** 122, (21), 214507.

21.   Zhu, A. M.; Zhang, X. B.; Liu, Q. L.; Zhang, Q. G., A Fully Flexible Potential Model for Carbon Dioxide. *Chinese J Chem Eng* **2009,** 17, (2), 268-272.

22.   Merker, T.; Engin, C.; Vrabec, J.; Hasse, H., Molecular model for carbon dioxide optimized to vapor-liquid equilibria. *J Chem Phys* **2010,** 132, (23), 034312.

23.   Persson, R. A. X., Gaussian charge polarizable interaction potential for carbon dioxide. *J Chem Phys* **2011,** 134, (3), 034312.

24.   Tsuzuki, S.; Uchimaru, T.; Mikami, M.; Tanabe, K.; Sako, T.; Kuwajima, S., Molecular dynamics simulation of supercritical carbon dioxide fluid with the model potential from ab initio molecular orbital calculations. *Chem Phys Lett* **1996,** 255, (4-6), 347-349.

25.   Tsuzuki, S.; Uchimaru, T.; Tanabe, K.; Kuwajima, S.; Tajima, N.; Hirano, T., Refinement of nonbonding interaction parameters for carbon dioxide on the basis of the pair potentials obtained by MP2/6-311+G(2df)-level ab initio molecular orbital calculations. *J Phys Chem-Us* **1996,** 100, (11), 4400-4407.

26.   Bukowski, R.; Sadlej, J.; Jeziorski, B.; Jankowski, P.; Szalewicz, K., Intermolecular potential of carbon dioxide dimer from symmetry-adapted perturbation theory. *J Chem Phys* **1999,** 110, (8), 3785-3803.

27.   Domanski, K. B.; Kitao, O.; Nakanishi, K., A New Potential Model for Carbon-Dioxide from Ab-Initio Calculations. *Mol Simulat* **1994,** 12, (3-6), 343-353.

28.   Welker, M.; Steinebrunner, G.; Solca, J.; Huber, H., Ab initio calculation of the intermolecular potential energy surface of $(CO_2)(2)$ and first applications in simulations of fluid CO_2. *Chem Phys* **1996,** 213, (1-3), 253-261.

29.   Steinebrunner, G.; Dyson, A. J.; Kirchner, B.; Huber, H., Structural and thermodynamic properties of fluid carbon dioxide from a new ab initio potential energy surface. *J Chem Phys* **1998,** 109, (8), 3153-3160.

30.   Bock, S.; Bich, E.; Vogel, E., A new intermolecular potential energy surface for carbon dioxide from ab initio calculations. *Chem Phys* **2000,** 257, (2-3), 147-156.

31.   Williams, H. L.; Chabalowski, C. F., Using Kohn-Sham orbitals in symmetry-adapted perturbation theory to investigate intermolecular interactions. *J Phys Chem A* **2001,** 105, (3), 646-659.

32.   Hesselmann, A.; Jansen, G., First-order intermolecular interaction energies from Kohn-Sham orbitals. *Chem Phys Lett* **2002,** 357, (5-6), 464-470.

33.   Hesselmann, A.; Jansen, G., Intermolecular induction and exchange-induction energies from coupled-perturbed Kohn-Sham density functional theory. *Chem Phys Lett* **2002,** 362, (3-4), 319-325.

34.   Hesselmann, A.; Jansen, G., Intermolecular dispersion energies from time-dependent density functional theory. *Chem Phys Lett* **2003,** 367, (5-6), 778-784.

35.   Hesselmann, A.; Jansen, G., The helium dimer potential from a combined density functional theory and symmetry-adapted perturbation theory approach using an exact exchange-correlation potential. *Phys Chem Chem Phys* **2003,** 5, (22), 5010-5014.

36.   Hesselmann, A.; Jansen, G.; Schutz, M., Density-functional theory-symmetry-adapted intermolecular perturbation theory with density fitting: A new efficient method to study intermolecular interaction energies. *J Chem Phys* **2005,** 122, (1), 014103.

37.   Everitt, K. F.; Skinner, J. L., Isotropic Raman line shapes of N-2 and O-2 along their liquid-gas coexistence lines. *J Chem Phys* **2001,** 115, (18), 8531-8539.

38.   Johnson, J. D.; Shaw, M. S.; Holian, B. L., The Thermodynamics of Dense Fluid Nitrogen by Molecular-Dynamics. *J Chem Phys* **1984,** 80, (3), 1279-1294.

39.   Aquilanti, V.; Bartolomei, M.; Cappelletti, D.; Carmona-Novillo, E.; Pirani, F., The N-2-N-2 system: An experimental potential energy surface and calculated rotovibrational levels of the molecular nitrogen dimer. *J Chem Phys* **2002,** 117, (2), 615-627.

40.   Goharshadi, E. K.; Abbaspour, M.; Jorabchi, M. N.; Nahali, M., Computation of some thermodynamic properties of nitrogen using a new intermolecular potential from molecular dynamics simulation. *Chem Phys* **2009,** 358, (3), 185-195.

41.   Jordan, P. C.; Van Maaren, P. J.; Mavri, J.; Van Der Spoel, D.; Berendsen, H. J. C., Towards Phase Transferable Potential Functions - Methodology and Application to Nitrogen. *J Chem Phys* **1995,** 103, (6), 2272-2285.

42.   Berns, R. M.; Vanderavoird, A., N-2-N-2 Interaction Potential from Abinitio Calculations, with Application to the Structure of (N-2)2. *J Chem Phys* **1980,** 72, (11), 6107-6116.

43.   Vanderavoird, A.; Wormer, P. E. S.; Jansen, A. P. J., An Improved Intermolecular Potential for Nitrogen. *J Chem Phys* **1986,** 84, (3), 1629-1635.

44.   Stallcop, J. R.; Partridge, H., The N-2-N-2 potential energy surface. *Chem Phys Lett* **1997,** 281, (1-3), 212-220.

45.   Strak, P.; Krukowski, S., Molecular nitrogen-N-2 properties: The intermolecular potential and the equation of state. *J Chem Phys* **2007,** 126, (19), 194501.

46.   Gomez, L.; Bussery-Honvault, B.; Cauchy, T.; Bartolomei, A.; Cappelletti, D.; Pirani, F., Global fits of new intermolecular ground state potential energy surfaces for N-2-H-2 and N-2-N-2 van der Waals dimers. *Chem Phys Lett* **2007,** 445, (4-6), 99-107.

47.   Cappelletti, D.; Pirani, F.; Bussery-Honvault, B.; Gomez, L.; Bartolomei, M., A bond-bond description of the intermolecular interaction energy: the case of weakly bound N-2-H-2 and N-2-N-2 complexes. *Phys Chem Chem Phys* **2008,** 10, (29), 4281-4293.

48.   Bartolomei, M.; Carmona-Novillo, E.; Hernandez, M. I.; Campos-Martinez, J.; Hernandez-Lamoneda, R., Long-Range Interaction for Dimers of Atmospheric Interest: Dispersion, Induction and Electrostatic Contributions for O-2-O-2, N-2-N-2 and O-2-N-2. *J Comput Chem* **2011,** 32, (2), 279-290.

49.   H.-J.Werner; Knowles, P. J.; Lindh, R.; Manby, F. R.; Schutz, M.; Celani, P.; Korona, T.; Mitrushenkov, A.; Rauhut, G.; Adler, T. B.; Amos, R. D.; Bernhardsson, A.; Berning, A.; Cooper, D. L.;

Deegan, M. J. O.; Dobbyn, A. J.; Eckert, F.; Goll, E.; Hampel, C.; Hetzer, G.; Hrenar, T.; Knizia, G.; K¨oppl, C.; Liu, Y.; Lloyd, A. W.; Mata, R. A.; May, A. J.; McNicholas, S. J.; Meyer, W.; Mura, M. E.; Nicklass, A.; Palmieri, P.; Pfluger, K.; Pitzer, R.; Reiher, M.; Schumann, U.; Stoll, H.; Stone, A. J.; Tarroni, R.; Thorsteinsson, T.; M.Wang; Wolf, A. *MOLPRO, version 2009.1, a package of ab initio programs, see http://www.molpro.net*.

50.   Perdew, J. P.; Burke, K.; Ernzerhof, M., Generalized Gradient Approximation Made Simple. *Phys Rev Lett* **1996,** 77, (18), 3865.

51.   Perdew, J. P.; Burke, K.; Ernzerhof, M., Generalized Gradient Approximation Made Simple [Phys. Rev. Lett. 77, 3865 (1996)]. *Phys Rev Lett* **1997,** 78, (7), 1396.

52.   Gruning, M.; Gritsenko, O. V.; van Gisbergen, S. J. A.; Baerends, E. J., Shape corrections to exchange-correlation potentials by gradient-regulated seamless connection of model potentials for inner and outer region. *J Chem Phys* **2001,** 114, (2), 652-660.

53.   Williams, H. L.; Mas, E. M.; Szalewicz, K.; Jeziorski, B., On the Effectiveness of Monomer-Centered, Dimer-Centered, and Bond-Centered Basis Functions in Calculations of Intermolecular Interaction Energies. *J Chem Phys* **1995,** 103, (17), 7374-7391.

54.   Hess, B.; Kutzner, C.; van der Spoel, D.; Lindahl, E., GROMACS 4: Algorithms for highly efficient, load-balanced, and scalable molecular simulation. *J Chem Theory Comput* **2008,** 4, (3), 435-447.

55.   http://towhee.sourceforge.net/

56.   Lindan, P. J. D.; Gillan, M. J., Shell-Model Molecular-Dynamics Simulation of Superionic Conduction in Caf2. *J Phys-Condens Mat* **1993,** 5, (8), 1019-1030.

57.   Cracknell, R. F.; Nicholson, D.; Parsonage, N. G.; Evans, H., Rotational Insertion Bias - a Novel Method for Simulating Dense Phases of Structured Particles, with Particular Application to Water. *Mol Phys* **1990,** 71, (5), 931-943.

58.   Rick, S. W.; Stuart, S. J., Potentials and algorithms for incorporating polarizability in computer simulations. *Rev Comp Ch* **2002,** 18, 89-146.

59.   Thole, B. T., Molecular Polarizabilities Calculated with a Modified Dipole Interaction. *Chem Phys* **1981,** 59, (3), 341-350.

60.   Yu, H. B.; Whitfield, T. W.; Harder, E.; Lamoureux, G.; Vorobyov, I.; Anisimov, V. M.; MacKerell, A. D.; Roux, B., Simulating Monovalent and Divalent Ions in Aqueous Solution Using a Drude Polarizable Force Field. *J Chem Theory Comput* **2010,** 6, (3), 774-786.

61.   Lewis, M.; Wu, Z. Y.; Glaser, R., Polarizabilities of carbon dioxide and carbodiimide. Assessment of theoretical model dependencies on dipole polarizabilities and dipole polarizability anisotropies. *J Phys Chem A* **2000,** 104, (48), 11355-11361.

62.   Levy, M.; Perdew, J. P.; Sahni, V., Exact Differential-Equation for the Density and Ionization-Energy of a Many-Particle System. *Phys Rev A* **1984,** 30, (5), 2745-2748.

63.   Yu, K.; McDaniel, J. G.; Schmidt, J. R., Physically Motivated, Robust, ab Initio Force Fields for CO(2) and N(2). *J Phys Chem B* **2011,** 115, (33), 10054-10063.

64.   McQuarrie, D. A., *Statistical Mechanics*. p 228.

65.   Span, R.; Wagner, W., A new equation of state for carbon dioxide covering the fluid region from the triple-point temperature to 1100 K at pressures up to 800 MPa. *J Phys Chem Ref Data* **1996,** 25, (6), 1509-1596.

66.   Vantricht, J. B.; Fredrikze, H.; Vanderlaan, J., Neutron-Diffraction Study of Liquid Carbon-Dioxide at 2-Thermodynamic States. *Mol Phys* **1984,** 52, (1), 115-127.

67.   Etesse, P.; Zega, J. A.; Kobayashi, R., High-Pressure Nuclear-Magnetic-Resonance Measurement of Spin-Lattice Relaxation and Self-Diffusion in Carbon-Dioxide. *J Chem Phys* **1992,** 97, (3), 2022-2029.

68.   Gross, T.; Buchhauser, J.; Ludemann, H. D., Self-diffusion in fluid carbon dioxide at high pressures. *J Chem Phys* **1998,** 109, (11), 4518-4522.

69.   Herzberg, G., *Molecular spectra and molecular structure*. Vol. 2, p 173.

70.   Frenkel, D.; Smit, B., *Understanding Molecular Simulation, from algorithms to applications*.

71.   Ewing, M. B.; Trusler, J. P. M., Second Acoustic Virial-Coefficients of Nitrogen between 80-K and 373-K. *Physica A* **1992,** 184, (3-4), 415-436.

72.   http://webbook.nist.gov/chemistry/ NIST Chemistry WebBook.

73.   Dore, J. C.; Walford, G.; Page, D. I., Structure Factor for Liquid-Nitrogen and Liquid-Oxygen from Neutron-Scattering Studies .1. Orientation Correlation Effects. *Mol Phys* **1975,** 29, (2), 565-580.

74.   Cheung, P. S. Y.; Powles, J. G., Properties of Liquid-Nitrogen .4. Computer-Simulation. *Mol Phys* **1975,** 30, (3), 921-949.

75.   Krynicki, K.; Rahkamaa, E. J.; Powles, J. G., Properties of Liquid-Nitrogen .1. Self-Diffusion Coefficient. *Mol Phys* **1974,** 28, (3), 853-855.

76.   Brugge, H. B.; Holste, J. C.; Hall, K. R.; Gammon, B. E.; Marsh, K. N., Densities of carbon dioxide plus nitrogen from 225 K to 450 K at pressures up to 70 MPa. *J Chem Eng Data* **1997,** 42, (5), 903-907.

77.   Sala, J.; Guardia, E.; Masia, M., The polarizable point dipoles method with electrostatic damping: Implementation on a model system. *J Chem Phys* **2010,** 133, (23), 234101.

78.   Andersen, H. C., Molecular-Dynamics Simulations at Constant Pressure and-or Temperature. *J Chem Phys* **1980,** 72, (4), 2384-2393.

Chapter 3. Three-Body Effects in the SYM

CO$_2$ Model

Table of Contents

3.1 Introduction

In the previous chapter, we developed an *ab initio*, physically-motivated CO_2 model based on density functional theory-symmetry adapted perturbation theory (DFT-SAPT) calculations on CO_2 dimers, known as the "SYM" (Schmidt, Yu, and McDaniel) model.[1] Utilizing the SAPT energy decomposition, each physically meaningful component of the SAPT energy (electrostatic, exchange, induction, dispersion, etc.) was fit *individually* to a corresponding term in the force field, employing a physically-appropriate functional form. Since some several of these terms (e.g. exchange-induction and exchange-dispersion) are mathematically well-defined but not physically meaningful, and vanish outside regimes of strong charge overlap, we group these terms with their conventional induction/dispersion counterparts. This is in line with literature recommendations and avoids unphysical divergences in the individual terms that cancel in their summation (e.g. induction + exchange-induction)[2]. Furthermore, Stone has shown that the summation of the SAPT dispersion terms (dispersion + exchange-dispersion) better reproduces the asymptotic behavior than either term by itself.[3] For this reason, we believe that this physically-motivated methodology offers a compelling advantage over both conventional approaches (where only the total interaction energy is fit), and opposite extreme where all terms (including unphysical and ill-behaved) are fit individually.

The resulting force field is polarizable (via a Drude model), naturally incorporating many-body *electrostatic* effects, and yields quantitative agreement with a diverse set of structural, thermodynamic, and dynamic observables (density, heat capacity, diffusion constants, vapor-liquid equilibrium…). However this model does not explicitly treat *non-electrostatic* many-body effects such as many-body exchange/dispersion.

Although the SYM model was parameterized almost exclusively on the basis of *ab initio* SAPT calculations (e.g. all parameters where fit to *ab initio* data rather than experimental results), we were forced to introduce a *single* empirical parameter to achieve excellent agreement with properties across the

phase diagram: a scale factor of 0.935 was applied to the original fitted dispersion coefficients (i.e. reducing the SAPT-calculated dispersion by ~6%), a fact we attributed to omission of non-electrostatic three-body effects (whereas induction is included explicitly via polarizability). As expected, application of this empirical scale factor decreases the accuracy of the calculated second virial coefficient (which is sensitive to only the two-body potential), especially in the low temperature region, although predictions of all bulk properties were dramatically improved.

Although neglected by nearly all empirical potentials, such three-body interactions have been demonstrated to be small but important in many cases, such as rare gases,[4-9] simple diatomic molecules,[10, 11] alkali ions,[12] large fullerene molecules,[13] metal-ligand complexes[14] and water.[15] Such many-body effects can be partitioned into simple many-body electrostatic effects (e.g. induction), and complex non-electrostatic many-body effects (e.g. many-body exchange / dispersion). While the former have been incorporated into a host of polarizable empirical force fields, the latter are nearly universally neglected.[14, 15]

Currently, Persson's empirical Gaussian charge polarizable potential for carbon dioxide (GCPCDO) model[16] and the model of Oakley and Wheatley (OW)[17] are the only CO_2 potentials to include explicit non-electrostatic three-body interactions, and thus the only potentials that are (in principle) capable of reproducing both experimental second / third virial coefficients and bulk properties. The GCPCDO model utilizes a "smeared" Gaussian model for electrostatic interactions, incorporating polarization via a molecular point-dipole approximation. Model parameters were empirically refined to reproduce the experimental second virial coefficient over a range of temperatures. Persson incorporates many-body dispersion effects (neglecting other many-body effects, such as exchange) via an Axilrod-Teller form, treating the *magnitude* of these interactions as an adjustable empirical parameter to reproduce experimentally measured third virial coefficients. Unfortunately, this model suffers from a complicated and computationally expensive functional form (no simple analytic gradients are possible), and yields substantial errors when applied to the *bulk*, particularly in the medium density region.[16]

The OW model employs a different strategy, parameterizing the CO_2 pair potential interaction using MP2 calculations on CO_2 dimers with a variety of basis sets. This *ab inito* data is fit to an anisotropic Lennard-Jones plus point charge form, yielding a pairwise-additive, non-polarizable dimer potential. (Note that the anisotropic form of the OW potential, Eq. 2 in Ref. 17, does not obey exchange symmetry with respect to the CO_2 molecules, possibly due to a sign error in the fourth or fifth term!) Three-body dispersion contributions are approximated at the Hartree-Fock SAPT level and fit to an Axilrod-Teller form. Three-body exchange contributions are estimated by subtracting the fitted three-body dispersion and induction components from the sum of the non-additive MP2 energies and three-body SAPT dispersion. However, the authors do not validate the underlying pair potential via second virial calculations prior to the addition of the three-body terms. Our calculations (using the isotropic form of their potential, due to the above error) show that the second virial predicted by this model are, for a wide range of temperatures, approximately 10% lower the experimental values[18] (see supplemental material of reference 19); furthermore, calculation on our own MP2 CO_2 dimers show that anisotropy has only a small effect on the virial. This large virial error is not surprising as MP2 is known to overestimate dispersion energies for large basis sets.[20] As such, the resulting bulk properties predicted by this model are not particularly accurate (e.g. 5-10% error in enthalpy of vaporization and ~20% in the gas-liquid coexistence densities and pressures).

Nonetheless, the basic approach employed by Oakley *et. al* is promising – using explicit electronic structure data to parameterize many-body interactions. As such, we report in this chapter an extension of our SAPT-based "SYM" CO_2 model to include explicit three-body exchange and dispersion terms based on three-body DFT-SAPT calculations. Consistent with the physically-motivated philosophy of the SYM model, we utilize the inherent SAPT energy decomposition to add corresponding three-body exchange and dispersion terms to our SYM model, fitting these components term-by-term (once again, grouping physically ill-defined terms such as exchange-induction and exchange-disperions with the induction/exchange counterparts) to mitigate spurious cancellation of errors both between the various

three-body terms (e.g. between three-body dispersion and three-body exchange) and across terms of different order (e.g. between two- and three-body terms). We show that although the energetic contribution of the non-electrostatic three-body terms is quite small, these terms make an extremely large contribution to the internal pressure, and are thus indispensable in a truly physically-motivated model (as opposed to including them as an *ad hoc* correction to the two-body potential.) With this modification, we obtain highly accurate results for both the second/third virial coefficients and bulk properties, thus making significant progress towards a robust, transferable, physically-motivated and truly parameter-free CO_2 model – achieving the "right answer, for the right reason."

Finally, we discuss how this explicit three-body model can be reduced, using rigorous statistical-mechanical considerations, to a density- and temperature-dependent effective two-body potential that can be efficiently implemented in existing molecular simulation packages. Intriguingly, we show that in the limit of liquid-like density this new effective potential reduces almost exactly to our prior extremely successful SYM model, thus essentially "deriving" this model from its more rigorous many-body counterpart. As such, this density- and temperature-dependent effective $SYM[\rho, T]$ model should retain the extremely high accuracy (for a vast array of properties across the phase diagram) and computational efficiency of the SYM model, while also gaining asymptotic correctness via accurate second/third virial coefficients.

3.2 Methods

3.2.1 Electronic Structure Calculations

Our methodology requires a set of representative CO_2 trimers from which to parameterize a physically-motivated three-body potential. We employ the TraPPE force field[21] to run a bulk CO_2 MD simulation with a liquid-like density and 3000K temperature, such that both repulsive and attractive regions are sampled. Approximately 200 trimer geometries are randomly selected from the trajectory and three-body

DFT-SAPT calculations are conducted utilizing the SAPT2008 suite of codes.[22] We use the Perdew-Burke-Ernzerhof (PBE) exchange-correlation functional[23, 24] in conjunction with Dunning-style aug-cc-pVDZ and aug-cc-pVTZ basis sets; a complete basis set (CBS) extrapolation is conducted for the dispersion term (which converges slowly),[25]

$$E^{CBS} = \frac{3^{\beta}}{3^{\beta} - 2^{\beta}} E^{tz} - \frac{2^{\beta}}{3^{\beta} - 2^{\beta}} E^{dz} \tag{3.1}$$

Based on test calculations for a selection of Ar trimers with corresponding DZ/TZ/QZ bases, a value of 2.01 is adopted for the exponent β in the equation above, comparable to values of 2.2 and 2.4 that have been reported for MP2 and CCSD(T) correlation calculations, respectively.[25]

The resulting total three-body interaction energy can be written as a summation of physically meaningful terms,[22]

$$E_{\text{int}}^{SAPT(DFT)}[3,3] = E_{exch}^{3b} + E_{disp}^{3b} + E_{ind}^{3b} \tag{3.2}$$

$$E_{exch}^{3b} = E_{exch}^{(1)}[3,3](KS) + \tilde{E}_{exch-disp}^{(2)}[3,3](CKS) \tag{3.3}$$

$$E_{disp}^{3b} = E_{disp}^{(3)}[3,3](CKS) \tag{3.4}$$

$$E_{ind}^{3b} = E_{ind}^{(2)}[3,3](CKS) + \tilde{E}_{exch-ind}^{(2)}[3,3](CKS) \tag{3.5}$$

3.2.2 Validation of Three-body Induction and Two-body Potentials

In equation (3.5), $E_{ind}^{3b} = E_{ind}^{(2)}[3,3](CKS) + \tilde{E}_{exch-ind}^{(2)}[3,3](CKS)$ represents the induction contribution to the interaction energy, and has already been included (implicitly) in the polarizable Drude oscillator approach of the existing SYM model. In Figure 3.1, we compare the results of our Drude model with the three-body induction calculated from 3B SAPT calculations, yielding overall very good agreement for almost all sampled trimers. Note that the results are not a "fit", in that we are simply taking the results of

our Drude model (which was parameterized for dimer induction energy) and applying it to many-body induction.
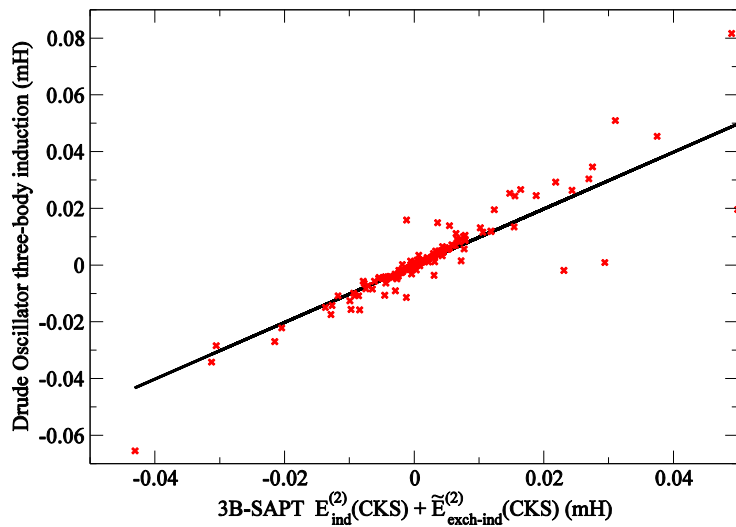
Figure 3.1. Comparision of the SAPT calculated three-body induction energy, compared to the corresponding quantity from the Drude model. Data is shown for 208 CO_2 trimers with a total interaction energy of less than 15 kJ/mol (i.e. excluding highly repulsive configurations). The RMS error between the Drude model and SAPT is 5.4 µH.
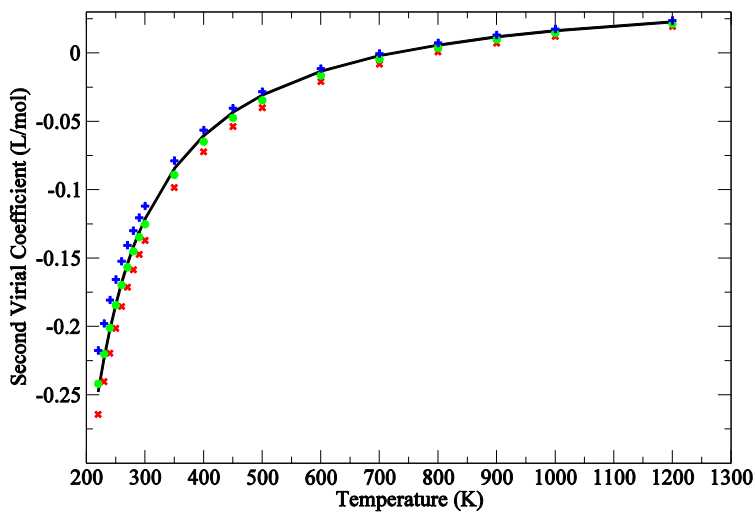
Figure 3.2. The second virial coefficients. Experimental data[1] (black solid line) is shown alongside simulation data from the SYM-1.0 (red cross), SYM-0.935 (blue plus), and SYM-0.970 (green dot, present work).

We utilize these three-body terms in conjunction with an accurate dimer potential. Here we employ our former SYM model,[1] which was parameterized in a consistent, physically-motivated manner to SAPT calculations on CO_2 dimers. The SYM model was fit to the SAPT energy decomposition separately for each interaction energy component to mitigate error cancellation, with explicit and physically-appropriate functional forms for exchange, electrostatics, induction and dispersion. It is important to note that the SYM potential is itself polarizable (via a Drude oscillator approach), and thus the resulting dimer potential will also be polarizable. This polarizability will give rise to additional electrostatic many-body interactions in our final many-body potential. Since this induction term was previously accurately parameterized to reproduce the SAPT dimer induction energy, and the resulting Drude polarizability reproduces the experimentally measured polarizability tensor,[1] we do not alter this many-body electrostatic treatment during the development of our present explicit many-body model.

The SYM model contains a *single* empirical scale factor, $\lambda = 0.935$, applied to the two-body dispersion term to achieve accurate bulk properties. This model will also be noted as SYM-0.935 later in this chapter, to be distinguished from other scaled SYM models we use for our three-body model construction, which will be referred to as SYM-λ, in which λ is the corresponding scale factor. SYM-0.935 thus accounts in an average sense for the neglected many-body terms, but somewhat compromises the accuracy of the dimer potential. As we have shown in Chapter 2 (also see Figure 3.2), the unscaled potential SYM-1.0 slightly underestimates B_2 in the low temperature region, corresponding to a small error in the underlying two-body potential that we attribute to the inherent limitations in underlying SAPT calculations. Our prior SYM-0.935 slightly *overestimates* B_2 in low temperature region, thus yielding an "incorrect" two-body potential (although bulk properties are dramatically improved over the unscaled model!) As such, prior to introducing three-body terms, we compensate for this (small) error by substituting a scale factor of 0.97 for dispersion (SYM-0.970), yielding essentially perfect B_2 coefficients in the range 200-1300K. Note that this scale factor is much smaller than 0.935, as the latter included effective three-body interactions to yield the correct experimental bulk density. In contrast, here we

correct *only* for errors in the two-body potential, guaranteeing a clean separation of two- and three-body portions of the total potential. Therefore, SYM-0.970 is used throughout all the calculations later in this work, in conjunction with the newly introduced three-body terms.

3.2.3 Three-body Dispersion Fitting

The SAPT three-body dispersion energies $E_{disp}^{3b} = E_{disp}^{(3)}[3,3](CKS)$ are fit with a generalized Axilrod-Teller form in the basis of atomic sites:

$$E_{disp}^{3b} \cong \sum_{\{A,B,C\}} C_1^{t_A t_B t_C} (1 + 3\cos\theta_A \cos\theta_B \cos\theta_C) / R_{AB}^3 R_{BC}^3 R_{CA}^3 + C_2^{t_A t_B t_C} / R_{AB}^3 R_{BC}^3 R_{CA}^3 \qquad (3.6)$$

where A, B, C runs over all intermolecular atom trimers, and t_A, t_B, t_C stand for the atom types (C, O) of A, B and C. The traditional Axilrod-Teller functional form, which is derived for identical spherical symmetric atoms, is inadequate to fit the SAPT energies for CO_2. We therefore incorporate an additional isotropic term (as given above) to increase the flexibility of the fitting function. The final fitting is shown in Figure 3.3 and fitted parameters are Table 3.1.
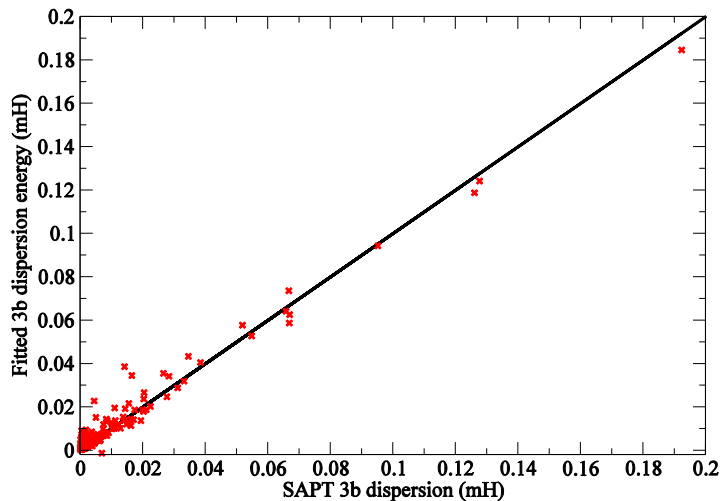
Figure 3.3. Three-body dispersion fitting. The RMS error in the fit is 3.7µH.

trimer type	C_1 /100 (kJ/mol·Å^9)	C_2 /100 (kJ/mol·Å^9)
OOO	18.978	4.9638
COO	-8.1498	10.261
CCO	9.6611	1.1445
CCC	-50.381	-44.709

Table 3.1. Three-body dispersion parameters.

3.2.4 Three-body Exchange Terms

We also examine the effect of the three-body exchange interaction $E_{exch}^{3b} = E_{exch}^{(1)}[3,3](KS) + \tilde{E}_{exch-disp}^{(2)}[3,3](CKS)$. Although this term is smaller in magnitude (at typical intermolecular separations) and faster decaying (exponential vs. algebraic), we find its inclusion to be important for quantitative accuracy. We note that the GCPCDO model does not account for this effect, although it was likely included implicitly in the empirical fitting procedure. Unfortunately, a physically appropriate functional form for three-body exchange has been derived only for atomic species and is extremely complex; generalization to molecular species would yield many free parameters that would need to be parameterized based on our SAPT data. Furthermore, current three-body DFT-SAPT methods do not explicitly calculate three-body exchange-dispersion under the coupled Kohn-Sham (CKS) approximation, $E_{exch-disp}^{(2)}[3,3](CKS)$, but rather $E_{exch-disp}^{(2)}[3,3](KS)$, the far less accurate uncoupled counterpart. Following the recommendations of Podeszwa and Szalewicz,[22] we approximated $E_{exch-disp}^{(2)}[3,3](CKS)$ via its uncoupled Kohn-Sham (KS) counterpart and scaling based on the ratio of the CKS and KS dispersion,

$$\tilde{E}_{exch-disp}^{(2)}(CKS) = E_{exch-disp}^{(2)}(KS)\frac{E_{disp}^{(3)}(CKS)}{E_{disp}^{(3)}(KS)} \tag{3.7}$$

The associated scale factor can be quite large, with corresponding uncertainty. Due to the low accuracy of this term, it is not grouped altogether with dispersion energies and fit explicitly, like what we did in our

previous work. Instead, it is combined with the exchange part and will be treated in a much cruder way. Given these considerations, we therefore treat the total many body exchange potential E_{exch}^{3b} in a simplified, mean-field way via a completely isotropic form,

$$E_{exch}^{3b} \cong \sum_{O_A O_B O_C} \alpha \exp(-\beta^{(3)}(R_{AB} + R_{BC} + R_{CA})) \tag{3.8}$$

approximating the three-body exchange energy as proportional to the mutual overlap of all three electron densities. Although the above form neglects the complex angular dependence, it will still allow us to capture the average (attractive) effect of three-body exchange. In particular, the three-body exchange is dominated by trimers in near equilateral triangular configurations where all three monomers exhibit strong overlap. The above approximate form works well in this regime, and the magnitude of the three-body exchange itself rapidly decreases as the mutual trimer overlap decreases. For simplicity, we account only for interactions between intermolecular oxygen trimers (since the carbon atoms are "buried"). We approximate the three-body exchange exponent, $\beta^{(3)}$, in terms of the corresponding two-body exponent, $\beta^{(3)} \approx \beta^{(2)} / 2 = 1.9644 \text{Å}^{-1}$. This approximation has been verified by Ne, Ar, Kr trimer calculations in an equilateral geometry, and should be fairly robust in quasi-equilateral cases that dominate the three-body exchange energy.

Given the above approximations, we do not attempt to fit the remaining pre-factor, α, to the explicit three-body SAPT exchange energies. Rather, we treat α as a quasi-empirical parameter fit to experimental third virial / density, and obtain a final value of -3.0×10^7 kJ/mol. Although this "empirical" term consist of less than 2% of the total bulk energy even under liquid-like conditions, the resulting many-body potential cannot be considered a strictly "ab initio" potential as this term was fit to experimental data! Advances in the implementation of three-body SAPT, yielding accurate three-body exchange at the coupled Kohn-Sham level, would presumably facilitate the development of a truly *ab initio* many-body model.

3.3 Results and Discussions

3.3.1 Many-body SYM-3B model

Third virial coefficients at selected temperatures were calculated using these parameters and are listed in Table 3.2. Compared to non-polarizable EPM2 and TraPPE model, our underlying polarizable SYM-0.970 model (which omits explicit non-electrostatic three-body effects) does not yield improved the third virial coefficients. However, addition of the new three-body terms (SYM-3B model) yields a *dramatic* improvement. Thus in contrast to other systems like water,[15] the non-additivity of CO_2 potential mainly comes from dispersion and exchange effects rather than induction (a result which is unsurprising given the vanishing dipole of CO_2).

T (K)	EPM2	TraPPE	SYM-3B	GCPCDO	Exp
280	2910	3080	4700 (2814)	5140	5636[a], 5165[b]
300	2922	3060	4538 (2956)	4790	4927[a], 4753[b]
320	2700	2870	4263 (2908)	4460	4423[a], 4360[b]
340	2560	2680	3963 (2850)	4046	3996[b]

Table 3.2. Third virial coefficients of different models. All numbers are given in $(mL/mol)^2$; numbers given in parenthesis omit the three-body portion of the potential, so is effectively calculated with SYM-0.970 model.[2]   [a]Reference 26; [b]Reference 27.

The bulk density of the SYM-3B model was examined at three phase points, representing gas, liquid and supercritical states, respectively. All explicit three-body simulations were carried out using a hybrid Monte Carlo algorithm[28] with a cutoff of 12Å for both two-body and three-body interactions. Long range dispersion corrections for two-body parts[29] are included in conjunction with a particle mesh Ewald treatment for electrostatic interactions. The three-body energy of a certain trimer ABC is explicitly calculated only when all three involving distances (r_{AB}, r_{BC} and r_{CA}) are smaller than the cutoff value. The remaining part of three-body energy (the long range part) is treated using Kirkwood approximation, and more details will be discussed later. The system size is set to 400 molecules. All MD simulations were

carried out in an NVT ensemble with a cutoff of 14Å for two-body dispersion interaction. Hybrid MC calculations are done using a modified version of Towhee,[30] and all MD simulations were conducted using Gromacs 4.[31] The percentage errors compared to experimental data are quite small and are shown in Table 3.3. It is worth noting that although GCPCDO exhibits excellent third virial coefficients (by construction, as these were explicitly fit), it displays typically 8% error in the same density region (below 20 mol/L). The structure of bulk CO_2 was also tested via radial distribution functions and are nearly identical to our previous SYM-0.935 potential (see Figure 3.4), which in turn are in excellent agreement with the experimental bulk structure.

T (K)	P (bar)	density (mol/L)	Exp.[a]	error%
300	60	3.99	4.14	-3.6
300	100	17.64	18.21	-3.1
320	140	15.73	15.98	-1.6

Table 3.3. Comparison of calculated and experimental bulk densities in the gas (300K, 60 bar), liquid (300K, 100 bar), and supercritical (320K, 140 bar) regions. [a]Reference 32.
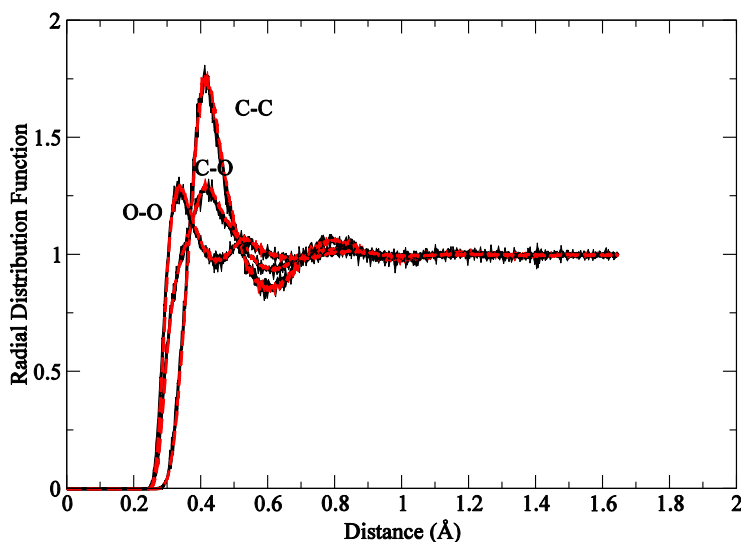
Figure 3.4. Radial distribution functions for bulk CO_2 (320K, 18mol/L), Black solid lines are calculated with explicit SYM-3B model. Results from SYM-0.935 model are plotted along the side with red dashed lines.

3.3.2 Effective ρ/T-dependent SYM[ρ,T] model

Inclusion of an explicit three-body term is computationally expensive. However, in a homogeneous system the total three-body energy can be calculated under Kirkwood approximation,

$$E_{ABC}^{3b} = N_{atom} \frac{\rho_{atom}^2}{6} \int d\mathbf{r_{AB}} d\mathbf{r_{AC}} g^{t_A t_B}(r_{AB}) g^{t_B t_C}(r_{BC}) g^{t_C t_A}(r_{CA}) V^{3b}(\mathbf{r_{AB}}, \mathbf{r_{AC}}) \tag{3.9}$$

$$E^{3b} = \frac{8}{27} E_{OOO}^{3b} + \frac{1}{27} E_{CCC}^{3b} + \frac{4}{27} (E_{COO}^{3b} + E_{OCO}^{3b} + E_{OOC}^{3b}) + \frac{2}{27} (E_{CCO}^{3b} + E_{COC}^{3b} + E_{OCC}^{3b}) \tag{3.10}$$

where the necessary radial distribution functions , $g(r)$, are estimated from our previous SYM model at a variety of (fixed) densities and temperatures using Monte Carlo simulations in an NVT ensemble. The validity of Kirkwood approximation at 320K is illustrated in Figure 3.5.
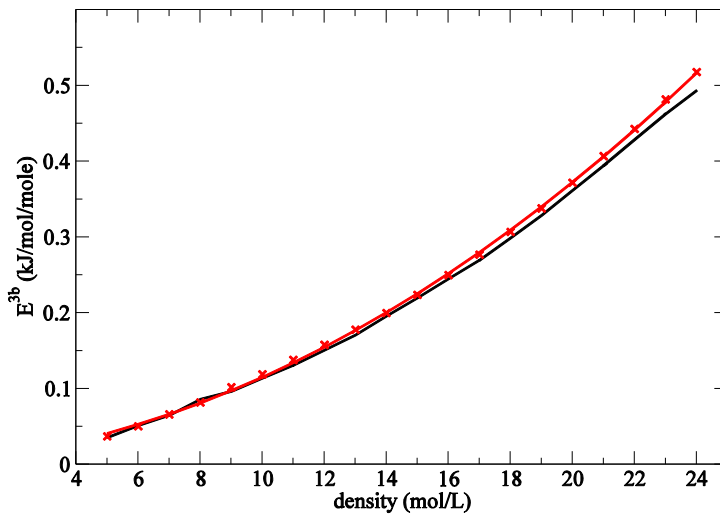
Figure 3.5. Evaluation of Kirkwood approximation to thee three-body energy, E^{3b}, at 320K. The black solid line is the result from explicit three-body simulation. And the red crosses are calculated via Kirkwood approximation. A quadratic fit is also shown in the figure.

We find this approximation to be excellent in other regions of the phase diagram as well, except at high temperature / high density zones (e.g. 800K and 24 mol/L). As we mentioned, after excluding the short range part of the integration ($r_{AB} < r_c$, $r_{BC} < r_c$ and $r_{CA} < r_c$), the equation above is also used to calculate the long range corrections for the three-body energies in our explicit three-body simulations.

Using the three-body energy, $E^{3b}(\rho,T)$, we then derive a *density/temperature-dependent* two-body *polarizable* effective potential (the $\mathrm{SYM}[\rho,T]$ model) such that,

$$\left\langle E^{2b}_{SAPT-disp}\right\rangle + \lambda(\rho,T)\left\langle E^{2b}_{disp}\right\rangle = \left\langle E^{2b}_{SAPT-disp}\right\rangle + 0.97\left\langle E^{2b}_{disp}\right\rangle + \left\langle E^{3b}\right\rangle \tag{3.11}$$

where the angle brackets denote an equilibrium average at a given density and temperature, evaluated from explicit Monte Carlo simulations, and $\left\langle E^{2b}_{SAPT-disp}\right\rangle$ is the average calculated two-body energy at a given density and temperature (excluding dispersion contributions), $\left\langle E^{2b}_{disp}\right\rangle$ is the average two-body dispersion contribution, and 0.97 is the scale factor (determined above) which yields the correct B_2 (and thus the correct two-body potential). In other words, we develop an effective two-body potential such that the average potential energy of the homogeneous fluid (at a given density and temperature) for the effective two-body model and the explicit many-body model are equal,

$$\left\langle E^{\mathrm{SYM}[\rho,T]}\right\rangle_{\rho,T} = \left\langle E^{\mathrm{SYM\text{-}3B}}\right\rangle_{\rho,T} \tag{3.12}$$

This constraint is enforced by choosing an appropriate temperature/density-dependent scale factor, $\lambda(\rho,T)$, applied to the SAPT two-body dispersion, as in the prior SYM model. Results for $\lambda(\rho,T)$ are tabulated in the supporting material of Reference 19. Note that although the resulting $\mathrm{SYM}[\rho,T]$ model contains no *explicit* many-body terms, it is polarizable and thus implicitly retains many-body electrostatic contributions.

In contrast to the single empirical scale factor (0.935) we introduced in our previous SYM-0.935 model, the parameter $\lambda(\rho,T)$ in the $\mathrm{SYM}[\rho,T]$ model is rigorously determined from the three-body terms in the SYM-3B model and is density- and (weakly) temperature-dependent. However, note that at liquid-like densities and moderate temperatures, we find that $\lambda(\rho,T) \approx 0.94$, very close to the empirical value utilized previously, *thus motivating our prior SYM model on rigorous statistical mechanical grounds*!

We calculate density profiles at two different temperatures just above the critical temperature, as shown in Figure 3.6; liquid phase data is also examined, yielding accuracy within ~3% (see supporting material of reference 19). Note that since our potential is density/dependent, and small correction is required when evaluating the pressure in an NVT ensemble,

$$P_{corr}^{3b} = \frac{\rho^2}{N} \left\langle E_{disp}^{2b} \right\rangle \frac{\partial \lambda(\rho,T)}{\partial \rho} \tag{3.13}$$

In general, most of the density errors are between 1-4%, slightly worse than our prior SYM model; this is not surprising, as the latter was empirically tuned to reproduce the experimental density. The maximum error, at 320K and 110bar, is due to the near divergence of the compressibility near the critical point (thus, the corresponding error in pressure is *much* smaller).
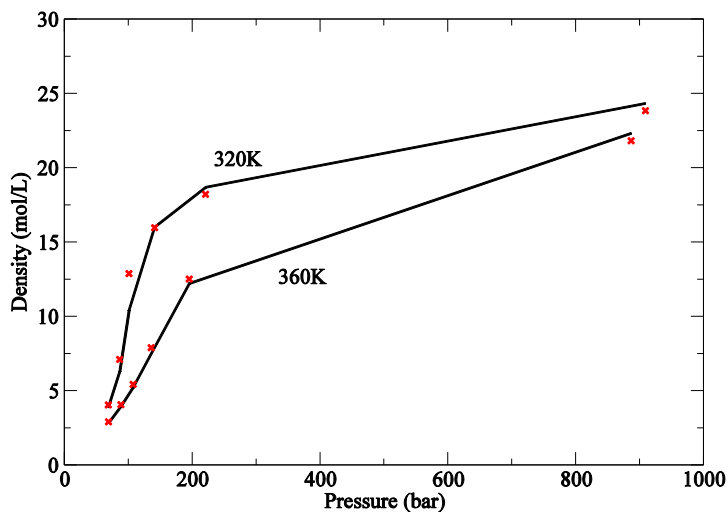
Figure 3.6. Density profiles in 320K and 360K. Black solid lines are experimental data[32] and red crosses are from the $SYM[\rho,T]$ model simulations.

In the high density (liquid-like) regions of the phase diagram, the present SYM-3B / $SYM[\rho,T]$ models yields very similar (and even slightly better) densities than our prior SYM model, which is not unexpected as they employ very similar scale factors in this region. Given that the structure and density are nearly identical to the SYM-0.935 model, other bulk properties should be similarly unchanged (and

thus in excellent agreement with experimental values). Furthermore, in the low density region $\lambda(\rho,T)$ asymptotically approaches 0.97 (as the three-body potential vanishes in the low density limit), yielding the correct two-body potential and thus correct $B_2(T)$. While correct in these two limits, the present SYM-3B / $SYM[\rho,T]$ is slightly *less* accurate in the medium density region, possible due to the approximate treatment of three-body exchange, and particular uncertainty in the choice of the *range* (as given by $\beta^{(3)}$) of the interaction.

We contrast the present approach for converting an explicit many-body potential to an effective two-body potential with that of Oakley *et al.*[17] In the latter case, the authors found that the non-additive (many-body) component of the potential scaled approximately as $\rho^{2.5}$, with a proportionality constant that was fit by comparing with an explicit many-body simulation. They used this density-dependent fit in conjunction with the pair potential to efficiently approximate the many-body energy in their underlying Monte Carlo simulations. Note that the procedure advocated by Oakley *et al.* is equivalent to introducing an *external* density-dependent pressure (which may be either positive or negative) on the system. While this pressure can account for the mean-field effect on the system, e.g. enforcing the correct density due to average many-body effects, it *cannot* reproduce the alterations in the structure of the liquid due to these many body effects. In contrast, we outline a methodology to arrive at an explicitly density- and temperature-dependent pair potential, which accounts for the average three-body effects at the level of effective intermolecular interactions. This approach does allow for such structural alterations via a modified, effective pair potential. In the limit of weak, perturbative three-body interactions, these methodologies will be equivalent, but may yield significantly different answers when applied to systems with significant many-body effects.

3.4 Conclusions

Overall, the explicit SYM-3B CO_2 model we present here is particular exciting as it is physically-motivated in all aspects, with two- and three-body terms parameterized on the basis of the corresponding SAPT energy decomposition and extremely minimal empirical input. The model reproduces not only bulk properties, but also second/third virial coefficients, demonstrating correct two- and three-body interactions. The latter are *critical* for bulk CO_2, accounting for the pressure corrections as large as 100 bar and density changes of up to 10% in condensed phase. Although it is certainly possible to account for such three-body effects via a (density-independent) two-body potential, as in our previous SYM-0.935 model, this necessarily leads to at least some physically incorrect behavior in some regimes, as manifested by, for example, incorrect third virial coefficients, and somewhat violates the tenants of a "physically-motivated" model.

We show that we can accurately approximate this three-body SYM-3B model in terms of a computationally efficient density/temperature-dependent two-body effective potential, yielding the $\text{SYM}[\rho, T]$ model. This model essentially reduces to our prior SYM model in the limit of liquid-like densities, thus providing a rigorous "derivation" of our previous model. Since the SYM model offers excellent agreement with a wide range of bulk structural, thermodynamic, and dynamic properties, we thus also expect (by construction) similarly excellent agreement for the SYM-3B and $\text{SYM}[\rho, T]$ models. We thus anticipate that the present SYM-3B and $\text{SYM}[\rho, T]$ models will be extremely robust and transferable, from clusters to the bulk, across the phase diagram, and with possible applications to heterogeneous environments and/or extreme conditions.

Bibliography

1.   Yu, K.; McDaniel, J. G.; Schmidt, J. R., Physically Motivated, Robust, ab Initio Force Fields for CO(2) and N(2). *J Phys Chem B* **2011,** 115, (33), 10054-10063.

2.   Misquitta, A. J.; Stone, A. J., Accurate induction energies for small organic molecules: 1. Theory. *J Chem Theory Comput* **2008,** 4, (1), 7-18.

3.   Misquitta, A. J.; Stone, A. J., Dispersion energies for small organic molecules: first row atoms. *Mol Phys* **2008,** 106, (12-13), 1631-1643.

4.   Jansen, L.; Lombardi, E., Three-body exchange forces in rare-gas crystals. *Chem Phys Lett* **1967,** 1, (2), 33-35.

5.   Loubeyre, P., Three-body exchange interaction in dense helium. *Phys Rev Lett* **1987,** 58, (18), 1857.

6.   Loubeyre, P., Three-body-exchange interaction in dense rare gases. *Phys Rev B* **1988,** 37, (10), 5432.

7.   Thakkar, A. J.; Hettema, H.; Wormer, P. E. S., Abinitio Dispersion Coefficients for Interactions Involving Rare-Gas Atoms. *J Chem Phys* **1992,** 97, (5), 3252-3257.

8.   van der Hoef, M. A.; Madden, P. A., Three-body dispersion contributions to the thermodynamic properties and effective pair interactions in liquid argon. *J Chem Phys* **1999,** 111, (4), 1520-1526.

9.   Jäger, B.; Hellmann, R.; Bich, E.; Vogel, E., Ab initio virial equation of state for argon using a new nonadditive three-body potential. *J. Chem. Phys.* **2011,** 135, (8), 084308.

10.   McDowell, S. A. C.; Meath, W. J., Isotropic and anisotropic triple-dipole dispersion energy coefficients for three-body interactions involving He, Ne, Ar, Kr, Xe, H-2, N-2, CO, O-2 and NO. *Mol Phys* **1997,** 90, (5), 713-719.

11.   Stogryn, D. E., Pairwise Nonadditive Dispersion Potential for Asymmetric Molecules. *Phys Rev Lett* **1970,** 24, (18), 971.

12.   Patil, S. H.; Tang, K. T., Multipolar polarizabilities and two- and three-body dispersion coefficients for alkali isoelectronic sequences. *J Chem Phys* **1997,** 106, (6), 2298-2305.

13.   Pacheco, J. M.; Prates Ramalho, J. P., First-Principles Determination of the Dispersion Interaction between Fullerenes and Their Intermolecular Potential. *Phys Rev Lett* **1997,** 79, (20), 3873.

14.   Chaudret, R.; Gresh, N.; Parisel, O.; Piquemal, J.-P., Many-body exchange-repulsion in polarizable molecular mechanics. I. orbital-based approximations and applications to hydrated metal cation complexes. *J Comput Chem* **2011,** 32, (14), 2949-2957.

15.   Tainter, C. J.; Pieniazek, P. A.; Lin, Y. S.; Skinner, J. L., Robust three-body water simulation model. *J Chem Phys* **2011,** 134, (18), 184501.

16.   Persson, R. A. X., Gaussian charge polarizable interaction potential for carbon dioxide. *J Chem Phys* **2011,** 134, (3), 034312.

17.   Oakley, M. T.; Wheatley, R. J., Additive and nonadditive models of vapor-liquid equilibrium in CO_2 from first principles. *J. Chem. Phys.* **2009,** 130, (3), 034110.

18.   See Supplementary Material Document No. xxx for full model parameters and additional benchmark data. For information of Supplementary Materials, see http://www.aip.org/pubservs/epaps.html. In.

19.   Yu, K.; Schmidt, J. R., Many-body effects are essential in a physically motivated CO_2 force field. *J Chem Phys* **2012,** 136, (3).

20.   Tkatchenko, A.; DiStasio, R. A.; Head-Gordon, M.; Scheffler, M., Dispersion-corrected Møller-Plesset second-order perturbation theory. *J. Chem. Phys.* **2009,** 131, (9), 094106.

21.   Potoff, J. J.; Siepmann, J. I., Vapor-liquid equilibria of mixtures containing alkanes, carbon dioxide, and nitrogen. *Aiche J* **2001,** 47, (7), 1676-1682.

22.   Podeszwa, R.; Szalewicz, K., Three-body symmetry-adapted perturbation theory based on Kohn-Sham description of the monomers. *J Chem Phys* **2007,** 126, (19), 194101.

23.   Perdew, J. P.; Burke, K.; Ernzerhof, M., Generalized Gradient Approximation Made Simple. *Phys Rev Lett* **1996,** 77, (18), 3865.

24.   Perdew, J. P.; Burke, K.; Ernzerhof, M., Generalized Gradient Approximation Made Simple [Phys. Rev. Lett. 77, 3865 (1996)]. *Phys Rev Lett* **1997,** 78, (7), 1396.

25.   Truhlar, D. G., Basis-set extrapolation. *Chem Phys Lett* **1998,** 294, (1-3), 45-48.

26.   Duschek, W.; Kleinrahm, R.; Wagner, W., Measurement and Correlation of the (Pressure, Density, Temperature) Relation of Carbon-Dioxide .2. Saturated-Liquid and Saturated-Vapor Densities and the Vapor-Pressure Along the Entire Coexistence Curve. *J Chem Thermodyn* **1990,** 22, (9), 841-864.

27.   Holste, J. C.; Hall, K. R.; Eubank, P. T.; Esper, G.; Watson, M. Q.; Warowny, W.; Bailey, D. M.; Young, J. G.; Bellomy, M. T., Experimental (P,Vm,T) for Pure CO_2 between 220-K and 450-K. *J Chem Thermodyn* **1987,** 19, (12), 1233-1250.

28.   Clamp, M. E.; Baker, P. G.; Stirling, C. J.; Brass, A., Hybrid Monte-Carlo - an Efficient Algorithm for Condensed Matter Simulation. *J Comput Chem* **1994,** 15, (8), 838-846.

29.   Frenkel, D.; Smit, B., *Understanding Molecular Simulation, from algorithms to applications*.

30.   http://towhee.sourceforge.net/

31.   Hess, B.; Kutzner, C.; van der Spoel, D.; Lindahl, E., GROMACS 4: Algorithms for highly efficient, load-balanced, and scalable molecular simulation. *J Chem Theory Comput* **2008,** 4, (3), 435-447.

32.   http://webbook.nist.gov/chemistry/ NIST Chemistry WebBook.

Chapter 4. Ab initio, Physically Motivated Force Fields for CO$_2$ Adsorption in Zeolitic Imidazolate Frameworks — ZIFFF

Table of Contents

4.1 Introduction

As it is mentioned in Chapter 1, nanoporous metal-organic frameworks (MOFs) have been shown to exhibit high CO_2 uptake with excellent adsorption selectively over nitrogen and other gases, and have thus received a large amount of research interest as potential CO_2 separation materials. Zeolitic imidazolate frameworks (ZIFs),[1-35] a type of MOF consisting of metal cations bridged by organic imidazolate anions, have received particular attention due to their selective CO_2 adsorption,[1, 2, 7, 8] excellent chemical and thermal stability,[6, 36] and potential for tunability via functionalization of the organic linker groups.[2, 4, 7, 8]

Uptake and selective adsorption of CO_2, N_2, and CH_4 in ZIFs is relevant to many applications, including natural gas recovery and carbon capture and storage (CCS).[1-3, 5, 7, 8, 37-40] A wide variety of ZIFs with different topologies, pore/aperture sizes, and chemical functionality have previously been developed.[1-11, 15, 16, 18, 20, 24, 25, 35] This tunability has led to the description of ZIF synthesis as structural "design" as opposed to materials "discovery".[7] Yet in order to develop and synthesize ZIFs optimized for a particular application, it is essential to have a fundamental understanding of the detailed interactions between different gas molecules and ZIF frameworks.

Molecular dynamics (MD) and Monte Carlo (MC) computer simulations are important tools for studying gas adsorption isotherms and diffusion in porous materials such as ZIFs. The use of *accurate* and *physically appropriate* force fields in these simulations can provide valuable insight into the important interactions between gas and framework that dictate adsorption capacity and/or selectivity. There has been a significant amount of previous computational work modeling the uptake and diffusion of various gases in different ZIFs. Much of this computational work has utilized standard "generic" force fields such as UFF[41] or Drieding[42] to describe the interactions of gas molecules with the ZIF framework, yielding mixed results and raising concerns regarding the applicability of these standard force fields to these systems. Nonetheless, many previous grand canonical Monte Carlo (GCMC) and MD studies have

examined the uptake and separation of various gases including CO_2, N_2, CH_4, and H_2 with ZIFs, characterizing adsorption isotherms of these gases,[5, 38, 43-57] separation and selective adsorption of gas mixtures,[44-46, 49] diffusion,[43-45, 48, 49] and important interaction sites in the ZIFs.[38, 43, 58]

Various force fields have been used in these studies with mixed conclusions. For example, describing both CO_2-CO_2 interactions and CO_2-ZIF interactions using the UFF force field yields reasonable agreement with the experimentally measured CO_2 adsorption,[50] although it is well known that the UFF force field does a poor job of describing bulk CO_2-CO_2 interactions. It is therefore perhaps not surprising that utilizing either the UFF / Drieding parameters for the CO_2-ZIF interactions in conjunction with the (accurate) TraPPE[59] force field for CO_2-CO_2 interactions led to dramatic over prediction of CO_2 adsorption.[48] Other authors resorted to scaling the UFF parameters describing CO_2-ZIF interactions so that interactions were less attractive, then yielding good agreement with experimental isotherms.[46] Recently it was also noted that by blocking small pores that were deemed "inaccessible" to gas molecules, either a UFF or Drieding description of gas-framework interaction could reproduce experimental isotherms to reasonable accuracy.[47]

Other notable applications of standard force fields to ZIFs include the simulations by Perez-Pellitero *et al.*, in which adsorption isotherms for CO_2, CH_4, and N_2 in ZIF-8, ZIF-76 and ZIF-69 were found to agree with experiment only after introducing empirical scaling factors of 0.69 for ε values and 0.95 for UFF σ values,[38] indicating a very significant empirical correction. Battisti *et al.* utilized this same scaling of the UFF gas-framework parameters to systematically study the adsorption and dynamics of CO_2, CH_4, N_2, and H_2 and mixtures thereof in ZIF-2 through ZIF-10.[49] Morris *et al.* examined ZIFs 25, 71, 93, 96, and 97,[5] using the EPM2 force field[60] for CO_2 and the UFF force field to describe the framework and were for the most part able to reproduce the experimental trends in CO_2 adsorption with functionalization of the imidazolate linker groups, with the exception of ZIF-96. In the latter case they found that by using OPLS-ua parameters[61] to describe the nitrile and amine groups they were able to obtain better agreement with the experimental isotherm for this system.

The literature contains few examples of ab initio-based force fields to describe gas adsorption/diffusion processes in MOFs. Schmid and coworkers have developed ab initio force fields to describe framework flexibility in a variety of MOFs,[62-64] this being of potential importance in understanding gas diffusion in these systems. Goddard and coworkers have parameterized functional group-H_2 interactions based on ab initio calculations,[53, 54, 65, 66] enabling first principles calculation of H_2 uptake in MOFs doped with metal cations. They have also investigated H_2 adsorption in ZIFs,[53, 54] using their developed methodology. Almost no other work has focused on developing force fields tailored specifically to ZIFs, and in nearly all cases force field construction has been limited to deriving atomic charges from ab initio calculations and coupling these with Lennard-Jones (LJ) parameters of a generic force field such as UFF or Dreiding.[5, 38, 43, 47, 48, 50] To our knowledge, there have not been any attempts to develop rigorous ab intio force fields for the interaction of ZIFs with species relevant to flue gas separation.

Thus overall, previous simulations of gas uptake and selective adsorption have often been forced to resort to arbitrary scaling factors parameterized to prior experimental data and a patchwork of standard force fields to achieve semi-quantitative agreement with experiment. This is somewhat unsatisfying as this scaling procedure may not capture the correct underlying physics. In other words, there are likely *many* possible scaling procedures (and thus many force fields) that reproduce the same isotherm, leading to an underspecified fitting problem and the possibility of "unphysical" parameters.

These considerations motivated us to develop entirely first-principles based force fields for CO_2-ZIF interactions. In this chapter, following the methodology established in the Chapter 2 and 3, we present a new *ab initio* force field for ZIFs (namely ZIFFF), based on symmetry adapted perturbation theory (SAPT)[67] calculations, fit term by term. As we showed in the CO_2/N_2 case, SAPT naturally decomposes the interaction energy into the fundamental components of electrostatic, exchange, induction and dispersion interactions. This allows for the utilization of separate, physically-appropriate terms to represent each of these interaction types. For the ZIF systems, all metal centers are coordinatively saturated and weak interactions such as electrostatic, induction or dispersion dictate the adsorption

behavior. Since SAPT has shown immense power in describing the nonbonding interactions between molecules in the CO_2/N_2 case, it provides enough accuracy as the underlying electronic structure method to construct a reliable *ab initio* force field for ZIFs.

We validate our approach via calculations on ZIF-8 and ZIF-71, as these ZIFs contain relatively "simple" linker groups. However the methodologies developed here are equally applicable to a vast array of existing and novel ZIFs. In order to ensure robust, physical, and asymptotically valid parameters in our force field, we obtain parameters from monomer calculations (polarizabilities, charge distribution…) whenever possible, and fitting remaining parameters that rely on charge-density overlap to the SAPT interaction energies.

We should note that many previous interaction potentials have been derived based on SAPT interaction energy calculations,[68-74] and we briefly comment on the primary differences between our methodology and techniques used in previous works. Almost all previous works have fit the *total* interaction energy between molecules,[68, 69, 71, 73, 74] while we choose to independently fit each *individual* interaction energy component. This not only allows for greater physical interpretation when such a force field is used in a computer simulation, but also reduces the possibility of error cancelation and helps to ensure physically meaningful parameters, especially in larger molecules. Our procedure is probably most similar to that of Misquitta et al.,[72] with the major difference being that we abandon the use of explicit anisotropic force field terms so that our final force field has a form amenable to standard simulation packages.

This chapter will be mainly focusing on the model system constructions and electronic structure calculations underlying the force field development. The force field fitting and classical simulation results are only briefly summarized for completeness, and readers are referred to reference 75 for further details.

4.2 Model System Construction and Validation

SAPT was used to compute the interaction energies necessary to fit parameters in our force field. This technique is not amenable to periodic systems, and thus our first step was to develop a finite model

system that was large enough to be representative of the bulk crystal, but small enough to enable tractable SAPT calculations.

Our goal in constructing this model system was to reproduce the full three-dimensional electron density on the imidazolate rings and surrounding Zn^{2+} cations as compared to the corresponding bulk. In creating this model system, we considered a ZIF system with the simplest possible linker group, an unfunctionalized imidazolate ring. The periodic ZIF crystal used as a precursor was created by obtaining the XRD crystal structure of ZIF-8 from the Cambridge Structural Database (CSD), replacing the methyl groups with hydrogen. Bader charge analysis[76] was employed to characterize the electron density of the imidazolate rings in both the periodic system and the model fragment computed utilizing the PBE density functional with a plane wave basis (500eV energy cutoff). The electron density for both the model fragment and the periodic system was computed using the VASP[77, 78] package.

From the periodic system, we constructed a $Zn_2Im_7Li_6^{3+}$ fragment in which two Zn ions were each attached to three outer imidazolate rings, and connected through a common imidazolate ring. The outer six imidazolate rings were capped with Li ions (see Figure 4.1). This system was constructed by cutting out the appropriate fragment from the periodic system and capping the dangling nitrogen lone pairs with Li ions to mimic dative ligand bonding. The Li-N bond distances were adjusted until the Bader charges on the fragment rings matched those on the periodic system. Shown in Table 4.1 is a comparison of the Bader charges of the imidazolate rings in the $Zn_2Im_7Li_6^{3+}$ fragment to the charges of the imidazolate rings in the corresponding periodic crystal. Comparing the electron density difference and Bader charges for ring atoms (see electron density difference isosurface in Figure 4.1), it is evident that the $Zn_2Im_7Li_6^{3+}$ fragment does an excellent job of reproducing the electron density of the periodic system in the central region, although differences obviously arise near the terminating Li groups. Finally, a constrained geometry optimization was carried out on the fragment, where all metal-organic bond lengths and angles were kept fixed. The main purpose for this optimization was to generate physical C-H, C-C, and C-N bond distances and compensate for the finite resolution of the XRD structure.
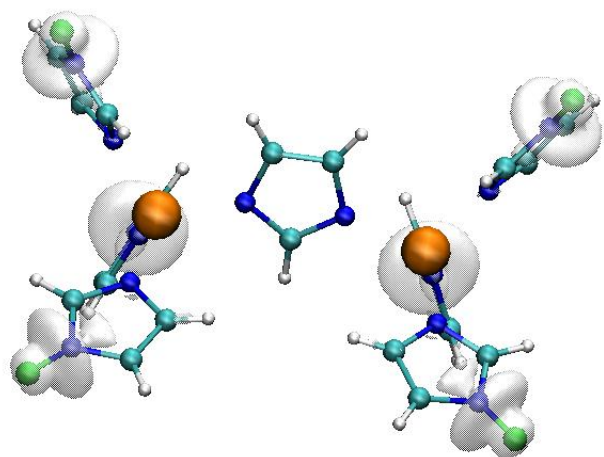
Figure 4.1. Isosurface of electron density difference between the $Zn_2Im_7Li_6^{3+}$ fragment and the corresponding periodic system. The isosurface value shown corresponds to ~3% difference in the electron density of the two systems.

Atom	Periodic	Cluster central ring	Cluster outer rings (average)
C1	1.062	1.075	1.061
N	-1.292	-1.305	-1.274
N	-1.292	-1.300	-1.353
C2	0.588	0.596	0.596
C2	0.676	0.660	0.621
H1	0.024	0.027	0.025
H2	-0.180	-0.155	-0.119
H2	-0.180	-0.168	-0.149
Total	-0.594	-0.570	-0.593

Table 4.1. Comparison of Bader charges on imidazolate rings of periodic system and $Zn_2Im_7Li_6^{3+}$ fragment. The ring atom types are shown in Figure 4.2.
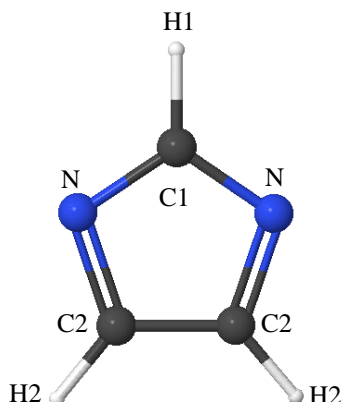
Figure 4.2. Imidazolate atom types.

4.3 SAPT Calculations

We subsequently carried out approximately 200 SAPT calculations for different configurations of CO_2 interacting with the frozen $Zn_2Im_7Li_6^{3+}$ fragment. The configurations used were taken from snapshots of an NVT MD simulation using a box with a CO_2 molecule and the $Zn_2Im_7Li_6^{3+}$ fragment. The GROMACS package[79, 80] was used to generate these conformations. A temperature of 3000K was utilized to generate sampling in repulsive regions, and the intermolecular interactions were described using the OPLS force field[61] for the fragment, and the TraPPE[59] force field for CO_2; the results do not depend sensitively on the choice of force field due to the high temperature, and our goal is simply to sample a wide variety of representative inter-molecular conformations. The details for the calculations were almost identical to those done in Chapter 2. The density fitting DFT-SAPT (DF-DFT-SAPT) method[81-91] was used as implemented in the MolPro 2009 package.[92] The PBE exchange-correlation functional[93, 94] was used with an asymptotic correction, which is essential for accurate interaction energies.[86, 91] Ionization potentials required for the asymptotic correction were computed at the aug-cc-pVTZ (AVTZ)/PBE0 level. We used a dimer-centered basis set consisting of Dunning style aug-cc-pVDZ (AVDZ) basis[95] for organic atoms and def2-SVP basis[96] for metal atoms (AVDZ/def2-SVP). For twelve of these points, dispersion interactions were calculated, and as done previously,[97] mid bond basis

functions were used, as these are essential to converge dispersion energies.[98] The mid bond basis are even tempered functions (3s2p1d1f) for each site, and the exponents center at ζ = 0.3, 0.3, 0.35, 0.35 au respectively, with ratio of 3.0. Three sites were used for the mid bond functions, with the sites placed between the CO_2 molecule and the three closest imidazolate rings, and the locations are determined using the method of Podeszwa et al.[73] Moreover, in order to accelerate the calculation, the energy-consistent pseudopotential of the Stuttgart/Cologne group[99] (ECP10MDF) is used for Zn, and 10 core electrons are taken out for each Zn atom.

The SAPT calculations were extremely time-consuming (4-5 days per point on 8 processors, without computing dispersion interactions), and are infeasible for more than one type of ZIF. However, the results provide *benchmark* interaction energies against which we evaluate smaller model systems. We thus move forward to consider a much simpler model which contains one Imidazolate ring capped with two Li+ on both nitrogen atoms. Approximately 700 single point DF-DFT-SAPT calculations were carried out using the same methodology as before. In contrast to the large model system, these smaller SAPT calculations took only several processor-hours, thus allowing for many of these calculations to be done for various systems. Using the methodology described in the next section, force fields were developed for each of these three ring systems. We find that the force field generated from the small Li-imidazolate (Li_2Im) SAPT calculations, in combination with charges for the Zn ions determined using the methodology described below, was able to accurately reproduce the SAPT interaction energies between CO_2 and the larger $Zn_2Im_7Li_6^{3+}$ fragment (see supporting information of reference 75). We thus utilize Li-capped imidazolate-type rings in all subsequent calculations to efficiently generate force fields for various bulk ZIFs.

4.4 Force Field Development
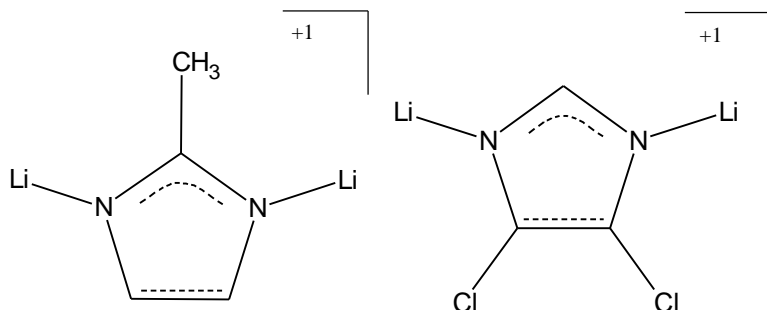
Figure 4.3. Structures of Li_2mIm ring (left) and Li_2dcIm ring (right).

Based on the above results, we developed corresponding small model systems for ZIF-8 and ZIF-71. For ZIF-8, a Li-capped methyl-imidazolate ring (Li_2mIm) was used and for ZIF-71 a Li-capped dichloro-imidazolate ring (Li_2dcIm) was employed (see Figure 4.3).

Using a similar methodology as Chapter 2, we separately fit each physically distinct term in our force field to the corresponding SAPT term in our calculations. The fitting procedure is roughly summarized in this session and more details are available in reference 75.

The SAPT interaction energy decomposition is as follows:

$$E_{\text{int}} = E_{pol}^{(1)} + E_{exch}^{(1)} + E_{ind}^{(2)} + E_{ind-exch}^{(2)} + E_{disp}^{(2)} + E_{disp-exch}^{(2)} + E_{\delta hf} \tag{4.1}$$

To fit the first order exchange repulsion energy, $E_{exch}^{(1)}$, we utilized a pairwise additive Buckingham functional form,

$$E_{exch}^{(1)} \cong \sum_{i,j} A_{ij}^{exch} \exp(-B_{ij} r_{ij}) \tag{4.2}$$

The exponents, B_{ij}, were determined using the procedure used in Chapter 2. Then, the pre-factors A_{ij}^{exch} along with a scaling factor, λ, such that $B_{ij} = \lambda B_{ij}^0$, were fit to the SAPT first-order exchange interaction energies. Combination rules ($A_{ij}^{exch} = (A_{ii}^{exch} A_{jj}^{exch})^{1/2}$) are used to reduce the number of parameters.

The electrostatic term, $E_{pol}^{(1)}$, was fit using a combination of screened atom-centered point charges and Buckingham-type terms to account for charge penetration. The atom-centered point charges were obtained by fitting the potential created by each multipole calculated using distributed multipole analysis (DMA).[100, 101] And the pre-factors in charge penetration terms are fitted to the SAPT calculation results, and the final functional form used to fit the electrostatic SAPT term was:

$$E_{pol}^{(1)} \cong \sum_{i,j} f_1(B_{ij}, r_{ij}) \frac{q_i q_j}{r_{ij}} + \sum_{i,j} A_{ij}^{elec} \exp(-B_{ij} r_{ij}) \tag{4.3}$$

For the screening function, the Tang-Toennies functional form[102] was used:

$$f_n(\lambda, r) = 1 - e^{-\lambda r} \sum_{m=0}^{n} \frac{(\lambda r)^m}{m!} \tag{4.4}$$

where the parameters required for the screening function were taken to be the exponents used in all Buckingham terms, $\lambda = B_{ij}$.

The second order polarization/induction energy, $E_{pol}^{(2)} = E_{ind}^{(2)} + E_{ind-exch}^{(2)}$, was fit using an explicitly polarizable treatment for CO_2. This explicit polarization was accomplished with the use of a shell model, and is described in Chapter 2. All *inter*-molecular charge-charge interactions, whether static or shell, were screened using the Tang-Toennies function as described above. The total functional form used to model the induction energy is:

$$E_{pol}^{(2)} \cong U_{shell} + \sum_{i,j} A_{ij}^{ind} \exp(-B_{ij} r_{ij}) \tag{4.5}$$

Here, A_{ij}^{ind} parameters were fit to reproduce the SAPT second-order polarization/induction energy, $E_{pol}^{(2)}$, accounting for the charge penetration effects.

The second-order dispersion energy, $E_{VdW}^{(2)} = E_{disp}^{(2)} + E_{disp-exch}^{(2)}$, was fit using the following functional:

$$E_{VdW}^{(2)} \cong \sum_{i,j} A_{ij}^{disp} \exp(-B_{ij}r_{ij}) - \sum_{n=6,8,10} \sum_{i,j} f_n(\beta_{ij},r_{ij}) \frac{C_n^{ij}}{r_{ij}^n} \qquad (4.6)$$

Where the C_n^{ij} is computed using CAMCASP program,[103-106] as monomer properties, and $A_{ij}^{disp} = -(A_{ii}^{disp} A_{jj}^{disp})^{1/2}$ was the fit to SAPT calculation results, accounting charge penetration effects.

The delta Hartree-Fock terms, $E_{\delta hf}$, have been described previously[86, 97] and were fit using exponential functions,

$$E_{\delta hf} \cong \sum_{i,j} A_{ij}^{\delta hf} \exp(-B_{ij}r_{ij}) \qquad (4.7)$$

The atomic ring parameters $A_{jj}^{\delta hf}$ were fit to reproduce the calculated $E_{\delta hf}$ interaction energies, using a slightly different combination rule to generate the pairwise parameters $A_{ij}^{\delta hf}$. The combination rule used here was $A_{ij}^{\delta hf} = \sqrt{|A_{ii}^{\delta hf}| * |A_{jj}^{\delta hf}|}$, where the sign of $A_{ij}^{\delta hf}$ was determined to be positive if $A_{ii}^{\delta hf} * A_{jj}^{\delta hf}$ was positive, and negative otherwise.

Force fields for *bulk* ZIF-8 and ZIF-71 were constructed by treating Zn atoms as bare point charges (since they are fully coordinated, buried, and cationic), and using the parameters developed for the Li_2mIm and Li_2dcIm ring systems respectively.

Finally, it is worth emphasizing that despite the technical nature of the fitting procedure outlined above, the resulting force field is of the relatively simple function form,

$$U_{tot} = \sum_{i,j} f_1(B_{ij},r_{ij}) \frac{q_i q_j}{r_{ij}} + \sum_{i,j} \left(A_{ij}^{tot} \exp(-B_{ij}r_{ij}) - \sum_{n=6,8,10} f_n(\beta_{ij},r_{ij}) \frac{C_n^{ij}}{r_{ij}^n} \right) + U_{shell} \qquad (4.8)$$

consisting of electrostatics, Buckingham (exponential) short range repulsion, damped dispersion, and Drude oscillator polarization. This makes it straightforward to implement in existing standard simulation packages, such as GROMACS[79, 80] or Towhee.[107]

4.5 Results and Discussion

GCMC simulations were carried out to compute CO_2 adsorption isotherms in ZIF-8 and ZIF-71 and validate our empirical-parameter-free ZIFFF force fields. The SYM CO_2 model, which has been derived in a similar fashion and benchmarked against various bulk CO_2 properties, was used to describe CO_2-CO_2 interactions.[97] Further simulation details can be found in reference 75, and the simulated CO2 loading isotherms are plotted along the side with experimental results in Figure 4.4 and Figure 4.5.
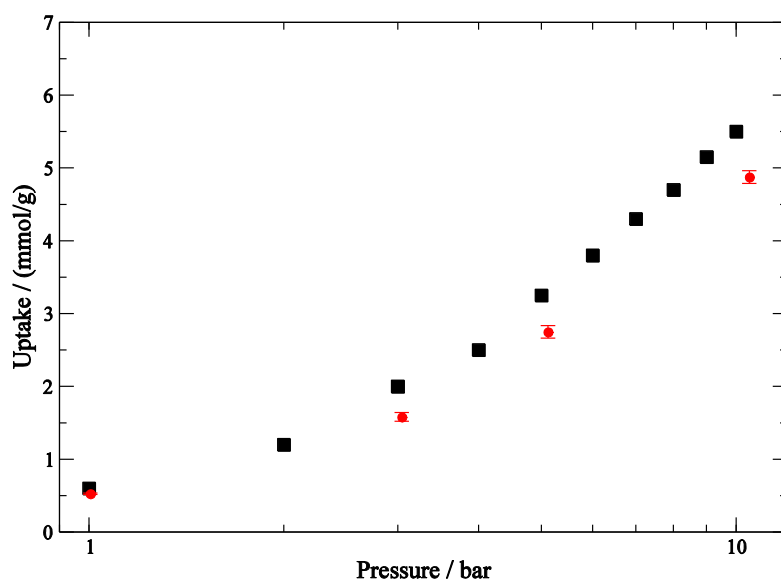
Figure 4.4 CO_2 adsorption isotherm in ZIF-8 at 303K. Experimental results from reference 38 are shown as black squares. Simulation results from this work are shown as the red circles.
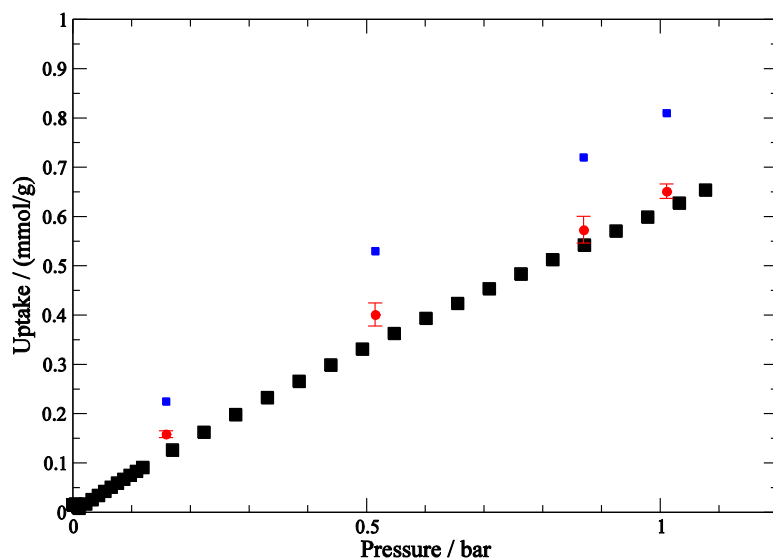
Figure 4.5 CO_2 adsorption isotherm in ZIF-71 at 298K. Experimental results from reference 5 are shown as the black squares . Simulation results utilizing the UFF force field also from reference 5 are shown as the blue squares. Simulation results from this work are shown as the red circles.

As it is shown, for both systems with functionalized or unfunctionalized imidazolate rings, the SAPT based ZIFFF predicts the loading capacity accurately compared to the experimental value. In the ZIF-71 case, ZIFFF, which is essentially empirical parameter-free, outperforms the UFF, the empirical potential used widely to date. These results prove the validity of both our force field as well as our methodology for force field development, which can be easily generalized to suit a wide range of applications. More analysis results can be found in reference 75.

4.6 Conclusion:

We have developed parameter-free ab initio force fields tailored to describe the interactions between CO_2 and ZIFs, specifically ZIF-8 and ZIF-71. These physically-motivated force fields are novel in that they contain separate terms to explicitly account for the distinct types of physical interactions, namely exchange, electrostatic, induction, and dispersion. We have made the effort to ensure physically meaningful parameters in our force fields, obtaining as many parameters as possible based on isolated

molecular properties, and relying on SAPT interaction energy calculations to obtain parameters that are related to the overlap of charge densities. Using these novel force fields, we find excellent agreement with experimental CO_2 adsorption isotherms for both of these systems.

Overall, the approach outlined in the present work offers several compelling advantages over the use of standard, empirical force fields. Most significantly, our methodology generates force fields entirely from ab initio SAPT calculations with absolutely no empirical parameters. Thus, although the present work focuses on two minimally-functionalized ZIFs, the methodology outlined here is entirely general and easily extendable to novel and/or highly functionalized ZIFs (or even adsorption of other gases, e.g. N_2). In contrast, previous approaches have often relied on a patchwork of force fields or empirical scale factors based on post-facto comparison with experiment. Furthermore, our newly generated force fields are extremely accurate, yielding semi-quantitative to quantitative accuracy, surpassing the level required for the purposes of computational screening.

Bibliography

1.   Banerjee, R.; Furukawa, H.; Britt, D.; Knobler, C.; O'Keeffe, M.; Yaghi, O. M., Control of Pore Size and Functionality in Isoreticular Zeolitic Imidazolate Frameworks and their Carbon Dioxide Selective Capture Properties. *J Am Chem Soc* **2009,** 131, (11), 3875-3877.

2.   Banerjee, R.; Phan, A.; Wang, B.; Knobler, C.; Furukawa, H.; O'Keeffe, M.; Yaghi, O. M., High-throughput synthesis of zeolitic imidazolate frameworks and application to CO_2 capture. *Science* **2008,** 319, (5865), 939-943.

3.   Hayashi, H.; Cote, A. P.; Furukawa, H.; O'Keeffe, M.; Yaghi, O. M., Zeolite a imidazolate frameworks. *Nat. Mater.* **2007,** 6, (7), 501-506.

4.   Morris, W.; Doonan, C. J.; Furukawa, H.; Banerjee, R.; Yaghi, O. M., Crystals as molecules: Postsynthesis covalent functionalization of zeolitic imidazolate frameworks. *J Am Chem Soc* **2008,** 130, (38), 12626-+.

5.   Morris, W.; Leung, B.; Furukawa, H.; Yaghi, O. K.; He, N.; Hayashi, H.; Houndonougbo, Y.; Asta, M.; Laird, B. B.; Yaghi, O. M., A Combined Experimental-Computational Investigation of Carbon Dioxide Capture in a Series of Isoreticular Zeolitic Imidazolate Frameworks. *J Am Chem Soc* **2010,** 132, (32), 11006-11008.

6.   Park, K. S.; Ni, Z.; Cote, A. P.; Choi, J. Y.; Huang, R. D.; Uribe-Romo, F. J.; Chae, H. K.; O'Keeffe, M.; Yaghi, O. M., Exceptional chemical and thermal stability of zeolitic imidazolate frameworks. *Proc. Natl. Acad. Sci. U. S. A.* **2006,** 103, (27), 10186-10191.

7.   Phan, A.; Doonan, C. J.; Uribe-Romo, F. J.; Knobler, C. B.; O'Keeffe, M.; Yaghi, O. M., Synthesis, Structure, and Carbon Dioxide Capture Properties of Zeolitic Imidazolate Frameworks. *Accounts Chem. Res.* **2010,** 43, (1), 58-67.

8.   Wang, B.; Cote, A. P.; Furukawa, H.; O'Keeffe, M.; Yaghi, O. M., Colossal cages in zeolitic imidazolate frameworks as selective carbon dioxide reservoirs. *Nature* **2008,** 453, (7192), 207-U6.

9.   Huang, X. C.; Lin, Y. Y.; Zhang, J. P.; Chen, X. M., Ligand-directed strategy for zeolite-type metal-organic frameworks: Zinc(II) imidazolates with unusual zeolitic topologies. *Angew Chem Int Edit* **2006,** 45, (10), 1557-1559.

10. Tian, Y. Q.; Zhao, Y. M.; Chen, Z. X.; Zhang, G. N.; Weng, L. H.; Zhao, D. Y., Design and generation of extended zeolitic metal-organic frameworks (ZMOFs): Synthesis and crystal structures of zinc(II) imidazolate polymers with zeolitic topologies. *Chem-Eur J* **2007,** 13, (15), 4146-4154.

11. Wu, T.; Bu, X. H.; Zhang, J.; Feng, P. Y., New Zeolitic Imidazolate Frameworks: From Unprecedented Assembly of Cubic Clusters to Ordered Cooperative Organization of Complementary Ligands. *Chem. Mat.* **2008,** 20, (24), 7377-7382.

12. Liu, Y. L.; Kravtsov, V. C.; Larsen, R.; Eddaoudi, M., Molecular building blocks approach to the assembly of zeolite-like metal-organic frameworks (ZMOFs) with extra-large cavities. *Chem Commun* **2006**, (14), 1488-1490.

13. Zhang, J. P.; Chen, X. M., Crystal engineering of binary metal imidazolate and triazolate frameworks. *Chem Commun* **2006**, (16), 1689-1699.

14. Rettig, S. J.; Storr, A.; Summers, D. A.; Thompson, R. C.; Trotter, J., Iron(II) 2-methylimidazolate and copper(II) 1,2,4-triazolate complexes: systems exhibiting long-range ferromagnetic ordering at low temperatures. *Can. J. Chem.-Rev. Can. Chim.* **1999,** 77, (4), 425-433.

15. Tian, Y. Q.; Cai, C. X.; Ren, X. M.; Duan, C. Y.; Xu, Y.; Gao, S.; You, X. Z., The silica-like extended polymorphism of cobalt(II) imidazolate three-dimensional frameworks: X-ray single-crystal structures and magnetic properties. *Chem-Eur J* **2003,** 9, (22), 5673-5685.

16. Tian, Y. Q.; Cai, C. X.; Ji, Y.; You, X. Z.; Peng, S. M.; Lee, G. H., Co-5(im)(10) center dot 2MB (x): A metal-organic open-framework with zeolite-like topology. *Angew Chem Int Edit* **2002,** 41, (8), 1384-1386.

17. Masciocchi, N.; Bruni, S.; Cariati, E.; Cariati, F.; Galli, S.; Sironi, A., Extended polymorphism in copper(II) imidazolate polymers: A spectroscopic and XRPD structural study. *Inorg Chem* **2001,** 40, (23), 5897-5905.

18. Huang, X. C.; Zhang, J. P.; Chen, X. M., Zn(bim)(2) center dot (H2O)(1.67): A metalorganic open-framework with sodalite topology. *Chin. Sci. Bull.* **2003,** 48, (15), 1531-1534.

19. Zhang, H.-X.; Wang, F.; Yang, H.; Tan, Y.-X.; Zhang, J.; Bu, X., Interrupted Zeolite LTA and ATN-Type Boron Imidazolate Frameworks. *J Am Chem Soc* **2011,** 133, (31), 11884-7.

20. Zhang, J.; Wu, T.; Zhou, C.; Chen, S.; Feng, P.; Bu, X., Zeolitic boron imidazolate frameworks. *Angewandte Chemie (International ed. in English)* **2009,** 48, (14), 2542-5.

21. Lehnert, R.; Seel, F., PREPARATION AND CRYSTAL-STRUCTURE OF THE MANGANESE(II) AND ZINC(II) DERIVATIVE OF IMIDAZOLE. *Z Anorg Allg Chem* **1980,** 464, (5), 187-194.

22. Sturm, M.; Brandl, F.; Engel, D.; Hoppe, W., CRYSTAL-STRUCTURE OF DIIMIDAZOLYLCOBALT. *Acta Crystallogr. Sect. B-Struct. Commun.* **1975,** 31, (OCT15), 2369-2378.

23. Masciocchi, N.; Ardizzoia, G. A.; Brenna, S.; Castelli, F.; Galli, S.; Maspero, A.; Sironi, A., Synthesis and ab-initio XRPD structure of group 12 imidazolato polymers. *Chem Commun* **2003**, (16), 2018-2019.

24. Tian, Y. Q.; Chen, Z. X.; Weng, L. H.; Guo, H. B.; Gao, S.; Zhao, D. Y., Two polymorphs of cobalt(II) imidazolate polymers synthesized solvothermally by using one organic template N,N-dimethylacetamide. *Inorg Chem* **2004,** 43, (15), 4631-4635.

25. Huang, X. C.; Zhang, J. P.; Lin, Y. Y.; Yu, X. L.; Chen, X. M., Two mixed-valence copper(I,II) imidazolate coordination polymers: metal-valence tuning approach for new topological structures. *Chem Commun* **2004**, (9), 1100-1101.

26. Rettig, S. J.; Storr, A.; Summers, D. A.; Thompson, R. C.; Trotter, J., Transition metal azolates from metallocenes .2. Synthesis, X-ray structure, and magnetic properties of a three-dimensional polymetallic Iron(II) imidazolate complex, a low-temperature weak ferromagnet. *J Am Chem Soc* **1997,** 119, (37), 8675-8680.

27. Rettig, S. J.; Sanchez, V.; Storr, A.; Thompson, R. C.; Trotter, J., Polybis(4-azabenzimidazolato)-iron(II) and -cobalt(II). 3-D single diamond-like framework materials which exhibit spin canting and ferromagnetic ordering at low temperatures. *J. Chem. Soc.-Dalton Trans.* **2000**, (21), 3931-3937.

28. Liu, Y. L.; Kravtsov, V. C.; Eddaoudi, M., Template-Directed Assembly of Zeolite-like Metal-Organic Frameworks (ZMOFs): A usf-ZMOF with an Unprecedented Zeolite Topology. *Angew Chem Int Edit* **2008,** 47, (44), 8446-8449.

29. Muller-Buschbaum, K., 3D- Pr(Im)(3)(ImH) @ImH: A three-dimensional network with complete nitrogen coordination obtained from an imidazole melt. *Z.Naturforsch.(B)* **2006,** 61, (7), 792-798.

30. Fu, Y. M.; Zhao, Y. H.; Lan, Y. Q.; Wang, Y.; Qiu, Y. Q.; Shao, K. Z.; Su, Z. M., A chiral 3D polymer with right- and left-helices based on 2,2 '-biimidazole: Synthesis, crystal structure and fluorescent property. *Inorg Chem Commun* **2007,** 10, (6), 720-723.

31. Lorente, M. A. M.; Dahan, F.; Sanakis, Y.; Petrouleas, V.; Bousseksou, A.; Tuchagues, J. P., NEW FERROUS COMPLEXES BASED ON THE 2,2'-BIIMIDAZOLE LIGAND - STRUCTURAL, MOSSBAUER, AND MAGNETIC-PROPERTIES OF FE-II(BIIMH(2))(3)(CH3OH)(2) OAC(2), FE-II(BIMH(2))3, CO3 FE-II(BIMH)(2) (N), AND (FE-II(BIM))(N). *Inorg Chem* **1995,** 34, (21), 5346-5357.

32. Han, J. Y.; Fang, J.; Chang, H. Y.; Dong, Y.; Liang, S., Poly mu(2)-4,4 '-bipyridine-di-mu(2)-imidazolidocadmium(II). *Acta Crystallogr. Sect. E.-Struct Rep. Online* **2005,** 61, M2667-M2669.

33.   Lehnert, R.; Seel, F., CRYSTAL-STRUCTURE OF IRON(II) DERIVATIVE OF IMIDAZOLE. *Z Anorg Allg Chem* **1978,** 444, (SEP), 91-96.

34.   Spek, A. L.; Duisenberg, A. J. M.; Feiters, M. C., THE STRUCTURE OF THE 3-DIMENSIONAL POLYMER POLY MU-HEXAKIS(2-METHYLIMIDAZOLATO-N,N')-TRIIRON(II) , FE3(C4H5N2)6 N. *Acta Crystallogr. Sect. C-Cryst. Struct. Commun.* **1983,** 39, (SEP), 1212-1214.

35.   Wu, T.; Bu, X. H.; Liu, R.; Lin, Z. E.; Zhang, J.; Feng, P. Y., A new zeolitic topology with sixteen-membered ring and multidimensional large pore channels. *Chem-Eur J* **2008,** 14, (26), 7771-7773.

36.   Kusgens, P.; Rose, M.; Senkovska, I.; Frode, H.; Henschel, A.; Siegle, S.; Kaskel, S., Characterization of metal-organic frameworks by water adsorption. *Microporous Mesoporous Mat.* **2009,** 120, (3), 325-330.

37.   Nune, S. K.; Thallapally, P. K.; Dohnalkova, A.; Wang, C. M.; Liu, J.; Exarhos, G. J., Synthesis and properties of nano zeolitic imidazolate frameworks. *Chem Commun* **2010,** 46, (27), 4878-4880.

38.   Perez-Pellitero, J.; Amrouche, H.; Siperstein, F. R.; Pirngruber, G.; Nieto-Draghi, C.; Chaplais, G.; Simon-Masseron, A.; Bazer-Bachi, D.; Peralta, D.; Bats, N., Adsorption of CO(2), CH(4), and N(2) on Zeolitic Imidazolate Frameworks: Experiments and Simulations. *Chem-Eur J* **2010,** 16, (5), 1560-1571.

39.   Venna, S. R.; Carreon, M. A., Highly Permeable Zeolite Imidazolate Framework-8 Membranes for CO(2)/CH(4) Separation. *J Am Chem Soc* **2010,** 132, (1), 76-+.

40.   Wu, H.; Zhou, W.; Yildirim, T., Methane Sorption in Nanoporous Metal-Organic Frameworks and First-Order Phase Transition of Confined Methane. *J Phys Chem C* **2009,** 113, (7), 3029-3035.

41.   Rappe, A. K.; Casewit, C. J.; Colwell, K. S.; Goddard, W. A.; Skiff, W. M., Uff, a Full Periodic-Table Force-Field for Molecular Mechanics and Molecular-Dynamics Simulations. *J Am Chem Soc* **1992,** 114, (25), 10024-10035.

42.   Mayo, S. L.; Olafson, B. D.; Goddard, W. A., Dreiding - a Generic Force-Field for Molecular Simulations. *J Phys Chem-Us* **1990,** 94, (26), 8897-8909.

43.   Sirjoosingh, A.; Alavi, S.; Woo, T. K., Grand-Canonical Monte Carlo and Molecular-Dynamics Simulations of Carbon-Dioxide and Carbon-Monoxide Adsorption in Zeolitic Imidazolate Framework Materials. *J Phys Chem C* **2010,** 114, (5), 2171-2178.

44.   Keskin, S., Atomistic Simulations for Adsorption, Diffusion, and Separation of Gas Mixtures in Zeolite Imidazolate Frameworks. *J Phys Chem C* **2011,** 115, (3), 800-807.

45.   Krishna, R.; van Baten, J. M., In silico screening of zeolite membranes for CO(2) capture. *J Membrane Sci* **2010,** 360, (1-2), 323-333.

46.   Liu, B.; Smit, B., Molecular Simulation Studies of Separation of CO(2)/N(2), CO(2)/CH(4), and CH(4)/N(2) by ZIFs. *J Phys Chem C* **2010,** 114, (18), 8515-8522.

47.   Babarao, R.; Dai, S.; Jiang, D. E., Effect of Pore Topology and Accessibility on Gas Adsorption Capacity in Zeolitic-Imidazolate Frameworks: Bringing Molecular Simulation Close to Experiment. *J Phys Chem C* **2011,** 115, (16), 8126-8135.

48.   Rankin, R. B.; Liu, J. C.; Kulkarni, A. D.; Johnson, J. K., Adsorption and Diffusion of Light Gases in ZIF-68 and ZIF-70: A Simulation Study. *J Phys Chem C* **2009,** 113, (39), 16906-16914.

49.   Battisti, A.; Taioli, S.; Garberoglio, G., Zeolitic imidazolate frameworks for separation of binary mixtures of CO(2), CH(4), N(2) and H(2): A computer simulation investigation. *Microporous Mesoporous Mat.* **2011,** 143, (1), 46-53.

50.   Liu, D. H.; Zheng, C. C.; Yang, Q. Y.; Zhong, C. L., Understanding the Adsorption and Diffusion of Carbon Dioxide in Zeolitic Imidazolate Frameworks: A Molecular Simulation Study. *J Phys Chem C* **2009,** 113, (12), 5004-5009.

51.   Assfour, B.; Leoni, S.; Seifert, G., Hydrogen Adsorption Sites in Zeolite Imidazolate Frameworks ZIF-8 and ZIF-11. *J Phys Chem C* **2010,** 114, (31), 13381-13384.

52.   Guo, H. C.; Shi, F.; Ma, Z. F.; Liu, X. Q., Molecular Simulation for Adsorption and Separation of CH(4)/H(2) in Zeolitic Imidazolate Frameworks. *J Phys Chem C* **2010,** 114, (28), 12158-12165.

53.   Han, S. S.; Choi, S. H.; Goddard, W. A., Zeolitic Imidazolate Frameworks as H(2) Adsorbents: Ab Initio Based Grand Canonical Monte Carlo Simulation. *J Phys Chem C* **2010,** 114, (27), 12039-12047.

54.   Han, S. S.; Choi, S. H.; Goddard, W. A., Improved H(2) Storage in Zeolitic Imidazolate Frameworks Using Lit, Na(+), and K(+) Dopants, with an Emphasis on Delivery H(2) Uptake. *J Phys Chem C* **2011,** 115, (8), 3507-3512.

55.   Liu, Y.; Liu, H. L.; Hu, Y.; Jiang, J. W., Development of a Density Functional Theory in Three-Dimensional Nanoconfined Space: H(2) Storage in Metal-Organic Frameworks. *J Phys Chem B* **2009,** 113, (36), 12326-12331.

56.   Zhou, M.; Wang, Q.; Zhang, L.; Liu, Y. C.; Kang, Y., Adsorption Sites of Hydrogen in Zeolitic Imidazolate Frameworks. *J Phys Chem B* **2009,** 113, (32), 11049-11053.

57.   Pantatosaki, E.; Pazzona, F. G.; Megariotis, G.; Papadopoulos, G. K., Atomistic Simulation Studies on the Dynamics and Thermodynamics of Nonpolar Molecules within the Zeolite Imidazolate Framework-8. *J Phys Chem B* **2010,** 114, (7), 2493-2503.

58.   Hou, X. J.; Li, H. Q., Unraveling the High Uptake and Selectivity of CO_2 in the Zeolitic Imidazolate Frameworks ZIF-68 and ZIF-69. *J Phys Chem C* **2010,** 114, (32), 13501-13508.

59.   Potoff, J. J.; Siepmann, J. I., Vapor-liquid equilibria of mixtures containing alkanes, carbon dioxide, and nitrogen. *Aiche J* **2001,** 47, (7), 1676-1682.

60.   Harris, J. G.; Yung, K. H., Carbon Dioxides Liquid-Vapor Coexistence Curve and Critical Properties as Predicted by a Simple Molecular-Model. *J Phys Chem-Us* **1995,** 99, (31), 12021-12024.

61.   Jorgensen, W. L.; Tiradorives, J., THE OPLS POTENTIAL FUNCTIONS FOR PROTEINS - ENERGY MINIMIZATIONS FOR CRYSTALS OF CYCLIC-PEPTIDES AND CRAMBIN. *J Am Chem Soc* **1988,** 110, (6), 1657-1666.

62.   Tafipolsky, M.; Schmid, R., Systematic First Principles Parameterization of Force Fields for Metal-Organic Frameworks using a Genetic Algorithm Approach. *J Phys Chem B* **2009,** 113, (5), 1341-1352.

63.   Tafipolsky, M.; Amirjalayer, S.; Schmid, R., First-Principles-Derived Force Field for Copper Paddle-Wheel-Based Metal-Organic Frameworks. *J Phys Chem C* **2010,** 114, (34), 14402-14409.

64.   Tafipolsky, M.; Amirjalayer, S.; Schmid, R., Ab initio parametrized MM3 force field for the metal-organic framework MOF-5. *J Comput Chem* **2007,** 28, (7), 1169-1176.

65.   Han, S. S.; Goddard, W. A., Lithium-doped metal-organic frameworks for reversible H-2 storage at ambient temperature. *J Am Chem Soc* **2007,** 129, (27), 8422-+.

66.   Han, S. S.; Goddard, W. A., High H-2 storage of hexagonal metal-organic frameworks from first-principles-based grand canonical Monte Carlo simulations. *J Phys Chem C* **2008,** 112, (35), 13431-13436.

67.   Jeziorski, B.; Moszynski, R.; Szalewicz, K., PERTURBATION-THEORY APPROACH TO INTERMOLECULAR POTENTIAL-ENERGY SURFACES OF VAN-DER-WAALS COMPLEXES. *Chem Rev* **1994,** 94, (7), 1887-1930.

68.   Bukowski, R.; Sadlej, J.; Jeziorski, B.; Jankowski, P.; Szalewicz, K., Intermolecular potential of carbon dioxide dimer from symmetry-adapted perturbation theory. *Journal of Chemical Physics* **1999,** 110, (8), 3785-3803.

69.   Bukowski, R.; Szalewicz, K.; Chabalowski, C. F., Ab initio interaction potentials for simulations of dimethylnitramine solutions in supercritical carbon dioxide with cosolvents. *J Phys Chem A* **1999,** 103, (36), 7322-7340.

70.   Li, X.; Volkov, A. V.; Szalewicz, K.; Coppens, P., Interaction energies between glycopeptide antibiotics and substrates in complexes determined by X-ray crystallography: application of a theoretical

databank of aspherical atoms and a symmetry-adapted perturbation theory-based set of interatomic potentials. *Acta Crystallogr. Sect. D-Biol. Crystallogr.* **2006,** 62, 639-647.

71.   Mas, E. M.; Szalewicz, K.; Bukowski, R.; Jeziorski, B., Pair potential for water from symmetry-adapted perturbation theory. *Journal of Chemical Physics* **1997,** 107, (11), 4207-4218.

72.   Misquitta, A. J.; Welch, G. W. A.; Stone, A. J.; Price, S. L., A first principles prediction of the crystal structure of C(6)Br(2)ClFH(2). *Chem Phys Lett* **2008,** 456, (1-3), 105-109.

73.   Podeszwa, R.; Bukowski, R.; Szalewicz, K., Potential energy surface for the benzene dimer and perturbational analysis of pi-pi interactions. *J Phys Chem A* **2006,** 110, (34), 10345-10354.

74.   Podeszwa, R.; Bukowski, R.; Rice, B. M.; Szalewicz, K., Potential energy surface for cyclotrimethylene trinitramine dimer from symmetry-adapted perturbation theory. *Phys Chem Chem Phys* **2007,** 9, (41), 5561-5569.

75.   McDaniel, J. G.; Yu, K.; Schmidt, J. R., Ab Initio, Physically Motivated Force Fields for CO_2 Adsorption in Zeolitic Imidazolate Frameworks. *J Phys Chem C* **2012,** 116, (2), 1892-1903.

76.   Henkelman, G.; Arnaldsson, A.; Jonsson, H., A fast and robust algorithm for Bader decomposition of charge density. *Comput. Mater. Sci.* **2006,** 36, (3), 354-360.

77.   Kresse, G.; Furthmuller, J., Efficient iterative schemes for ab initio total-energy calculations using a plane-wave basis set. *Physical Review B* **1996,** 54, (16), 11169-11186.

78.   Kresse, G.; Joubert, D., From ultrasoft pseudopotentials to the projector augmented-wave method. *Physical Review B* **1999,** 59, (3), 1758-1775.

79.   Hess, B.; Kutzner, C.; van der Spoel, D.; Lindahl, E., GROMACS 4: Algorithms for highly efficient, load-balanced, and scalable molecular simulation. *J Chem Theory Comput* **2008,** 4, (3), 435-447.

80.   Van der Spoel, D.; Lindahl, E.; Hess, B.; Groenhof, G.; Mark, A. E.; Berendsen, H. J. C., GROMACS: Fast, flexible, and free. *J Comput Chem* **2005,** 26, (16), 1701-1718.

81.   Hesselmann, A.; Jansen, G., Intermolecular induction and exchange-induction energies from coupled-perturbed Kohn-Sham density functional theory. *Chem Phys Lett* **2002,** 362, (3-4), 319-325.

82.   Hesselmann, A.; Jansen, G., First-order intermolecular interaction energies from Kohn-Sham orbitals. *Chem Phys Lett* **2002,** 357, (5-6), 464-470.

83.   Hesselmann, A.; Jansen, G., Intermolecular dispersion energies from time-dependent density functional theory. *Chem Phys Lett* **2003,** 367, (5-6), 778-784.

84.   Hesselmann, A.; Jansen, G., The helium dimer potential from a combined density functional theory and symmetry-adapted perturbation theory approach using an exact exchange-correlation potential. *Phys Chem Chem Phys* **2003,** 5, (22), 5010-5014.

85.   Hesselmann, A.; Jansen, G.; Schutz, M., Density-functional theory-symmetry-adapted intermolecular perturbation theory with density fitting: A new efficient method to study intermolecular interaction energies. *Journal of Chemical Physics* **2005,** 122, (1).

86.   Williams, H. L.; Chabalowski, C. F., Using Kohn-Sham orbitals in symmetry-adapted perturbation theory to investigate intermolecular interactions. *J Phys Chem A* **2001,** 105, (3), 646-659.

87.   Bukowski, R.; Podeszwa, R.; Szalewicz, K., Efficient calculation of coupled Kohn-Sham dynamic susceptibility functions and dispersion energies with density fitting. *Chem Phys Lett* **2005,** 414, (1-3), 111-116.

88.   Misquitta, A. J.; Jeziorski, B.; Szalewicz, K., Dispersion energy from density-functional theory description of monomers. *Physical Review Letters* **2003,** 91, (3).

89.   Misquitta, A. J.; Podeszwa, R.; Jeziorski, B.; Szalewicz, K., Intermolecular potentials based on symmetry-adapted perturbation theory with dispersion energies from time-dependent density-functional calculations. *Journal of Chemical Physics* **2005,** 123, (21).

90.   Misquitta, A. J.; Szalewicz, K., Intermolecular forces from asymptotically corrected density functional description of monomers. *Chem Phys Lett* **2002,** 357, (3-4), 301-306.

91.   Misquitta, A. J.; Szalewicz, K., Symmetry-adapted perturbation-theory calculations of intermolecular forces employing density-functional description of monomers. *Journal of Chemical Physics* **2005,** 122, (21).

92.   Werner, H.-J.; Knowles, P. J.; Lindh, R.; Manby, F. R.; Schutz, M.; Celani, P.; Korona, T.; Mitrushenkov, A.; Rauhut, G.; Adler, T. B.; Amos, R. D.; Bernhardsson, A.; Berning, A.; Cooper, D. L.; Deegan, M. J. O.; Dobbyn, A. J.; Eckert, F.; Goll, E.; Hampel, C.; Hetzer, G.; Hrenar, T.; Knizia, G.; K¨oppl, C.; Liu, Y.; Lloyd, A. W.; Mata, R. A.; May, A. J.; McNicholas, S. J.; Meyer, W.; Mura, M. E.; Nicklass, A.; Palmieri, P.; Pfluger, K.; Pitzer, R.; Reiher, M.; Schumann, U.; Stoll, H.; Stone, A. J.; Tarroni, R.; Thorsteinsson, T.; M.Wang; Wolf, A. *MOLPRO, a package of ab initio programs, version 2009.1; see http://www.molpro.net*.

93.   Perdew, J. P.; Burke, K.; Ernzerhof, M., Generalized gradient approximation made simple. *Physical Review Letters* **1996,** 77, (18), 3865-3868.

94.   Perdew, J. P.; Burke, K.; Ernzerhof, M., Generalized gradient approximation made simple (vol 77, pg 3865, 1996). *Physical Review Letters* **1997,** 78, (7), 1396-1396.

95.   Dunning, T. H., Gaussian-Basis Sets for Use in Correlated Molecular Calculations .1. The Atoms Boron through Neon and Hydrogen. *Journal of Chemical Physics* **1989,** 90, (2), 1007-1023.

96.   Weigend, F.; Ahlrichs, R., Balanced basis sets of split valence, triple zeta valence and quadruple zeta valence quality for H to Rn: Design and assessment of accuracy. *Phys Chem Chem Phys* **2005,** 7, (18), 3297-3305.

97.   Yu, K.; McDaniel, J. G.; Schmidt, J. R., Physically Motivated, Robust, ab Initio Force Fields for CO(2) and N(2). *Journal of Physical Chemistry. B* **2011,** 115, (33), 10054-63.

98.   Williams, H. L.; Mas, E. M.; Szalewicz, K.; Jeziorski, B., On the Effectiveness of Monomer-Centered, Dimer-Centered, and Bond-Centered Basis Functions in Calculations of Intermolecular Interaction Energies. *Journal of Chemical Physics* **1995,** 103, (17), 7374-7391.

99.   H.-J.Werner; Knowles, P. J.; Lindh, R.; Manby, F. R.; Schutz, M.; Celani, P.; Korona, T.; Mitrushenkov, A.; Rauhut, G.; Adler, T. B.; Amos, R. D.; Bernhardsson, A.; Berning, A.; Cooper, D. L.; Deegan, M. J. O.; Dobbyn, A. J.; Eckert, F.; Goll, E.; Hampel, C.; Hetzer, G.; Hrenar, T.; Knizia, G.; K¨oppl, C.; Liu, Y.; Lloyd, A. W.; Mata, R. A.; May, A. J.; McNicholas, S. J.; Meyer, W.; Mura, M. E.; Nicklass, A.; Palmieri, P.; Pfluger, K.; Pitzer, R.; Reiher, M.; Schumann, U.; Stoll, H.; Stone, A. J.; Tarroni, R.; Thorsteinsson, T.; M.Wang; Wolf, A. *MOLPRO, version 2009.1, a package of ab initio programs, see http://www.molpro.net*.

100.   Stone, A. J., DISTRIBUTED MULTIPOLE ANALYSIS, OR HOW TO DESCRIBE A MOLECULAR CHARGE-DISTRIBUTION. *Chem Phys Lett* **1981,** 83, (2), 233-239.

101.   Stone, A. J.; Alderton, M., DISTRIBUTED MULTIPOLE ANALYSIS - METHODS AND APPLICATIONS. *Mol Phys* **1985,** 56, (5), 1047-1064.

102.   Tang, K. T.; Toennies, J. P., AN IMPROVED SIMPLE-MODEL FOR THE VANDERWAALS POTENTIAL BASED ON UNIVERSAL DAMPING FUNCTIONS FOR THE DISPERSION COEFFICIENTS. *Journal of Chemical Physics* **1984,** 80, (8), 3726-3741.

103.   Misquitta, A. J.; Stone, A. J., Accurate induction energies for small organic molecules: 1. Theory. *J Chem Theory Comput* **2008,** 4, (1), 7-18.

104.   Misquitta, A. J.; Stone, A. J., Dispersion energies for small organic molecules: first row atoms. *Mol Phys* **2008,** 106, (12-13), 1631-1643.

105.   Misquitta, A. J.; Stone, A. J.; Price, S. L., Accurate induction energies for small organic molecules. 2. Development and testing of distributed polarizability models against SAPT(DFT) energies. *J Chem Theory Comput* **2008,** 4, (1), 19-32.

106.   http://www-stone.ch.cam.ac.uk/programs.html#CamCASP

107.   http://towhee.sourceforge.net/

Chapter 5. An Efficient Multi-scale Lattice Model Approach to Screening Nano-Porous Adsorbents

Table of Contents

5.1 Introduction

As we discussed in Chapter 1, metal organic frameworks (MOFs) are crystalline nano-porous materials with many applications in gas separation and storage.[1, 2] The diverse possible MOF structural topologies, metal centers, and bridging ligands leads to a vast parameter space that can be exploited to design materials tailored and optimized for particular applications. In spite of many recent advances with high-throughput synthesis and characterization methods,[3, 4] the immense size of this parameters space does not admit a comprehensive evaluation via experimental methods.

Computer simulation techniques, such as molecular dynamics (MD) and Monte Carlo (MC) have been widely used to facilitate screening MOF structures for particular applications. Snurr and coworkers developed a library of over 100,000 hypothetical MOF structures.[5] They then utilized standard grand canonical ensemble Monte Carlo (GCMC) algorithms in conjunction with a simple atomistic force field to screen these materials for methane adsorption, identifying promising candidates for subsequent experimental study. In order to make the screening tractable, they exploited the fact that methane is essentially spherically symmetric (eliminating the need to sample adsorbate orientations) and that electrostatic interactions could be reasonably ignored (since methane is nearly completely non-polar). They also utilized a pre-screening approach to efficiently discard poor candidates prior to full GCMC simulation. This approach is extremely promising, and has more recently been utilized to study related

systems such as Xe/Kr separations.[6] Nonetheless, this "brute force" approach is limited by the computational expense imposed by running conventional GCMC simulations on a large number of candidate materials.

With even moderately polar adsorbates, such as CO_2, electrostatic contributions are essential, and the long-range nature of these interactions introduces significant additional computational cost to the MC/MD simulations. Furthermore, in some cases sophisticated/accurate polarizable force fields, such as the SYM/ZIFFF force field introduced in the previous few chapters, may be necessary to obtain robust results, greatly increasing cost of the associated simulation.[7, 8] While addressing either (or both) of these complications is straightforward for a *modest* number of MOFs, application to vast libraries of MOF structures becomes intractable. Circumventing these limitations requires either a dramatic increase in accessible computational power or fundamentally new approaches to screening. Along the former lines, Smit and coworkers[9, 10] demonstrated how graphics processing units (GPUs) could be exploited to massively parallelize the search over candidate materials. In this chapter, we take a complementary approach and propose a new technique based on a coarse-grained lattice model, which greatly improves the simulation efficiency while retaining semi-quantitative to quantitative accuracy over all pressure regimes.

The use of lattice models to study adsorption and diffusion in nano-porous material has a long history, particularly in the study of zeolites. Compared to atomistic simulation, lattice models dramatically reduce the degrees of freedom and discretize those that remain, yielding substantial performance increases.[11-25] Yet these early lattice models typically make extensive use of empirical parameters (e.g. empirical site adsorption energies) fitted to experimental data, thus limiting their application to strictly previously characterized materials. Alternatively, these lattice parameters can be derived from underlying atomistic simulations in a "hierarchical" approach as proposed by June *et al.*[26] and Snurr *et al.*[27-29] Frequently the lattice structure is considered as a partition of the *adsorption* space (as opposed to physical space), and each lattice point represents a well-defined adsorption site. Configuration integrals within and between

adsorption sites, representing the adsorption and guest-guest interaction free energies, were computed using standard MC simulation techniques. The resulting lattice simulation yields excellent agreement with the corresponding fully atomistic one. Others have successfully generalized this method and applied it to various zeolite systems, incorporating effects such as multiple site occupation and correlation.[30-37]

These previous multi-scale "hierarchical" lattice models have been largely limited to zeolite systems, since zeolites possess well-defined adsorption sites (pores and channels) comparable in size to a typical adsorbate. For such systems the map between the lattice sites the zeolite cages/channels is relatively straightforward, and the size of the cages naturally limits the maximum occupation number in each site. Furthermore, due to high symmetry, there are typically only two or three unique types of adsorption sites in the system, so well-converged sampling for these sites is not particularly expensive. Furthermore, the large spatial separation between adsorption sites mitigates many-body effects.

In contrast, we focus on MOFs, which exhibit larger, nanometer-scale pores able to accommodate tens or even hundreds of guest molecules. As such, MOFs do not exhibit well-defined, discrete, adsorption sites, and are thus not amenable to partition in adsorption space. In contrast, we directly partition the MOF unit cell into a lattice model in *physical* space into a series of molecular-sized cells. We then utilize a multi-scale approach to derive lattice free energies for each lattice site based on explicit atomistic simulation. Due to the large number of lattice sites, it is not a priori obvious that the requisite sampling at each of these lattice sites will result in significant efficiency gains over a fully atomistic simulation. Nonetheless, we show that this approach enables the utilization of several novel algorithmic modifications that yield orders-of-magnitude performance increase. We also present a more general approach to guest-guest interactions that accounts for the significant contribution from many-body effects.

Similar sampling-based approaches have been used previously to efficiently calculate the Henry's constant for nano-porous sorbents.[38-40] However, these existing methods yield *only* the Henry's constant (and not an associated lattice model) and thus cannot be applied outside of infinitesimal pressures. While this may be sufficient in the case of a dilute adsorbate (e.g. flue gas separation), it is insufficient for

general applications. In contrast, we show that, using appropriate guest-guest interactions, we are able to semi-quantitatively to quantitatively reproduce the adsorption properties of large pore MOFs from the Henry's regime through saturation while simultaneously achieving simulation speeds two to three orders-of-magnitude faster than conventional atomistic MD/MC simulations. Furthermore, we demonstrate that (via appropriate calibration) our lattice approach can be also applied to estimate dynamic properties, such as self-diffusivity.

5.2 Methods and implementation details

5.2.1 Lattice Model Description

For a given MOF, we partition the MOF unit cell into a $N_a \times N_b \times N_c$ sub-lattice, where N_α is the number of divisions along the direct lattice vector $\boldsymbol{\alpha}$ and controls the resolution of the grid. As such, the shape of each lattice cell is commensurate with that of the original unit cell. A lattice model is constructed on the basis of this partition under the assumption that a maximum of one guest molecule is allowed in each lattice cell. This assumption limits the maximum size of each lattice cell (to no more than approximately 2.5Å per side, for CO_2), and could be relaxed with a more sophisticated model allowing for multiple site occupancy.

We begin by making the observation that the partition function for a single guest adsorbate within the MOF unit cell, Q, can be written as,

$$Q = \sum_{\mathbf{i}} Q_{\mathbf{i}} \tag{5.1}$$

where the indices $\mathbf{i} = (ijk)$ denote a given lattice point in three dimensional space and

$$Q_i = \int_{V_{\mathbf{i}}} d\nu \, \mathrm{e}^{-\beta U} \tag{5.2}$$

is the partition function for a guest molecule within the specific lattice cell $\mathbf{i}$. Here U is the interaction energy between the guest and the MOF framework, calculated using an atomistic force field, β is the inverse temperature, and the integration is taken over all guest positions and rigid body orientations, $v = (\mathbf{r}, \theta, \varphi)$, with the center of mass restricted to lattice cell $\mathbf{i}$. This averaged Boltzmann factor is computed using the standard Monte Carlo integration techniques, as discussed in detail below.

The contribution to the free energy of a guest in cell $\mathbf{i}$ is thus given by $F(\mathbf{i}) = -kT \ln Q_{\mathbf{i}}$. The overall partition function can be exactly re-expressed in terms of the lattice free energies as,

$$Q = \sum_{\mathbf{i}} e^{-\beta F(\mathbf{i})} = \int dv\, e^{-\beta U} \tag{5.3}$$

This form emphasizes the *exact* mapping from the original continuous potential to the discrete lattice by simply replacing the continuous interaction potential energy with the corresponding discretized free energy, $F(\mathbf{i})$.

For a given occupation configuration, the total free energy is *approximated*,

$$F_{tot} = \sum_{\mathbf{i}}^{N} F(\mathbf{i}) + \sum_{\mathbf{i} < \mathbf{j}} F_{int}(\mathbf{i}, \mathbf{j}) \tag{5.4}$$

Here indices $\mathbf{i}, \mathbf{j}$ run over all N *occupied* lattice sites, and $F_{int}(\mathbf{i}, \mathbf{j})$ represents the effective interaction energy between two occupied sites, as discussed below. Note that this expression is no longer exact for $N > 1$, and its accuracy will depend on the approximation used for $F_{int}(\mathbf{i}, \mathbf{j})$, as discussed below.

Subsequent on-lattice GCMC simulations are conducted on the basis of this lattice model. Three types of move are performed: particle translations, insertions and deletions. In the particle translation moves a random guest is displaced to a random lattice site, and the acceptance probability is calculated using the standard Metropolis scheme,

$$p = \min\left(1, \exp\left(\beta(F_{tot}^{try} - F_{tot})\right)\right) \tag{5.5}$$

For particle deletion moves, a random particle is removed from the lattice site with acceptance probability

$$p = \min\left(1, \frac{\Lambda^3 N}{V}\exp\left(\beta(F_{tot}^{try} - F_{tot} - \mu)\right)\right)$$

(5.6)

For particle insertions, a particle is inserted to a random site with acceptance probability

$$p = \min\left(1, \frac{V}{\Lambda^3(N+1)}\exp\left(\beta(F_{tot}^{try} - F_{tot} + \mu)\right)\right)$$

(5.7)

Here Λ is the thermal De Broglie wavelength, V is the total unit cell volume, N is the number of particles, and μ is the chemical potential.

Given the free energy maps, the lattice GCMC simulations are extremely rapid since they make use exclusively on the pre-tabulated adsorption and interaction free energies. These simulations typically finish in well under 15 seconds on a single modern CPU core. As such, the majority of the computational cost arises from the generation of the free energy maps.

5.2.2 Evaluation of Long-range Potential

In the following sub-sections, we describe how the lattice partitioning can be exploited to rapidly estimate these lattice free energy maps, $F(\mathbf{i})$. Following Haldoupis *et al.*[40] and assuming that all framework atoms are rigidly fixed, we pre-calculate portions of the potential surface and store it on a grid in memory. In general, we grid the long-range (slowly spatially varying) portions of the potential while explicitly calculating the short-range (rapidly varying) portions on the fly; gridding the latter would require an inefficiently fine grid.

For electrostatic interactions, the particle mesh Ewald (PME)[41] algorithm is utilized. Here we calculate the *electrostatic potential* created by the framework atoms (rather than the electrostatic energy), resulting in modifications from the standard PME algorithm. The electrostatic potential is decomposed into the reciprocal part and real space part: $U_{elect} = U_{elect}^{real} + U_{elect}^{recip}$. We store the reciprocal part of the electrostatic potential on a grid and calculate it only once at the beginning of the simulation, while the real part of the

energy is calculated on fly. All the points in the potential grid are generated simultaneously using a discrete fast Fourier transform (FFT):

$$U_{elect}^{recip}(u_1,u_2,u_3) = \sum_{m_1,m_2,m_3=0}^{K-1} \exp\left(-2\pi i \frac{m_1 u_1 + m_2 u_2 + m_3 u_3}{K}\right) S(\mathbf{m}) \frac{1}{\pi V m^2} \exp\left(\frac{-\pi^2 m^2}{\beta^2}\right)$$
$$= FT^{-1}\left(S(\mathbf{m})C(\mathbf{m})\right)$$

(5.8)

where

$$C(\mathbf{m}) = \frac{1}{\pi V m^2} \exp\left(\frac{-\pi^2 m^2}{\beta^2}\right)$$

(5.9)

In the above expressions (u_1,u_2,u_3) are the indices for the real space grids, running from 0 to $K-1$, in which $K=100$ controls the PME grid size, $\mathbf{m}=(m_1,m_2,m_3)$ are the corresponding indices in reciprocal space, V is the total volume of the simulation box, and $\beta=0.6$ (for electrostatic interactions) controls the width of the screening charge distribution.

As in standard PME implementations, the structure factor $S(\mathbf{m})$ can be calculated using 6th order cardinal B-spline interpolation (for details see equation 4.5 in Ref 41),

$$S(\mathbf{m}) = \sum_j q_j \exp(2\pi i \mathbf{m}\cdot\mathbf{r}_j)$$
$$\approx b_1(m_1)b_2(m_2)b_3(m_3)FT(Q)(m_1,m_2,m_3)$$

(5.10)

Plugging equation (5.10) into the expression for the potential (5.8) yields the final working expression,

$$U_{elect}^{recip}(u_1,u_2,u_3) = FT^{-1}(FT(Q)(\mathbf{m})b_1(m_1)b_2(m_2)b_3(m_3)C(\mathbf{m}))$$

(5.11)

The reciprocal part of the electrostatic energy is computed using the potential interpolated from the potential grid using Lagrange's functions,

$$E_{elect}^{recip} = \sum_i q_i \cdot U_{elect}^{recip}(\mathbf{u}_i)$$

$$u_{i\alpha} = K\mathbf{r}_i \cdot \mathbf{a}_\alpha^*$$

$$U_{elect}^{recip}(\mathbf{u}) = \sum_{k_1=-p+1}^n \sum_{k_2=-p+1}^n \sum_{k_3=-p+1}^n W_{2n}(k_1-(u_1-[u_1]))W_{2n}(k_2-(u_2-[u_2]))W_{2n}(k_3-(u_3-[u_3]))$$

$$\cdot U_{elect}^{recip}([u_1]+k_1,[u_1]+k_2,[u_1]+k_3)$$

(5.12)

Here, index i runs over all the guest atoms, q_i is the associated atomic charge, and $\mathbf{u}_i$ is the atom

positions $\mathbf{r}_i$ scaled using reciprocal vectors $\mathbf{a}_\alpha^*$, and α denotes the spatial dimension. W_{2n} is the

Lagrange weighting function, and n is the order of the interpolation. If $n=1$, then a linear interpolation

scheme is restored; we set $n=2$ in this work.

It is also straightforward to calculate the reciprocal contribution of the electrostatic field,

$$\mathbf{E}_{elect}^{recip}(\mathbf{u}) = -\frac{\partial}{\partial \mathbf{u}}E_{elect}^{recip}(\mathbf{u})$$

$$= -\sum_{k_1=-p+1}^n \sum_{k_2=-p+1}^n \sum_{k_3=-p+1}^n \frac{\partial}{\partial \mathbf{u}}\left(W_{2n}(k_1-(u_1-[u_1]))W_{2n}(k_2-(u_2-[u_2]))W_{2n}(k_3-(u_3-[u_3]))\right)$$

$$U_{elect}^{recip}([u_1]+k_1,[u_1]+k_2,[u_1]+k_3)$$

(5.13)

which is utilized in applications involving polarizable force fields.

This PME scheme can be generalized to any potential with the form $\dfrac{C_p}{r^p}$, with charges replaced by

C_p parameters and the $C(\mathbf{m})$ matrix modified accordingly: [41]

$$C(\mathbf{m}) = \frac{\pi^{3/2}\beta^{p-3}}{V}f_p\left(\frac{\pi|\mathbf{m}|}{\beta}\right)$$

$$f_p(x) = \frac{2x^{p-3}}{\Gamma(p/2)}\int_x^\infty s^{2-p}\exp(-s^2)ds$$

(5.14)

As such, we also use this formalism to calculate the dispersion energies, where $p = 6$, 8, or 10. This

offers two major advantages. First, the long range dispersion effect is calculated exactly, without the need

for arbitrary cutoffs. This is vital as simple cutoff schemes for dispersion converges relatively slowly with

respect to the cutoff radius (a cutoff radius beyond 15Å is needed to generate high quality isotherms within an error of 10%), and no simple long-range correction is possible for anisotropic crystalline systems. Additionally, as we show below, proper choice of the screening parameter, β (set to 1.2 for all dispersion terms), allows for use of very short range real-space cutoffs, leading to extremely high computational efficiency.

To avoid the restriction that C_p be decomposable into products of atomic parameters (as is trivially obeyed for Coulomb interactions), different reciprocal dispersion grids are created for different types of guest atoms. This slightly increases memory utilization, but is not a concern unless the guest contains a very large number of atom types. Due to the use of FFT algorithms, generation of the various PME grids is quite computationally efficient, requiring ~20% of the overall lattice generation time.

5.2.3 Evaluation of Short-range Potential

In the formalism of the PME algorithm, the real-space part of the guest-framework interactions is damped,

$$
E^{real} = \sum_i \sum_j \frac{C_{ij} g_p(\beta r_{ij})}{r_{ij}^p}
$$

$$
g_p(x) = \frac{2}{\Gamma(p/2)} \int_x^\infty s^{p-1} \exp(-s^2) ds
$$

(5.15)

where i runs over all guest atoms, and j runs over all framework atoms within a certain cutoff distance. For electrostatics, $p=1$ and $C_{ij} = q_i q_j$; for dispersion, $p = 6,\ 8,\ 10$, and C_{ij} is simply dispersion coefficients C_6, C_8 or C_{10} for the given interacting pair. The damping function $g_p(\beta r_{ij})$ decays as a complementary error function (for $p=1$), allowing us to utilize extremely short real-space cutoffs. We utilize cutoffs of 5.0 Å and of 6.5 Å for electrostatics and dispersion, respectively. Due to the rapid, exponential, decay, this cutoff generates essentially no error.

We also utilize a cell list to further accelerate the real-space portion of the calculation.[42] The simulation box is divided into 20×20×20 cells. For each cell, we tabulate a list of all framework atoms located in this cell, and this list can be used to facilitate fast neighbor searching in the simulations. Since all framework atoms are held fixed during simulation, the cell list is constructed only once, and thus the computation time is negligible. The combination of the short-range real space cutoffs and the cell list leads to tremendous computational savings. Note that although many of these approaches can also be employed in conventional MC/MD simulations, the calculation of guest-guest interactions would rapidly become rate limiting in a fully atomistic simulation.

5.2.4 Utilization of Symmetry

Our lattice algorithm allows us to exploit the inherent space-group symmetry of the MOF by sampling over only the smallest asymmetric unit cell; this symmetry is extremely difficult (if not impossible) to exploit in standard MC/MD techniques. As such, we calculate our free energy map only for the smallest asymmetric unit cell, and then utilize the associated symmetry operations to generate the remaining (symmetry equivalent) portions of the map. This provides for efficiency gains proportional to the symmetry of the MOF, typically a factor of 3-5.

5.2.5 Sampling Scheme

The evaluation of average of the Boltzmann factor in Equation (5.2) determines the efficiency and accuracy of the lattice method. A naïve integration scheme leads to dramatic over-sampling of high-energy (statistically irrelevant) configurations and under-sampling of important adsorption sites (where high accuracy is required). We find that cells in which has part of the cell volume lies within the pore and part of the volume overlaps with the framework are particularly challenging. Large variations of the Boltzmann factors are observed, with strong coupling between the various translational and rotation adsorbate degrees of freedom, and making this case difficult even for more advanced Monte Carlo integration techniques such as Vegas sampling.[43] Fortunately, these cells are not particularly statistically

important and modest errors in the sampling of these cells do not appreciably affect the accuracy of the resulting lattice model.

Given the above considerations, we therefore utilized two different convergence criterions for the free energy samplings. If the average Boltzmann factor is smaller than 100 (corresponding to an excess free energy higher than -11.5 kJ/mol), we adopt an absolute error threshold (θ_{abs}) on the Boltzmann factor. Otherwise, a relative error threshold (θ_{rel}) is applied to evaluate converge of the Boltzmann factor; this relative error threshold on the Boltzmann factor corresponds to a fixed absolute uncertainty in the corresponding free energy, ΔF, as listed in Table 5.1. Since this uncertainty is extremely small (much less than 1 kJ/mol in all cases), we anticipate that statistical errors will be negligible in most cases, as verified below. Absolute and relative statistical errors are computed once every ten samples and are used to evaluate convergence. In conjunction with different cell sizes, we examined three different sets of thresholds in all test cases: high precision (HP), medium precision (MP) and low precision (LP). For all threshold sets, the maximum sampling size for each cell is always 2000, and the details of these thresholds can be found in Table 5.1. Note that the lattice model is *exact* in the low density limit for *all* cell sizes, although the restriction on single site occupation and the discretization of guest-guest interactions (vide infra) favor small cell sizes.

	cell size	θ_{abs}	θ_{rel} (%)	ΔF (kJ/mol)
HP	~ 0.3Å	1	1	0.02
MP	~ 1.0 Å	3	5	0.12
LP	~ 1.0 Å	10	10	0.24

Table 5.1. The free energy map sampling conditions for high (HP), medium (MP) and low (LP) sampling precisions. θ_{abs} and θ_{rel} are the absolute and relative error thresholds used in the statistical estimation of the Boltzmann factor, used in regimes of high and low free energy, respectively. The relative error threshold corresponds to an uncertainty in the free energy, ΔF.

Using the sampling scheme and the efficient grid-based energy evaluation approach, the average of the Boltzmann factor, Equation (5.2), is evaluated for each of the lattice cells to determine the complete free energy map, $F(\mathbf{i})$. The generation of this free energy map is the most time consuming step of our lattice approach, but is nonetheless orders-of-magnitude faster than the corresponding molecular simulation. As detailed below, generation of a free energy map takes mere minutes on a single modern CPU core. Coupled with a model for guest-guest interactions, this free energy maps can then be used within on-lattice GCMC calculations and even full adsorption isotherms with essentially no additional computational cost.

5.2.6 Guest-guest Interactions

GCMC calculations at moderate at finite pressures require a model for the guest-guest interaction, $F_{\mathrm{int}}(\mathbf{i}, \mathbf{j})$; this term can be neglected for low pressures in the Henry's regime. Note that although the mapping from atomistic to lattice model is *exact* in the low pressure limit, no such (simple) exact mapping exists for finite pressure. Nonetheless, we will show that even very simple models for guest-guest interactions yield semi-quantitative to quantitative agreement with the corresponding fully atomistic simulations.

Typically, two steps are involved in developing this effective guest-guest lattice interaction potential. First, a continuous, isotropic, single-site guest-guest interaction potential is constructed, either by fitting to experimental data or by coarse graining existing atomistic force fields. Subsequently, this continuous potential is discretized commensurate with the lattice grid.

The simplest possible approximation for guest-guest interactions is a hard sphere potential. Although crude, it naturally enforces an "excluded volume" constraint and thus introduces an important correction to the calculated adsorption isotherms at high pressures. Nonetheless, it omits the long-range dispersive interaction between adsorbates and thus typically underestimates adsorption at moderate pressures. For the specific case of CO_2, several more sophisticated single-site isotropic models can be found in the

literature.[44] Most of these potentials are empirical and are benchmarked to various experimental data, such as viscosity, virial coefficients, diffusivity or critical properties. For the present work, we use the single site Lennard-Jones potential developed by Liu *et al.*[45] (henceforth, the Liu potential), which is fit to reproduce combined viscosity and virial coefficients.

Subsequently, the continuous interaction potentials must be discretized commensurate with the lattice grid. This discretization can be done exactly for the case of an interacting *dimer*,

$$F_{\text{int}}(\mathbf{i}, \mathbf{j}) = -kT \ln\left(\left\langle \exp(-U(\mathbf{r}_1, \mathbf{r}_2) / kT\right\rangle_{\mathbf{r}_1, \mathbf{r}_2}\right) \tag{5.16}$$

where $\mathbf{i}, \mathbf{j}$ denote the two different lattice cells, and the average is taken over all possible guest orientations with the restriction that their center-of-mass is confined to their respective cells. However, we also examine the straightforward discretization

$$F_{\text{int}}(\mathbf{i}, \mathbf{j}) = U(r_{\mathbf{ij}}) \tag{5.17}$$

where $r_{\mathbf{ij}}$ is the distance between the centers of the respective lattice cells. Obviously these two methods are equivalent in the limit of small lattice cells. Surprisingly, Equation (5.17) seems to work just as well or even better than its more "rigorous" counterpart. This is likely due to the fact that many-body effects are introduced by the discretization and likely some fortuitous error cancellation. However, since the differences are very modest, we utilize the simpler approach. Equation (5.16) is used only in the hard sphere simulations to smooth the abrupt change of the hard sphere potential.

5.2.7 Test Cases and Simulation Details

We carried out both atomistic GCMC and corresponding lattice model simulations for CO_2 adsorption in several MOFs as test cases. ZIF-96, ZIF-8 and MOF-5 are used to benchmark the lattice model's performance with standard non-polarizable force field simulations. For ZIF-96 and ZIF-8, we utilize the UFF force field,[46] distributed multipole fit charges,[8] and the EPM2[47] CO_2 potential. For MOF-5, the UFF force field is used in conjunction with charges and CO_2 potentials taken from Ref. 48. In each case,

conventional GCMC calculations are carried out using PME electrostatics and dispersion to provide benchmark values. Subsequently, lattice simulations are conducted at various precision levels (HP, MP and LP), in conjunction with the Liu potential for guest-guest interactions, and the results are compared to atomistic simulations. Simulations utilizing hard sphere (HS) guest-guest potentials are also given for comparison, with the hard sphere radius set to 2.5Å.

ZIF-8 and ZIF-71 are utilized to illustrate how this lattice model can also be extended to polarizable force fields. Polarizable models validated in Ref. 7 (for ZIF-8) and 8 (for ZIF-71) are used to run both conventional (atomistic) and lattice GCMC simulations. In the latter case, we also examine and contrast several possible models for guest-guest interactions.

For all atomistic GCMC simulations, 20% of the moves are particle insertions/deletions, and a rotational bias method[49] is used to aid particle insertion. (Note that when comparing *efficiencies* we utilize up to 80% insertions, *vide infra*.) A hybrid MD/MC algorithm,[50] which is much more efficient in polarizable simulations, is used for all particle translation moves. In general, ~2,000,000 MC steps are performed, and in some high pressure cases, more MC moves are conducted to ensure convergence. For all the lattice GCMC simulations, 80% of the moves are test particle insertion/deletion moves, and 5,000,000 MC steps are conducted in each simulation. All Monte Carlo simulations are conducted using in-house codes. For all GCMC calculations, chemical potentials are calculated via the Peng-Robinson equation of state.[51] The total numbers of grids used in the lattice GCMC and the simulation temperatures are listed in Table 5.2.

	simulation box	box size (Å)	T (K)	N_{HP}	N_{MP}	N_{LP}
ZIF-96	unit cell	28.4	300	100	30	30
MOF-5	unit cell	25.8	300	100	30	30
ZIF-8	2×2×2	34.0	303	120	40	40
ZIF-71	unit cell	28.3	298	100	30	30

Table 5.2. Simulation box information for various test cases. The number of lattice discretizations in each dimension is given for the high (N_{HP}), medium (N_{MP}) and low (N_{HP}) precision simulations.

5.3 Results and Discussions

5.3.1 Non-polarizable Force Field Test Cases

Simulated adsorption isotherms for ZIF-96, MOF-5 and ZIF-8 are plotted in Figure 5.1, Figure 5.2 and Figure 5.3.
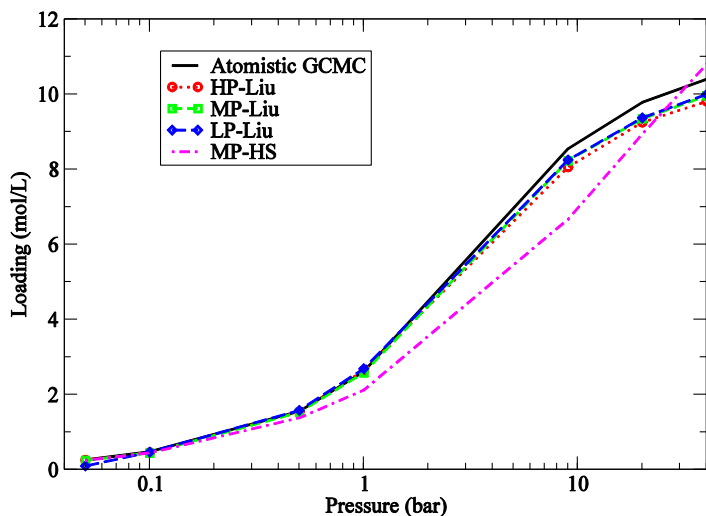
Figure 5.1. Adsorption isotherms for ZIF-96. Lattice GCMC results plotted alongside the reference atomistic GCMC results.
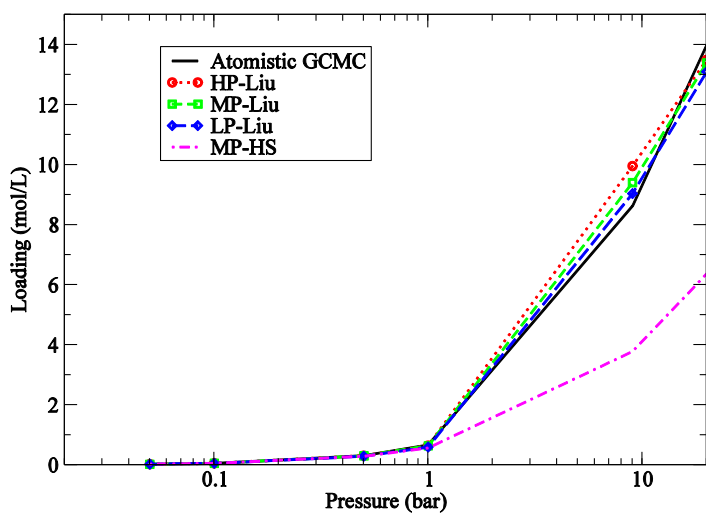
Figure 5.2. Adsorption isotherms for MOF-5. Lattice GCMC results plotted alongside the reference atomistic GCMC results.
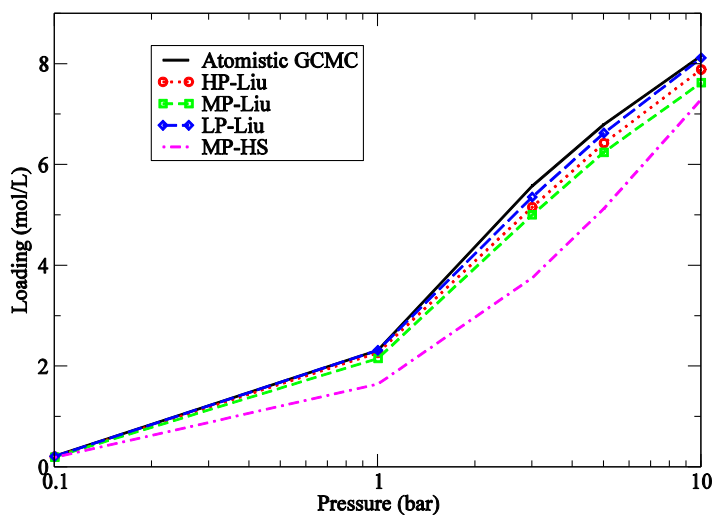
Figure 5.3. Adsorption isotherms for ZIF-8. Lattice GCMC results plotted alongside the reference atomistic GCMC results.

For ZIF-96, we studied the pressures ranging from 0.05 bar to 40 bar, representing conditions ranging from independent adsorption to near saturation. For MOF-5 and ZIF-8, adsorption conditions beyond 10 bar are also investigated. In all cases agreement in the low pressure regime up to ~1 bar is essentially quantitative. This follows from the fact that the mapping between atomistic and lattice model is exact in the absence of guest-guest interactions; the small deviations in this regime are merely the result of statistical uncertainty. From moderate to saturation pressures, agreement between atomistic and lattice/Liu simulations is still semi-quantitative, with maximum errors of less than 15% and average errors of only a few percent. These modest deviations are directly attributable to the approximate treatment of the guest-guest interactions. Differences between the various precision levels are extremely modest, and for all three cases, and even the LP level sampling turns to be accurate enough to reproduce the whole isotherm within few percent of error. As such, we henceforth only consider MP.

To examine the role of attractive guest-guest interactions, we contrast these results with the corresponding simulations employing the hard sphere (HS) guest-guest interaction model. At finite pressure conditions, the HS calculations significantly underestimate the loading due to the omission of long-range attractive guest-guest dispersive interactions. Results in the low-pressure Henry's law regime

are unaffected, since guest-guest interactions are unimportant at these modest pressures. Adding even the simple empirical Lennard-Jones-type Liu potential significantly improves the results by accounting qualitatively for the attractive guest interactions. Approaching the saturating regime (see, for example, ZIF-96 and ZIF-8 at the highest reported pressures), the error of the HS simulation decreases again with increasing pressure, likely because packing effects dominate in this regime. These packing effects are captured using even the simple hard sphere potential.

We also examined the details of the adsorption by comparing the distribution of adsorbed CO_2 molecules between the atomistic and lattice simulations. Using the ZIF-96 adsorption at 1 bar as an example, we show in Figure 5.4 the projections of the CO_2 distributions in two perspectives, along (001) and (111) directions, respectively. The CO_2 location distributions are essentially exactly reproduced within the lattice model.
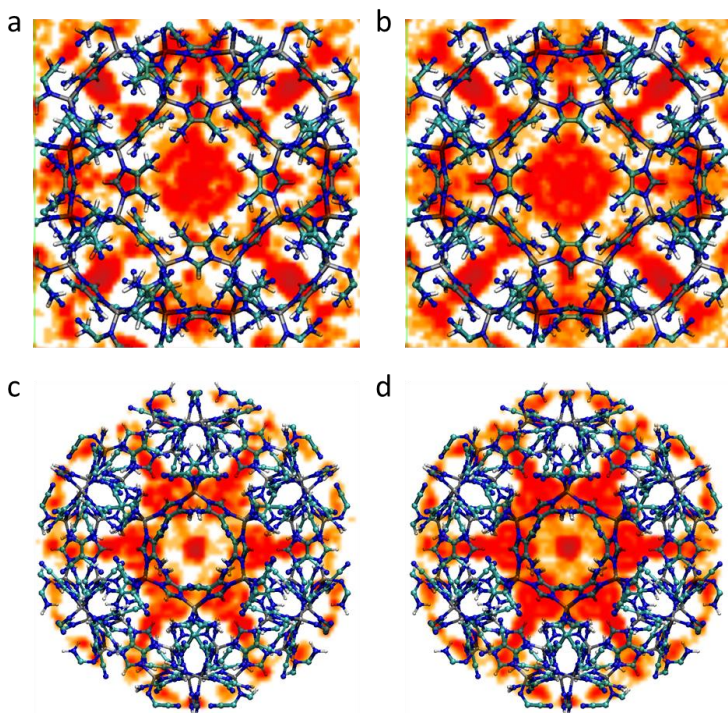
Figure 5.4. CO_2 density distributions in ZIF-96. (a-b) Plots show the (001) perspective from atomistic (a) and lattice (b) simulations; (c-d) (111) perspective from atomistic (c) and lattice (d) simulations.

5.3.2 Polarizable Force Field Test Cases

One advantage of our lattice model as compared to the traditional MC/MD is that it is easily and *efficiently* generalizable to polarizable force fields. Since polarizable force fields are typically an order of magnitude more computationally expensive than their conventional (non-polarizable) counterparts, the efficiency gains of the lattice approach are further magnified. Application of the lattice approach to polarizable force fields proceeds identically as described above, although additional computational effort is required to converge the induced dipoles at each sample point.

We benchmark our lattice model against explicit atomistic simulations for ZIF-8 and ZIF-71 employing the polarizable "SYM" CO_2 force field;[7, 8, 52] results are plotted in Figure 5.5 and Figure 5.6. As expected, the deviations in the low-pressure regime are very small, independent of the model employed for guest-guest interaction. Using the Liu model, errors in the moderate- to high-pressure regime are modest, with maximum errors less than 20%, and typically within 15%. Deviations between atomistic and lattice simulations for ZIF-8 are slightly larger than for ZIF-71 or the previous non-polarizable results, possibly due to the smaller sizes of its pores; in a confined space, adjacent adsorption sites likely interact, leading to a stronger CO_2-CO_2 orientational correlation which is omitted in the lattice model. The average deviation from atomistic simulation is about 12% and maximum error is controlled within 20%. These errors are certainly small enough for high-throughput screening applications. Comparing levels of precision, we find excellent agreement between the MP and HP precision sampling schemes.
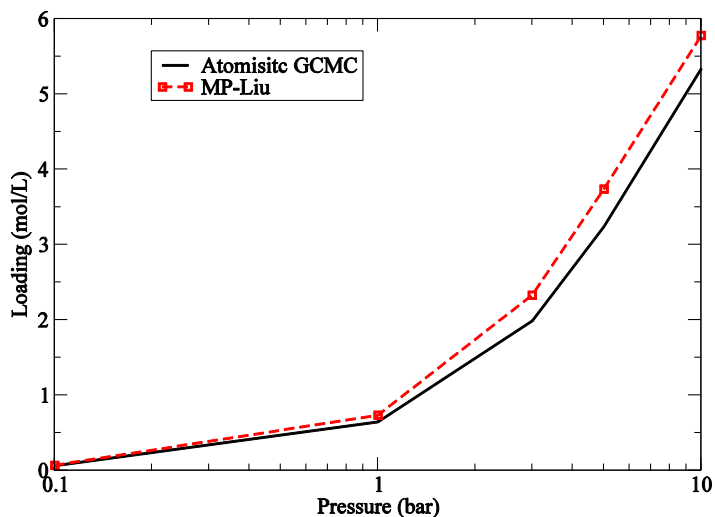
Figure 5.5. Adsorption isotherms for ZIF-8 with the polarizable SYM model force field. Lattice GCMC results plotted alongside the reference atomistic GCMC results.
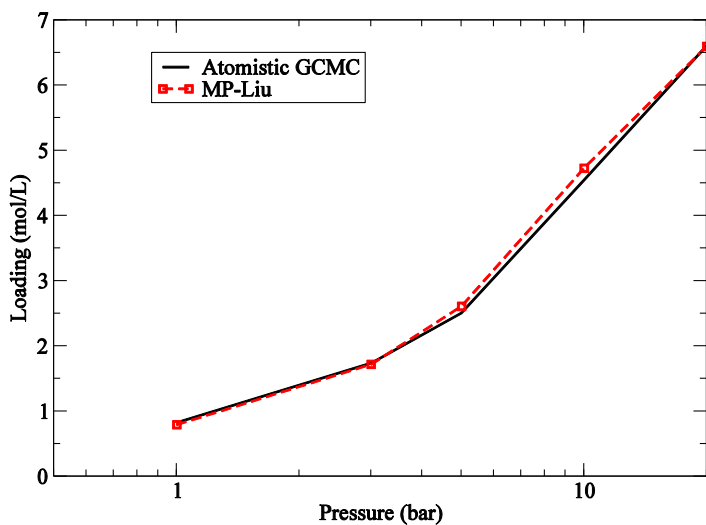
Figure 5.6. Adsorption isotherms for ZIF-71 with polarizable force field. Lattice GCMC results plotted alongside the reference atomistic GCMC results.

5.3.3 Effective Guest-guest Interactions from Force Matching

Although the Liu guest-guest interaction potential does excellent in reproducing adsorption isotherms in all relevant pressure regions, this empirical approach is somewhat incompatible with the "hierarchical" spirit of our lattice approach and also leads to an inconsistency with the atomistic simulations (which

often utilize *different* underlying atomistic CO_2 force fields). As a more rigorous alternative, we explore a force matching procedure[53] in order to coarse grain an existing atomistic CO_2 force field. We take as a starting point our prior well-characterized, physically-motivated, polarizable "SYM" CO_2 model.[52] The SYM model is essentially free of empirical parameters and was developed on the basis of symmetry-adapted perturbation theory electronic structure calculations and physical considerations. The model naturally yields excellent agreement with bulk structural, thermodynamic, and dynamic properties over the phase diagram.

Using the force matching approach,[53] we coarse grained our SYM potential to a single site model. Starting with simulations of neat CO_2 at 320K and varying density, ρ, we analyzed the resulting trajectories using the force matching method. The single-site potential derived depends on the simulation conditions, particularly ρ. Ideally, this force matching should be conducted at densities similar to the adsorbed CO_2 phase in the MOF. Here, considerable uncertainty arises due to the free volume of the MOF and the appropriate pressure under which to evaluate this density. To estimate this free volume for a representative MOF, we define all the grid points with free energies higher than $3k_bT$ as blocked. Since guest-guest interactions are most important at high pressures, we coarse grain the potential with a focus on the moderate- to high-pressure regimes. Taking ZIF-71 a prototypical example, we thus estimate that moderate/high densities are between 10 mol/L and 20 mol/L.

We tested four different densities: 13, 14, 15 and 16 mol/L; the resulting single site potentials are plotted in Figure 5.7. There are very minor differences between the potentials developed at different densities. Although the adsorption is exponentially sensitive to these changes, the differences of the corresponding isotherms are still rather modest and effectively unchanged from 14-16 mol/L. As shown in Figure 5.8, all the SYM potentials underestimate the loading, and the best agreement is obtained using the result at 15 mol/L, SYM(15), with the errors below 10%. It is perhaps not surprising that the optimum

force matching density is close to the center of the density range, balancing the performance in all loading conditions.
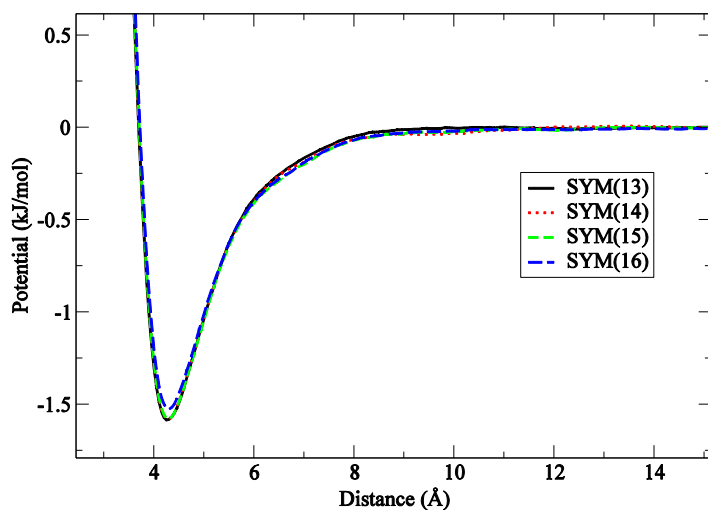
Figure 5.7. Force-matched potentials derived at difference densities, ranging from 13-16 mol/L.
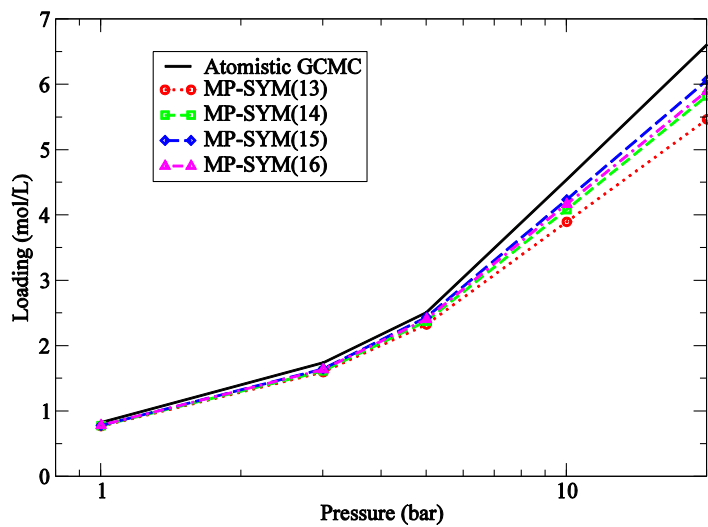
Figure 5.8. Adsorption isotherms for force matching guest-guest potentials, plotted alongside of reference atomistic GCMC results.

5.3.4 Simulation Efficiency

The principal advantage of our lattice approach is its overwhelming efficiency as compared to conventional, atomistic Monte Carlo. Taking ZIF-96 as a prototypical test case, we compared the simulation efficiency of the new lattice model approach with the traditional GCMC method. The benchmark GCMC simulations are conducted using standard PME for electrostatic interactions with a 14 Å simple cutoff for dispersion interactions. Using a dispersion cutoff is more efficient, but less accurate, than the PME treatment for dispersion. As such, it represents the most favorable comparison for conventional GCMC. We conducted two types of simulation, corresponding to two different scenarios in the screening process. The first type of scenario, equilibration (eq), starts with a single adsorbate in the simulation box and is carried out with 80% particle insertion and deletion ratio. These simulations estimate the speed of the initial pre-screening process as compared with our LP lattice simulation. In a second scenario, we compare "production" simulations (prod). These simulations start from well-equilibrated configurations and are performed with 20% particle insertion and deletion ratio. These simulations are used to refine the results from the previous crude pre-screening process and determine the loading to within a specified uncertainty. The production simulations are terminated when the trajectory lengths exceed three times the correlation time of the loading (as determined from the auto-correlation function of the particle number), and the computational cost is compared with the MP level sampling. The CPU time costs for the simulations at different pressures are shown in Table 5.3.

CPU time (s)	GCMC / 10^3	Lattice model	Acceleration
0.05bar (eq)	-[a]	101	-
0.05bar (prod)	44	198	220
1bar (eq)	14	101	137
1bar (prod)	49	198	249
20bar (eq)	62	101	612
20bar (prod)	97	198	492

Table 5.3. Performance comparison between atomistic and lattice simulations. GCMC and lattice model simulation times are shown in the second and third column. In the fourth column gives the corresponding acceleration, the ratio of the atomistic to the lattice timings. a). The equilibration time at this pressure is essentially instantaneous.

At all conditions, the lattice simulations are two to three orders of magnitude faster than the standard GCMC scheme. The lattice offers a comparatively larger advantage at moderate to high pressures where long equilibration times are required with atomistic GCMC and traditional GCMC exhibits serious sampling issues. Note that the lattice approach offers an even greater acceleration when calculation of an entire isotherm is required. In this case, the lattice model is generated only *once* (typically ~100 s at LP), followed by subsequent lattice GCMC simulations at varying pressure. Since the lattice GCMC simulations take only an insignificant amount of CPU time (< ~15 s for each pressure), the resulting acceleration of complete isotherm calculation is over three orders of magnitude faster than the corresponding atomistic GCMC simulations while maintaining semi-quantitative to quantitative agreement. As such, we feel that this lattice approach offers a new approach to the screening of novel adsorption materials.

We note that, recently, Kim and Smit[9, 10] developed a GPU-based GCMC algorithm that significantly improves the efficiency as compared to the conventional (CPU-based) GCMC. Using their GPU-based code, it is possible to calculate an isotherm within 200 to 1800 seconds, depending on the level of approximation and the omission of certain interactions. This speed is slightly slower (but of the same order-of-magnitude) to our (CPU-based) lattice simulation method. However, we anticipate that it would

be possible to generalize our lattice method to GPU based algorithm, leading to significant *additional* computational efficiencies.

The acceleration offered by our lattice approach is further magnified in the case of polarizable force fields. Here, conventional GCMC typically takes several *weeks* of CPU time to calculate a complete isotherm, making screening using such accurate force fields completely prohibitive. In contrast, the corresponding lattice model can be generated in less than half an hour on a single processor, followed by lattice GCMC simulations that add mere additional seconds. This enables full isotherm calculation within an hour instead of a month, and opens the door to the utilization of accurate, physically-motivated polarizable force fields in high-throughput calculations.

5.3.5 Dynamic Properties

Transport properties within nano-porous materials are an additional important consideration when evaluating a candidate material: large absolute and relative permeabilities favor rapid and efficient gas transport and separation, respectively. Therefore, we also investigated the performance of our lattice model in estimating self-diffusivities. Unlike equilibrium properties, dynamic properties cannot be calculated exactly within the context of a coarse-grained lattice approach. Nonetheless, we find that via calibration with fully atomistic MD simulations, we can accurate estimate self-diffusivity with extremely high accuracy on the basis of appropriately crafted lattice simulations.

We employed an NVT ensemble for both atomistic MD and lattice MC simulations. The atomistic simulations are conducted using Gromacs package,[54] with UFF Lennard-Jones parameters and charges fit to distributed multi-pole analysis (DMA). For all lattice MC simulations, only single particle moves to adjacent sites are allowed. Fifteen systems are tested, spanning various unit cell topologies, sizes, shapes, and functionality (see Table 5.4). The number of CO_2 molecules is determined from the observed loading of each MOF at ~3 bar, as determined form the corresponding equilibrium adsorption isotherm. For each

system, a 10 ns MD trajectory and a 100,000 cycle MC trajectory are used to estimate the self-diffusivity, $\mathbf{D}_{self}$.

	topology	N_a	N_b	N_c	# CO_2
IRMOF-3	cubic	30	30	30	50
MOF-5	cubic	30	30	30	50
ZIF-25	RHO	30	30	30	50
ZIF-71	RHO	30	30	30	50
ZIF-93	RHO	30	30	30	50
ZIF-96	RHO	30	30	30	50
ZIF-97	RHO	30	30	30	50
ZIF-8[a]	SOD	40	40	40	90
ZIF-68[b]	GME	30	30	45	60
ZIF-69	GME	30	30	45	60
ZIF-70	GME	30	30	45	60
ZIF-78	GME	30	30	45	60
ZIF-79	GME	30	30	45	60
ZIF-80	GME	30	30	45	60
ZIF-81	GME	30	30	45	60

Table 5.4. Description of the test systems for evaluating transport properties. The lattice simulations are conducted on an N_a x N_b x N_c lattice grid. a). 2×2×2 supercell is used for ZIF-8 simulations. b). 1×1×2 supercells are used for all ZIFs with GME topology.

The effective MC-calculated diffusivity obvious varies with the size (and shape) of the lattice cell, determined by the chosen lattice discretization. Furthermore, non-orthorhombic unit cells (and thus non-orthorhombic lattices) yield inherently non-isotropic diffusivity, even in free space. We therefore scale the diffusivities obtained with MC simulation, using the following relation:

$$\tilde{\mathbf{D}}_{self} = \left(\mathbf{L}^{-1}\right)^{T} \mathbf{D}_{self} \mathbf{L}^{-1} \qquad (5.18)$$

Here, $\mathbf{D}_{self}$ and $\tilde{\mathbf{D}}_{self}$ are the original and scaled diffusivity tensor, the trace of which are plotted in Figure 5.9. The $\mathbf{L}$ matrix is a row matrix of the direct lattice vectors of the lattice (i.e. the direct lattice vectors of the unit cell, scaled by N_a, N_b, and N_c, respectively). For arbitrary box shapes and sizes this scaling approach rigorously restores the isotropy of free diffusion in the low density limit (but only *approximately* so outside of this regime).

We partially validated this scaling method using the ZIF-80 system, which has GME topology and a hexagonal unit cell. We discretized the ZIF-80 simulation box utilizing three sets of grids with different resolutions: 30×30×45, 40×40×50 and 50×50×60. We conducted lattice MC on each set of grid and self-diffusivities are computed and scaled as shown in Table 5.5. As it is shown, with increasing grid numbers, the unscaled MC diffusivity decreases by more than 50% due to the reduced step size, while the scaled diffusivity remains stable.

	$\mathbf{D}_{self} \times 10^4\,(\text{nm}^2/\text{ps})$	$\tilde{\mathbf{D}}_{self} \times 10^1\,(\text{Cycle}^{-1})$
30×30×45	8.88	1.30
40×40×50	6.06	1.52
50×50×60	4.08	1.46

Table 5.5. Comparison of $\mathbf{D}_{self}$ and scaled $\tilde{\mathbf{D}}_{self}$ for ZIF-80. Scaled $\tilde{\mathbf{D}}_{self}$ is numerically more stable compared to the unscaled $\mathbf{D}_{self}$, with respect to grid numbers.
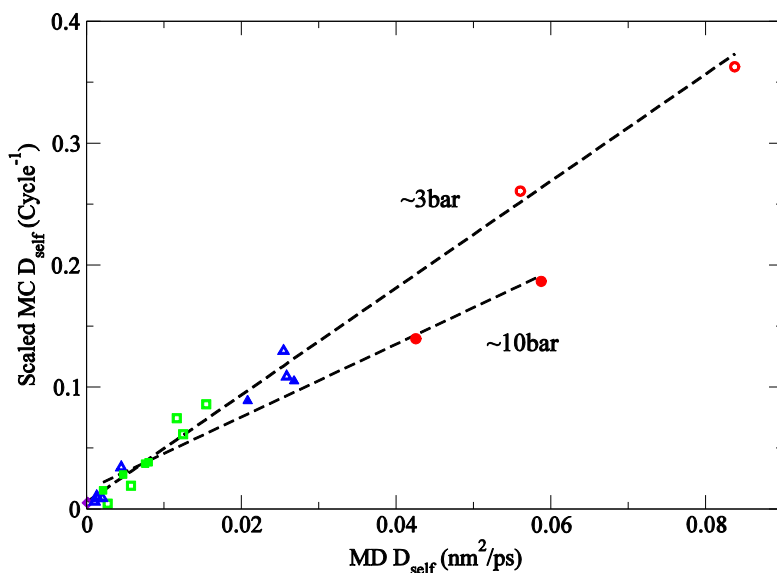
Figure 5.9. Scaled MC diffusivities plotted against MD diffusivities. Red circles represent the cubic isoreticular series (IRMOF3, MOF5); green squares represent ZIFs with RHO topology; purple diamonds represents ZIF-8 with SOD topology and blue triangles represent the ZIFs with GME topology. Data from simulations at two different loading conditions are plotted, with open (~3bar) and filled (~10bar) symbols, respectively.

A comparison of our scaled MC and atomistic MD diffusivities for the fifteen model systems is shown in Figure 5.9. We find that the scaled lattice MC diffusivities are strongly and nearly perfectly linearly correlated with the MD diffusivities. These trends hold over a variety of MOF topologies (cubic, RHO, SOD, GME) and functionalities. As such, restricting our lattice MC simulations to utilize only simple nearest neighbor single-particle moves, it is possible to map MC dynamics to real dynamics and thus employ our lattice model to estimate transport properties. It is, however, important to note that the lattice model simulation fails to reproduce the *loading dependence* of the self-diffusivities. Generally, with increasing loading amount, our MD simulations show that diffusivity first increases (due to saturation of strong adsorption sites) and then decreases with continued loading (due to crowding). We find that this steric crowding is overemphasized in the lattice MC simulations, likely due to the omission of collective adsorbate moves. As a consequence, the MC diffusivity reaches maximum at much lower densities than

the MD situations, and the map between the MC dynamics and real dynamics is therefore necessarily loading-dependent (as it is shown in Figure 5.9). It is possible that inclusion of carefully crafted many-particle MC moves may restore the correct loading dependence, but at the expense of a more complicated lattice MC simulation protocol. Nonetheless, when screening for a particular application, the approximate working conditions are typically known, determining a relevant "working pressure". Since the observed correlation holds across materials at any given fixed pressure, the loading-dependence of the correlation should therefore not present a significant restriction.

5.4 Conclusions

We have developed a new simulation method based on a hierarchically constructed lattice model, exact in the low-pressure limit. In conjunction with appropriately coarse-grained guest-guest interactions, we demonstrate that this model offers semi-quantitative to quantitative agreement as compared to atomistic GCMC simulation from low pressure through saturation. We also show that appropriate and accurate coarse grained potentials can be derived in a systematic manner via standard force matching techniques. Crucially, this lattice approach offers significant two to three orders-of-magnitude acceleration as compared to conventional GCMC simulations, and further gains when dealing with full isotherm calculations or polarizable force fields. We also demonstrate the applicability of the resulting lattice model for estimating transport properties via calibration against fully atomistic MD simulations. This calibration is necessary because dynamic properties are not rigorously derivable from equilibrium considerations. Nonetheless, we find that many dynamical *trends* survive this discretization process, thus also facilitating efficient screening of transport properties via our lattice model. Although our example applications focused on CO_2 adsorption in MOFs, this algorithm is readily generalizable to various nano-porous materials (MOFs, zeolites…) and guest adsorbates (CO_2, H_2, hydrocarbons).

Bibliography

1.   Li, J. R.; Kuppler, R. J.; Zhou, H. C., Selective gas adsorption and separation in metal-organic frameworks. *Chem Soc Rev* **2009,** 38, (5), 1477-1504.

2.   Ma, S. Q.; Zhou, H. C., Gas storage in porous metal-organic frameworks for clean energy applications. *Chem Commun* **2010,** 46, (1), 44-53.

3.   Banerjee, R.; Phan, A.; Wang, B.; Knobler, C.; Furukawa, H.; O'Keeffe, M.; Yaghi, O. M., High-throughput synthesis of zeolitic imidazolate frameworks and application to CO_2 capture. *Science* **2008,** 319, (5865), 939-943.

4.   Sumida, K.; Horike, S.; Kaye, S. S.; Herm, Z. R.; Queen, W. L.; Brown, C. M.; Grandjean, F.; Long, G. J.; Dailly, A.; Long, J. R., Hydrogen storage and carbon dioxide capture in an iron-based sodalite-type metal-organic framework (Fe-BTT) discovered via high-throughput methods. *Chem Sci* **2010,** 1, (2), 184-191.

5.   Wilmer, C. E.; Leaf, M.; Lee, C. Y.; Farha, O. K.; Hauser, B. G.; Hupp, J. T.; Snurr, R. Q., Large-scale screening of hypothetical metal-organic frameworks. *Nat Chem* **2012,** 4, (2), 83-89.

6.   Sikora, B. J.; Wilmer, C. E.; Greenfield, M. L.; Snurr, R. Q., Thermodynamic analysis of Xe/Kr selectivity in over 137 000 hypothetical metal-organic frameworks. *Chem Sci* **2012,** 3, (7), 2217-2223.

7.   McDaniel, J. G.; Schmidt, J. R., Robust, Transferable, and Physically Motivated Force Fields for Gas Adsorption in Functionalized Zeolitic Imidazolate Frameworks. *J Phys Chem C* **2012,** 116, (26), 14031-14039.

8.   McDaniel, J. G.; Yu, K.; Schmidt, J. R., Ab Initio, Physically Motivated Force Fields for CO_2 Adsorption in Zeolitic Imidazolate Frameworks. *J Phys Chem C* **2012,** 116, (2), 1892-1903.

9.   Kim, J.; Smit, B., Efficient Monte Carlo Simulations of Gas Molecules Inside Porous Materials. *J Chem Theory Comput* **2012,** 8, (7), 2336-2343.

10.   Kim, J.; Lin, L.; L., M. R.; Swisher, J. A.; Haranczyk, M.; Smit, B., Large-Scale Computational Screening of Zeolites for Ethane/Ethene Separation. *Langmuir* **2012,** 28, (32), 11914-11919.

11.   Pan, D. F.; Mersmann, A., Multilevel Adsorption and Hysteresis in Well-Defined Zeolite Sorbents. *Zeolites* **1990,** 10, (3), 210-212.

12.   Lee, C. K.; Chiang, A. S. T.; Wu, F. Y., Lattice Model for the Adsorption of Benzene in Silicalite-I. *Aiche J* **1992,** 38, (1), 128-135.

13.   Vantassel, P. R.; Davis, H. T.; Mccormick, A. V., New Lattice Model for Adsorption of Small Molecules in Zeolite Micropores. *Aiche J* **1994,** 40, (6), 925-934.

14.   Vantassel, P. R.; Somers, S. A.; Davis, H. T.; McCormick, A. V., Lattice Model And Simulation Of Dynamics Of Adsorbate Motion In Zeolites. *Chemical Engineering Science* **1994,** 49, (17), 2979-2989.

15.   Keffer, D.; McCormick, A. V.; Davis, H. T., Diffusion and percolation on zeolite sorption lattices. *J Phys Chem-Us* **1996,** 100, (3), 967-973.

16.   Saravanan, C.; Auerbach, S. M., Modeling the concentration dependence of diffusion in zeolites .1. Analytical theory for benzene in Na-Y. *J Chem Phys* **1997,** 107, (19), 8120-8131.

17.   Saravanan, C.; Auerbach, S. M., Modeling the concentration dependence of diffusion in zeolites .2. Kinetic Monte Carlo simulations of benzene in Na-Y. *J Chem Phys* **1997,** 107, (19), 8132-8137.

18.   Trout, B. L.; Chakraborty, A. K.; Bell, A. T., Diffusion and reaction in ZSM-5 studied by dynamic Monte Carlo. *Chemical Engineering Science* **1997,** 52, (14), 2265-2276.

19.   Saravanan, C.; Jousse, F.; Auerbach, S. M., Modeling the concentration dependence of diffusion in zeolites. III. Testing mean field theory for benzene in Na-Y with simulation. *J Chem Phys* **1998,** 108, (5), 2162-2169.

20.   Ayappa, K. G.; Kamala, C. R.; Abinandanan, T. A., Mean field lattice model for adsorption isotherms in zeolite NaA. *J Chem Phys* **1999,** 110, (17), 8714-8721.

21.   Narkiewicz-Michalek, J.; Szabelski, P.; Rudzinski, W.; Chiang, A. S. T., Heterogeneous three-site lattice model for adsorption of aromatics in ZSM-5 zeolites: Temperature dependence of adsorption isotherms. *Langmuir* **1999,** 15, (18), 6091-6102.

22.   Maceiras, D. B.; Sholl, D. S., Analysis of binary transport diffusivities and self-diffusivities in a lattice model for silicalite. *Langmuir* **2002,** 18, (20), 7393-7400.

23.   Demontis, P.; Pazzona, F. G.; Suffritti, G. B., Effective interactions in multisite cells for adsorption in microporous materials. *J Chem Phys* **2009,** 130, (16), 164701.

24.   Pazzona, F. G.; Demontis, P.; Suffritti, G. B., From thermodynamic cell models to partitioning cellular automata for diffusion in zeolites. I. Structure of the algorithm. *J Chem Phys* **2009,** 131, (23), 234703.

25.   Pazzona, F. G.; Demontis, P.; Suffritti, G. B., From thermodynamic cell models to partitioning cellular automata for diffusion in zeolites. II. Static and dynamic properties. *J Chem Phys* **2009,** 131, (23), 234704.

26.   June, R. L.; Bell, A. T.; Theodorou, D. N., Transition-State Studies of Xenon and Sf6 Diffusion in Silicalite. *J Phys Chem-Us* **1991,** 95, (22), 8866-8878.

27.   Snurr, R. Q.; Bell, A. T.; Theodorou, D. N., A Hierarchical Atomistic Lattice Simulation Approach for the Prediction of Adsorption Thermodynamics of Benzene in Silicalite. *J Phys Chem-Us* **1994,** 98, (19), 5111-5119.

28.   Snurr, R. Q.; Bell, A. T.; Theodorou, D. N., Investigation of the Dynamics of Benzene in Silicalite Using Transition-State Theory. *J Phys Chem-Us* **1994,** 98, (46), 11948-11961.

29.   Czaplewsi, K. F.; Snurr, R. Q., Hierarchical approach for simulation of binary adsorption in silicalite. *Aiche J* **1999,** 45, (10), 2223-2236.

30.   Jousse, F.; Auerbach, S. M., Activated diffusion of benzene in NaY zeolite: Rate constants from transition state theory with dynamical corrections. *J Chem Phys* **1997,** 107, (22), 9629-9639.

31.   Saravanan, C.; Jousse, F.; Auerbach, S. M., Ising model of diffusion in molecular sieves. *Phys Rev Lett* **1998,** 80, (26), 5754-5757.

32.   Tunca, C.; Ford, D. M., A transition-state theory approach to adsorbate dynamics at arbitrary loadings. *J Chem Phys* **1999,** 111, (6), 2751-2760.

33.   Dubbeldam, D.; Calero, S.; Maesen, T. L. M.; Smit, B., Incommensurate diffusion in confined systems. *Phys Rev Lett* **2003,** 90, (24), 245901.

34.   Tunca, C.; Ford, D. M., A hierarchical approach to the molecular modeling of diffusion and adsorption at nonzero loading in microporous materials. *Chemical Engineering Science* **2003,** 58, (15), 3373-3383.

35.   Tunca, C.; Ford, D. M., Coarse-grained nonequilibrium approach to the molecular modeling of permeation through microporous membranes. *J Chem Phys* **2004,** 120, (22), 10763-10767.

36.   Dubbeldam, D.; Beerdsen, E.; Vlugt, T. J. H.; Smit, B., Molecular simulation of loading-dependent diffusion in nanoporous materials using extended dynamically corrected transition state theory. *J Chem Phys* **2005,** 122, (22), 224712.

37.   Jee, S. E.; Sholl, D. S., Carbon Dioxide and Methane Transport in DDR Zeolite: Insights from Molecular Simulations into Carbon Dioxide Separations in Small Pore Zeolites. *J Am Chem Soc* **2009,** 131, (22), 7896-7904.

38.   June, R. L.; Bell, A. T.; Theodorou, D. N., Prediction of low occupancy sorption of alkanes in silicalite. *The Journal of Physical Chemistry* **1990,** 94, (4), 1508-1516.

39.   Keffer, D.; Gupta, V.; Kim, D.; Lenz, E.; Davis, H. T.; McCormick, A. V., A compendium of potential energy maps of zeolites and molecular sieves. *J Mol Graphics* **1996,** 14, (2), 108-&.

40.   Haldoupis, E.; Nair, S.; Sholl, D. S., Finding MOFs for Highly Selective CO_2/N_2 Adsorption Using Materials Screening Based on Efficient Assignment of Atomic Point Charges. *J Am Chem Soc* **2012,** 134, (9), 4313-4323.

41.   Essmann, U.; Perera, L.; Berkowitz, M. L.; Darden, T.; Lee, H.; Pedersen, L. G., A Smooth Particle Mesh Ewald Method. *J Chem Phys* **1995,** 103, (19), 8577-8593.

42.   Allen, M. P.; Tildesley, D. J., *Computer Simulation of Liquids*. Oxford University Press: New York, 1991.

43.   Press, W. H., *Numerical recipes in C : the art of scientific computing*. 2nd ed.; Cambridge University Press: Cambridge ; New York, 1992; p xxvi, 994 p.

44.   Avendano, C.; Lafitte, T.; Galindo, A.; Adjiman, C. S.; Jackson, G.; Muller, E. A., SAFT-gamma Force Field for the Simulation of Molecular Fluids. 1. A Single-Site Coarse Grained Model of Carbon Dioxide. *J Phys Chem B* **2011,** 115, (38), 11154-11169.

45.   Liu, H. Q.; Silva, C. M.; Macedo, E. A., New equations for tracer diffusion coefficients of solutes in supercritical and liquid solvents based on the Lennard-Jones fluid model. *Ind Eng Chem Res* **1997,** 36, (1), 246-252.

46.   Rappe, A. K.; Casewit, C. J.; Colwell, K. S.; Goddard, W. A.; Skiff, W. M., Uff, a Full Periodic-Table Force-Field for Molecular Mechanics and Molecular-Dynamics Simulations. *J Am Chem Soc* **1992,** 114, (25), 10024-10035.

47.   Harris, J. G.; Yung, K. H., Carbon Dioxides Liquid-Vapor Coexistence Curve and Critical Properties as Predicted by a Simple Molecular-Model. *J Phys Chem-Us* **1995,** 99, (31), 12021-12024.

48.   Babarao, R.; Hu, Z. Q.; Jiang, J. W.; Chempath, S.; Sandler, S. I., Storage and separation of CO_2 and CH_4 in silicalite, C-168 schwarzite, and IRMOF-1: A comparative study from monte carlo simulation. *Langmuir* **2007,** 23, (2), 659-666.

49.   Cracknell, R. F.; Nicholson, D.; Parsonage, N. G.; Evans, H., Rotational Insertion Bias - a Novel Method for Simulating Dense Phases of Structured Particles, with Particular Application to Water. *Mol Phys* **1990,** 71, (5), 931-943.

50.   Clamp, M. E.; Baker, P. G.; Stirling, C. J.; Brass, A., Hybrid Monte-Carlo - an Efficient Algorithm for Condensed Matter Simulation. *J Comput Chem* **1994,** 15, (8), 838-846.

51.   Peng, D.-Y.; Robinson, D. B., A New Two-Constant Equation of State. *Ind Eng Chem Fund* **1976,** 15, (1), 59-64.

52.   Yu, K.; McDaniel, J. G.; Schmidt, J. R., Physically Motivated, Robust, ab Initio Force Fields for CO(2) and N(2). *J Phys Chem B* **2011,** 115, (33), 10054-10063.

53.   Izvekov, S.; Parrinello, M.; Burnham, C. J.; Voth, G. A., Effective force fields for condensed phase systems from ab initio molecular dynamics simulation: A new method for force-matching. *J Chem Phys* **2004,** 120, (23), 10896-10913.

54.   Hess, B.; Kutzner, C.; van der Spoel, D.; Lindahl, E., GROMACS 4: Algorithms for highly efficient, load-balanced, and scalable molecular simulation. *J Chem Theory Comput* **2008,** 4, (3), 435-447.

Chapter 6. Microscopic Origins of Cooperativity in MTV-MOF5 Adsorption and Selectivity

Table of Contents

6.1 Introduction

The number of potential MOF structures dramatically increases if more than two secondary building units (SBUs) are considered. Particular attention has resulting been paid to mixed linker MOFs, which combine a single inorganic SBU with *multiple* types of organic SBUs, to create a single MOF crystal.[1, 2] Such MOFs have been referred to as MIXMOFs[3, 4], MTV-MOFs[5], coordination copolymers[6], or MC-MOFs;[1] henceforth we refer to these compounds simply as mixed MOFs. Such mixed MOFs been synthesized using either co-crystallization of different types of isosteric ligands[5, 7, 8] or post synthetic grafting approaches.[9-13] While the properties of mixed MOFs often interpolate between that of their parent (pure, unmixed) MOFs, they can occasionally exhibit properties that are actually unique and *superior* than those of either parent! For example, the mixed MOF UMCM-1 developed by Magtzer and coworkers exhibits higher surface area than the two respective pure parent MOFs (MOF-5, MOF-177), due to the formation of both micropores and mesopores.[6] Other studies have demonstrated the presence of unique topologies,[14] magnetic,[15] or catalytic[3, 4] properties arising from mixtures of various organic or inorganic components.

Several recent studies have focused on the gas adsorption behavior of mixed MOFs. Chun *et al.* investigated the functionalization of the important mixed "paddle-wheel" $Zn_2(1,4\text{-bdc})_2\text{-(dabco)}$ MOF,[16] demonstrating that the H_2 loading capacity of a ternary mixture system is higher than either of the two possible binary ligand MOFs (the dabco linker concentration is fixed). Note, however, that this enhancement was only found in a certain pressure range and therefore is likely due to the competing effects of higher surface area and higher free volume. In a related study, Yaghi and coworkers

systematically synthesized a series of mixed MOFs based on the well-studied MOF-5 system, with up to eight types of linkers (termed MTV-MOF-5).[5] They studied the gas adsorption (CO_2, H_2) capabilities of a subset of these systems, and identified a ternary system with H_2 loading capacity significantly enhanced as compared to the corresponding binary systems. In contrast to the previously mentioned work of Chun et al.[16], this enhancement is observed over the whole pressure range studied, and the magnitude of this enhancement is much more significant. These prior experimental studies clearly demonstrate that the presence of multiple, mixed ligands may lead to cooperative or "synergistic" interactions that yield unique (and potentially superior) physical or chemical properties, further illustrating the potential advantages for mixed MOFs in the area of gas adsorption and separation.

The primary motivation for the present work is an understanding of both the underlying microscopic mechanism and generality of this synergistic effect, focusing specifically on the MTV-MOF-5 systems. In the previous four chapters of this thesis, several general simulation techniques have been developed to study the MOF gas adsorption problem. We constructed force fields based on rigorous *ab initio* energy decompositions, with physically-motivated fitting functional forms (SYM/ZIFFF).[17-19] Also, new lattice-model based simulation algorithms[20] are developed, accelerating the normal GCMC simulations by two to three orders of magnitude, while retaining comparable accuracy. More importantly, facilitated by the new simulation algorithm, we are able to utilize the polarizable SYM/ZIFFF force field in the large scale screening. In this chapter, we exploit both the superior property of our force field over all other empirical potentials, and the speed advantage of computer simulations over experiments. We demonstrate that our methods provide a straightforward way to both understand the physical origin of the synergistic effects, and help identifying the most promising synergistic MOF systems for CO_2 and H_2 adsorption. Furthermore, we conclude that such cooperativity could be a fairly general phenomenon, and suggest some design guidelines that could be exploited to synthesize synergisitically-enhanced mixed MOFs.

6.2 Methods and Computational Details

6.2.1 H_2 Force Field and Nuclear Quantum Correction

Our molecular simulations rely on accurate inter-atomic potentials to describe the interaction of the adsorbates(s) and MOF. We previously developed a protocol for generating accurate, "physically-motivated", parameter-free force fields from ab inito symmetry-adapted perturbation theory (SAPT) calculations. We then applied this procedure to derive accurate force field for gas adsorption (CO_2, N_2) in MOFs. Before starting any simulations, a H_2 model was developed following the same philosophy, so the H_2 adsorption data from Yaghi and coworkers' experiment[5] could be reproduced. The details of this new H_2 force field will not be discussed in this thesis; a more complete description can be found in reference 21.

Due to the small mass of H_2, quantum effects make an important contribution at low temperature. In this chapter, all the low temperature (77K) simulations are conducted in conjunction with a semi-classical Feynman-Hibbs correction.[22] The Feynman-Hibbs potential is an effective pair potential, generated from a classical pair potential, that when used in place of the original potential in classical expressions for thermodynamic quantities, gives variationally optimized quantities with respect to the exact quantum mechanical result. The form of the (second order) Feynman-Hibbs effective pair potential is

$$U^{FH}(r_{ij}) = U(r_{ij}) + \frac{\beta\hbar^2}{24m_r}\left[\frac{\partial^2 U(r_{ij})}{\partial r_{ij}^2} + \frac{2}{r_{ij}}\frac{\partial U(r_{ij})}{\partial r_{ij}}\right] \tag{6.1}$$

While this Feynman-Hibbs effective potential is only rigorously derived for non-rigid bodies, we employ this formula for our H_2 model as discussed in the supporting information of reference 21.

6.2.2 Lattice Model Parameters

Previously, we developed a lattice simulation method to accelerate calculations of gas loading isotherms for rigid porous materials. This approach derives a coarse-grained lattice model from an

underlying atomistic one using rigorous statistical mechanics principles, yielding nearly quantitative isotherms from the low pressure limit through saturation, with orders of magnitude efficiency over the original atomistic model;[20] this lattice approach is employed for all isotherm calculations in this work unless stated otherwise. For all the MTV-MOF-5 lattice simulations, the PME grid size is set to 120 for all three dimensions, and the simulation grid size is set to 60. The electrostatic and dispersion real space cutoff are set to 5.0 and 7.5Å, respectively. For each grid, the maximum sampling size is 2000, and the relative and absolute Boltzmann factor error thresholds are 5% and 3.0, respectively. The empirical single-site CO_2 adsorbate-adsorbate potential is the same as that used in reference 20. For H_2, we employ the single-site Lennard-Jones potential from the work of Darkrim *et al.*[23].

6.2.3 MTV-MOF-5 Structures

The mixed ligand MOF-5 structures (MTV-MOF-5) are constructed on the basis of the 2×2×2 supercell of the original MOF-5, which includes 192 benzene dicarboxylate ligands in total. We study five of the functionalized ligands from Yaghi's previous work;[5] following Yaghi's notation, they are labeled as A, E, G, H, and I, respectively (see Figure 6.1). As stated in Yaghi's paper, the positions of the functional groups are disordered (and thus not resolvable from the crystal structure),[5] and we model these structures accordingly. To model the disorder phases of MTV-MOF-5, ligands A in the MOF-5 supercell are randomly substituted with the other four functionalized ligands. Distance checks are performed between each pair of functional group atoms to eliminate configurations with overlapping side chains. We further relax any side chain positions via MD simulations at 300K using the GROMACS software[24, 25] and the OPLS-AA force field,[26] keeping the metal clusters and all the backbone benzene atoms fixed. The resulting structures are then utilized in the following atomistic and lattice Monte Carlo simulations.
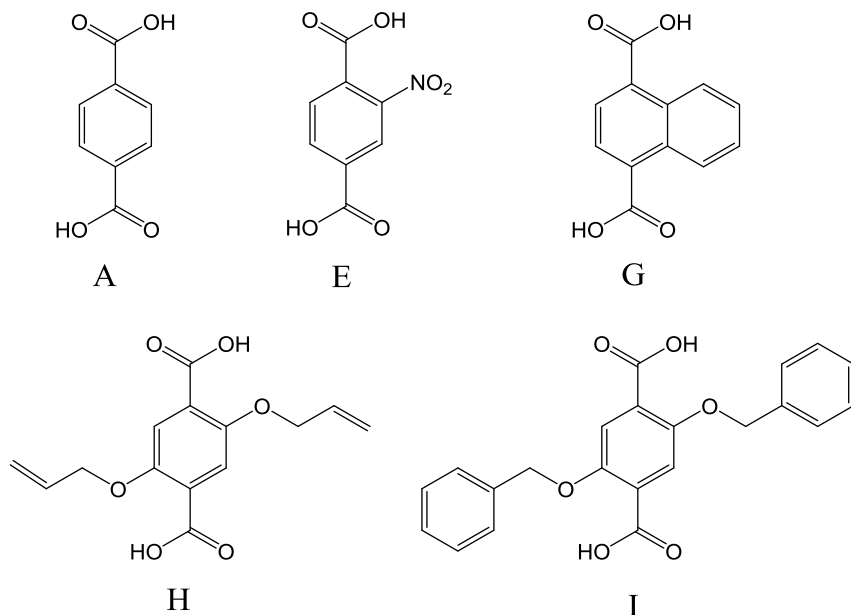
Figure 6.1. MTV-MOF-5 functionalized ligands studied in this work.

Models for *ordered* phases of ternary ligand mixtures (*vide infra*) are created on the basis of the MOF-5 unitcell and are replicated eight times to form a 2×2×2 supercell. In all cases, the structures contain an equal number of three types of ligands, and all ligands of the same type are aligned with the same orientation. For example, in MOF5-AGH, all A are aligned with the x-axis, all G are aligned with the y-axis and all H are aligned with the z-axis. For each functionalized ligand (E, G, H, and I), there are at most four different positions for the functional side chains, an uncertainty that leads to more than one ordered structure. To (partially) remove this ambiguity, we constrain the resulting final structure to maintain all the translational symmetries of the original MOF-5 unitcell. Even with this constraint, however, there is still a vast possible number (about a few thousands) of structures to explore; we study only a small subset of these ordered structures as a proof of principle.

6.3 Results and Discussions

6.3.1 Experimental MTV-MOF-5 Isotherms

We validate our general methodology against the prior experimental CO_2 and H_2 MTV-MOF adsorption isotherms of Yaghi and coworkers,[5] using both atomistic GCMC simulation and lattice simulation. The results are plotted in Figure 6.2 and Figure 6.3, for CO_2 and H_2, respectively. We calculate H_2 adsorption isotherms (77K) for MOF-5, MOF-5-AH, MOF-5-AI, and MOF-5-AHI. Both the atomistic and lattice simulations reproduce the experimental data with high fidelity, validating the force field, the application of the Feynman-Hibbs effective potential, as well as the reconstructions of the MTV-MOF-5 crystal structures. Due to the quantitative agreement between lattice and atomistic simulations, we use the former for all subsequent calculations.
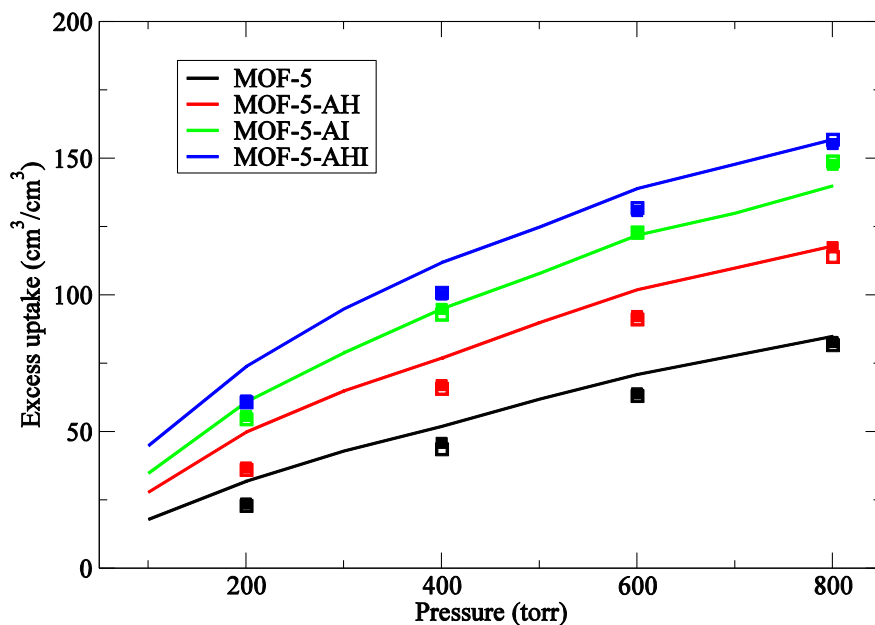
Figure 6.2. H_2 loading isotherms at 77K compared to experimental results of Yaghi and coworkers. Solid lines are experimental values, filled squares are GCMC simulation data and open squares are lattice simulation results.
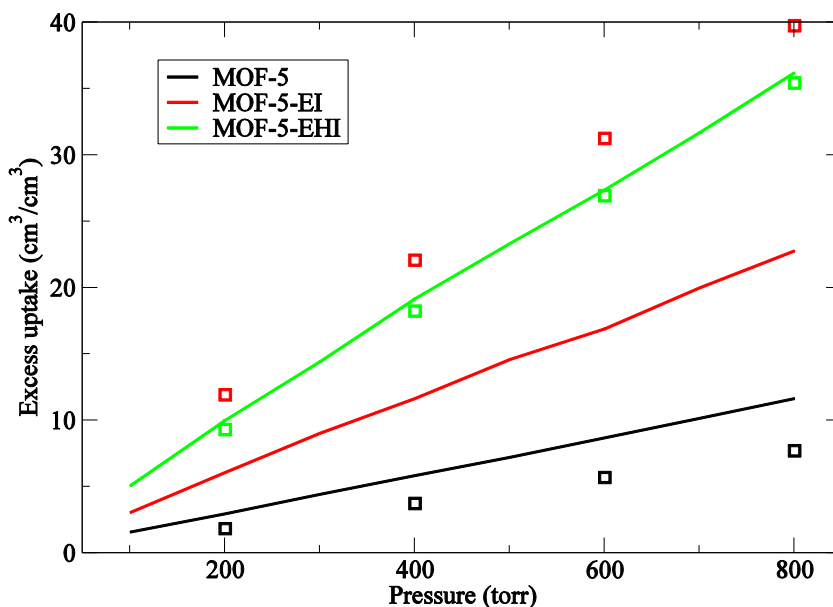
Figure 6.3. CO$_2$ loading isotherms compared to experimental results of Yaghi and coworkers. Solid lines are experimental values, open squares are lattice simulation results.

   As shown in Figure 6.3, there is also good agreement between the experimental and simulated CO$_2$ adsorption isotherms for MOF-5 and MOF-5-EHI. However, there is significant discrepancy between the simulated and experimental isotherms for MOF-5-EI, in which the simulation results are almost 100% higher than the experimental values. We note that the experimental MOF-5-EI contains a high percentage (about 80%) of ligand I, which has two bulky benzene rings on its side chains. Therefore, it is possible that these large side chains aggregate via dispersion interactions and block some channels, making part of the crystal space inaccessible to the gas molecules. In order to test this hypothesis, we analyzed the channel dimensionality of our generated MOF-5-EI structures using the Zeo++ suite of codes.[27, 28] Assuming the probe radius to be 1.5Å (consistent with the kinetic diameter of CO$_2$), we find that depending on the structure details, the channels are either one or two dimensional, rather than three dimensional – indicative of pore blocking. This pore blocking presumably reduces the experimental gas uptake of structures with high concentration of I by hindering the entrance of the gas, and we expect this effect would be even more prominent in the pure MTV-MOF5-I structure. No pore blocking was

considered in our Monte Carlo simulations, where gas molecules can be readily inserted even into inaccessible pores, thus explaining the significant deviation between experiment and theory. This also illustrates the advantage of employing an accurate and robust force field such as "ZIF FF" which has been shown to reproduce experimental gas adsorption isotherms in numerous systems.[18, 19] Without an accurate force field, it is difficult to decouple factors such as pore blocking from errors in the force field, and indeed generic force fields such as UFF have been found to overpredict gas adsorption by greater than 100%.[29-31]

6.3.2 Definition of Synergistic Effects

It is important to precisely define the concept of a synergistic effect so that the magnitude of any such observed cooperativity can be quantified. One possible definition of a synergistic effect would be "Any effect that enhances the performance of a compound composed of mixed ligands relative to all corresponding pure parent structures." Although this definition is practical, and relevant to corresponding synthetic efforts aimed at optimizing gas sorption, it does not admit a simple way to *quantify* the magnitude of the cooperativity.

Microscopically, we anticipate that synergistically-enhanced adsorption must be due to favorable simultaneous interactions between the gas molecules and multiple ligands of different types, thus requiring multiple simultaneous contacts between the solute and the framework side chains. In contrast, the idealized (non-synergistic) system should have completely isolated ligands, so that the gas molecules interact with one ligand at a time. In the latter situation, at low pressure (i.e. neglecting the adsorbate-adsorbate interactions), the change in the loading amount with increasing functionalization should be a simple summation of local contributions from all the isolated ligands. Therefore, for idealized mixed MTV-MOF-5 systems, we can extrapolate the loading capacity using a simple linear equation:

$$N_a(n_X, n_Y, n_Z, \cdots) = N_a(X) + \alpha_Y n_Y + \alpha_Z n_Z + \cdots \tag{6.2}$$

Here N_a is the uptake of a particular system, and n_X, n_Y, n_Z are the number of ligands X, Y and Z, whose summation equals n_{tot} the total number of ligands in the supercell. In words, we start from the uptake of a reference pure ligand structure $N_a(X)$ (X is typically ligand A, and sometimes E), and add up contributions from replacing some number of X with Y or Z. The variables α_Y and α_Z represent the uptake enhancement per ligand substitution, and are computed from the initial slope of uptake vs. composition fraction of binary mixtures (XY, XZ…).

Any significant deviations from this linear extrapolation are defined as a synergistic effect. The magnitude of such an effect can be quantified by percentage difference between actual simulation gas uptake and the idealized extrapolated value. Note that even though the mathematical definition is well defined and also physical, it is also much looser than the practical definition. Even if a mixture is better than the linear extrapolation, it does not guarantee that it would outperform all the pure ligand structures. However, the mathematical definition does represent the right physics that must be satisfied for any practical useful synergistic effects. Therefore, in this study, we will discuss synergistic effects from both perspectives.

6.3.3 Synergistic Effects for H_2–MTV-MOF-5 Systems

We initially investigate H_2 loading capacities at 77K and 800 torr for three ternary mixtures: AHI, AGH and EHI. For AHI and AGH, the extrapolations are performed using pure A (MOF-5) loading as reference, and for EHI, pure E loading is used as a reference.

We first calculate the H_2 uptakes for a series of corresponding binary mixtures (AH, AI, AG, EH, EI) with different composition ratio. The results are plotted in Figure 6.4 and are fit to straight lines, from which the necessary slope parameters used in the future linear extrapolations are computed. For most systems, the linear relationship between the loading capacities and mixture compositions holds extraordinarily well, indicating idealized behavior and no cooperative effects. For two systems involving

ligand I (AI and EI), we can observe significant *anti*-synergistic effects in the I-rich end, meaning that the simulated loadings are lower than the extrapolated ones. Noting that I is the largest of the five ligands, it is possible that the side chains of ligand I aggregate and pack together, significantly reducing the total surface area. For all the ternary mixtures we studied, the ligand I concentrations are all located in the linear region (below 33%), and thus this anti-synergistic effect is not considered in the ternary system extrapolations.

For each of the three ternary mixture systems, we tested various composition ratios; detailed loading data can be found in Table 6.1. For most of the ternary systems, including the AHI system examined by Yaghi and coworkers, the simulated loadings agree with the extrapolation within 1%, showing no synergistic effects. Thus our data suggests that the particular apparent synergistic effect observed in Reference 5 is actually due to the increasing functional group concentrations, rather than true cooperative interactions between ligands. The remaining systems actually show *anti*-synergistic effects, due to similar reasons as in the binary systems.

AHI Ternary Mixture	Number of A	Number of I	Number of H	Simulation (mol/L)	Extrap (mol/L)	Syn (%)
	120	24	48	6.11	6.19	-1.3
	120	48	24	6.62	6.91	-4.2
	96	48	48	6.92	7.47	-7.4
	72	60	60	7.50	8.40	-10.7

EHI Ternary Mixture	Number of E	Number of H	Number of I	Simulation (mol/L)	Extrap (mol/L)	Syn (%)
	144	24	24	6.22	6.18	0.8
	120	24	48	7.10	7.16	-0.8
	120	48	24	6.57	6.58	-0.1
	96	48	48	7.16	7.56	-5.3
	82	55	55	7.47	7.96	-6.2
	72	60	60	7.65	8.25	-7.3
	62	65	65	7.72	8.54	-9.6
	52	70	70	7.77	8.83	-12.0
	64	64	64	8.43	8.48	-0.6

AGH Ternary Mixture	Number of A	Number of G	Number of H	Simulation (mol/L)	Extrap (mol/L)	Syn (%)
	144	24	24	4.60	4.58	0.4
	120	24	48	5.13	5.14	-0.1
	120	48	24	4.90	4.86	0.7
	96	48	48	5.47	5.43	0.9
	72	60	60	5.92	5.85	1.2
	64	64	64	6.04	5.99	0.9

Table 6.1. Simulated and extrapolated H_2 loading capacities for the ternary mixtures.
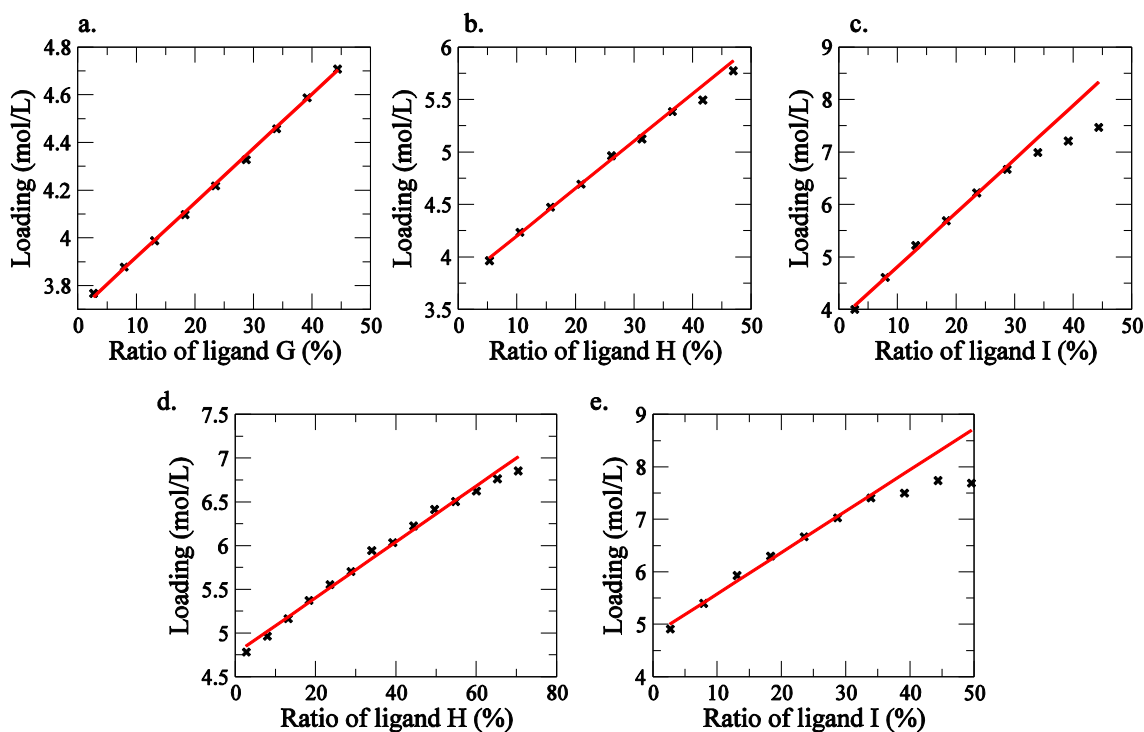
Figure 6.4. H$_2$ loading capacities for binary mixture MTV-MOF-5 systems: a) AG mixture, b) AH mixture, c) AI mixture, d) EH mixture, e) EI mixture. Black crosses are simulated data and the red solid lines are the linear fits.

The anti-synergistic effect observed in the I-containing binary mixtures indicates that the H$_2$ loading capacities of MTV-MOF-5 are mainly determined by surface area. As expected, this implies that the interactions between H$_2$ and the framework are essentially localized and non-specific, probably due to the small size and the neutral characteristics of H$_2$ molecule. As per our working hypothesis, cooperative interaction may happen only when the gas molecule can interact with more than one ligand simultaneously, which is unlikely in the H$_2$ case.

6.3.4 Synergistic Effects for CO$_2$ – Pure Compounds and Binary Mixtures

We further examined CO$_2$ adsorption in MTV-MOF-5 series. CO$_2$ is a slightly larger molecule with also larger quadrupole moment, with both factors contributing towards the possibility of simultaneous interaction with multiple linker groups. As a baseline, we calculated the loading capacities for the four

pure ligand compounds (A, E, G, H). Pure MTV-MOF-5-I is omitted since it suffers from pore blocking and its structure is extremely difficult to generate, due to the ligands' steric bulk. In the following analysis, we use the EI system with the experimental ratio (~80% of I) to represent the system with a high concentration of I, and both experimental and simulated results are reported for comparison. All the CO_2 loading data are calculated at 298K and 800 torr; the single component data are summarized in Table 6.2.

We subsequently calculated the loading capacities for all the relevant binary compounds (AE, AG, AH, AI) to obtain the necessary coefficients used in the ternary extrapolations. Results for various composition fractions are shown in Figure 6.5.
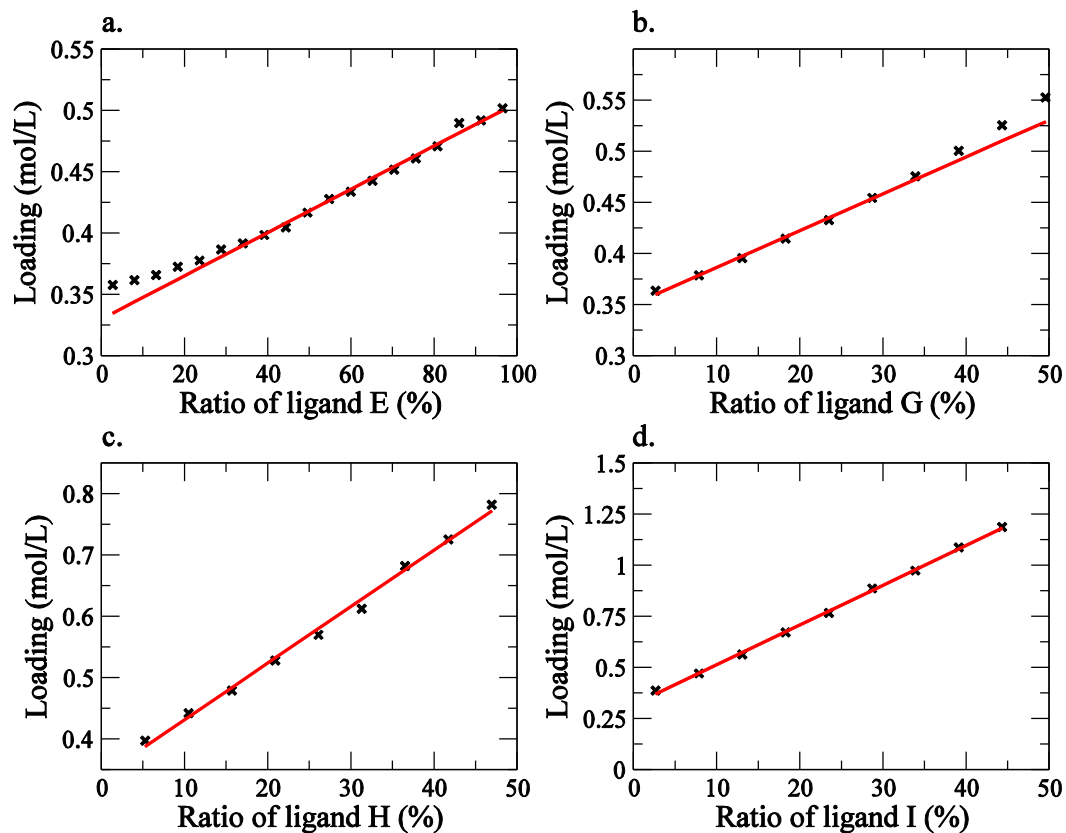
Figure 6.5. CO_2 loading capacities for binary mixture MTV-MOF-5 systems: a) AE mixture, b) AG mixture, c) AH mixture, d) AI mixture. Black crosses are simulated data and the red solid lines are the linear fits. Note, instead of fitting the initial slope (the infinite dilute region), we interpolate the part of the curve that correspond to the composition ratio in the ternary compounds. As it is discussed in the text, by

using this fitting (at finite functional group concentration) in the ternary mixture extrapolation we separate the self-synergistic effect from the true heterogeneous ternary synergistic effect.

Similar to H_2, most of the binary results for CO_2 can be fit to straight lines very well, indicating that in most of the concentration regions of concern, no synergistic effects are observed for binary mixtures. However, for particular systems like AE and AG, some non-linear behavior can be observed, and these curves are convex instead of concave, indicating a positive, self-synergistic effect. We hypothesize that this effect arises due to cooperative interactions between two functional groups of the *same* type. Even though this effect is not observed in the AH systems we studied (with H ratio smaller than 50%), we find that the uptake of pure H system is 11% higher than the linear extrapolation. Therefore the self-synergistic effect also exists in AH systems, in the region with high H concentration, specifically showing that the self-synergistic effect is a very common phenomenon that exists in many different systems.

Physically, the self-synergistic effect comes from the cooperative interactions between two ligands of the same type, creating a non-linear performance improvement. However, this phenomenon is not very useful in practice because, for a convex curve, the best performance always occurs at the one of the ends, corresponding to a pure parent compound rather than a mixture. While studying the ternary mixtures, this self-synergistic effect should be taken into account, so that only cooperative interactions between different types of ligands are considered. Therefore, a slight modification is made to the linear extrapolation scheme (equation (6.2)): instead of using the initial slopes (α_Y, α_Z) to evaluate the enhancement contribution from ligand Y and Z ($\alpha_Y n_Y$, $\alpha_Z n_Z$), we directly use the enhancement from the binary mixture simulations ($\Delta N_a(n_Y)$, $\Delta N_a(n_Z)$):

$$
\begin{aligned}
N_a(n_X, n_Y, n_Z, \cdots) &= N_a(X) + \Delta N_a(n_Y) + \Delta N_a(n_Z) + \cdots \\
\Delta N_a(n_Y) &= N_a(n_{tot} - n_Y, n_Y) - N_a(X) \\
\Delta N_a(n_Z) &= N_a(n_{tot} - n_Z, n_Z) - N_a(X)
\end{aligned}
\tag{6.3}
$$

The uptakes of binary mixtures $N_a(n_{tot} - n_Y, n_Y)$ and $N_a(n_{tot} - n_Z, n_Z)$ are linearly interpolated using the adsorption data in the corresponding region (see the red solid lines in Figure 6.5).

We also examined the uncertainties of the uptakes caused by the disordered nature of the structures, using the EI binary system as an example. For fixed ligand composition ratios, five different disorder structures were generated randomly and their loading capacities were calculated. Depending on the detailed positions of the functional groups, we observe approximately 3% of fluctuation in uptakes, which corresponds to the uncertainty in all our calculations. Therefore, in the following analysis, we define the synergistic effect only when it is larger than twice this uncertainty (6%).

6.3.5 Synergistic Effects for CO_2 – Ternary Mixtures

We start our examination of ternary mixtures from MTV-MOF-5-EHI, since Yaghi and coworkers showed that this system has synergistic effects on CO_2/CO *selectivity*. Here, for mathematical simplicity, we only focus on the CO_2 adsorption *capacity*. As shown in Table 6.2, we explore various composition ratios for the EHI systems, and all of the simulated results agree with the extrapolation within 5%, indicating no synergistic effect. Furthermore, we extended our scope and studied all the possible equal-molar ternary mixtures with the five ligands included in this work. As summarized in Table 6.2, half of the systems do not show synergistic effects, while the others (AGH, AIH, HGE, IGE and IHG) perform better than extrapolation by more than 6%.

	Number of A	Number of E	Number of G	Number of H	Number of I	simulation (mol/L)	extrapolation (mol/L)	Syn (%)
Single component	192	-	-	-	-	0.35	-	-
	-	192	-	-	-	0.51	-	-
	-	-	192	-	-	0.90	-	-
	-	-	-	192	-	1.41	-	-
	-	32	-	-	160	1.79 (1.04)a		
EHI	-	144	-	24	24	0.81	0.82	-1.2
	-	120	-	24	48	1.05	1.04	0.3
	-	120	-	48	24	0.92	0.91	0.1
	-	96	-	48	48	1.10	1.14	-2.7
	-	82	-	55	55	1.21	1.23	-1.3
	-	72	-	60	60	1.33	1.29	3.1
	-	72	-	60	60	1.27	1.29	-1.9
	-	72	-	60	60	1.27	1.29	-1.9
	-	72	-	60	60	1.26	1.29	-2.1
	-	72	-	60	60	1.23	1.29	-5.0
	-	62	-	65	65	1.34	1.36	-1.1
	-	52	-	70	70	1.43	1.42	0.5
AGE	64	64	64	-	-	0.52	0.51	0.7
AGH	64	-	64	64	-	0.88	0.77	13.7
AHE	64	64	-	64	-	0.70	0.70	1.0
AIE	64	64	-	-	64	1.03	1.04	-0.6
AIG	64	-	64	-	64	1.18	1.11	6.0
AIH	64	-	-	64	64	1.38	1.29	6.9
HGE	-	64	64	64	-	0.90	0.82	9.1
IGE	-	64	64	-	64	1.24	1.16	7.0
IHE	-	64	-	64	64	1.30	1.34	-3.5
IHG	-	-	64	64	64	1.57	1.42	10.7

Table 6.2. Synergistic effect search for disorder phase ternary mixtures. a) The experimental value is reported in the parenthesis as a comparison, note it is much lower than the simulated value due to the pore blocking effect discussed above.

It is worth noting that ligands H, G and I are involved in four of the synergistic systems, while E and A are only involved in two. Therefore, it is evident that in this particular case, larger ligands (with greater dispersion interactions) are more likely to produce synergistic effects, while smaller ligands and charged groups are less important. This finding is in contrast to the finding that the synergistic effect in the nitro functionalized SOD ZIF was due to mainly electrostatic interactions, with the small, highly charged nitro group (details of the study about the SOD ZIF synergistic effects can be found in reference 21).

Therefore, it is evident that among different MOF topologies, there could be different sources of cooperative ligand effects that may enhance gas uptake. The MOF-5 topology is characterized by relatively large apertures and pore volume compared to the ZIF-8 topology (~11 Å compared to 3.5Å aperture size and ~80% compared to 60% free volume respectively), and therefore larger, bulkier functional groups are required to create cooperative local interactions with adsorbed gas molecules. For functionalized ZIF-8 systems, smaller functional groups will already be in close proximity to each other due to the topology, and therefore strongly interacting small functional groups such as nitro groups will most likely create synergistic effects.

Even though the synergistic effects are observable in these ternary systems, the magnitudes of the effects are still small, especially considering the 3% uncertainty due to the structure variations. From the perspective of entropy, it is essentially difficult to find prominent synergistic effects in disordered phases: since the number of favored adsorption configurations is likely much fewer than the disfavored (or neutral) ones, any loading enhancements from the favored sites would be diminished by the other disfavored sites. In an ordered phase, however, all the local effects are magnified compared to the disorder phase, due to the symmetry of the unitcell. Although such ordered phases may be difficult to access synthetically (at least for the MTV-MOF series, although perhaps possible due to steric effects, long range electrostatic ligand-ligand interaction…), we examine such phases to investigate the potential limits of cooperativity.

6.3.6 Synergistic Effects for CO_2 – Order Phases

For each of the five synergistic ternary systems, we investigated three different ordered structures, the results of which are summarized in Table 6.3.

	sim (mol/L)	extrap (mol/L)	syn (%)
	0.90	0.77	17.2
AGH	0.89	0.77	16.0
	0.89	0.77	15.0
	1.58	1.29	22.1
AIH	1.58	1.29	22.3
	1.40	1.29	8.6
	0.94	0.82	14.5
HGE	0.94	0.82	14.1
	0.98	0.82	18.8
	1.27	1.16	8.9
IGE	1.26	1.16	8.3
	1.15	1.16	-1.0
	1.51	1.42	6.5
IHG	1.88	1.42	32.3
	1.88	1.42	32.7
EHI	1.61	1.34	19.9

Table 6.3. Synergistic effects of the order phases of the ternary systems.

As shown, the observed synergistic effects in the ordered phases are much stronger than the disorder phases, consistent with our previous hypothesis. The strongest synergistic effects, which are observed in IHG system (for the structure see Figure 6.6), are over 30%, and most of the other systems also show over 10% of a synergistic effect. Note that we have examined only a small subset of the possible arrangements and compositions of these ordered phases, and we anticipate that even superior structures may exist! We also examine the "ordered" analogue of the EHI system investigated by Yaghi and cowokers. Here we find that the uptake of is enhanced by 20% compared to the extrapolation and its disorder counterpart. Hence, the synergistic effects are even more general in ordered phases compared to disordered phases.
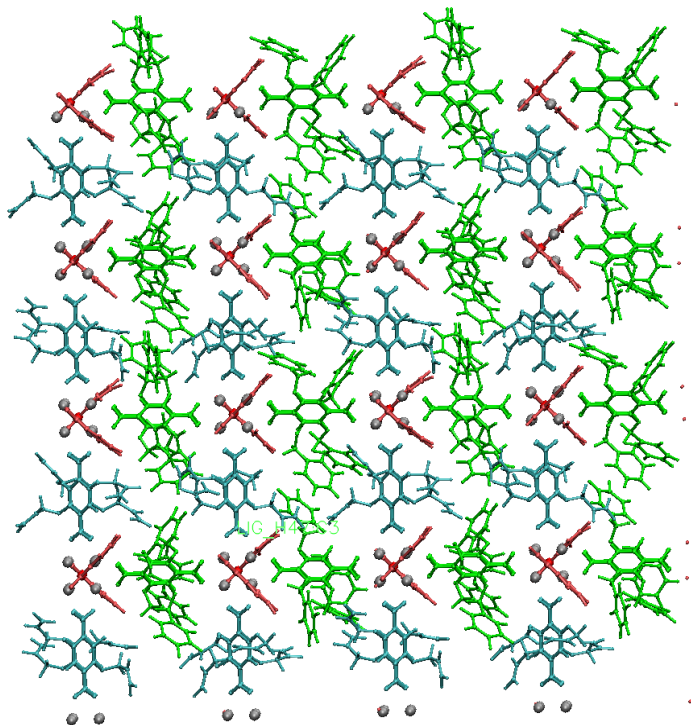
Figure 6.6. Supercell of the order phase of the IHG ternary mixture. Ligand I is shown in green, ligand H in cyan, and ligand G in red.

More practically, the loading capacity of the IHG order phase is 1.88 mol/L, much higher than the loadings of pure H and G systems. This loading capacity is also higher than the loading capacity of EI (1.79 mol/L), which contains more than 80% of ligand I. Due to the pore blocking effect, the EI (or pure I) system has even lower loading capacities experimentally. As such, the ordered phase of IHG mixture presents an actual example of a mixed-ligand system outperforming all of its pure parent compounds.

We analyzed the channel dimensionality of the IHG systems and found no evidence for pore blocking in either the ordered or disordered crystal structures (except for one of the ordered phases, which is a special case as the G linkers are pointed towards the same pore), and therefore expect that any future experimental adsorption isotherms should be close to our predictions. This is significant, as these IHG systems (both ordered and disordered) exhibit higher CO_2 uptake than any previously reported MTV-MOF-5 system.

While these ordered MTV-MOFs may not be easily accessible synthetically, other ordered mixed MOFs have already synthesized. For example, the Zn_2(1,4-bdc)$_2$-(dabco) MOFs (and varients thereof)[16], consist of two dimensional layers of Zn_2 paddle-wheel units bridged by the 1,4-bdc linkers, with the dabco linkers coordinating the "top and bottom" of the Zn_2 units to connect these layers and complete the three dimensional structure. As such, the conclusions drawn from our study of ordered phase MTV-MOFs are directly relevant to such systems.

6.4 Conclusions

In this work, we use computer simulations to systematically study the synergistic effects for the MTV-MOF-5 systems synthesized in Yaghi's group. We focus on the cooperative effect on the MOF for the H_2 and CO_2 loading capacities. Five isosteric ligands used in Yaghi's experiments are investigated in this paper.

For H_2, the loading amounts of three different ternary mixtures with various composition ratios are calculated and no significant cooperative enhancements are found. Instead, high concentration of large functional groups introduces anti-synergistic effects due to the aggregation of the ligand side chains, reducing the surface area of the system. The previous synergistic effect claimed by Yaghi's group is due to the increment of functional group concentration in the system, which is not related to the cooperative behavior of different ligands.

On the other hand, a thorough search identifies five ternary mixture systems showing significant synergistic effect for CO_2 adsorption capacity. Most of these synergistic systems are composed of ligands with bulky side chains, indicating that the observed synergistic effect is due to the cooperative dispersion interactions. The fact that synergistic effects are more general for CO_2 compared to H_2 also illustrates the importance of the guest molecule size, as larger gas molecules are more likely to simultaneously interact with more than one ligand. This factor is expected to be even more important for topologies with larger pores or for ligands with smaller side chains.

Further studies find that the synergistic effect is even more general and significant in the ordered phases of MTV-MOF-5. The ordered phase enhances the loading performance by maintaining the favorable adsorption sites across the whole crystal, while the disordered phase diminishes it by introducing large amount of neutral or even disfavored sites. Hence, it is better to synthesize the mixed ligand structure whilst paying attention to the microscopic details of the adsorption sites, rather than simply adoopting a random mixing scheme. It is of particular note that the ordered phase of the IHG system shows both the highest percentage synergistic enhancement and the highest performance out of all of the corresponding pure ligand structures. The results from the IHG system illustrate the importance of exploiting synergistic effects in the mixed ligand systems, especially when the pure ligand compounds suffer from pore blocking issues arising from high concentration of large functional groups.

In summary, through a study of MTV-MOF-5, we find several hypothetical mixed-ligand systems that display both strong and experimentally useful synergistic effects. We identify several factors that may affect the magnitude and generality of the synergistic effects: the size of the guest molecules, the topology of the MOFs, the size and the interaction characteristics of the functional side chains, and also the order of the functional group positions. Our searching is far from thorough, but these principles provide basic guidelines for future experimental and theoretical studies.

Bibliography

1.   Burrows, A. D., Mixed-component metal-organic frameworks (MC-MOFs): enhancing functionality through solid solution formation and surface modifications. *Crystengcomm* **2011,** 13, (11), 3623-3642.

2.   Bunck, D. N.; Dichtel, W. R., Mixed Linker Strategies for Organic Framework Functionalization. *Chemistry – A European Journal* **2013,** 19, 818-827.

3.   Kleist, W.; Jutz, F.; Maciejewski, M.; Baiker, A., Mixed-Linker Metal-Organic Frameworks as Catalysts for the Synthesis of Propylene Carbonate from Propylene Oxide and CO_2. *Eur J Inorg Chem* **2009**, (24), 3552-3561.

4.   Kleist, W.; Maciejewski, M.; Baiker, A., MOF-5 based mixed-linker metal-organic frameworks: Synthesis, thermal stability and catalytic application. *Thermochim Acta* **2010,** 499, (1-2), 71-78.

5.   Deng, H. X.; Doonan, C. J.; Furukawa, H.; Ferreira, R. B.; Towne, J.; Knobler, C. B.; Wang, B.; Yaghi, O. M., Multiple Functional Groups of Varying Ratios in Metal-Organic Frameworks. *Science* **2010,** 327, (5967), 846-850.

6.   Koh, K.; Wong-Foy, A. G.; Matzger, A. J., A crystalline mesoporous coordination copolymer with high microporosity. *Angew Chem Int Edit* **2008,** 47, (4), 677-680.

7.   Banerjee, R.; Furukawa, H.; Britt, D.; Knobler, C.; O'Keeffe, M.; Yaghi, O. M., Control of Pore Size and Functionality in Isoreticular Zeolitic Imidazolate Frameworks and their Carbon Dioxide Selective Capture Properties. *J Am Chem Soc* **2009,** 131, (11), 3875-3877.

8.   Banerjee, R.; Phan, A.; Wang, B.; Knobler, C.; Furukawa, H.; O'Keeffe, M.; Yaghi, O. M., High-throughput synthesis of zeolitic imidazolate frameworks and application to CO_2 capture. *Science* **2008,** 319, (5865), 939-943.

9.   Burrows, A. D.; Frost, C. G.; Mahon, M. F.; Richardson, C., Post-Synthetic Modification of Tagged Metal-Organic Frameworks. *Angew Chem Int Edit* **2008,** 47, (44), 8482-8486.

10.   Garibay, S. J.; Wang, Z. Q.; Tanabe, K. K.; Cohen, S. M., Postsynthetic Modification: A Versatile Approach Toward Multifunctional Metal-Organic Frameworks. *Inorg Chem* **2009,** 48, (15), 7341-7349.

11.   Kim, M.; Cahill, J. F.; Prather, K. A.; Cohen, S. M., Postsynthetic modification at orthogonal reactive sites on mixed, bifunctional metal-organic frameworks. *Chem. Commun.* **2011,** 47, 7629-7631.

12.   Kim, M.; Cahill, J. F.; Fei, H.; Prather, K. A.; Cohen, S. M., Postsynthetic Ligand and Cation Exchange in Robust Metal–Organic Frameworks. *J. Am. Chem. Soc.* **2012,** 134, (43), 18082-18088.

13.   Taylor-Pashow, K. M. L.; Rocca, J. D.; Xie, Z.; Tran, S.; Lin, W., Postsynthetic Modifications of Iron-Carboxylate Nanoscale Metal−Organic Frameworks for Imaging and Drug Delivery. *J. Am. Chem. Soc.* **2009,** 131, (40), 14261-14263.

14.   Hu, J. S.; Yao, X. Q.; Zhang, M. D.; Qin, L.; Li, Y. Z.; Guo, Z. J.; Zheng, H. G.; Xue, Z. L., Syntheses, Structures, and Characteristics of Four New Metal-Organic Frameworks Based on Flexible Tetrapyridines and Aromatic Polycarboxylate Acids. *Cryst Growth Des* **2012,** 12, (7), 3426-3435.

15.   Zang, S. Q.; Su, Y.; Song, Y.; Li, Y. Z.; Ni, Z. P.; Zhu, H. Z.; Meng, Q. J., Tuning the framework formation of Ni(II) complexes by controlling the hydrolysis of 2,2 ',3,3 '-thiodiphthalic dianhydride: Syntheses, crystal structures, and physical properties. *Cryst Growth Des* **2006,** 6, (10), 2369-2375.

16.   Chun, H.; Dybtsev, D. N.; Kim, H.; Kim, K., Synthesis, X-ray Crystal Structures, and Gas Sorption Properties of Pillared Square Grid Nets Based on Paddle-Wheel Motifs: Implications for Hydrogen Storage in Porous Materials. *Chemistry – A European Journal* **2005,** 11, (12), 3521-3529.

17.   Yu, K.; McDaniel, J. G.; Schmidt, J. R., Physically Motivated, Robust, ab Initio Force Fields for CO(2) and N(2). *J. Phys. Chem. B* **2011,** 115, (33), 10054-63.

18.   McDaniel, J. G.; Schmidt, J. R., Robust, Transferable, and Physically-Motivated Force Fields for Gas Adsorption in Functionalized Zeolitic Imidazolate Frameworks. *J. Phys. Chem. C* **2012,** 116, 14031-14039.

19.   McDaniel, J. G.; Schmidt, J. R., Physically-Motivated Force Fields from Symmetry-Adapted Perturbation Theory. *J. Phys. Chem. A* **2013,** 117, 2053-2066.

20.   Yu, K.; McDaniel, J. G.; Schmidt, J. R., An efficient multi-scale lattice model approach to screening nano-porous adsorbents. *The Journal of Chemical Physics* **2012,** 137, (24), 244102.

21.   Yu, K.; McDaniel, J. G.; Schmidt, J. R., Microscopic Origins of Enhanced Gas Adsorption and Selectivity in Mixed-Linker Metal-Organic Frameworks. *J Phys Chem C, submitted* **2013**.

22.   Feynman, R. P., *Statistical Mechanics: A Set of Lectures*. Westview Press: Boulder, 1998.

23.   Darkrim, F.; Levesque, D., Monte Carlo simulations of hydrogen adsorption in single-walled carbon nanotubes. *J Chem Phys* **1998,** 109, (12), 4981-4984.

24.   Van der Spoel, D.; Lindahl, E.; Hess, B.; Groenhof, G.; Mark, A. E.; Berendsen, H. J. C., GROMACS: Fast, flexible, and free. *J. Comput. Chem.* **2005,** 26, (16), 1701-1718.

25.   Hess, B.; Kutzner, C.; van der Spoel, D.; Lindahl, E., GROMACS 4: Algorithms for highly efficient, load-balanced, and scalable molecular simulation. *J Chem Theory Comput* **2008,** 4, (3), 435-447.

26.   Jorgensen, W. L.; Maxwell, D. S.; TiradoRives, J., Development and testing of the OPLS all-atom force field on conformational energetics and properties of organic liquids. *J Am Chem Soc* **1996,** 118, (45), 11225-11236.

27.   Martin, R. L.; Smit, B.; Haranczyk, M., Addressing Challenges of Identifying Geometrically Diverse Sets of Crystalline Porous Materials. *J Chem Inf Model* **2012,** 52, (2), 308-318.

28.   Willems, T. F.; Rycroft, C.; Kazi, M.; Meza, J. C.; Haranczyk, M., Algorithms and tools for high-throughput geometry-based analysis of crystalline porous materials. *Micropor Mesopor Mat* **2012,** 149, (1), 134-141.

29.   Perez-Pellitero, J.; Amrouche, H.; Siperstein, F. R.; Pirngruber, G.; Nieto-Draghi, C.; Chaplais, G.; Simon-Masseron, A.; Bazer-Bachi, D.; Peralta, D.; Bats, N., Adsorption of CO(2), CH(4), and N(2) on Zeolitic Imidazolate Frameworks: Experiments and Simulations. *Chem. Eur. J.* **2010,** 16, (5), 1560-1571.

30.   McDaniel, J. G.; Yu, K.; Schmidt, J. R., Ab Initio, Physically Motivated Force Fields for CO_2 Adsorption in Zeolitic Imidazolate Frameworks. *J. Phys. Chem. C* **2011,** 116, (2), 1892-1903.

31.   Liu, B.; Smit, B., Molecular Simulation Studies of Separation of CO(2)/N(2), CO(2)/CH(4), and CH(4)/N(2) by ZIFs. *J. Phys. Chem. C* **2010,** 114, (18), 8515-8522.

Chapter 7. Trace Flue Gas Contaminants Effects on Open Metal Sites

Table of Contents

7.1 Introduction

In previous chapters, all the MOF systems we studied interact with the guest molecules via weak physical interactions, mainly through organic linker groups. However, another class of MOFs that incorporate coordinatively unsaturated "open metal" sites (CUS) often exhibit dramatically enhanced uptake of CO_2 at low partial pressures due to increased adsorption enthalpy.[1, 2] These CUS yield steep adsorption isotherms that are ideal for flue gas separation applications. However, the impact of common flue gas contaminants on these CUS has previously received only cursory examination. The Lewis acidic nature of these CUS also implies a strong binding of *other* Lewis basic or amphoteric substances – potentially including common trace flue gas contaminants. In this chapter, we utilize sophisticated electronic structure methods to identify several problematic contaminants and to develop some general guidelines regarding the impact of such species on the utilization of CU MOFs in flue gas separation.

Of all available CUS MOFs, Mg/MOF-74[3, 4] and MIL-101[5] (see Figure 7.1) are two promising candidates. Mg/MOF-74, with CUS Mg^{2+} sites, exhibits a steep adsorption isotherm (5.28 mmol/g of CO_2 loading at 0.15 bar) and excellent CO_2 selectivity, making it an attractive candidate for either temperature or pressure swing adsorption (TSA/PSA) of dilute CO_2 from flue gas.[4, 6] MIL-101, with CUS Cr^{3+} metal centers, yields a CO_2 capacity as high as 40 mmol/g at 304K and 50 bar,[7, 8] although its performance at lower pressure is poorer than Mg/MOF-74.[9]

Significant uptake of Lewis bases by CUS MOFs is well known for the case of water vapor, which is present in significant amounts in flue gas. Focusing specifically on MOF-74, many authors have found a significant detrimental effect of humidity on CO_2 separation behavior, increasing with repeated exposure and eventually becoming completely inactive, with activity restored only after extended regeneration at high temperature.[10, 11] As such, water mitigation will likely be required in practical usage scenarios, possibly by placing a guard bed of desiccant prior to the MOF.[12]

In contrast, the interaction of other ubiquitous trace flue gas contaminants (sulfur oxides [SO_x], nitrogen oxide [NO_x] and their hydrates) with coordinatively unsaturated (CU) MOFs has not been well studied. While typically found at trace (parts per million, ppm) levels, our computational results demonstrate that such contaminants also bind much more strongly, with significant implications for both the equilibrium and separation behavior of the MOFs. Experimental data regarding these contaminants are extremely limited. Glover *et al.* examined the dynamic loading of a variety of toxic gases, including SO_2, in Mg/MOF-74, under humid, breakthrough conditions; they found evidence for SO_2 uptake on Mg/MOF-74. Nevertheless, their results are hard to interpret in terms of equilibrium behavior, particularly due to the presence of water.[13] Motivated by the biological activity of NO and potential drug delivery applications, several experimental studies are available for NO adsorption in CU MOFs (HKUST-1, Co/Ni-MOF-74). In general, these studies find significant NO uptake.[14-16] However, data regarding SO_x, NO_x, and their respective hydrates, not to mention associated implications for flue gas separation, are largely non-existent.

In this work, we utilize dispersion corrected density functional theory (DFT-D) and MP2 calculations in conjunction with a Langmuir model to quantify the impact of trace contaminant species (SO_2, SO_3, NO, NO_2) and their hydrates on several CU MOFs under realistic flue gas conditions. *We find that, despite their low concentration, some of these trace contaminants would likely dominate the equilibrium adsorption over CO_2 under flue gas conditions, and may prove difficult to remove under practical regeneration conditions. Furthermore, we argue that this phenomenon is apt to be fairly common among CUS MOFs.* This work provides guidelines for identifying relevant contaminant species and illustrates the practical concerns for utilizing MOFs in realistic flue gas separation applications.

7.2 Methods and Computation Details
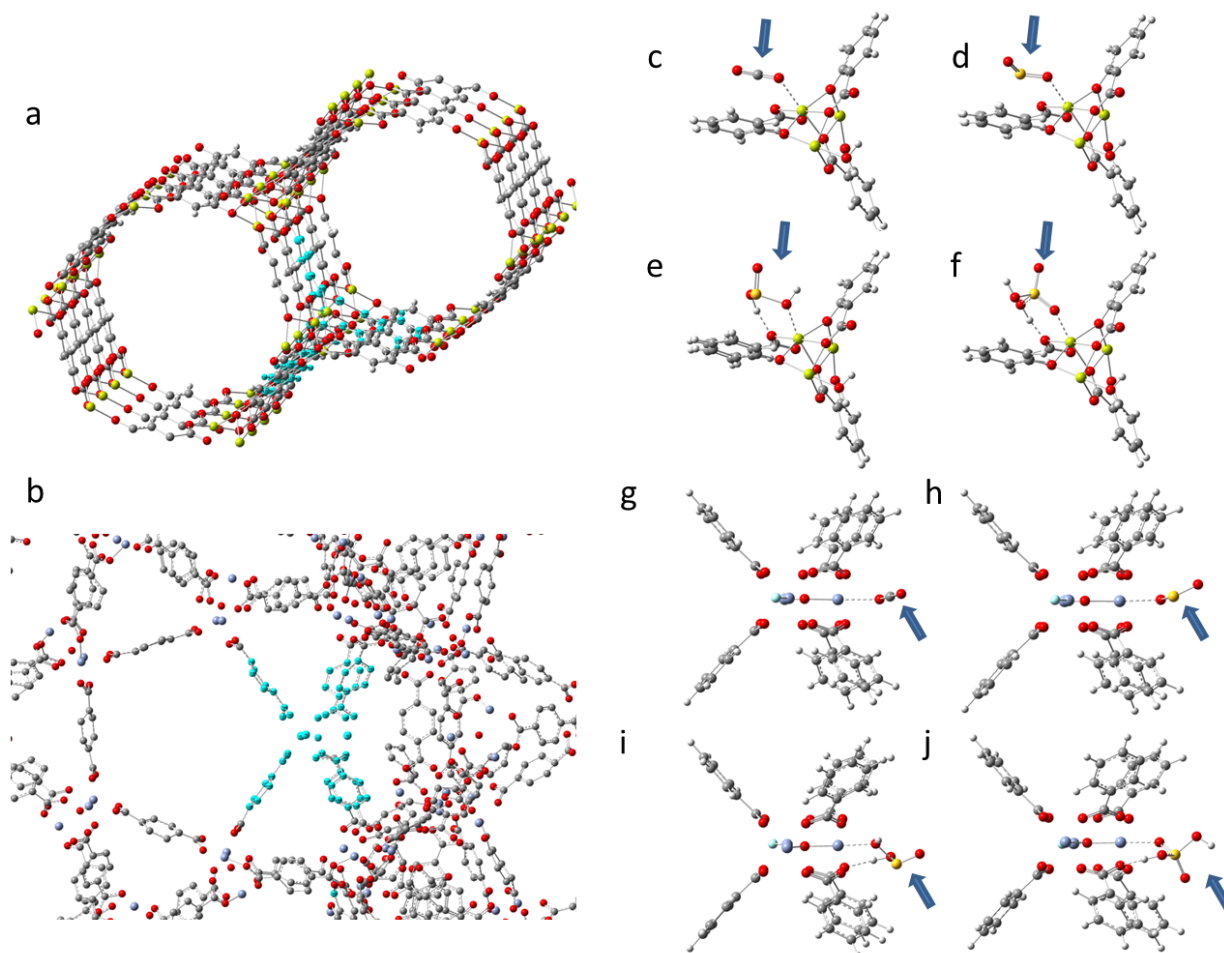
Figure 7.1. a-b) Crystal structure of Mg/MOF-74 and MOL-101; the blue highlighted atoms show the cluster model within its crystalline environment; c-f) CO_2 (c), SO_2 (d), H_2SO_3 (e), and H_2SO_4 (f) adsorption geometry on Mg/MOF-74 cluster model; g-j) CO_2 (g), SO_2 (h), H_2SO_3 (i), and H_2SO_4 (j) adsorption geometry on MIL-101 cluster model.

7.2.1 Model System Construction

Full periodic electronic structure calculations involving Mg/MOF-74 and (particularly) MIL-101 are complicated by the large size of the unit cell and limitations in periodic electronic structure methodologies. We therefore construct and utilize appropriate cluster models of these MOFs for the

present study. Correcting for the additional long-range dispersion interaction, we find the cluster model approximation to be excellent due to the local nature of the binding interaction.

For Mg/MOF-74, a cluster model containing three Mg^{2+} ions and four linker groups was carved from the x-ray diffraction (XRD) crystal structure (see Figure 7.1), with all dangling bonds to non-metal atoms terminated by H atoms. Other than the central Mg^{2+}, the remaining two Mg^{2+} sites are under coordinated (3 and 4 coordinate). We add a water molecule to partially satisfy the valence of the 3 coordinate Mg^{2+}, which also stabilizes the SCF convergence by removing a quasi-degenerate state. The resulting cluster $(Mg_3(C_7H_4O_3)_2(C_7H_5O_2)(C_6H_5O)(H_2O))$ model is neutral, and the central Mg^{2+} has an identical chemical environment as in the crystal structure. During all optimizations and normal mode analysis of this model system only the central Mg and the nearest five oxygen atoms are allowed to move, forming an active pocket. All of the other atoms outside of this pocket are held fixed, representing the relatively rigid crystal framework. This procedure allows the local environment surrounding the binding pocket to relax upon adsorption and accounts for uncertainties in the experimental crystal structure while effectively constraining to the experimental lattice constant.

We validate our Mg/MOF-74 model via comparison with the bulk. The cluster model was placed in a box with the same size and shape of the unit cell, and a plane wave DFT calculation was conducted using the Vienna Atomistic Simulation Package (VASP).[17-22] The energy cutoff was set to 520 eV, and the PBE functional and projected augmented wave (PAW) method for the core electrons were used. The resulting electron density is compared with the density from a corresponding calculation on the bulk crystal (see Figure 7.2). The electron density difference near the central Mg^{2+} is extremely small, suggesting that our model system replicates the bulk crystal electronic structure very well in this region.
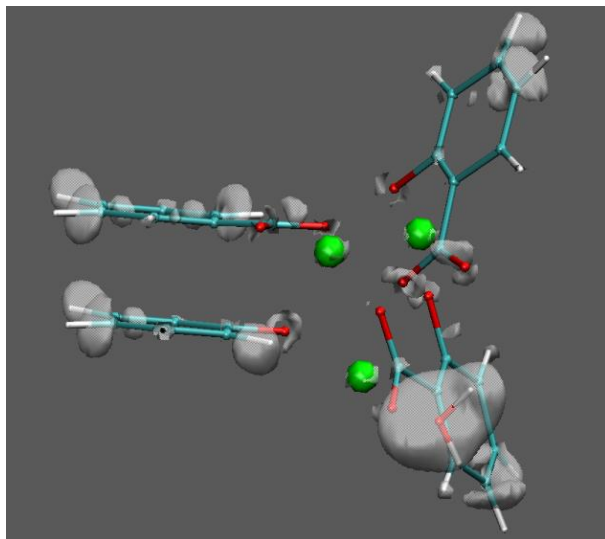
Figure 7.2. Electron density difference between the Mg/MOF-74 model system and the bulk system. The isosurface that is plotted represents about 5% of error.

For MIL-101, the experimental XRD structure exhibits severe unphysical distortions due to the limited resolution in the XRD experiment and/or symmetry constraints during data analysis. Therefore, we manually construct the model system based on several critical bond lengths, angles and dihedrals obtained in the crystal structure and an enforced C_3 symmetry. A charge balancing F^- anion (the experimental counter ion) was placed coordinated to one of the Cr^{3+} to neutralize the total charge. We first optimize the atoms in the benzene ring that are outside of the pocket using the range-separated ωB97X-D functional[23] in conjunction with the def2-SVP basis, holding the pocket fixed, in order to relax strained bonds due to limited crystallographic resolution. All atoms in the benzene rings are then fixed, representing the rigid crystal framework, and the active pocket is optimized. We do not further evaluate the cluster model via comparison to the bulk since all broken bonds are more than 10Å away from the active pocket, and since the unit cell is prohibitively large. The final chemical formula for this model is $Cr_3O(C_7H_5O_2)_6F$, with an active pocket including the Cr^{3+} trimer, the bridging oxygen, the F^- counter ion, and all carboxylate groups. The structure of the model system is shown in Figure 7.1.

We also examined the spin state of the MIL-101 model system, which contains a Cr^{3+} trimer cluster at its center. Based on comparison with previous work on $[Cr_3O(CH_3CO_2)_6(H_2O)_3]Cl \cdot 6H_2O$,[24] we anticipate high spin ($S = 3/2$) Cr^{3+} cations coupled together to form a trimer. The all-parallel configuration ($S = \dfrac{9}{2}$) has the lowest energy, but at finite temperature the most populated state is likely $S = \dfrac{3}{2}$. Since adsorption is localized to one Cr^{3+}, the weak coupling amongst the trimer should be largely irrelevant. As such, we compared the interaction energies of MIL-101 / CO_2 system, for both $m_s = 9/2$ and $m_s = 3/2$ spin states. Spin density constrained DFT[25] was utilized to obtain the low spin state, with the constraints that the spin density in all three Cr^{3+} should be either 3 or -3. With this appropriate initial guess, the final converged states are guaranteed to have the correct high spin configuration in each individual Cr^{3+}. The adsorption energy difference between the results of the high m_s state and the low m_s state is within 1kJ/mol, confirming our previous conjecture. We use $m_s = 9/2$ state in all subsequent calculations.

7.2.2 Details for Energy Calculations and Thermal Corrections

For each contaminant molecule, the initial structure is constructed by placing the molecule near the CUS. The geometry of the gas molecule and the active pocket is then optimized at the ωB97X-D/def2-SVP level of theory while fixing all other atoms. This optimized structure is used in subsequent interaction energy calculations, which utilize both B3LYP-D[26] and ωB97X-D.[23] Both functionals employ an empirical dispersion correction based on the D2 scheme proposed by Grimme.[26] The latter functional is a range-separated hybrid that has shown exceptional accuracy in weak intermolecular interactions. The basis set convergence was also investigated for both functionals, and the Ahlrichs def2-SVP[27] basis set was found to give interaction energies converged to within 2 kJ/mol, comparable to the accuracy of the empirical dispersion correction. Additional MP2 calculations were also conducted for the Mg/MOF-74 systems, yielding qualitatively identical results (See supporting information of reference 28). A partial

Hessian harmonic normal mode analysis[29] is conducted at the ωB97X-D/def2-SVP level of theory, in accord with the optimization method, and thermal contributions to the enthalpies and free energies are computed using standard harmonic oscillator formulas.[30]

All geometry optimizations are done utilizing the QCHEM[31] package, and all single point and hessian calculations are done using the QCHEM and GAUSSIAN09[32] packages.

The final electronic contribution to the interaction energy is given by:

$$\Delta E_{elec}^{tot} = \Delta E_{elec} + \Delta E_{deform} + \Delta E_{lr-disp} \tag{7.1}$$

$$\Delta E_{elec} = E_{dim}^{DCBS} - E_{MOF}^{DCBS}(dim) - E_{gas}^{DCBS}(dim) \tag{7.2}$$

$$\Delta E_{deform} = E_{MOF}^{MCBS}(dim) - E_{MOF}^{MCBS}(mon) + E_{gas}^{MCBS}(dim) - E_{gas}^{MCBS}(mon) \tag{7.3}$$

$$\Delta E_{lr-disp} = -s_6 \sum_i \sum_j f(r_{ij}) \frac{C_6^{ij}}{r_{ij}^6} \tag{7.4}$$

The total electronic interaction energy ΔE_{elec}^{tot} has two short-range components, the direct electronic interaction energy, ΔE_{elec}, and the geometric deformation energy, ΔE_{deform}. The interaction energy is counterpoise-corrected using a dimer centered basis sets (DCBS). The deformation energy is defined as the energy cost for each monomer to deform its geometry to the adsorbed geometry. It is calculated using monomer center basis sets (MCBS), as the difference between monomer energies in the dimer geometry, $E^{MCBS}(dim)$, and monomer geometry, $E^{MCBS}(mon)$.

An additional long-range dispersion correction, $\Delta E_{lr-disp}$, is added to the total electronic interaction energy in order to account for the long-range dispersion interactions between the gas molecule and the framework atoms which are omitted in the cluster model. To correct this error, we place the adsorbate in the corresponding position in the bulk structure and evaluate the empirical dispersion energy, $\Delta E_{lr-disp}$, using equation (7.4), where i runs over all gas atoms, and j runs over all the atoms missing from the

model system within a cutoff distance of 24Å (at which point the results have converged). All parameters and the functional form in this equation are directly taken from Grimme's dispersion correction for the B3LYP functional.[26] Note that geometric relaxation in the cluster model upon binding leading to a small uncertainty in the position of the adsorbate in the bulk, and a corresponding small uncertainty in the long range correction. However, the deformations are typically very small and the long-range dispersion energy should be insensitive to these minor changes (within 1 kJ/mol).

The thermal contributions to enthalpy, entropy, and free energy calculations are calculated using harmonic approximations at a temperature of 300K:

$$\Delta H_{ads} = \Delta E_{elec}^{tot} + H_{dimer}^{harmonic} - H_{model}^{harmonic} - H_{gas}^{harmonic} - \frac{n}{2}RT - PV \tag{7.5}$$

$$\Delta S_{ads} = S_{dimer}^{harmonic} - S_{model}^{harmonic} - S_{gas}^{harmonic} - S_{gas}^{rot} - S_{gas}^{trans} \tag{7.6}$$

$$\Delta G_{ads} = \Delta H_{ads} - T\Delta S_{ads} = \Delta G_{ads}^{excess} - \mu_{ideal-gas}^{o} \tag{7.7}$$

In these equations, all harmonic terms represent the vibrational thermal contributions. The $\frac{n}{2}RT$ term in the enthalpy equation represents the non-vibrational enthalpy contributions, where n is the number of non-vibrational degrees of freedom for a single gas molecule. The adsorption entropy, ΔS_{ads}, consists of vibrational (harmonic), rotational, and translational components, evaluated using standard expressions.[30] The PV term is approximated using an ideal gas, RT. $\mu_{ideal-gas}^{o}$, the ideal gas part of the free energy, is calculated at a reference pressure p_0 of 1bar.

Many low frequency vibrational modes exist in the dimer complex, which are typically associated with the hindered rotations of the adsorbed gas molecules. A harmonic approximation for these shallow modes is often inaccurate. One extreme example is the Mg/MOF-74 + NO dimer, in which a small imaginary frequency is present in the phonon spectrum of the optimized structure due to the extremely flat potential surface. We use three systems (NO, N_2, CO_2) to estimate the associated error in the free energy due to the

harmonic approximation. Potential energy surface scans are performed along each of the five lowest frequency modes (including the imaginary mode), and the exact anharmonic eigenstates are computed using the discretized value representation (DVR) method.[33] The vibrational partition functions and free energies are calculated directly from these eigenvalues. Although this approach still neglects the anharmonic coupling between different modes, it accounts for the potential energy surface anharmonicity within each mode. Based on this comparison, we estimate the associated uncertainty between 2-6 kJ/mol, comparable to the accuracy of the underlying density functional approximation. The largest errors are found for *weak* binding molecule, such as N_2, because the rotation modes are very shallow and highly anharmonic. For stronger binding CO_2 the associated error decreases to within 1 kJ/mol; we anticipate that strong binding contaminants should have comparable errors. As such, we use the harmonic approximation for all remaining systems. The entropies, which are directly calculated from energies and free energies, will have a corresponding uncertainty of few tens of J/mol/K.

7.3 Results and Discussions

7.3.1 Adsorption Enthalpies, Entropies and Free Energies

The final calculated ωB97X-D adsorption energies, enthalpies, free energies and entropies are summarized in Mg/MOF-74 and MIL-101 in Table 7.1. Comparable B3LYP-D and MP2 calculated results are presented in the supporting information of reference 28. In general, both DFT functionals gave similar results, with B3LYP-D typically 5-10% more strongly binding. As detailed in the supporting information of reference 28, we also ran corresponding MP2 calculations, and find (by and large) much better agreement between MP2 and ωB97X-D than with B3LYP-D. Note that the modest additional binding predicted by B3LYP-D can cause rather significant increases in the predicted contaminant loading to the exponential sensitivity to the binding energy. However, the qualitative conclusions regarding the relevance of a given contaminant are typically insensitive to the choice of functional. As

described below, we find generally that the ωB97X-D results better correspond to available experimental adsorption enthalpies, where available. Given this observation, the general consistency between ωB97X-D and MP2, and the overbinding of B3LPY-D as compared to the latter, we tend to put more weight on the ωB97X-D predictions.

	Mg/MOF-74			MIL-101		
	ΔH_{ads}	ΔS_{ads}	ΔG_{ads}^{excess}	ΔH_{ads}	ΔS_{ads}	ΔG_{ads}^{excess}
CO	-38.9	-117.5	-45.1	-37.4	-129.9	-39.9
CO_2	-44.9	-139.9	-46	-29.2	-122.8	-35.4
H_2O	-79.9	-134.1	-79.4	-77.9	-144.2	-74.4
N_2	-28.5	-114.3	-35.7	-21.1	-122.7	-25.7
NO	-33.2	-148.9	-30.2	-26.9	-119.1	-32.8
NO_2	-41.3	-136.2	-43.7	-25.6	-139.8	-27
SO_2	-72.8	-167	-67.2	-45.9	-149.8	-45.5
SO_3	-60.3	-165.7	-55.9	-45.6	-168.6	-40.3
H_2SO_3	-101.9	-180	-93.4	-67	-177.6	-59.2
H_2SO_4	-128.8	-170.5	-123.8	-83.4	-164.6	-80.2
HNO_2	-66.5	-150.4	-64.7	-46.5	-152.7	-44
HNO_3	-62.5	-162.4	-58.2	-50.9	-168.3	-44.9

Table 7.1. Adsorption properties calculated with ωB97X-D for Mg/MOF-74 and MIL-101. All energies are in kJ/mol, and entropies are in J/mol/K. All values are given at 300K.

We partially validate our contaminant calculations via comparison with experimental results, where available. Motivated by flue gas separation applications, Mg/MOF-74 + CO_2 is currently the best characterized system. The isosteric heat of adsorption has been measured by many groups, with modest variations amongst measurements: 38-43,[34] 39,[6] 42,[35] 47.[4, 36] The calculated ωB97X-D $\Delta H_{ads} = -44.9$ in this work lie within the range the experimental data, with B3LYP-D slightly above the upper end of this range. Comparing with prior computational results,[36-39] we note that Park *et. al.* obtained a slightly lower CO_2 adsorption energy of 41.4 kJ/mol using the dispersion corrected PBE-D2 functional.[38]

A direct comparison can be made between our B3LYP-D results (see supporting information of reference 28) and the B3LYP-D* results from Valenzano *et. al.*[36, 37] They obtain adsorption enthalpies of 37.9 kJ/mol for CO_2 and 25.2 kJ/mol for N_2. All these numbers are systematically lower than our B3LYP-D results, a fact which can be partially attributed to the different dispersion parameters (the dispersion parameters in B3LYP-D* were empirically tuned to reproduce the lattice energies of organic molecular crystals). However, we also find that even using identical adsorption geometry, our underlying pure B3LYP adsorption energy (omitting dispersion correction) is significantly higher than their results. It is important to understand this discrepancy and validate our model system and calculation scheme before we perform any further analysis.

The principal differences between the two calculations are: loading (1/6 CO_2 loading in present work vs. full loading); basis set (double zeta vs. triple zeta); and model system (cluster vs. periodic). To investigate the loading effects, we carry out the full loading and low loading calculations on the periodical system using the PBE functional in conjunction with the trimmed triple-zeta basis from Valenzano *et. al.*[36, 37] The difference between these two calculations is small, only 0.5 kJ/mol, showing that the loading level cannot explain this discrepancy. This is consistent with the common understanding that the CO_2-CO_2 interaction is mainly dispersive, which should be missing in pure GGA calculations.

Furthermore, properly accounting for BSSE, we find only minimal basis set dependence on our reported adsorption energies for the cluster model, with typical differences of only 1-2 kJ/mol when moving to a triple zeta basis. In contrast, we find significant basis set effects when examining a corresponding periodic model system. Utilizing the CRYSTAL09[40] package, we attempted to reproduce the CO_2 data using the identical geometry and basis set as in Valenzano *et. al*. The calculations with full triple zeta basis fail to converge due to the well-known linear dependency problem diffuse bases in a crystalline environment. Trimming out diffuse basis functions facilitates the convergence, leading to a interaction energy of ~18 kJ/mol, consistent with that reported in Ref. 36. *In contrast to our cluster model, however, this result is extremely sensitive to the details of how these basis functions are trimmed.* In some

extreme cases, removing one or two more diffuse basis functions leads to an energy difference up to 10 kJ/mol. As recommended by the CRYSTAL09 manual, we also conducted calculations with smaller (untrimmed) double zeta basis from CRYSTAL basis set database,[40-42] yielding an adsorption energy of 23.5 kJ/mol. The challenge here is that while part of this system is partially anionic (O atoms), requiring diffuse basis functions for an accurate description, using too large of a basis will cause numerical instability in SCF iterations. Ideally, the exponents of the basis sets should be re-optimized with respect to periodic systems. Simply trimming ordinary basis sets optimized for isolated molecules does not yield robust results.

In order to circumvent this issue and conclusively verify the quality of our model system, we repeated the full periodic B3LYP calculation using a plane wave basis set. Here, the basis can be systematically enlarged to the basis set limit without introducing numerical instability via linear dependencies. These calculations were conducted using the Quantum Espresso[43] program, with a 40 Ryd energy cutoff, and pseudo potentials taken from Ref. 44 for elements C, H, and O, and generated using Quantum Espresso pslibrary code for Mg. The resulting B3LYP interaction energy is 27.1 kJ/mol; adding Grimme's dispersion yields a B3LYP-D results of 52.7kJ/mol, close to our B3LYP-D cluster model result (see supporting information of reference 28), and confirming the accuracy of our model system.

For the MIL-101 system, recent measurements estimate the CO_2 adsorption enthalpy at between 24-29 kJ/mol, in reasonable agreement with the present work.[8, 45] In contrast, a more recent measurement by Munusamy et al. gives a CO_2 adsorption energy close to 40 kJ/mol and a surprisingly high CO_2 uptake, which lies in contrast to both our calculation and previous experiments.[9] Since co-adsorbed water is known to significantly increase CO_2 adsorption via dipole-quadruple interactions, this is possibly an effect of the residual adsorbed water; note that the drying process utilized in the latter work was significantly less aggressive than that in prior work.

7.3.2 Adsorption Structure

We also compare the adsorption geometries of our cluster model calculations with previous experimental studies.[46] The comparison of some key geometry parameters are listed in Table 7.2. Moderate discrepancies with the experimental geometry occur for the O1-C-O2 bond angle and C-O bond lengths, although the corresponding experimental uncertainties are very large. In particular, for the Mg-O1-C bond angles, the experimental data have uncertainties up to 15 degrees; furthermore, the deduced bond angle increases drastically (and unphysically) with an increasing amount of loading. In general, these large uncertainties have been previously attributed to residual structural disorder.[46]

	This work	Exp.[a]
Mg-O (Å)	2.265	2.39±0.06
C-O1[c] (Å)	1.173	1.04±0.09
C-O2 (Å)	1.154	1.1±0.1
Mg-O1-C (degrees)	120.45	125±7
O1-C-O2 (degrees)	177.07	150±15

Table 7.2. Geometry parameters for absorbed CO_2 in Mg/MOF-74 system, O1 is the CO_2 oxygen atom which is coordinated to Mg^{2+}, O_2 is the other CO_2 oxygen. a) Reference 46.

7.3.3 Langmuir Model Calculations

The calculated contaminant adsorption free energy data are utilized in a single site Langmuir model to estimate the actual occupancy of CUS, θ, for different species under conditions of finite pressure,

$$\theta = \frac{\exp(-\Delta G_{ads}/kT)\,p/p_0}{1+\exp(-\Delta G_{ads}/kT)\,p/p_0} \tag{7.8}$$

$$\Delta G_{ads} = \Delta H_{ads} - T\Delta S_{ads} = \Delta G_{ads}^{excess} - \mu_{ideal-gas}^{o} \tag{7.9}$$

A single-site Langmuir model is inappropriate for describing adsorption in CUS MOFs above moderate pressures. For example, there is some evidence showing that for Mg/MOF-74, CO_2 might partially

occupy some weaker binding sites at pressures below 1 bar, although this secondary site should be minimally occupied at flue gas relevant pressures of ~0.1 bar.[35, 46]

For Mg/MOF-74 at 313K, the experimentally measured CO_2 loading is 5.28 mmol/g at 0.15 bar,[35] and N_2 loading is 0.6 mmol/g at 0.69 bar.[35] In conjunction with a single site Langmuir model, and with anharmonicity error corrected using DVR, our ωB97X-D (MP2) calculations predict loading amounts to be 1.09 (1.52) mmol/g and 0.03 (0.13) mmol/g, respectively. These predicted results are ~4 (CO_2) to 20 (N_2) times lower than the experimental value. However, particularly in the case of N_2, we would *expect* our single site model to substantially under predict due to the omission of the numerous secondary ligand binding sites, the relatively weak binding of N_2 to the metal sites, and the relatively high pressure. These secondary ligand sites will rapidly diminish in importance for strongly associating trace contaminants. It is also worth noting that, even neglecting the contribution from secondary sites, this difference corresponds to only 2-6 kJ/mol of free energy, within our estimated accuracy limits of the calculations. As the trend in the magnitude of the binding enthalpies (B3LYP-D > ωB97X-D ~ MP2) is relatively consistent, the ωB97X-D results should provide a conservative *lower-bound* on the impact of the contaminants, with B3LYP-D almost always predicting additional deleterious effects.

We estimate the occupancies for the various contaminants using partial pressures representative of actual flue gas conditions at 40°C (adsorption) and 110°C (regeneration).[47] Since regeneration in a TSA process would typical utilizes a purge gas, we assume this purge mixture is identical in composition to the flue gas with the N_2 removed. For simplicity, and due to uncertainties regarding the actual water concentration, we present results for *single component* adsorption at the partial pressure of the specified contaminant (since in the absence of some water mitigation water would dominate adsorption). Results are shown in Table 7.3 and Table 7.4 and are plotted in Figure 7.3.

Note that available data only provides estimates for NO_x concentrations. We utilize this estimate for each NO and NO_2. In addition, equilibrium between the acid gases and their hydrates will depend sensitively on the water concentration, and we provide data for both the anhydrous and hydrated forms of

all contaminants. The equilibrium constant for SO_3 hydration to H_2SO_4 strongly favors H_2SO_4 at any reasonable temperature and water concentrations. Furthermore, while sulfurous acid, H_2SO_3, is not stable in solution, it is observed in the gas phase.

	313K (θ, %)			383K (θ, %)		
	p/p_0 [a]	ωB97X-D	B3LYP-D	p/p_0 [b]	ωB97X-D	B3LYP-D
CO_2	0.13	17	60	0.46	3	14
H_2O	0.15	~100	~100	0.54	~100	~100
N_2	0.69	4	7	-	-	-
	p/p_0 ($\times 10^6$)	ωB97X-D	B3LYP-D	p/p_0 ($\times 10^6$)	ωB97X-D	B3LYP-D
NO	53	< 0.1	< 0.1	190	< 0.1	< 0.1
NO_2	53	< 0.1	0.1	190	< 0.1	< 0.1
SO_2	80	17	92	290	0.5	11
SO_3	10	< 0.1	2	36	< 0.1	< 0.1
H_2SO_3	80	~100	~100	290	90	99
H_2SO_4	10	~100	~100	36	~100	~100
HNO_2	53	9	13	190	0.3	0.5
HNO_3	53	0.5	3	190	< 0.1	0.1

Table 7.3. The contaminant occupancies as percentage of CUS, θ, for Mg/MOF-74. a) These data are taken from reference [48] for bituminous flue gas at 80°C. These partial pressures are the upper bound of the real concentrations, assuming that all sulfur or nitrogen exist in the particular form. b) For regeneration conditions, these partial pressures are calculated, assuming that N_2 gas has been removed completely, and all other components remain.

	313K (θ, %)			383K (θ, %)		
	p / p_0	ωB97X-D	B3LYP-D	p / p_0	ωB97X-D	B3LYP-D
CO_2	0.13	0.4	0.7	0.46	0.2	0.3
H_2O	0.15	~100	~100	0.54	~100	~100
N_2	0.69	0.1	0.1	-	-	-
	$p / p_0 (\times 10^6)$	ωB97X-D	B3LYP-D	$p / p_0 (\times 10^6)$	ωB97X-D	B3LYP-D
NO	53	< 0.1	< 0.1	190	< 0.1	< 0.1
NO_2	53	< 0.1	< 0.1	190	< 0.1	< 0.1
SO_2	80	< 0.1	< 0.1	290	< 0.1	< 0.1
SO_3	10	< 0.1	< 0.1	36	< 0.1	< 0.1
H_2SO_3	80	0.7	2	290	< 0.1	0.1
H_2SO_4	10	68	90	36	2	7
HNO_2	53	< 0.1	< 0.1	190	< 0.1	< 0.1
HNO_3	53	< 0.1	< 0.1	190	< 0.1	< 0.1

Table 7.4. The contaminant occupancies as percentage of CUS, θ, for MIL-101, with contaminant partial pressures calculated as in Table 7.3.
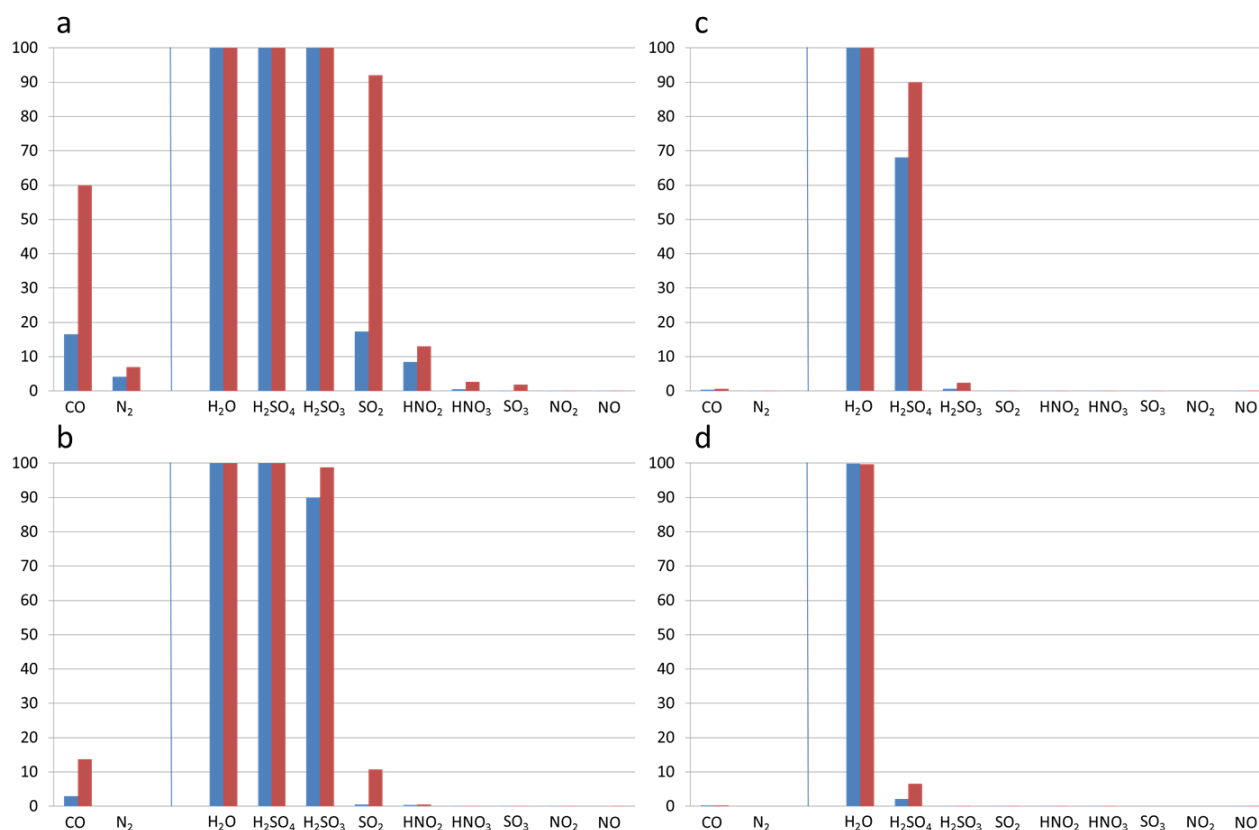
Figure 7.3. Coverage of different species adsorbed in Mg/MOF-74 and MIL-101: a) Mg/MOF-74 at 313K; b) Mg/MOF74 at 383K; c) MIL-101 at 313K; d) MIL-101 at 383K. Results for ωB97X-D are shown in blue, and the corresponding B3LYP-D results in red.

In accord with previous experimental results we find that both MOFs are extremely vulnerable to the presence of water vapor, occupying nearly all CUS at equilibrium, and further supporting the assertion that water mitigation would be required under practical usage scenarios. In contrast, adsorption enthalpies for NO_x and NO_x hydrates are comparable to that of CO_2, but with vastly lower partial pressures. NO binding to Mg/MOF-74 is likely mitigated since the absence of d-electrons in Mg^{2+} prevents backbonding. Thus, at least for the present MOFs, none of the nitrogen oxides appear to be important poisons under flue gas conditions, occupying a far smaller fraction of adsorption sites than CO_2 itself and trivially influencing separation behavior. Note that substantially stronger NO adsorption has been observed on

other CU MOFs (e.g. HKUST-1), and the presence of NO_x may be substantially more important with such MOFs.

In contrast, our data suggests that, despite their minute concentrations, SO_x species are potentially serious poisons for both sorbants, with the hydrates binding much stronger than the parent oxide. Focusing specifically on Mg/MOF-74, sulfurous and sulfuric acid bind extremely strongly (exceeding 100 kJ/mol), and saturate nearly all available metal sites under representative conditions. In particular, the acid hydrates coordinate to the CUS via the Lewis basic sulfur atom and also hydrogen bond to adjacent linker oxygen atoms via their acidic hydrogen (see Figure 7.1), yielding increased adsorption energies. In both MOFs, sulfuric acid binds significantly stronger than sulfurous acid, likely due to electrostatic effects. Even at putative regeneration temperatures of 383K, residual sulfurous and sulfuric acid are predicted to occupy a significant fraction of CUS. Based on purely equilibrium considerations, elimination of majority of these species would require regeneration temperatures of 500-600K. This suggests that the working capacity of the material will be dramatically reduced, and that the material will be subject to "poisoning" by the strong, semi-irreversible binding of flue gas contaminants.

Assuming that separation took place under extremely dry conditions, favoring anhydrous SO_x, our calculations suggest that SO_2 (but not SO_3) could still act as a significant contaminant under flue gas separation conditions, occupying between 20 to 90% of CUS at 313K. However, the situation is far less severe than with the hydrated species. Furthermore due its more modest binding energy, the adsorbed SO_2 should be largely desorbed under putative regeneration conditions. Note that due to the large equilibrium constant favoring hydrate formation, the reactions go to near completion and thus the flue gas stream would need to be very dry, with water concentrations less than that of the SO_x contaminant.

It is important to note that these are equilibrium arguments, and practical flue gas separation does not occur under equilibrium conditions. Rather, TSA would occur under breakthrough conditions, where flue gas mixture propagates through a column filled with MOF with the varying equilibrium between adsorbed and gas phase components dictating the propagation rates. In general, the weaker the molecule

binds, the faster it propagates. As such, the strong binding species will propagate much slower than CO_2, and would *not initially* interfere with the CO_2/N_2 separation. This likely explains why breakthrough experiments in the presence of humid CO_2/N_2 mixtures have observed some effect on breakthrough behavior, but not the profound effects one would expect based on the strong binding of H_2O. Nonetheless, under realistic conditions the sorbant will eventually approach steady state as the contaminant build up, likely characteristic of the equilibrium state at the given regeneration conditions.

7.4 Conclusion

Overall, our computational results suggest that coordinately unsaturated MOFs such as Mg/MOF-74 and MIL-101 are subject to poisoning by trace flue gas contaminants, especially SO_2, SO_3, and hydrates thereof. Despite the low (post-scrubbing) concentrations of such compounds in flue gas, their strong binding is sufficiently large to overcome the inherent chemical potential difference associated with their low partial pressure, outcompeting CO_2 for binding sites. Thus, under equilibrium conditions, we predict that these contaminants will poison a significant fraction of the CUS open metal sites at both plausible adsorption conditions. While the sites occupied by SO_2 and SO_3 can still be largely regenerated, their hydrates are so strong bonded that they cannot be driven out even in regeneration conditions. While these effects may be mitigated somewhat by the kinetics of the TSA process, they will nonetheless significantly diminish the working capacity of the MOFs.

Furthermore, the deleterious impact of such trace contaminants should be fairly ubiquitous: introducing CUS naturally increases the energy scales of Lewis base binding, and thus also the *differential* binding energies of the species also increases, sufficient to overcome the intrinsic chemical potential difference between CO_2 and trace contaminants. Comparing an ideal gas at 0.1 bar (CO_2) and 10^{-5} bar (trace contaminant at 10 ppm), this chemical potential difference is roughly 20 kJ/mol – an adsorption enthalpy difference threshold met or exceeded by a number of adsorbates in the present study, and likely in many of CU MOFs.

Beyond these considerations, it is also important to consider the structural *stability* of MOFs in the presence of flue gas contaminants. It is known that many MOFs are unstable in acidic aqueous solutions, and our calculations indicate that these contaminants, many of which are also Lewis/Bronsted acidic, are strongly bound at the CUS, directly adjacent to the crucial metal-ligand linkages. This suggests that these linkages may be subject to protonation and hydrolysis, with potential profound impact on MOF stability.

Bibliography

1.   Xiang, S. C.; He, Y. B.; Zhang, Z. J.; Wu, H.; Zhou, W.; Krishna, R.; Chen, B. L., Microporous metal-organic framework with potential for carbon dioxide capture at ambient conditions. *Nature Communications* **2012,** 3, 954.

2.   Xiang, S. C.; Zhou, W.; Zhang, Z. J.; Green, M. A.; Liu, Y.; Chen, B. L., Open Metal Sites within Isostructural Metal-Organic Frameworks for Differential Recognition of Acetylene and Extraordinarily High Acetylene Storage Capacity at Room Temperature. *Angew Chem Int Edit* **2010,** 49, (27), 4615-4618.

3.   Dietzel, P. D. C.; Blom, R.; Fjellvag, H., Base-induced formation of two magnesium metal-organic framework compounds with a bifunctional tetratopic ligand. *Eur J Inorg Chem* **2008**, (23), 3624-3632.

4.   Matzger, A. J.; Caskey, S. R.; Wong-Foy, A. G., Dramatic tuning of carbon dioxide uptake via metal substitution in a coordination polymer with cylindrical pores. *J Am Chem Soc* **2008,** 130, (33), 10870-10871.

5.   Ferey, G.; Mellot-Draznieks, C.; Serre, C.; Millange, F.; Dutour, J.; Surble, S.; Margiolaki, I., A chromium terephthalate-based solid with unusually large pore volumes and surface area. *Science* **2005,** 309, (5743), 2040-2042.

6.   Yaghi, O. M.; Britt, D.; Furukawa, H.; Wang, B.; Glover, T. G., Highly efficient separation of carbon dioxide by a metal-organic framework replete with open metal sites. *P Natl Acad Sci USA* **2009,** 106, (49), 20637-20640.

7.   Llewellyn, P. L.; Bourrelly, S.; Serre, C.; Vimont, A.; Daturi, M.; Hamon, L.; De Weireld, G.; Chang, J. S.; Hong, D. Y.; Hwang, Y. K.; Jhung, S. H.; Ferey, G., High uptakes of CO(2) and CH(4) in mesoporous metal-organic frameworks MIL-100 and MIL-101. *Langmuir* **2008,** 24, (14), 7245-7250.

8.   Chowdhury, P.; Bikkina, C.; Gumma, S., Gas Adsorption Properties of the Chromium-Based Metal Organic Framework MIL-101. *J Phys Chem C* **2009,** 113, (16), 6616-6621.

9.   Munusamy, K.; Sethia, G.; Patil, D. V.; Rallapally, P. B. S.; Somani, R. S.; Bajaj, H. C., Sorption of carbon dioxide, methane, nitrogen and carbon monoxide on MIL-101(Cr): Volumetric measurements and dynamic adsorption studies. *Chemical Engineering Journal* **2012,** 195-196, (1), 359-368.

10.   Kizzie, A. C.; Wong-Foy, A. G.; Matzger, A. J., Effect of Humidity on the Performance of Microporous Coordination Polymers as Adsorbents for CO(2) Capture. *Langmuir* **2011,** 27, (10), 6368-6373.

11.   Liu, J.; Benin, A. I.; Furtado, A. M. B.; Jakubczak, P.; Willis, R. R.; LeVan, M. D., Stability Effects on CO(2) Adsorption for the DOBDC Series of Metal-Organic Frameworks. *Langmuir* **2011,** 27, (18), 11451-11456.

12.   Liu, J.; Thallapally, P. K.; McGrail, B. P.; Brown, D. R.; Liu, J., Progress in adsorption-based CO_2 capture by metal-organic frameworks. *Chem Soc Rev* **2012,** 41, (6), 2308-2322.

13.   Glover, T. G.; Peterson, G. W.; Schindler, B. J.; Britt, D.; Yaghi, O., MOF-74 building unit has a direct impact on toxic gas adsorption. *Chem Eng Sci* **2011,** 66, (2), 163-170.

14.   Hinks, N. J.; McKinlay, A. C.; Xiao, B.; Wheatley, P. S.; Morris, R. E., Metal organic frameworks as NO delivery materials for biological applications. *Micropor Mesopor Mat* **2010,** 129, (3), 330-334.

15.   McKinlay, A. C.; Xiao, B.; Wragg, D. S.; Wheatley, P. S.; Megson, I. L.; Morris, R. E., Exceptional behavior over the whole adsorption-storage-delivery cycle for NO in porous metal organic frameworks. *J Am Chem Soc* **2008,** 130, (31), 10440-10444.

16.   Xiao, B.; Wheatley, P. S.; Zhao, X.; Fletcher, A. J.; Fox, S.; Rossi, A. G.; Megson, I. L.; Bordiga, S.; Regli, L.; Thomas, K. M.; Morris, R. E., High-Capacity Hydrogen and Nitric Oxide Adsorption and Storage in a Metal−Organic Framework. *J Am Chem Soc* **2007,** 129, (5), 1203-1209.

17.   Blochl, P. E., Projector Augmented-Wave Method. *Physical Review B* **1994,** 50, (24), 17953-17979.

18.   Kresse, G.; Furthmuller, J., Efficiency of ab-initio total energy calculations for metals and semiconductors using a plane-wave basis set. *Comp Mater Sci* **1996,** 6, (1), 15-50.

19.   Kresse, G.; Furthmuller, J., Efficient iterative schemes for ab initio total-energy calculations using a plane-wave basis set. *Physical Review B* **1996,** 54, (16), 11169-11186.

20.   Kresse, G.; Hafner, J., Ab initio molecular dynamics for liquid metals. *Physical Review B* **1993,** 47, (1), 558-561.

21.   Kresse, G.; Hafner, J., Ab initio molecular-dynamics simulation of the liquid-metal–amorphous-semiconductor transition in germanium. *Physical Review B* **1994,** 49, (20), 14251-14269.

22.   Kresse, G.; Joubert, D., From ultrasoft pseudopotentials to the projector augmented-wave method. *Physical Review B* **1999,** 59, (3), 1758-1775.

23.   Chai, J. D.; Head-Gordon, M., Long-range corrected hybrid density functionals with damped atom-atom dispersion corrections. *Phys Chem Chem Phys* **2008,** 10, (44), 6615-6620.

24.   Dubicki, L.; Day, P., The Electronic Spectrum of Trinuclear Chromium(III) Acetate. *Inorganic Chemistry* **1972,** 11, 1868-1875.

25.   Wu, Q.; Van Voorhis, T., Direct optimization method to study constrained systems within density-functional theory. *Phys Rev A* **2005,** 72, (2).

26.   Grimme, S., Semiempirical GGA-type density functional constructed with a long-range dispersion correction. *J Comput Chem* **2006,** 27, (15), 1787-1799.

27.   Weigend, F.; Ahlrichs, R., Balanced basis sets of split valence, triple zeta valence and quadruple zeta valence quality for H to Rn: Design and assessment of accuracy. *Phys Chem Chem Phys* **2005,** 7, (18), 3297-3305.

28.   Yu, K.; Kiesling, K.; Schmidt, J. R., Trace Flue Gas Contaminants Poison Coordinatively Unsaturated Metal-Organic Frameworks: Implications for CO_2 Adsorption and Separation. *J Phys Chem C* **2012,** 116, (38), 20480-20488.

29.   Ghysels, A.; Van Speybroeck, V.; Pauwels, E.; Catak, S.; Brooks, B. R.; Van Neck, D.; Waroquier, M., Comparative Study of Various Normal Mode Analysis Techniques Based on Partial Hessians. *J Comput Chem* **2010,** 31, (5), 994-1007.

30.   McQuarrie, D. A., *Statistical Mechanics*. p 228.

31.   Y. Shao, L. F.-M., Y. Jung, J. Kussmann, C. Ochsenfeld, S. T. Brown, A. T. B. Gilbert, L. V. Slipchenko,S. V. Levchenko, D. P. O'Neill, R. A. Distasio Jr., R. C. Lochan, T. Wang, G. J. O. Beran, N. A. Besley, J. M., Herbert, C. Y. Lin, T. Van Voorhis, S. H. Chien, A. Sodt, R. P. Steele, V. A. Rassolov, P. E. Maslen, P. P. Korambath, R. D. Adamson, B. Austin, J. Baker, E. F. C. Byrd, H. Dachsel, R. J. Doerksen, A. Dreuw, B. D. Dunietz, A. D. Dutoi, T. R. Furlani, S. R. Gwaltney, A. Heyden, S. Hirata, C.-P. Hsu, G. Kedziora, R. Z. Khalliulin, P. Klunzinger, A. M. Lee, M. S. Lee, W. Liang, I. Lotan, N. Nair, B. Peters, E. I. Proynov, P. A. Pieniazek, Y. M. Rhee, J. Ritchie, E. Rosta, C. D. Sherrill, A. C. Simmonett, J. E. Subotnik, H. L. Woodcock III, W. Zhang, A. T. Bell, A. K. Chakraborty, D. M. Chipman, F. J. Keil, A. Warshel, W. J. Hehre, H. F. Schaefer III, J. Kong, A. I. Krylov, P. M. W. Gill, M. Head-Gordon, Advances in methods and algorithms in a modern quantum chemistry program package. *Phys Chem Chem Phys* **2006,** 8, 3172-3191.

32.   M. J. Frisch, G. W. T., H. B. Schlegel, G. E. Scuseria, M. A. Robb, J. R. Cheeseman, G. Scalmani, V. Barone, B. Mennucci, G. A. Petersson, H. Nakatsuji, M. Caricato, X. Li, H. P. Hratchian, A. F. Izmaylov, J. Bloino, G. Zheng, J. L. Sonnenberg, M. Hada, M. Ehara, K. Toyota, R. Fukuda, J. Hasegawa, M. Ishida, T. Nakajima, Y. Honda, O. Kitao, H. Nakai, T. Vreven, J. A. Montgomery, Jr., J. E. Peralta, F. Ogliaro, M. Bearpark, J. J. Heyd, E. Brothers, K. N. Kudin, V. N. Staroverov, R. Kobayashi, J. Normand, K. Raghavachari, A. Rendell, J. C. Burant, S. S. Iyengar, J. Tomasi, M. Cossi, N. Rega, J. M. Millam, M. Klene, J. E. Knox, J. B. Cross, V. Bakken, C. Adamo, J. Jaramillo, R. Gomperts, R. E. Stratmann, O. Yazyev, A. J. Austin, R. Cammi, C. Pomelli, J. W. Ochterski, R. L. Martin, K. Morokuma, V. G. Zakrzewski, G. A. Voth, P. Salvador, J. J. Dannenberg, S. Dapprich, A. D. Daniels, Ö. Farkas, J. B.

Foresman, J. V. Ortiz, J. Cioslowski, and D. J. Fox *Gaussian 09, Revision A.1*, Gaussian, Inc.: Wallingford CT, 2009.

33.   Colbert, D. T.; Miller, W. H., A Novel Discrete Variable Representation for Quantum-Mechanical Reactive Scattering Via the S-Matrix Kohn Method. *J Chem Phys* **1992,** 96, (3), 1982-1991.

34.   Dietzel, P. D. C.; Besikiotis, V.; Blom, R., Application of metal-organic frameworks with coordinatively unsaturated metal sites in storage and separation of methane and carbon dioxide. *J Mater Chem* **2009,** 19, (39), 7362-7370.

35.   Mason, J. A.; Sumida, K.; Herm, Z. R.; Krishna, R.; Long, J. R., Evaluating metal-organic frameworks for post-combustion carbon dioxide capture via temperature swing adsorption. *Energ Environ Sci* **2011,** 4, (8), 3030-3040.

36.   Valenzano, L.; Civalleri, B.; Chavan, S.; Palomino, G. T.; Arean, C.; Bordiga, S., Computational and Experimental Studies on the Adsorption of CO, N_2, and CO_2 on Mg-MOF-74. *J Phys Chem C* **2010,** 114, (25), 11185-11191.

37.   Valenzano, L.; Civalleri, B.; Sillar, K.; Sauer, J., Heats of Adsorption of CO and CO_2 in Metal–Organic Frameworks: Quantum Mechanical Study of CPO-27-M (M = Mg, Ni, Zn). *J Phys Chem C* **2011,** 115, (44), 21777-21784.

38.   Park, J.; Kim, H.; Han, S. S.; Jung, Y., Tuning Metal−Organic Frameworks with Open-Metal Sites and Its Origin for Enhancing CO_2 Affinity by Metal Substitution. *J Phys Chem Lett* **2012,** 3, 826-829.

39.   Wu, H.; Simmons, J. M.; Srinivas, G.; Zhou, W.; Yildirim, T., Adsorption Sites and Binding Nature of CO(2) in Prototypical Metal-Organic Frameworks: A Combined Neutron Diffraction and First-Principles Study. *J Phys Chem Lett* **2010,** 1, (13), 1946-1951.

40.   Causa, M.; Dovesi, R.; Pisani, C.; Roetti, C., Electronic-Structure and Stability of Different Crystal Phases of Magnesium-Oxide. *Physical Review B* **1986,** 33, (2), 1308-1316.

41.   Dovesi, R.; Ermondi, C.; Ferrero, E.; Pisani, C.; Roetti, C., Hartree-Fock Study of Lithium Hydride with the Use of a Polarizable Basis Set. *Physical Review B* **1984,** 29, (6), 3591-3600.

42.   Gatti, C.; Saunders, V. R.; Roetti, C., Crystal-Field Effects on the Topological Properties of the Electron-Density in Molecular-Crystals - the Case of Urea. *J Chem Phys* **1994,** 101, (12), 10686-10696.

43.   Giannozzi, P.; Baroni, S.; Bonini, N.; Calandra, M.; Car, R.; Cavazzoni, C.; Ceresoli, D.; Chiarotti, G. L.; Cococcioni, M.; Dabo, I.; Dal Corso, A.; de Gironcoli, S.; Fabris, S.; Fratesi, G.; Gebauer, R.; Gerstmann, U.; Gougoussis, C.; Kokalj, A.; Lazzeri, M.; Martin-Samos, L.; Marzari, N.; Mauri, F.; Mazzarello, R.; Paolini, S.; Pasquarello, A.; Paulatto, L.; Sbraccia, C.; Scandolo, S.; Sclauzero, G.; Seitsonen, A. P.; Smogunov, A.; Umari, P.; Wentzcovitch, R. M., QUANTUM ESPRESSO: a

modular and open-source software project for quantum simulations of materials. *J Phys-Condens Mat* **2009,** 21, (39), 395502.

44.   Tozzini, V.; Bizzarri, A. R.; Pellegrini, V.; Nifosi, R.; Giannozzi, P.; Iuliano, A.; Cannistraro, S.; Beltram, F., The low frequency vibrational modes of green fluorescent proteins. *Chem Phys* **2003,** 287, (1-2), 33-42.

45.   Zhang, Z. J.; Huang, S. S.; Xian, S. K.; Xi, H. X.; Li, Z., Adsorption Equilibrium and Kinetics of CO(2) on Chromium Terephthalate MIL-101. *Energ Fuel* **2011,** 25, 835-842.

46.   Queen, W. L.; Brown, C. M.; Britt, D. K.; Zajdel, P.; Hudson, M. R.; Yaghi, O. M., Site-Specific CO(2) Adsorption and Zero Thermal Expansion in an An isotropic Pore Network. *J Phys Chem C* **2011,** 115, (50), 24915-24919.

47.   Berger, A. H.; Bhown, A. S., Comparing Physisorption and Chemisorption Solid Sorbents for use Separating CO_2 from Flue Gas using Temperature Swing Adsorption. *Energy Procedia* **2011,** 4, 562-567.

48.   *Carbon Capture 2020 Workshop summary*; NETL: University of Maryland Inn & Conference Center, College Park, MD 20742, 2009.

Chapter 8. Study of CO_2/H_2 Adsorption Sites in MOF-74 Series Using Infrared Spectroscopy

Table of Contents

8.1 Introduction

As mentioned in the previous chapter, the M/MOF-74 series[1-7] presents an extremely promising class of gas adsorption materials. These isostructural MOFs are composed of different divalent metal centers (Zn, Mg, Mn, Fe, Co, Ni), interconnected with DOBDC (2,5-dioxido-1,4-benzenedicarboxylate) linker groups. These MOFs form hexagonal honeycomb-like structures and one-dimensional channels, in which small guest molecules reside and interact with the open metal sites. As discussed previously, Mg/MOF-74 is among the best CO_2 adsorbent candidates, with both high loading capacity and excellent selectivity. Furthermore, many MOF-74 derivatives show strong H_2 affinities, and are potentially applicable to H_2 gas storage.[8-10] At the low-pressure limit, all M/MOF-74 structures have well-defined adsorption sites that are typically located around the unsaturated metal centers. However, with increasing loading level, the guest molecules may also occupy the secondary sites, which are close to the benzene ring and are dominated by nonbonding dispersion interactions.

While the positions and the binding strengths of the primary adsorption sites are clear, the detailed adsorption geometries and the physical properties of the interactions are not thoroughly studied. Currently, the six synthetically available metal centers in the MOF-74 series span a wide range of interactions strengths, and a deeper understanding to the binding mechanisms of these sites is critical to design new binding centers with better performance. Furthermore, the interaction between the primary and secondary adsorption sites also raises interests, since this interaction provides a new strategy to improve binding energy, especially in the H_2 adsorption case. Lastly, the generality and the magnitude of guest-guest interactions is still under debate, requiring more experimental evidence to understand the microscopic details associated with adsorption.

In order to resolve the aforementioned problems, highly accurate and sensitive experimental techniques are required to probe the local chemical environments of the adsorbed guest molecules. Fourier transform infrared (FT-IR) spectroscopy serves as an important tool in this regard because the vibrational

frequencies of many guest molecules are very sensitive to local interactions. Efforts have been made to measure the IR frequency shifts of different modes of H_2[11-13] and CO_2[14-17] adsorbed in MOF-74 structures with different metal centers. Experimental data has been successfully collected, however, interpretations to the frequency shifts data are still under debate.

Thorough experimental work has been performed for the frequency shifts of the H_2 stretching mode in the whole MOF-74 series by both Chabal *et. al.*[13] and Rowsell *et. al.*.[11, 12] Chabal's group proposed that the observed large frequency shifts are due solely to the H_2-H_2 interactions, while the later work conducted by Rowsell *et. al.* suggested otherwise. We believe this ambiguity can be clarified through theoretical computations; therefore in this chapter, we will show that we are able to reproduce the experimental frequency shifts using computer simulation techniques. Through our calculations, the microscopic origin of the observed frequency shifts will be clearly explained, simultaneously validating the accuracy and effectiveness of our computer simulations.

Existing experimental work for the adsorbed CO_2 is much less thorough: only a subset of available metal centers (Mg, Zn, Co, Ni) have been studied;[14-17] moreover, data for select vibrational modes are missing. Rowsell's group has been devoted to measure the IR spectroscopy for all six metal centers (Mg, Zn, Mn, Fe, Co, Ni), for both symmetric and asymmetric stretching modes of CO_2. For CO_2, both symmetric and asymmetric frequency shifts are much smaller compared to the H_2 case due to complicated coupling between the two local C-O modes. Currently available experimental data shows very delicate differences between different metal centers: the asymmetric stretching mode of CO_2 is red shifted around most of the metal centers, but is slightly blue shifted for Mg/MOF-74. Though these shifts undoubtedly contain important physical insights into the structure and bonding of the MOF-74 series, theoretical study is required for a proper interpretation of the experimental data.

It is also worth noting that several theoretical work do exist, all of which attempt to reproduce and explain the experimental IR spectroscopy. Valenzano *et. al.*[15, 16] examined the CO_2 frequency shifts in the Mg/ and Ni/MOF-74 systems, utilizing dispersion corrected periodical DFT calculations in conjunction

with atom-centered Gaussian basis. However, this work is not complete and the basis set linear dependency issue discussed in chapter 7 leads to extra complications. Langreth *et. al.*[13, 17] investigated both CO_2 and H_2 in a few MOF-74 systems, utilizing a nonlocal density functional with more robust plane wave basis sets. They studied guest-guest interactions within a periodic unit cell and obtained fairly accurate results compared to experiment, however, their data are also not complete. Moreover, even though some theoretical analysis has been conducted, the delicate blue shifts of CO_2 molecule in the Mg/MOF-74 system stay largely unexplained. In this work, we utilize a truncated model system, validated in the previous chapter, and systematically reproduce the experimental IR measurements. We conduct theoretical analyses to facilitate understanding the physical origin of the observed frequency shifts, and deduce the local environment of the adsorbate inside the MOF-74 series of MOFs.

8.2 Methods and Simulation Details

8.2.1 Cluster Model Construction

Our frequency calculations are based on truncated model systems, similar to the ones utilized in the chapter 7. To construct this cluster model, unit cell structures for Zn, Mg, Mn, Fe, Co, Ni/MOF-74 are optimized with plane wave DFT calculation using the VASP 4.0 package.[18-22] Besides the atomic positions, both box sizes and shapes are also optimized during the calculation. GGA (PW91/PBE) exchange correlation functional is used with a 520eV plane wave energy cutoff; a $2\times2\times2$ Monkhorst Pack grid is used to sample the reciprocal space. For each metal center, a cluster model system is carved out from the optimized unit cell structure. This cluster model includes three metal centers and four linker groups, to give a chemical formula $M_3(C_7H_4O_3)_2(C_7H_5O_2)(C_6H_5O)(H_2O)$. By removing all the benzene rings, this model system is further simplified to form a smaller model $(M_3(OH)_3(HCOO)_3)$, which is only used in MP2 geometry optimizations. Both model structures can be found in Figure 8.1.
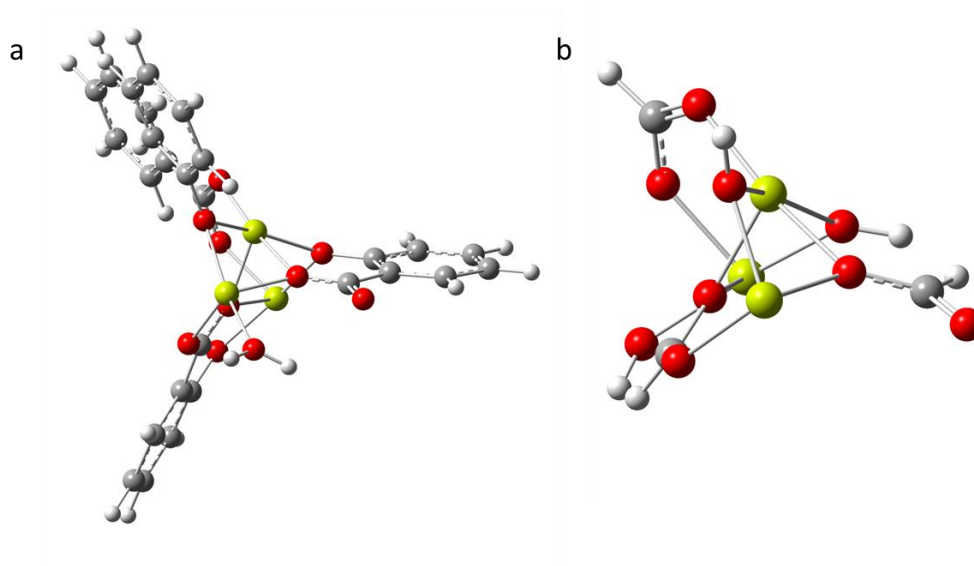
Figure 8.1 Model system structures: a) the truncated cluster model for all the DFT calculations; b) the smaller model system for the MP2 optimization.

During all DFT geometry optimizations and normal mode analyses, only the central metal ions and the five oxygen atoms directly coordinated to the central metal are allowed to move, defining the active pocket of the model. For the MP2 optimization, the whole model system is kept fixed and only the adsorbate geometry is optimized.

In order to further verify the validity of our model system for use in vibrational frequency calculations, we computed the anharmonic vibrational frequency of H_2-adsorbed Mg/MOF-74 using the PBE functional, both for the cluster model as well as the full periodic unit cell. Both results agree with each other to within $3 cm^{-1}$, verifying that our cluster model accurately reproduces the electronic structure property of the periodic crystal.

8.2.2 Electronic Structure Calculation Details

All DFT calculations (B3LYP/PBE0) are conducted with Grimme's D2 dispersion correction.[23] Ahlrichs def2-TZVP basis functions are used for the central metal ion and the adsorbate, while def2-SVP is used for all the other atoms.[24] Unless otherwise stated, DFT single point calculations and natural bond

orbital (NBO) analyses are carried out using the Gaussian 09[25] suite of code. DFT geometry optimizations are run through the Atomistic Simulation Environment (ASE) interface. We adopt high spin configurations for all the open shell metal centers, which are easier to converge, and give reasonable metal-ligand bond distances. All MP2 geometry optimizations are conducted using the MOLPRO[26] package with def2-SVP basis functions on all atoms. MP2 single point calculations in the discretized value representation (DVR) analysis are carried out using a hybrid DZ/TZ Dunning style basis sets (aug-cc-pVTZ for central metal and adsorbate and aug-cc-pVDZ for all other atoms).

8.2.3 Frequency Calculation Details

To compare with experimental data, we compute anharmonic vibrational frequencies using the discretized value representation (DVR)[27] method. In general, each DVR analysis contains three steps. First, a geometry optimizations is conducted (*e.g.* at a B3LYP-D level of theory). Second, normal modes of the active pocket are derived by diagonalizaing the mass weighed partial Hessian matrix, which are computed using the same level of theory as in the optimization. Finally, one dimensional potential energy scans (with at least 16 single points to ensure convergence) are performed along the relevant normal mode coordinate at a second level of theory (*e.g.* PBE0-D), at which point a DVR analysis is performed to compute the anharmonic frequency. For each DVR calculation, we denote the involved methods using the convention (using the aforementioned functionals as an example) B3LYP-D/PBE0-D, in which the first method is used for optimization and normal mode analysis and the latter method is used for DVR scans.

For CO_2 systems, to clarify the physical origin of the observed frequency shifts, we also performed a local mode analysis using a harmonic approximation. Following the notation of E.B. Wilson *et. al.*,[28] we define the three Cartesian coordinates ($\mathbf{X} = x_1, x_2, x_3$) as the displacements of the three CO_2 atoms (O1, C2, O3) along the principal axis, wherein O1 represents the oxygen coordinated to the metal center (see Figure 8.1). The two local modes $\mathbf{S}$ are then defined using rotation matrix $\mathbf{R}$:

$$\mathbf{S} = \mathbf{RX} \tag{8.1}$$

$$\mathbf{R} = \begin{bmatrix} -1 & 1 & 0 \\ 0 & -1 & 1 \end{bmatrix} \tag{8.2}$$

Here, the two modes of $\mathbf{S}$ (s_1, s_2) represent the stretching mode of the C2-O1 bond and the stretching mode of the C2-O3 bond, respectively. Then, the total Hamiltonian of the system can be expressed as FG decomposition:

$$\mathbf{H} = \frac{1}{2}\mathbf{P^T GP} + \frac{1}{2}\mathbf{S^T FS} \tag{8.3}$$

Where, $\mathbf{G}$ and $\mathbf{F}$ matrices are defined as:

$$\mathbf{G} = \mathbf{RM^{-1}R^T} = \begin{bmatrix} \dfrac{m_c + m_o}{m_c m_o} & -\dfrac{1}{m_c} \\ -\dfrac{1}{m_c} & \dfrac{m_c + m_o}{m_c m_o} \end{bmatrix} \tag{8.4}$$

$$\mathbf{F}_{ij} = \frac{\partial^2 U}{\partial s_i \partial s_j} \tag{8.5}$$

Here, momentum $\mathbf{P}$ is defined as:

$$\mathbf{P} = \mathbf{G^{-1}\dot{S}} \tag{8.6}$$

In this work, the elements of the $\mathbf{F}$ matrix are calculated numerically using the finite difference method. We set a step size $\delta s = 0.02\text{Å}$ and calculate potential energies at nine points ($s_1 = -\delta s, 0, \delta s$ and $s_2 = -\delta s, 0, \delta s$) around the local minimum. The resulting energies are fit to a quadratic form to obtain the $\mathbf{F}$ matrix elements.

The two local mode frequencies can be computed via the following equation:

$$\omega_i^{local} = \frac{1}{2\pi c}\sqrt{\mathbf{G}_{ii} \cdot \mathbf{F}_{ii}} \tag{8.7}$$

The coupling strength is represented as

$$\omega_{ij}^{couple} = \frac{1}{2\pi c}\sqrt{\left|\mathbf{G}_{ij}\cdot\mathbf{F}_{ij}\right|} \qquad (8.8)$$

while the normal mode harmonic frequencies are obtained by solving the secular equation:

$$\left|\mathbf{GF} - \lambda\mathbf{I}\right| = 0 \qquad (8.9)$$

$$\omega_i^{normal} = \frac{\sqrt{\lambda_i}}{2\pi c} \qquad (8.10)$$

In this manner, the normal and local harmonic frequencies for CO_2 can be calculated and further analysis can be carried out using these data.

8.3 Results and Discussion

8.3.1 Adsorption Geometries of H_2 and CO_2
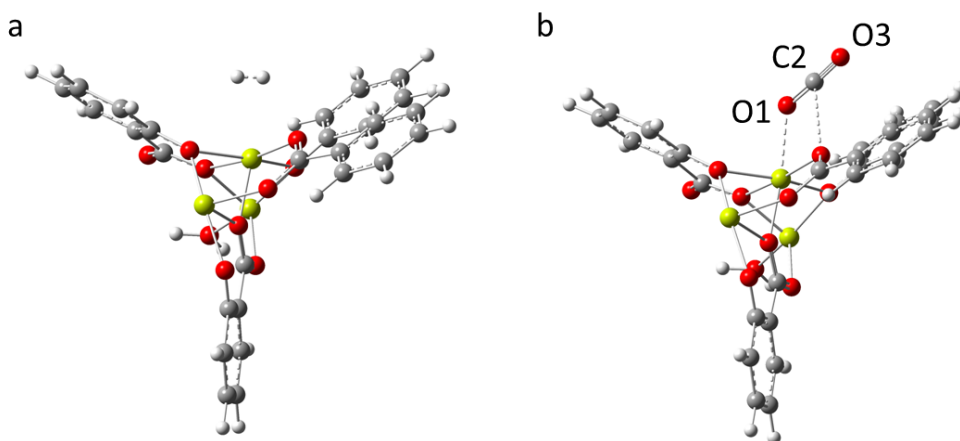
Figure 8.2. Adsorption geometries of H_2 and CO_2: a) the adsorption geometry of H_2; b) the adsorption geometry of CO_2. Here the atoms comprising CO_2 are labeled and will be referred to in the text as O1, C2, and O3.

For all metal centers studied, the optimized adsorption geometries of H_2 and CO_2 are very similar, and (see Figure 8.1). The H_2 molecule interacts with the metal ion in a side-on fashion, with the two M-H bond lengths being approximately symmetric. In the case of CO_2, the molecule adopts a slanted head-on

configuration with one of the oxygen atoms (O1) on CO_2 interacting directly with the metal center. Weak electrostatic interactions can be observed between the central carbon (C2) and one of the linker oxygen atoms.

8.3.2 H_2 Frequency Shifts

We begin by computing the anharmonic frequencies of the 0-1 transition of the H_2 stretching mode. All shift data, as well as comparisons to relevant gas phase H_2 vibrational frequencies, are shown in Table 8.1.

(cm^{-1})	Exp[a]	B3LYP-D/PBE0-D	PBE0-D/PBE0-D	MP2/PBE0-D[b]	MP2/MP2[b]
Co	-114	-104	-138	-87	-83
Fe	-100	-96	-148	-90	-85
Mg	-69	-71	-75	-66	-69
Mn	-73	-83	-85	-53	-56
Ni	-129	-139	-159	-114	-115
Zn	-65	-69	-79	-65	-72

Table 8.1. H_2 anharmonic frequency shifts compared to the experimentally observed gas phase frequency shifts; a) experimental values are taken from Ref. 11; b) Note these two calculations are done with smaller model systems, since MP2 geometry optimizations are not affordable with large model system.

Although it is too expensive for large model calculations, MP2 is utilized in this study as a standard to benchmark the quality of the density functional. As shown in Table 8.1, the MP2/PBE0-D and MP2/MP2 DVR results agree with each other within 7cm^{-1} for all M/MOF-74 systems, thereby verifying the accuracy of PBE0-D for our frequency shift calculations. Henceforth PBE0-D is always employed to calculate the vibrational frequencies.

Small models optimized with MP2 theory are not fully converged with respect to system size; therefore, to compare with experiment, larger models are necessary. As stated previously, geometry optimizations using an MP2 level of theory are cost prohibitive for these larger systems, and are consequently optimized using dispersion corrected density functional theory. Unfortunately, as it is shown in Table 8.1, the shift results are not consistent between different functionals (B3LYP-D and PBE0-D). For some particular

systems, B3LYP-D/PBE0-D and PBE0-D/PBE0-D differ by more than 20cm^{-1}, and PBE0-D/PBE0-D systematically overestimates the frequency shifts.
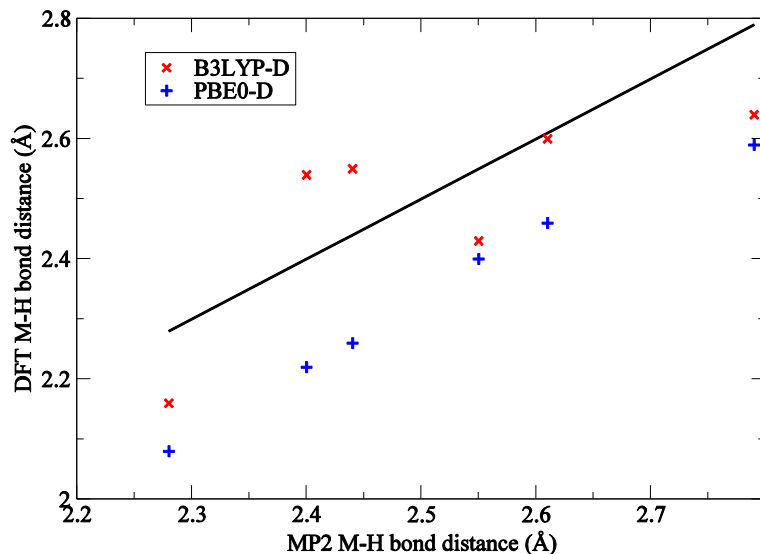
Figure 8.3. Averaged bond distances calculated with DFT, compared to the MP2 results. B3LYP-D results (red crosses) and PBE0-D results (blue pluses) are plotted along the side with the MP2 results (black solid diagonal line).

Since all DVR calculations are conducted at same level of theory, the discrepancy must come from differences in the geometry optimizations. We compute the average metal-hydrogen bond distances obtained using both density functionals, and compare them to the MP2 results from the small model calculations (see Figure 8.3). The data suggest that PBE0-D systematically underestimates the M-H bond distance compared to MP2, which implies that the functional tends to overestimate the interaction strength of H_2 binding. As a result, PBE0-D unphysically weakens the H-H bond and over predicts the corresponding frequency red shift, probably as a result of a poor treatment of the multi-reference characteristic of the metal center. On the other hand, B3LYP-D does not show significant systematic error and outperforms PBE0-D in terms of structure prediction. Our computational results can be directly compared to the experiments of Liu *et. al.*[8], whose neutron diffraction experiments on H_2 adsorbed in Zn/MOF-74 provide an experimental value for the M-H bond distance. Liu obtained an average M-H

bond distance of 2.64 Å, comparable with our B3LYP-D (2.60 Å) and MP2(2.61 Å) results but much longer than our PBE0-D prediction (2.46 Å). We therefore conclude that the large model system calculation at B3LYP-D/PBE0-D level generates the most reliable results and use this method for comparison with available experimental data (see Table 8.1 and Figure 8.4).
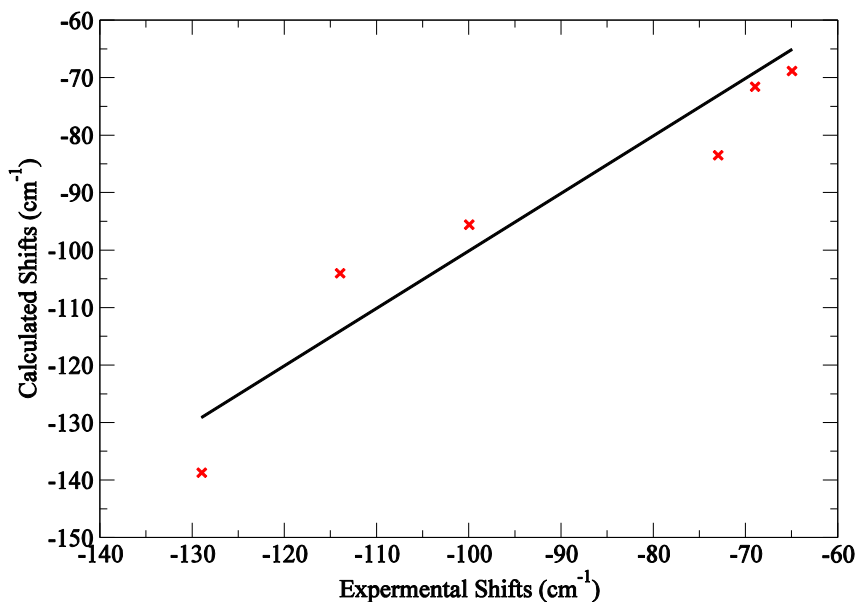
Figure 8.4. H_2 Frequency shifts predicted at B3LYP-D/PBE0-D level of theory plotted against experimental frequency shifts. The solid line corresponds to perfect agreement between experiment and theory and is provided merely to guide the eye.

As it is shown, the calculated results agree with the experimental data with around $10cm^{-1}$ of error . More importantly, the qualitative trends in frequency shifts for different metal centers are reproduced correctly. This agreement illustrates the capability of our computer simulation technique and confirms our hypothesis that the observed H_2 frequency shifts are only related to the primary adsorption sites (i.e., can be reproduced without considering any secondary sites).

8.3.3 CO_2 Frequency Shifts — Normal Modes

In contrast to the results for H_2, in the CO_2 frequency calculations we performed B3LYP-D and PBE0-D generate very similar structures and intrinsically same frequency shifts. For the sake of consistency, the

PBE0-D/PBE0-D level of theory is utilized in the remainder of the CO_2 study. Both the symmetric and asymmetric vibrational modes of CO_2 are investigated, results of which are shown in Table 8.2.

(cm^{-1})	$\Delta\omega_{sym}$	$\Delta\omega_{asym}$	$\Delta\omega_{asym}(exp^a)$	E_{ad} $(kJ/mol)^b$
Co	-4	-6	-8	-34.01
Fe	-4	-5	-8	-32.32
Mg	-2	2	4	-44.36
Mn	-4	-5	-6	-32.70
Ni	-5	-6	-6	-38.90
Zn	-4	-6	-9	-32.51

Table 8.2. CO_2 anharmonic frequency shifts ($\Delta\omega$) calculated at PBE0-D/PBE0-D level of theory for both symmetric and asymmetry vibration modes; a) experimental values are provided by Rowsell group; b) the adsorption energies are computed using PBE0-D method

Since systematic experimental data are currently not available for the symmetric mode, so we only list the asymmetric experimental data for comparison. Our calculation successfully reproduces the experimental shifts to within a few wave numbers, and captures the blue shift of Mg/MOF-74 system. As a comparison, we also calculated the adsorption energy of CO_2 on different metal centers. The results given in Table 8.2 show no obvious correlation can between the IR frequency shifts and the binding strength. Therefore, it is not immediately clear how the binding environment affects the experimental IR frequency data, and deeper analysis is required to understand the true physical meaning.

8.3.4 CO_2 Frequency Shifts — Local Modes

A characteristic of the CO_2 results is that the normal mode frequency shifts are relatively much smaller than in the H_2 case. Since the normal modes (symmetric and asymmetric stretching) are the results of two strongly coupled local vibrational modes (C2-O1 and C2-O3 bonds), the normal mode shifts are delicate and hard to understand. To avoid this problem, we conducted local mode analysis on all the systems using the harmonic approximation (Table 8.3).

(cm^{-1})	$\Delta\omega_{C2\text{-}O1}$	$\Delta\omega_{C2\text{-}O3}$	ω_{coupl}	$\Delta\omega_{sym}$	$\Delta\omega_{asym}$
Co	-48	38	-446	-5	-6
Fe	-43	34	-448	-4	-5
Mg	-53	53	-447	-3	2
Mn	-45	35	-446	-5	-5
Ni	-56	44	-446	-5	-6
Zn	-46	35	-448	-4	-6

Table 8.3. Local mode analysis results. The two local mode shifts are denoted as $\Delta\omega_{C2\text{-}O1}$ and $\Delta\omega_{C2\text{-}O3}$, the two normal mode shifts as $\Delta\omega_{sym}$ and $\Delta\omega_{asym}$, and the coupling strength as ω_{coupl}.

The normal mode frequencies in Table 8.3 are derived by solving the secular equation of harmonic local modes (Eqn. (8.9)), thus are calculated at harmonic level. Still, these shifts are highly comparable with the anharmonic ones in Table 8.2, showing that the harmonic approximation is fairly reasonable for calculating relative frequency shifts, even though it is not sufficiently accurate for calculating absolute vibrational frequencies. Since we are primarily interested in relative shifts, rather than absolute, no anharmonicity correction is performed in the following analysis.

As shown in Table 8.3, the C2-O1 modes of adsorbed CO_2 are red shifted compared to the gas phase, which makes sense in light of the M-O1 back bonding that weakens the C2-O1 bond. However, the other bond (C2-O3) is blue shifted in all systems, since the CO_2 molecule is deformed in the way that the C2-O3 bond is shortened, while C2-O1 bond is elongated. The coupling between the two local modes is approximately constant, thus the delicate shifts observed in the normal modes are merely a result of cancellation between the two local mode shifts. The local modes shifts are much more prominent compared to the normal modes, and are more directly related to the binding environment. It is these local mode shifts that carry physical meaning, rather than the normal modes.

	Δq_{CO2}	E_{ad}(kJ/mol)	$\Delta\omega_{C2\text{-}O1}$(cm^{-1})	$\Delta\omega_{C2\text{-}O3}$(cm^{-1})	$r_{C2\text{-}O1}$(Å)	$r_{C2\text{-}O3}$(Å)
Co	0.060	-34.01	-48.12	37.52	1.164	1.150
Fe	0.052	-32.32	-43.02	33.78	1.163	1.151
Mg	0.061	-44.36	-53.26	52.70	1.165	1.148
Mn	0.051	-32.70	-45.22	34.80	1.163	1.151
Ni	0.072	-38.90	-55.55	44.33	1.165	1.149
Zn	0.051	-32.51	-45.66	35.35	1.163	1.151

Table 8.4. Local mode frequency shifts and other relevant calculated properties. The CO_2 electron depletion Δq_{CO2} is calculated through NBO analysis. And the adsorption energies are computed at PBE0-D level of theory. The two bond lengths are also optimized at PBE0-D level of theory

In Table 8.4, we compare the calculated local mode shifts with various other calculated properties in order to understand the physical origins of the local mode frequency shifts and their relationship with the binding strength. First of all, the adsorption energy correlates with the local mode shifts and the two local bond lengths ($r_{C2\text{-}O1}$ and $r_{C2\text{-}O3}$) with excellent precision (see Table 8.4 and Figure 8.5 a-d). This result confirms the correlation between the binding strength and the deformation of the CO_2 geometry, as might be expected. Furthermore, the vibrational frequency shifts of the local modes are dominated by the magnitude of the CO_2 deformation. However, as shown in Figure 8.5a, Mg/MOF-74 system is an exception in the $E_{ad}/\Delta\omega_{C2\text{-}O1}$ correlation. Especially compared to the strong binding energy, the frequency of the C2-O1 vibrational mode is not red shifted to a corresponding degree, and behaves differently (generating a blue shifted asymmetric stretching normal mode, instead of red shifted) from the other local mode (C2-O3). This phenomenon explains the origin of the special blue shift of the CO_2 asymmetric stretch observed in the Mg/MOF-74 system, since one of two local modes of CO_2 is not red shifted enough.
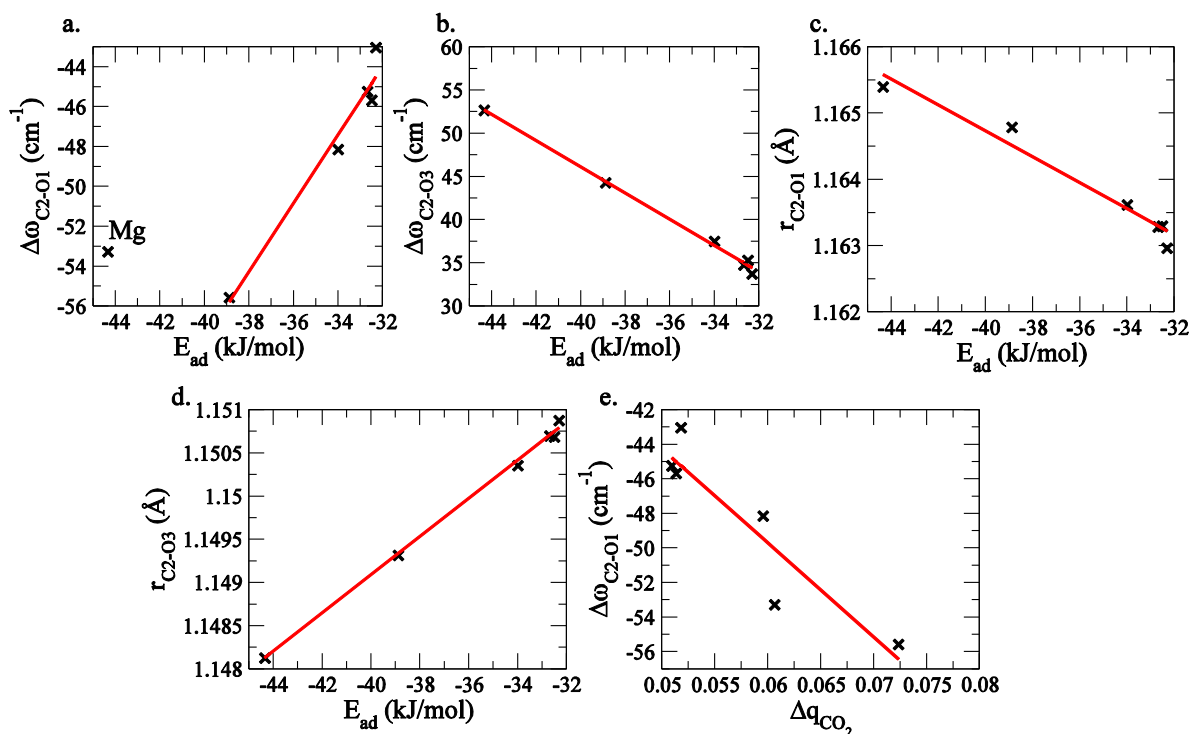
Figure 8.5. Correlations between various properties in Table 8.4; in plot a), Mg/MOF-74 system is labeled as an exception to the linear correlation.

In order to understand the specialty of the Mg/MOF-74 in more detail, we performed NBO analyses for each MOF-74 system, calculating the number of electrons depleted from CO_2 to the metal center. As shown in Table 8.4 and Figure 8.5e, the C2-O1 frequency shifts of all systems, including Mg/MOF-74, correlate well with the CO_2 electron depletion. This observation illustrates that the C2-O1 frequency shifts are in fact more correlated with the charge transfer between the CO_2 and the metal, rather than simply connected to geometry deformations. The Mg^{2+} center induces the greatest polarization in CO_2, leading to large CO_2 geometry deformations and a higher binding energy via electrostatics. However, the metal center does not show a high affinity for the CO_2 electron, probably due to a lack of low-lying unoccupied d/s orbitals. Therefore, the C2-O1 bond does not show a more prominent red shift, leading to the blue shift of the asymmetric stretching mode of CO_2.

8.4 Conclusion

IR spectroscopy has been utilized as an important tool to study the chemical environment of small gas molecules adsorbed in the metal organic frameworks. The vibrations of guest molecules are very sensitive to the local bonding environment, so the vibrational frequency shifts of certain modes may provide critical information about the interaction details between the adsorbate and adsorbent.

Recently, interest has been raised towards the M/MOF-74 systems due to their excellent performance on CO_2 adsorption and H_2 storage, and IR experiments have been conducted on these systems. In this study, utilizing computer simulation techniques, we successfully reproduced experimental data for the adsorbed CO_2 and H_2 molecules in M/MOF-74 systems. Furthermore, we resolved a few arguments exist in the experimental data. We clarified the physical meaning of the large red shifts arising from H_2 absorption, and deduced the origin of the delicate blue shift observed upon CO_2 absorption in Mg/MOF-74. We illustrated that the red shifts of the H_2 molecule are completely introduced through a metal-H_2 interaction, lending no evidence to the involvement of the secondary sites. We also demonstrated that the observed frequency shifts stemming from CO_2 absorption are a result of cancellations between the red shifted C2-O1 modes and blue shifted C2-O3 modes. And Mg/MOF-74 shows a slight blue shift due to the a weakened charge transfer between absorbed CO_2 and Mg^{2+}, likely due to a lack of low lying unoccupied d/s orbitals in Mg^{2+} that is present for other metals.

In conclusion, we demonstrate the advantage of computer simulation techniques for predicting experimental IR results and providing deep insights into the binding interactions between metals and adsorbates. Further calculations can be performed to study additional metal centers and offer more detailed guidelines on optimizing and designing new MOFs.

Bibliography

1.   Bhattacharjee, S.; Choi, J. S.; Yang, S. T.; Choi, S. B.; Kim, J.; Ahn, W. S., Solvothermal Synthesis of Fe-MOF-74 and Its Catalytic Properties in Phenol Hydroxylation. *J Nanosci Nanotechno* **2010,** 10, (1), 135-141.

2.   Bloch, E. D.; Murray, L. J.; Queen, W. L.; Chavan, S.; Maximoff, S. N.; Bigi, J. P.; Krishna, R.; Peterson, V. K.; Grandjean, F.; Long, G. J.; Smit, B.; Bordiga, S.; Brown, C. M.; Long, J. R., Selective Binding of O-2 over N-2 in a Redox-Active Metal-Organic Framework with Open Iron(II) Coordination Sites. *J Am Chem Soc* **2011,** 133, (37), 14814-14822.

3.   Dietzel, P. D. C.; Blom, R.; Fjellvag, H., Base-induced formation of two magnesium metal-organic framework compounds with a bifunctional tetratopic ligand. *Eur J Inorg Chem* **2008**, (23), 3624-3632.

4.   Dietzel, P. D. C.; Johnsen, R. E.; Blom, R.; Fjellvag, H., Structural changes and coordinatively unsaturated metal atoms on dehydration of honeycomb analogous microporous metal-organic frameworks. *Chem-Eur J* **2008,** 14, (8), 2389-2397.

5.   Dietzel, P. D. C.; Morita, Y.; Blom, R.; Fjellvag, H., An in situ high-temperature single-crystal investigation of a dehydrated metal-organic framework compound and field-induced magnetization of one-dimensional metaloxygen chains. *Angew Chem Int Edit* **2005,** 44, (39), 6354-6358.

6.   Matzger, A. J.; Caskey, S. R.; Wong-Foy, A. G., Dramatic tuning of carbon dioxide uptake via metal substitution in a coordination polymer with cylindrical pores. *J Am Chem Soc* **2008,** 130, (33), 10870-10871.

7.   Rosi, N. L.; Kim, J.; Eddaoudi, M.; Chen, B. L.; O'Keeffe, M.; Yaghi, O. M., Rod packings and metal-organic frameworks constructed from rod-shaped secondary building units. *J Am Chem Soc* **2005,** 127, (5), 1504-1518.

8.   Liu, Y.; Kabbour, H.; Brown, C. M.; Neumann, D. A.; Ahn, C. C., Increasing the density of adsorbed hydrogen with coordinatively unsaturated metal centers in metal-organic frameworks. *Langmuir* **2008,** 24, (9), 4772-4777.

9.   Rowsell, J. L. C.; Yaghi, O. M., Effects of functionalization, catenation, and variation of the metal oxide and organic linking units on the low-pressure hydrogen adsorption properties of metal-organic frameworks. *J Am Chem Soc* **2006,** 128, (4), 1304-1315.

10.   Zhou, W.; Wu, H.; Yildirim, T., Enhanced H-2 Adsorption in Isostructural Metal-Organic Frameworks with Open Metal Sites: Strong Dependence of the Binding Strength on Metal Ions. *J Am Chem Soc* **2008,** 130, (46), 15268–15269.

11.   FitzGerald, S. A.; Burkholder, B.; Friedman, M.; Hopkins, J. B.; Pierce, C. J.; Schloss, J. M.; Thompson, B.; Rowsell, J. L. C., Metal-Specific Interactions of H-2 Adsorbed within Isostructural Metal-Organic Frameworks. *J Am Chem Soc* **2011,** 133, (50), 20310-20318.

12.   FitzGerald, S. A.; Hopkins, J.; Burkholder, B.; Friedman, M.; Rowsell, J. L. C., Quantum dynamics of adsorbed normal- and para-H-2, HD, and D-2 in the microporous framework MOF-74 analyzed using infrared spectroscopy. *Physical Review B* **2010,** 81, (10), 104305.

13.   Nijem, N.; Kong, L. Z.; Zhao, Y. G.; Wu, H. H.; Li, J.; Langreth, D. C.; Chabal, Y. J., Spectroscopic Evidence for the Influence of the Benzene Sites on Tightly Bound H-2 in Metal-Organic Frameworks with Unsaturated Metal Centers: MOF-74-Cobalt. *J Am Chem Soc* **2011,** 133, (13), 4782-4784.

14.   Nijem, N.; Canepa, P.; Kong, L. Z.; Wu, H. H.; Li, J.; Thonhauser, T.; Chabal, Y. J., Spectroscopic characterization of van der Waals interactions in a metal organic framework with unsaturated metal centers: MOF-74-Mg. *J Phys-Condens Mat* **2012,** 24, (42), 424203.

15.   Valenzano, L.; Civalleri, B.; Chavan, S.; Palomino, G. T.; Arean, C. O.; Bordiga, S., Computational and Experimental Studies on the Adsorption of CO, N_2, and CO_2 on Mg-MOF-74. *J Phys Chem C* **2010,** 114, (25), 11185-11191.

16.   Valenzano, L.; Vitillo, J. G.; Chavan, S.; Civalleri, B.; Bonino, F.; Bordiga, S.; Lamberti, C., Structure-activity relationships of simple molecules adsorbed on CPO-27-Ni metal-organic framework: In situ experiments vs. theory. *Catal Today* **2012,** 182, (1), 67-79.

17.   Yao, Y. P.; Nijem, N.; Li, J.; Chabal, Y. J.; Langreth, D. C.; Thonhauser, T., Analyzing the frequency shift of physiadsorbed CO_2 in metal organic framework materials. *Physical Review B* **2012,** 85, (6), 064302.

18.   Kresse, G.; Furthmuller, J., Efficiency of ab-initio total energy calculations for metals and semiconductors using a plane-wave basis set. *Comput. Mater. Sci.* **1996,** 6, (1), 15-50.

19.   Kresse, G.; Furthmuller, J., Efficient iterative schemes for ab initio total-energy calculations using a plane-wave basis set. *Physical Review B* **1996,** 54, (16), 11169-11186.

20.   Kresse, G.; Hafner, J., Ab initio molecular dynamics for liquid metals. *Physical Review B* **1993,** 47, (1), 558-561.

21.   Kresse, G.; Hafner, J., Ab initio molecular-dynamics simulation of the liquid-metal–amorphous-semiconductor transition in germanium. *Physical Review B* **1994,** 49, (20), 14251-14269.

22.   Kresse, G.; Joubert, D., From ultrasoft pseudopotentials to the projector augmented-wave method. *Physical Review B* **1999,** 59, (3), 1758-1775.

23.   Grimme, S., Semiempirical GGA-type density functional constructed with a long-range dispersion correction. *J Comput Chem* **2006,** 27, (15), 1787-1799.

24.   Weigend, F.; Ahlrichs, R., Balanced basis sets of split valence, triple zeta valence and quadruple zeta valence quality for H to Rn: Design and assessment of accuracy. *Phys Chem Chem Phys* **2005,** 7, (18), 3297-3305.

25.   M. J. Frisch, G. W. T., H. B. Schlegel, G. E. Scuseria, M. A. Robb, J. R. Cheeseman, G. Scalmani, V. Barone, B. Mennucci, G. A. Petersson, H. Nakatsuji, M. Caricato, X. Li, H. P. Hratchian, A. F. Izmaylov, J. Bloino, G. Zheng, J. L. Sonnenberg, M. Hada, M. Ehara, K. Toyota, R. Fukuda, J. Hasegawa, M. Ishida, T. Nakajima, Y. Honda, O. Kitao, H. Nakai, T. Vreven, J. A. Montgomery, Jr., J. E. Peralta, F. Ogliaro, M. Bearpark, J. J. Heyd, E. Brothers, K. N. Kudin, V. N. Staroverov, R. Kobayashi, J. Normand, K. Raghavachari, A. Rendell, J. C. Burant, S. S. Iyengar, J. Tomasi, M. Cossi, N. Rega, J. M. Millam, M. Klene, J. E. Knox, J. B. Cross, V. Bakken, C. Adamo, J. Jaramillo, R. Gomperts, R. E. Stratmann, O. Yazyev, A. J. Austin, R. Cammi, C. Pomelli, J. W. Ochterski, R. L. Martin, K. Morokuma, V. G. Zakrzewski, G. A. Voth, P. Salvador, J. J. Dannenberg, S. Dapprich, A. D. Daniels, Ö. Farkas, J. B. Foresman, J. V. Ortiz, J. Cioslowski, and D. J. Fox *Gaussian 09, Revision A.1*, Gaussian, Inc.: Wallingford CT, 2009.

26.   H.-J.Werner; Knowles, P. J.; Lindh, R.; Manby, F. R.; Schutz, M.; Celani, P.; Korona, T.; Mitrushenkov, A.; Rauhut, G.; Adler, T. B.; Amos, R. D.; Bernhardsson, A.; Berning, A.; Cooper, D. L.; Deegan, M. J. O.; Dobbyn, A. J.; Eckert, F.; Goll, E.; Hampel, C.; Hetzer, G.; Hrenar, T.; Knizia, G.; K¨oppl, C.; Liu, Y.; Lloyd, A. W.; Mata, R. A.; May, A. J.; McNicholas, S. J.; Meyer, W.; Mura, M. E.; Nicklass, A.; Palmieri, P.; Pfluger, K.; Pitzer, R.; Reiher, M.; Schumann, U.; Stoll, H.; Stone, A. J.; Tarroni, R.; Thorsteinsson, T.; M.Wang; Wolf, A. *MOLPRO, version 2009.1, a package of ab initio programs, see http://www.molpro.net*.

27.   Colbert, D. T.; Miller, W. H., A Novel Discrete Variable Representation for Quantum-Mechanical Reactive Scattering Via the S-Matrix Kohn Method. *Journal of Chemical Physics* **1992,** 96, (3), 1982-1991.

28.   Wilson, E. B.; Decius, J. C.; Cross, P. C., *Molecular Vibrations: The Theory of Infrared and Raman Vibrational Spectra (Dover Books on Chemistry)*. Dover Publications Mineola, New York, 1980.

Chapter 9. Conclusions and Future Directions

Table of Contents

9.1 Conclusions

This thesis presents a systematic theoretical and computational study on the gas (particularly CO_2) adsorption behavior of metal organic frameworks (MOFs). Various techniques, including electronic structure calculations and classical MC/MD simulations, are utilized to understand the physics of adsorption and help designing MOFs with better performance.

In chapter 2 and 3, we develop a highly robust force field for CO_2 and N_2 (the so-called SYM model)[1,2] based on rigorous DFT-SAPT calculations. Intermolecular interactions are computed accurately and are decomposed into several physically meaningful terms, each of which is fit with physically-motivated functional forms. The resulting potential reproduces both various bulk properties and dimer/trimer

properties in extraordinary precision, outperforming all existing empirical models. This novel CO_2 model is particularly suited to CO_2 adsorption simulations in micro-porous systems due to the aforementioned capability of describing both local interactions and bulk behavior. The success of the SYM model also confirms the validity of our force field construction scheme, which is based on first-principles calculations and is free of empirical parameters.

Particularly, in chapter 3, we discuss the importance of non-electrostatic many-body effects in a real physically-motivated force field.[2] Using CO_2 as an example, we separate non-electrostatic many-body effects from other parts of the interaction energy, including them explicitly in our force field. Furthermore, we discuss the mean field approach of accounting for many-body effects, demonstrating a rigorous but simpler way of building a robust ab-initio force field.

Following the philosophy of the previous two chapters, in chapter 4, we parametrize a force field in order to study ZIFs, a particular class of MOFs.[3] The resulting ZIFFF force field is also based on rigorous SAPT energy decompositions and is constructed consistently with the SYM model. Combining the two potentials, we are able to reproduce the CO_2 adsorption isotherms of various ZIF systems without any empirical inputs. The accuracy and robustness of the new force field are verified; ZIFFF is ready to be applied to structure designing and large-scale screening.

Since the ZIFFF and SYM force fields are polarizable, self-consistent iterations are required to converge the Drude oscillator positions during the simulation. Compared to standard non-polarizable models, our force field is one order of magnitude slower in energy evaluation. Furthermore, it must be used in conjunction with a hybrid MC sampling algorithm, which is less efficient than traditional GCMC. Therefore, in order to accelerate calculations, we develop a lattice model based fast simulation technique in chapter 5.[4] We show that through mapping the continuous potential onto a discretized three-dimensional lattice, we can achieve two to three orders of magnitude of acceleration, while keeping

comparable accuracy. This method can be utilized in conjunction with both polarizable and non-polarizable force fields, enabling tremendous possibilities for more accurate and larger scale screening.

Combining both the potential and the fast simulation method, we study the "synergistic effects" observed in the mixed ligand MOFs in chapter 6.[5] We clarify that these synergistic effects are due to multiple contacts between the guest molecules and different types of ligand side chains. Based on this assumption, we discuss many factors that might affect synergistic effects, including guest molecule size, side chain length, functionalization order, and cell topology. More importantly, we screen over many different types of MOF geometries and identified the most promising structures for synergistic enhancement.

In chapter 7, we focus on the MOFs with coordinatively unsaturated metal centers, which are structurally and empirically distinct from the coordinatively saturated MOFs discussed in the previous chapters.[6] We are interested in studying the effects of the flue gas contaminants on the exposed metal sites, which are also the main adsorbing center of CO_2 molecules. Using Mg/MOF-74 and MIL-101 as model systems, we investigate the interactions of various contaminant species with metal centers. Through DFT calculations and Langmuir model analysis, the most problematic contaminants at the industrial relevant conditions are identified.

Finally, in chapter 8, we compute the vibrational frequency shifts of arising from H_2 and CO_2 absorption in the M/MOF-74 series of MOFs. Semi-quantitative agreement is achieved between our computed frequency shifts and experimental results. The physical origin of the observed shifts as well as their correlation with binding strength is discussed. Several arguments existing in the experimental community are clarified.

In general, we set up a common way of predicting the adsorption behaviors of different types of MOFs, based on both high accuracy electronic structure methods and fast simulation techniques. Using these

computational tools, we study various potentially useful MOF structures and contribute to the designing and discovering CO_2 adsorbents with better performance.

9.2 Future Directions

The work presented in this thesis can be extended in several pertinent directions. Firstly, all computer simulations in this thesis were conducted using the rigid framework approximation, in which guest molecules are allowed free movement and all MOF atoms are held fixed. This is a reasonable assumption for many loading isotherm calculations; still, framework flexibility is highly important for other classes of MOFs. For example, it is known that MOFs such as MIL-53[7] undergo structure deformations while interacting with guest molecules. Also, for systems with small window diameters, such as ZIF-8, thermal fluctuations of the framework atoms play critical role in guest molecule diffusion process.[8] Therefore, in order to simulate these phenomena, new terms should be implemented in the force filed to describe the intramolecular potential. While SAPT is accurate in computing weak intermolecular interactions, it is not suitable to study molecule deformations. Hence, new strategies are required to derive the intramolecular portion of the total system energy, possibly based on a DFT or MP2 level of theory.

Force field parameters are also needed for systems with open metal sites, which are dominated by strong electrostatic interactions. Some of these systems have well defined adsorption sites and can be described using simple Langmuir type models, while finite temperature sampling is necessary for other cases, especially at high pressure region. The truncated perturbation theory breaks down for strong guest-metal interactions, and the open shell multi-reference electronic structures of the transition metal ions can create extra complications. Therefore, more work needs to be done to explore the strengths and limitations of the SAPT methodology. New methodologies must be developed to decompose interaction energies in cases where a SAPT-based approach fails.

Finally, we are interested in generalizing our SAPT based strategy to construct a single force field for generic organic systems. In order to reproduce the bulk properties of various types of organic molecules, we need to implement intramolecular potentials as well as non-induction many body effects. A common approach needs to be developed to compute the transferrable many-body interaction parameters for general organic molecules. An accurate scheme will be required to account these many body contributions using simple and affordable functionals.

In summary, our ab initio force field development methodology needs to be extended to even more general situations. In order to accomplish this goal, new techniques are required to incorporate intramolecular potential, strong electrostatic interaction and many body effects.

Bibliography

1.   Yu, K.; McDaniel, J. G.; Schmidt, J. R., Physically Motivated, Robust, ab Initio Force Fields for CO_2 and N_2. *J Phys Chem B* **2011,** 115, (33), 10054-10063.

2.   Yu, K.; Schmidt, J. R., Many-body effects are essential in a physically motivated CO_2 force field. *Journal of Chemical Physics* **2012,** 136, (3), 034503.

3.   McDaniel, J. G.; Yu, K.; Schmidt, J. R., Ab Initio, Physically Motivated Force Fields for CO_2 Adsorption in Zeolitic Imidazolate Frameworks. *J Phys Chem C* **2012,** 116, (2), 1892-1903.

4.   Yu, K.; McDaniel, J. G.; Schmidt, J. R., An efficient multi-scale lattice model approach to screening nano-porous adsorbents. *Journal of Chemical Physics* **2012,** 137, (24), 244102.

5.   Yu, K.; McDaniel, J. G.; Schmidt, J. R., Microscopic Origins of Enhanced Gas Adsorption and Selectivity in Mixed-Linker Metal-Organic Frameworks. *J Phys Chem C, submitted* **2013**.

6.   Yu, K.; Kiesling, K.; Schmidt, J. R., Trace Flue Gas Contaminants Poison Coordinatively Unsaturated Metal-Organic Frameworks: Implications for CO_2 Adsorption and Separation. *J Phys Chem C* **2012,** 116, (38), 20480-20488.

7.   Walker, A. M.; Civalleri, B.; Slater, B.; Mellot-Draznieks, C.; Cora, F.; Zicovich-Wilson, C. M.; Roman-Perez, G.; Soler, J. M.; Gale, J. D., Flexibility in a Metal-Organic Framework Material Controlled by Weak Dispersion Forces: The Bistability of MIL-53(Al). *Angew Chem Int Edit* **2010,** 49, (41), 7501-7503.

8.   Fairen-Jimenez, D.; Moggach, S. A.; Wharmby, M. T.; Wright, P. A.; Parsons, S.; Duren, T., Opening the Gate: Framework Flexibility in ZIF-8 Explored by Experiments and Simulations. *J Am Chem Soc* **2011,** 133, (23), 8900-8902.